Experimental study of the Fe-Si-C system and application to carbon rich exoplanet

Francesca Miozzi Ferrini

Sorbonne Université

Ecole doctorale: Géosciences Ressources Naturelles et Environnement

Laboratoire: IMPMC/Equipe: Minéralogie, Pétrologie et physique planétaire

Experimental study of the Fe-Si-C system and application to carbon rich exoplanets

Par Francesca MIOZZI FERRINI

Thèse de doctorat en Science de la Terre

Dirigée par Guillaume MORARD et Guillaume FIQUET

Présentée et soutenue publiquement le 3 juillet 2019

Devant un jury composé de :

M. James BADRO	Directeur de recherche CNRS - Université de Paris	Rapporteur
Mme. Anat SHAHAR	Senior Scientist - Carnegie Institution for Science	Rapporteuse
M. Sébastien MERKEL	Professeur - Université de Lille	Examinateur
Mme. Chrystèle SANLOUP	Professeur - Sorbonne Université	Examinatrice
Mme. Giovanna TINETTI	Professor - University College London	Examinatrice
M. Pierre BECK	Maître de conference - Université Grenoble Alpes	Examinateur
M. Guillaume FIQUET	Directeur de recherche CNRS - Sorbonne Université	Co-directeur de thèse
M. Guillaume MORARD	Chargé de recherche CNRS - Sorbonne Université	Directeur de thèse

Per Marmot

Abstract

In recent years the quest for new habitable worlds outside our solar system lead to the discovery of thousands of different exoplanets orbiting around stars with variable compositions. For part of the planets, combining the parameters obtained through indirect observations (i.e. mass and radius), the mean density can be determined. However this observable is not sufficient to characterize the inner structure of observed planets. The composition of the host star serves as a proxy for the chemical composition. Within all the detected host stars, some are enriched in carbon compared to the Sun, with C/O close to unity (C/O = 0.78 ± 0.19). In these conditions, carbides are potentially the first phase to condensate instead of silicates, highlighting the potential existence of carbon enriched planets, which would represent a "negative" of the Earth enriched in oxygen and mainly composed by silicates. Planetary interiors represent the key for all the characteristics that make a planet habitable, as plate tectonic, the presence of a magnetic field and the possibility to retain an atmosphere. Given the particularity of carbon enriched planets, having a better understanding of their composition, interior structure and properties, as well as being able to identify them from astronomical observables, is fundamental to study planetary diversity and as well for future exoplanets missions that will require accurate target selection.

Using synchrotron X-ray diffraction and laser heated diamond anvil cells, alloys in the ternary Fe-Si-C and binary Si-C systems were studied up to 200 GPa and 4000 K. Together with the phase diagram and melting curves, the equations of state and thermal model of the stable phases were retrieved. The results, applied to exoplanets interior, provide an insight on the potential core composition and dynamic in carbon enriched planets, and the dynamic of an SiC mantle. The results are used to discuss the mass radius relation and mantle dynamic in carbon enriched planets with a SiC mantle and potential core composition with a higher light elements content than the Earth.

Contents

Chapter 1

Introduction

Exoplanets represent one of the most intriguing discovery of the last decades and a big step toward the discovery of potentially habitable worlds. Since the first exoplanets were discovered (Wolszczan and Frail, 1992) (Mayor and Queloz, 1995), the number of detections has exponentially increased. The progress in technology and the launch of dedicated missions such as Kepler (Borucki et al., 2011, 2010) and more recently Tess (Stassun et al., 2018) have been decisive for the detection of almost 4000 confirmed exoplanets (https://exoplanetarchive.ipac.caltech.edu/index.html) orbiting around different type of stars, not only sun like, but also pulsars and dwarfs.

The discovery of extrasolar planets has been a breakthrough in space science due to the many implications and research pathways it opened. One of the main quest of this research field is discovering planets with potential habitable surface (*An Astrobiology Strategy for the Search for Life in the Universe*, 2019; Lammer et al., 2009; Seager, 2013). The presence of many planets with Earth's like mass and radius orbiting around different type of stars provides a unique insight to explore planetary diversity and at the same time use our solar system as a reference. Understanding and being able to recognize the diversity of exoplanets potentially encountered (e.g. coreless planets (Elkins-Tanton and Seager, 2008); carbon rich planets (Madhusudhan et al., 2012); water worlds (Sotin et al., 2010)) is fundamental. The need of defining the main properties of such distant worlds and potentially restrain the search of Earth-like planets for future mission, boosted the interest in developing the techniques to gain more detail and improve the precision of the observations made on these planets.

The possibility of a planet to originate and maintain life is defined as its habitability (Lammer et al., 2009). As a first approximation, habitability can be defined by several requirements: i) the possibility of accumulating the necessary building blocks vital for life (i.e. C, H, O, N and several other elements); ii) the presence of liquid water and environmental conditions that allow the liquid water to exist and be maintained. These main requirements imply the presence of other characteristics related to the planetary interior that otherwise would make difficult the occurrence of life. For example, plate tectonics (Noack and Breuer, 2014; Unterborn et al., 2017; Valencia and O'Connell, 2009), an active dynamo (e.g. Gaidos et al., 2010), and an atmosphere (Madhusudhan et al., 2011; Seager, 2013) are those depending on the interior of the planet and require an evaluation of the mineralogy and interior structure to be assessed.

1.1 Detection, mass, radius and stellar composition

Detected exoplanets are characterized through indirect measurements, using parameters (i.e. observables) obtained through observations with different instrumentations. Mass and radius are the most common properties measured for an exoplanet, giving then an average density (Lissauer and De Pater, 2013).

To detect these planets a variety of techniques is available. The most successful method has been radial velocity. It consist in measuring the variation in the stellar motion induced by the gravitational pull of an orbiting planet on the line of sight of the observer. The amplitude of velocity variations is related to the planet's properties and thus permits the determination of the mass and the orbital period of the observed planet. A complementary technique is transit photometry, the one used by Kepler and Tess missions. Planets are detected while passing in front of a star, which creates reduction of the light flux or a change in colour of the stellar flux. In presence of an orbiting companion, the curve of the light emitted by a star display a dip. The depth of the dip reveals the planet's size compared to the star's size. Furthermore, the width of the signal dip can be used to determine the duration of the transit (Borucki and Summers, 1984; Duffy, 2015; Lissauer and De Pater, 2013). These two techniques are typically used for sun-like stars. Additionally, other techniques like gravitational microlensing, pulsar timing or direct imaging can be used when planets are orbiting other types of stars (Lissauer and De Pater, 2013; Winn and Fabrycky, 2015). Measures of mass and radius give access to the mean density of the planet, which is so far the only parameter that can be used to constrain the internal structure.

The correlation between the occurrence of different type of planets and the host star metallicity (i.e. the proportion of elements heavier than H and He) was widely investigated as it is considered to provide insights on the mechanisms of planetary formation (Adibekyan, 2019; Buchhave et al., 2012; Petigura

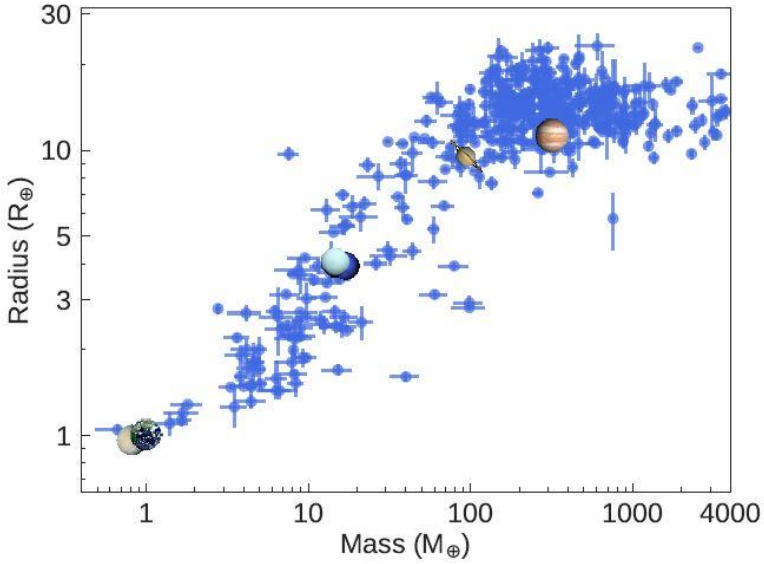

Figure 1.1: From Adibekyan et al. (2019). Mass and radius relation for discovered exoplanets. Planets of the solar system are shown for comparison.

et al., 2018; Thorngren et al., 2016). According to their mass and radius, planets are usually considered as terrestrial planets when their radius is less than 1.7 Earth radius. Neptune and sub neptune planets with a rocky core and H-He dominated envelope (radii between 1.7 and 3.9 Earth radii) or gas giant planets when the radii is above 3.9 the Earth radii as shown in Figure 1.1 (Buchhave et al., 2014; Fressin et al., 2013; Spiegel et al., 2014).

Obtained mass and radius are usually interpreted by comparison with the parameters calculated for synthetic planets, thus linking observations with an internal structure of exoplanets determined a priori (e.g. Howe et al., 2014; Seager et al., 2007; Sotin et al., 2010). Models of synthetic exoplanets consider the planet as spherically symmetric and in hydrostatic equilibrium and are constructed by solving differential equations for mass, radius and density as a function of the distance from the center (Duffy, 2015; Seager et al., 2007; Sotin et al., 2010, 2007; Valencia et al., 2006a). Density at a given radius depends on pressure and temperature and is computed through the equation of state of the chosen material. Accordingly, the chosen equation of state can strongly influence the computed mass and radius. It is thus of primary importance to have reliable equations of state for the mineral phases that are expected to be found (Baraffe et al., 2014; Sotin et al., 2010). Terrestrial planets orbiting sun-like stars are assumed to differentiate as the Earth with a metallic core surrounded by a silicate mantle (Baraffe et al., 2014; Dorn et al., 2015; Dressing et al., 2015; Howe et al., 2014; Valencia, 2013). The Earth provides the best analogue to study the thermal and compositional structure of such planets, as well as a database of physical properties for common minerals to be used for modelling. However, many other average compositions are possible, and reproducing such variability in synthetic models is fundamental to account for the observed planetary diversity and have accurate mass radius plots.

At the present state compositional variability is neglected and planetary cores are assumed to be made by pure iron. Though we know that modelling the Earth's core as a pure iron sphere leads to an overestimation of the density, as it does not take into account light elements (Poirier, 1994). An overestimation of the density translates into an underestimation of the planetary radius, thus affecting the obtained mass-radius plots as shown in Figure 1.2 (Seager et al., 2007; Unterborn et al., 2016; Wagner et al., 2011) and the interpretation of the observed data. Another factor influencing interpretation of the observational data is the degeneracy of exoplanets models. Many possible interior assemblages and compositions can result in the same mass and radius (Dorn et al., 2015; Rogers and Seager, 2010). Using self-consistent thermodynamic databases for the stable phases and correlating the properties of core and mantle to the Mg/Si and Fe/Si ratio of the host star have already proven to be a step forward in reducing this degeneracy (Dorn et al., 2017, 2015). However, additional independent constrains are needed to restrain the field of possible compositions and the chemical composition of the host star is one of those.

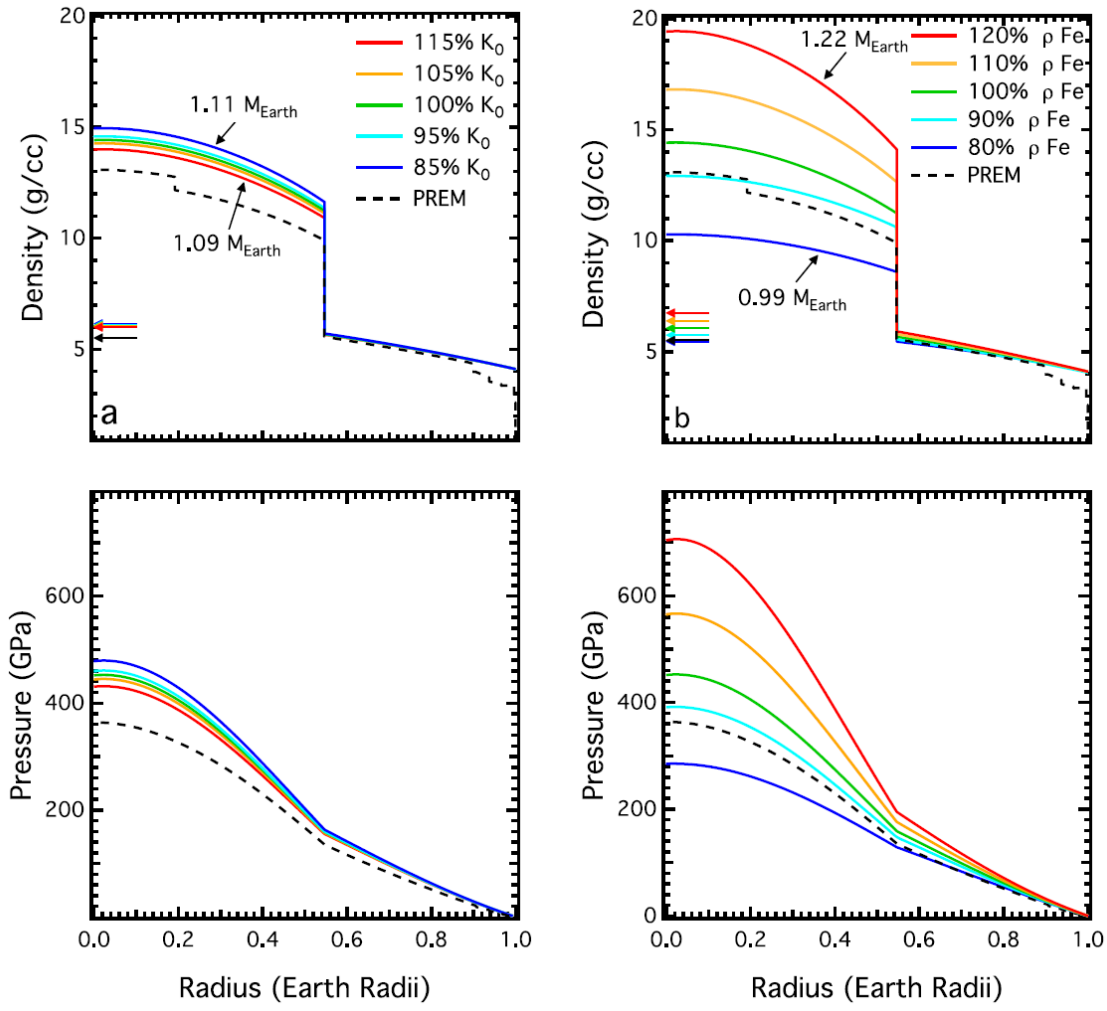

Figure 1.2: From Unterborn et al. (2016). Density pressure profiles for a one Earth radius planet with a Fe core and $MgSiO_3$ mantle.

Planets and host stars likely form in the same portion of a collapsing molecular cloud (Henning and Semenov, 2013). The chemical composition of the star is expected to reflect the one of the surrounding cloud and accordingly should be correlated with the composition of the forming planets. As such, it represents an observable useful to constrain the chemistry of exoplanets and consequently the internal structure (Hinkel and Unterborn, 2018). A first correlation between the host star metallicity and the composition of transiting giant planets was established by (Burrows et al., 2007).

Stars composition is determined through spectroscopic analyses of elemental abundances (e.g. Bond et al., 2008, 2006; Delgado Mena et al., 2010; Fischer and Valenti, 2005) and many studies focused on determining the characteristics of the observed host stars especially after the launch of Kepler (e.g. Petigura et al., 2018). Some stars have unusual chemical compositions, with systematic enrichment in Fe and smaller enrichment in other element (i.e. C. Si, Mg and Al) (Bond et al., 2006; Fischer and Valenti, 2005). Furthermore, stars with a carbon to oxygen ratio higher than the solar one (i.e. 0.55 ± 0.10) (Asplund et al., 2009; Bond et al., 2010, 2008; Delgado Mena et al., 2010) hosting planetary systems were discovered (see Figure 1.3). This boosted the interest toward carbon enriched stars (e.g. 55 Cancri) and consequently planets, providing new insights into the potential diversity of extrasolar planets and implying different formation scenarios (Bond et al., 2010; Fortney, 2012).

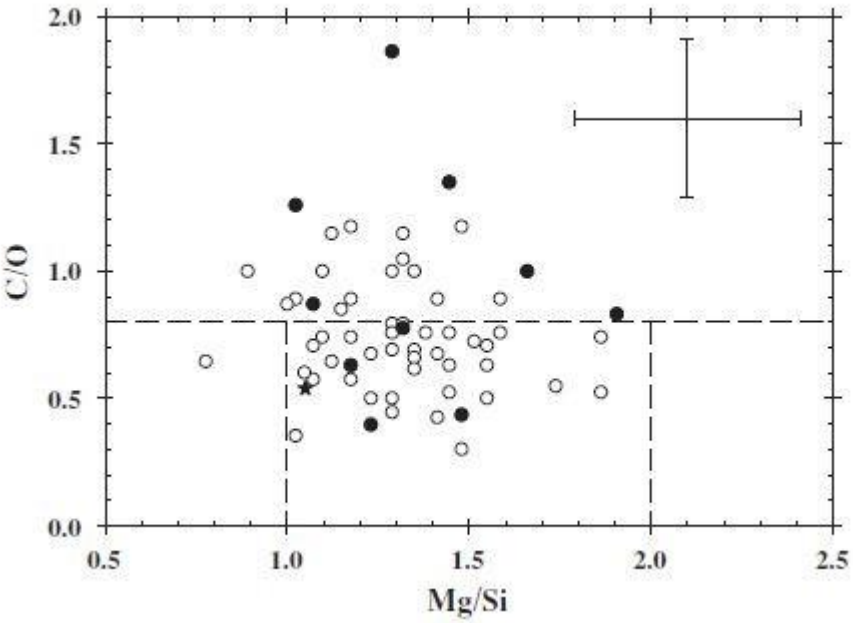

Figure 1.3: From Bond et al. (2010). C/O vs. Mg/Si for known host stars. The star symbol represents the composition of the Sun.

The composition of a planet is related to the one of the host star through the condensation of mineral species from the primordial nebula, described by the condensation sequence (e.g. Lodders, 2003; Moriarty et al., 2014). This is considered to be valid especially for refractory elements, which have a high equilibrium condensation temperature (Wang et al., 2019 and references therein). Within the planets building elements, the Mg/Si and C/O ratio play a fundamental role in defining the type of planets that are going to accrete. When the value of C/O is above 0.8 the first phase to condensate are carbides (Madhusudhan et al., 2012) (Figure 1.4) and should therefore be a major component of the forming planet. On the other hand, if the C/O ratio is lower than 0.8, Si should exist primarily in oxides, such as SiO_2. In addition, the Mg/Si ratio controls the mineralogy and the distribution among oxides and silicates (e.g. Bond et al., 2010).

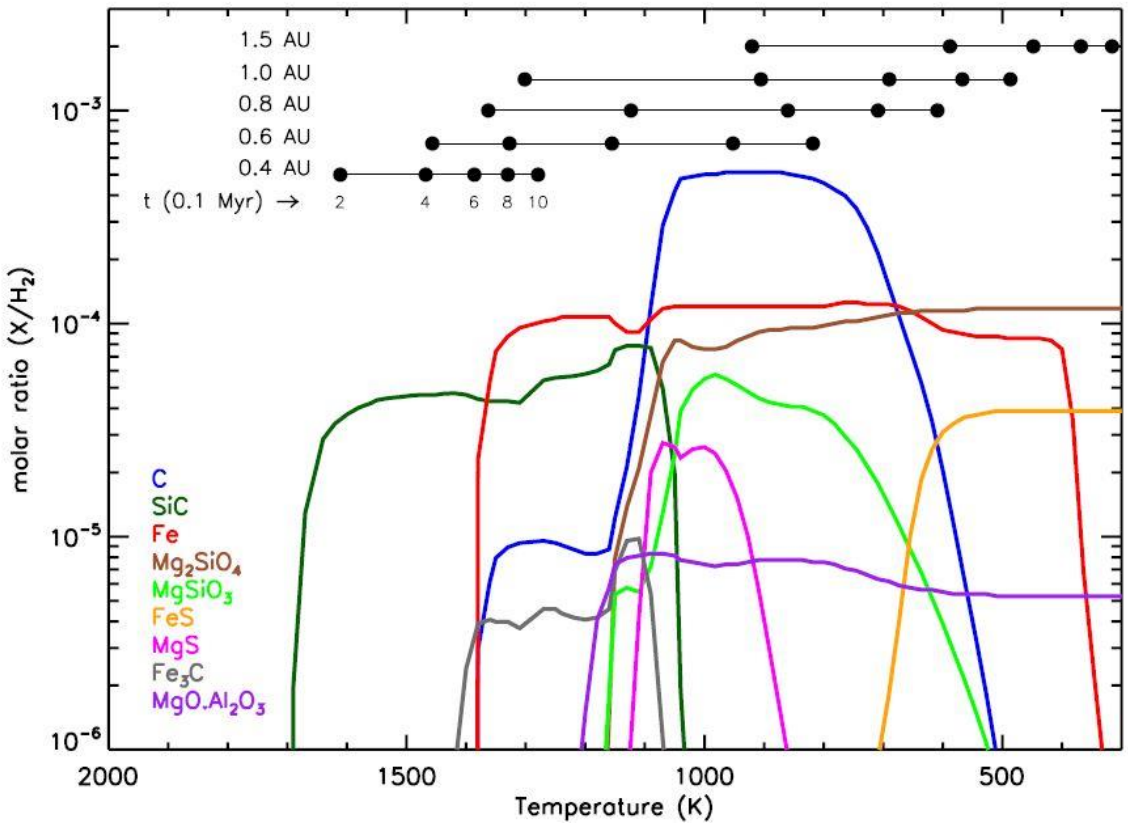

Figure 1.4: From Madhusudhan et al. (2012). Refractory condensates expected in the protoplanetary disk for the 55 Cancri system.

The potential existence of carbon enriched exoplanets has some interesting implications also in terms of planetary dynamics and consequently habitability. According to the work of (Unterborn et al., 2014) a higher carbon content in the Mg-Fe-Si-C-O system can determine the formation of extensive quantities of Fe and Si bearing carbides or diamonds. The latter, as a major component of a planetary mantle, would certainly change in the dynamics and thermal state of such a planetary body, due to the higher viscosity and a much higher thermal conductivity compared to silicates. A carbon rich interior was assumed for instance for one of the planets in the 55 Cancri system, 55 Cancri e, originally considered to have a C/O ratio of 1.12 ± 0.19 (Delgado Mena et al., 2010) and for which also mass and radius have been measured (Endl et al., 2012; Gillon et al., 2012). Using the composition of the star as a proxy, Madhusudhan and co-authors (2012) determined the possible range of interiors compositions that would satisfy the observed mass and radius. The planet was considered to be differentiated in an iron core, a silicon carbide mantle and a graphite crust. The results show how several different combinations of SiC and C would lead a planet with mass radius and density matching those observed, assuming a constant Fe content in the core. The same outcome was obtained by Wilson and Militzer (2014), assuming 55 Cancri e as formed solely by SiC.

The possibility of 55 Cancri e being a carbon enriched planet was later revised when the composition of many stars, included 55 Cancri, was reassessed (Nissen, 2013; Nissen et al., 2014; Teske et al., 2013). The newly calculated C/O (i.e. 0.78 ± 0.08) (Teske et al., 2013) is lower than previously determined.

Nevertheless, it does not exclude the possibility of local carbon enrichment in the gas or the formation of carbide grains (e.g. Ali-Dib et al., 2014; Öberg et al., 2011). The possibility of condensing carbon and silicon carbides is attested by their retrieval in both terrestrial and extra-terrestrial environments (Nazzareni et al., 2019; Zinner, 2007) and will be discussed in the following paragraph.

1.2 Occurrence of SiC in natural environments

Silicon carbide is stable at ambient conditions with a cubic (3C) structure, also referred as β-SiC, and an hexagonal (e.g. 4H, 6H and 15R) structure, referred as α-SiC (Daviau and Lee, 2018 and reference therein; Jepps and Page, 1983). The hexagonal polymorph has been named moissanite, after the first sample was discovered by Moissan in the Diablo Canyon meteorite (1905).Though the discovery has been object of controversy for almost 50 years, with Mason (1967) claiming the recovered sample to be a piece of the cutting tool. The name Moissanite usually refers only to the hexagonal polymorph, so SiC will be used in the text and the prefix α or β will be added when specification regarding the structure is needed. Natural SiC recovered on Earth, has both extra-terrestrial and terrestrial origin. The first consists in the pre solar grain found in meteorites, while the latter are inclusion found in rocks belonging to different geological contexts.

1.2.1 Extra-terrestrial SiC

After Moissan and Mason controversy, SiC presence in meteorites was ultimately confirmed when SiC grains were unambiguously found in the Murray and Murchinson meteorites (Bernatowicz et al., 1987; Ming et al., 1988; Zinner et al., 1989). Here β SiC and multi layered SiC, with 3C and 6H structures were observed together with Si aggregates nodules (Zinner, 2007). The distribution of key isotopes (e.g. Ba, C, N, Ne, and Si) ratio in the grains, displayed strong anomalies compared to the distribution known for the bulk Earth, pointing toward a pre-solar origin. The existing relation between the processes that lead to the formation of grains and isotopic composition makes it possible to trace history and evolution of the grains and ultimately the characteristics of the parent body. (Anders and Zinner, 1993; Clayton, 1988; Zinner et al., 1987). Murray and Murchinson are carbonaceous chondrites, typically enriched in volatiles (several weight % carbon), with a solar Mg/Si value but depleted in oxygen compared to the solar system. Nevertheless, SiC was found also in other type of chondrites, as enstatite chondrites dominated by $MgSiO_3$ and ordinary chondrites (Huss and Lewis, 1995), and not only in carbonaceous meteorites.

Pre-solar grains are considered as small residuals (diameter < 1μm) from stars that existed before the sun was formed (e.g. Bernatowicz and Walker, 1997; Nittler, 2003; Zinner, 2007). In star's interior, newly formed atoms condensate into dusty grains that can be expulsed in the interstellar medium by explosion or solar winds. This provides the material to form a molecular cloud that potentially will give birth to a new planetary system. At this stage, the grain's main and trace element composition is strictly

related to the parent star type, holding traces of the processes that took place (Bernatowicz and Walker, 1997; e.g. Clayton, 1988). Nevertheless, when grains composing the interstellar dust are part of an event such as the formation of a new star, their composition and isotopic ratio usually get equilibrated. The solar system experienced the same process, with the isotopic abundances determined from primitive meteorites (considered as the undifferentiated solar system material) displaying the same values as those spectroscopically determined for the Sun (Anders and Grevesse, 1989; Lodders, 2003). Some grains however present an exception, as they did not undergo the processes of homogeneization thus preserving the cosmic memory of their nucleosynthesis origin (e.g. Bernatowicz and Walker, 1997; Gallino et al., 1990; Nittler, 2003). Moreover, the recovered SiC pre-solar grains did not always show the same isotopic anomaly. Several (different) families were recognised (Figure 1.5), reflecting contributions to interstellar dust from different stars (Gallino et al., 1990; Hoppe et al., 2018; Ming et al., 1989; Nittler, 2003; O'D Alexander, 1993; Zinner, 2007)

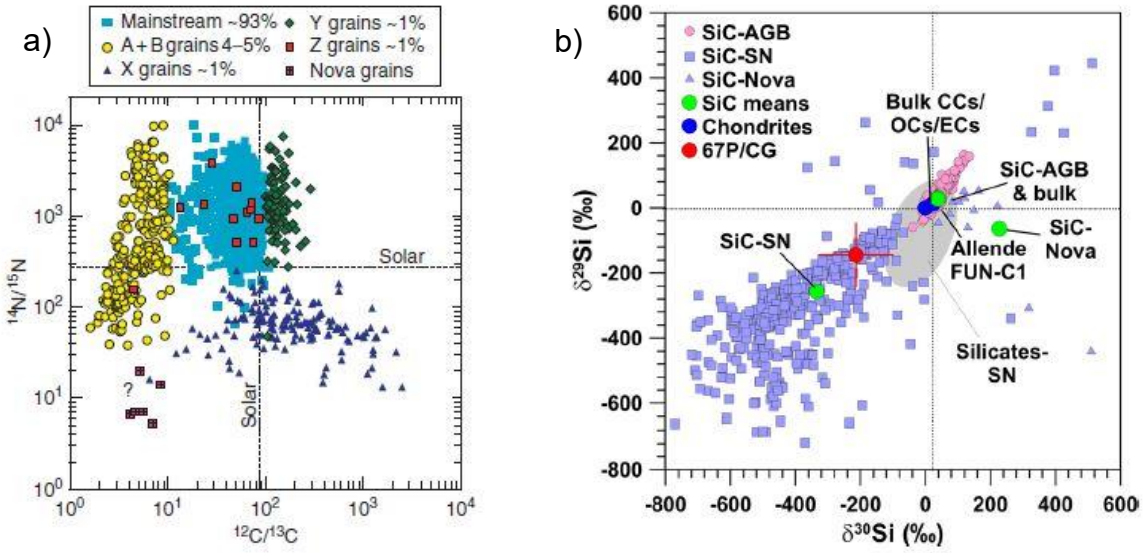

Figure 1.5: a) Isotopic ratio of C and N for several families of SiC pre-solar grains. Figure from Zinner (2007). b) isotopic composition of silicon for different group of SiC grains compared to the terrestrial abundance (chondrites) image from Hoppe et al. (2018).

Anomalies are displayed on main elements such as C, N, Si, noble gasses (e.g. He, Xe), Mg, Ca, as well as heavy elements (e.g. Sr, Zr Ba, Ru, Nd). Using the isotopic distribution, red giants from the AGB, novae and supernovae have been identified as parent stars of the retrieved grains. Red giant stars consumed almost all the available H and He, leaving a gas core surrounded by a still expanding outer layer. Here, minimum amount of He and H are still burning, producing large amount of ^{12}C and heavy elements via neutron captures in s-processes. The amount of produced carbon compared to oxygen (C/O) potentially affect the chemical assemblage and condensation temperature ultimately influencing the planetary disk. (e.g. Fortney, 2012; Larimer, 1975; Moriarty et al., 2014). When the threshold of 0.8 in the C/O is reached, stars are considered carbon enriched as well as the planets orbiting around (Bond et al., 2010). For a detailed dissertation on the occurrence of SiC in parent stars, their formation and

isotopic signature we suggest the reviews from (Bond et al., 2008; Nittler, 2003; Zinner, 2007; Zinner et al., 2006). In conclusion, the abundance of SiC and graphite in pre-solar grains serve as a demonstration that is possible to stabilize reduced phases into specific context, like carbon enriched stars (Bond et al., 2010; Madhusudhan et al., 2012).

1.2.2 SiC and FeSiC alloys in terrestrial environment

The Earth and the Sun formed in a protoplanetary disk with a carbon to oxygen ratio of 0.54 (Asplund et al., 2005; Carter-Bond et al., 2012; Delgado Mena et al., 2010). According to condensation sequences, silicates and oxides are going to be the major components of a planet accreting in such conditions, which is indeed reflected in the phases abundance observed in the Earth. However during accretion, several other processes took place, promoting mixing, re-equilibration and resulting in the actual planet. The Moon forming impact and the evolution toward a layered structure with an inner metallic core, for example, contributed to the diversity of the geological environments and consequently mineralogical assemblages (Cameron, 2001; Karato and Rama Murthy, 1997; Rama Murthy and Karato, 1997; Taylor and Esat, 2013; Walter and Trønnes, 2004). The reducing character of SiC precludes its coexistence with silicates and Fe^{2+}, thus in a typical Earth assemblage. It instead requires a highly reduced environment to form. Nevertheless, SiC grains have been found in equilibrium with different mineralogical assemblages in multiple geological contexts. For example, as inclusion in diamonds into kimberlite, rocks characterized by a fast ascent to the surface from great depths (~150 Km) (e.g. Shiryaev et al., 2011) and other mantle xenoliths, peridotites and serpentinites, minerals representative of the Earth's upper mantle (Xu et al., 2008) and in metasomatic rocks from a volcanic region (Di Pierro et al., 2003). In recent years more samples coming from volcanic environment and associated to alkali basalt eruptions were recovered (Dobrzhinetskaya et al., 2018; Nazzareni et al., 2019). All the recovered SiC grains had hexagonal (e.g. Dobrzhinetskaya et al., 2018; Xu et al., 2008) or cubic (e.g. Nazzareni et al., 2019) structures. The latter is usually associated to shallower depths and lower temperature processes (Leung et al., 1990). SiC grains often presented inclusions of iron silicides (FeSi) and Si^0 (Di Pierro et al., 2003; Dobrzhinetskaya et al., 2018; Mathez et al., 1995; Nazzareni et al., 2019; Xu et al., 2008).

The discussion regarding SiC genesis has always been complicated. The strongly reducing character impose oxygen fugacity (fO_2) conditions ten times lower than standard mantle's condition (Schmidt et al., 2014; Ulmer et al., 1998). It is often driven by the reaction $SiO_2 + C = SiC + CO_2$ and supported by the formation of FeSi and Si^0 (Figure 1.6).

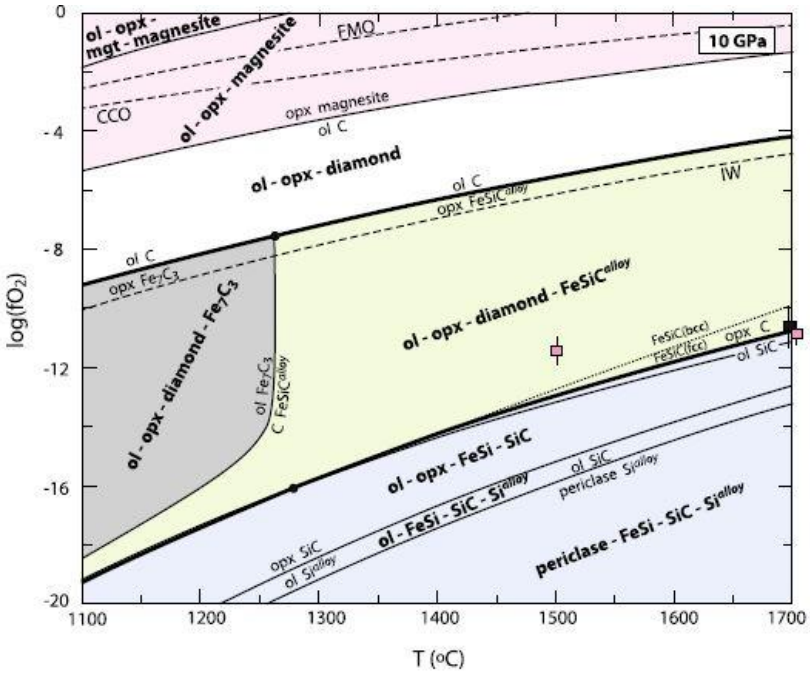

Figure 1.6: Evolution of the Mg-Fe-Si-C-O system in function of oxygen fugacity and temperature at constant pressure (10 GPa), from Schmidt et al. (2014).

In many cases, the mineralogical assemblage (i.e. silicates and in some case carbonates) coexisting with the reduced grains pin fO_2 to higher values. The main C isotopic contents place its origin in a light reservoir (i.e. sedimentary or biologic carbon) (Dobrzhinetskaya et al., 2018; Schmidt et al., 2014), thus clearly against any possibility of a formation contemporary with the primitive Earth (Mathez et al., 1995). Though, one of the possible formation scenarios supports the existence of an ultra-reduced and highly fractionated fluid, made by a FeSiC alloy. The precursor of such fluid would have been a COH fluid evolving toward more reducing conditions. The experimental work on a bulk earth composition (i.e. Mg-Si-Fe-C-O system) by (Schmidt et al., 2014) (Figure 1.6) displays how a ternary FeSiC metal solid solution produce carbides (i.e. Fe_3C, Fe_7C_3) as a result from a olivine + diamond mixture at high temperature. The occurrence of SiC in equilibrium with Mg silicates in Earth conditions attests its existence in oxidized systems and suggests a potential existence also in terrestrial exoplanets as a minor component.

1.2.3 Planetary cores

The possibility of stabilizing FeSiC alloys in mantle conditions open many interesting scenarios for planetary differentiation. During accretion a FeSiC liquid can differentiate in a planetary core thus forming a planet with different characteristics than the Earth-

As interpreting the data coming from observations requires the presence of a priori models taking in account all the plausible compositions, models of carbon enriched exoplanets need to be investigated to set boundaries on planetary diversity. Light elements incorporation would affect the properties of a planetary core and have multiple consequences on exoplanets. The density change induced by

incorporation would determine differences in the observables, such as mass and radius. Furthermore, a core crystallization process suitable to activate a dynamo implies the existence of a magnetic field and accordingly of an atmosphere (Dong et al., 2018, 2017; Dorn et al., 2018; Lammer et al., 2009). Planned missions (i.e. JWST https://www.jwst.nasa.gov/, PLATO http://sci.esa.int/plato/, CHEOPS http://cheops.unibe.ch/ and ARIEL https://ariel-spacemission.eu/) will focus on many aspects of planetary systems, providing enhanced data on host stars as well as exoplanets. With the expected increase in the precision of the data and considering the potential variability in the composition of planetary interiors state of the art models of different planetary interiors will be needed for the interpretation. Not only of Earth like planets but also for other compositions.

The present work focused on the Si-C and Fe-Si-C systems represent a first step in the investigation of planetary variability. Hopefully it can contribute to understand these new worlds and drive the attention toward a collaborative approach between geoscience and astronomy.

Chapter 2

Methods

2.1 High pressure and high temperature experimental methods

2.1.1 Diamond anvil cell

Diamond anvil cell (DAC) is a powerful and versatile high pressure tool, capable of attaining pressures over 800 GPa at ambient temperature (e.g. Dewaele et al., 2008b; Dubrovinskaia et al., 2016) or 377 GPa and 5700 K simultaneously (Tateno et al., 2010). The first record of diamonds used to apply pressure comes from 1959 (Jamieson et al., 1959) and has been followed by different developments and improvements. Pressure is defined as a force over an area, accordingly smaller the area higher the pressure. Hardness and optical transparency make diamond an ideal material to be used as anvils. The tip of the diamond (culet) for instance, equipped with toroidals diamond anvils, is suitable to reach relatively uniform pressures of 570 GPa, with a conventional gasket geometry (Dewaele et al., 2018). Cells are composed by two stainless steel support, one usually stationary (cylinder) and a sliding one (piston). Two rockers or tilting plates (seats), generally in tungsten carbide, are mounted in the center of the support. Seats are provided with a conical aperture, where diamonds with a conical support (Boehler and De Hantsetters, 2004) are glued with epoxy resin. The conical base (Boehler-Almax cut) can potentially double the optical aperture with respect to standard flat diamonds, thus making them particularly useful for angle dispersive diffraction experiments (Figure 2.1).

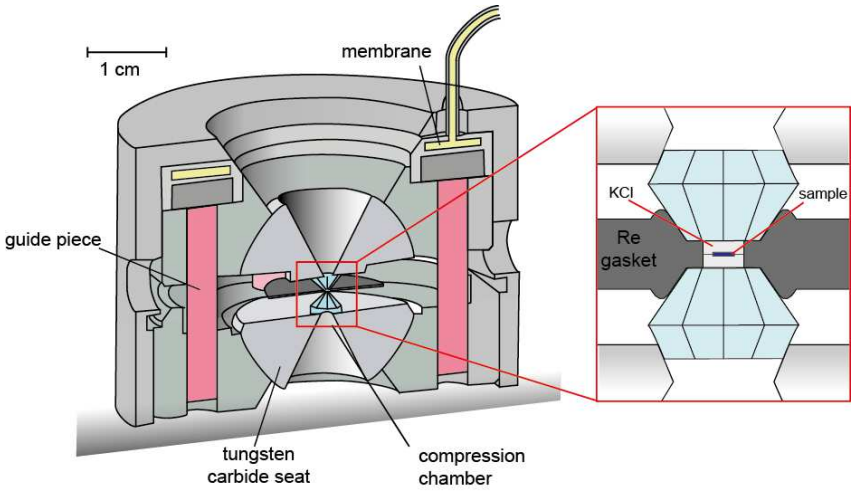

Figure 2.1: Transverse cut of a membrane type diamond anvil cell. In the box a magnification of the sample chamber.

Two different culet shapes were used. A standard flat polished was used for lower pressure while a bevelled shape was used for smaller culets, intended for higher pressures. The presence of the bevel is fundamental at Mbar pressures. In these conditions the tip of the diamond bends and elastically deforms due to stresses (Hemley et al., 1997). The bevel acts as a support by getting deformed and damaged

hence preventing the culet itself to be damaged (Li et al., 2018). With increasing pressure, the elastic behaviour of the diamond induces cupping, by bending the tip of the diamonds.

On the cell, the force is usually applied on the piston by pushing with a mechanical device, either a set of screws or a deformable membrane. The latter presents several advantages: i) The force exerted on the cell is proportional to the pressure of the injected gas, inducing an excellent reproducibility; ii) there is a better control on the rate of compression and decompression of the cell, giving the possibility to perform small pressure increment; iii) membranes can be connected to a pressure driver and be remotely controlled. This represents a major advantage for synchrotron experiments where the DAC is placed in separate hutch. All the experiments for this project were performed with a membrane diamond anvil cell and diamonds with culets of 300, 250, 150/300, 100/300 and 70/300 µm. In the notation with double number, as 70/300, the first number represents the diameter of the culet while the second is that of the bevel.

To avoid the sample extrusion from the diamond culet, a gasket with a sample chamber is placed within the two diamonds (Figure 2.1). The gasket is usually in rhenium, with a fixed thickness of 200 or 250 µm, depending on the pressure range investigated. The experimental chamber is obtained by pre-indenting the gasket with the diamonds, down to a specific thickness chosen accordingly to diamonds culet dimensions. A hole of a specific diameter is then drilled in the indentation using a femto-second laser, available at IMPMC. The dimensions of the chamber are related to the dimension of the diamond's culet, and consequently the pressures targeted. For membrane cells, the diameter of the hole (d) is chosen to be between 1/2 and 1/3 of the culet dimension, and the thickness to be between 1/2 and 1/4 the dimension of d, standards measures used are shown in Table 1.

Table 1: Dimension of the sample chamber and pressure medium for each used culet size

Ø Culet (µm)	Gasket thickness (µm)	Ø Gasket (µm)	Ø KCl (µm)	KCl thickness (µm)
300	50 ± 3	120	120	20
250	40 ± 3	120	120	15
150/300	30 ± 3	75	75	10
100/300	25 ± 3	50	50	10
70/300	20 ± 3	35	35	7

The gasket, together with providing a chamber for the sample, also provides lateral confinement for the diamonds by deforming plastically to accommodate elastic deformation of the diamonds. When pressure is applied on the gasket, part of the material get extruded from the sides and the central part starts getting

thinner. If the gasket is too thick there will be too much material between the two diamonds then part of the pressure medium can trigger the sample chamber opening. It is also important for the drilled hole to be well centred after the indentation, otherwise it can potentially slip on the side during pressurization thus compromising the possibility of making the experiment.

2.1.2 Pressure transmitting medium

To guarantee hydrostaticity during compression and thermal insulation of the sample during heating, sample chamber requires to be filled with a pressure transmitting medium. Such medium can be either solid (i.e. alkali halides, MgO or Al_2O_3), liquid (i.e. alcohol mixtures) or a gas (i.e. He, Ne, Ar). Fluid pressure media are preferable to maintain hydrostatic conditions in the sample chamber (Klotz et al., 2009). Above 12 GPa (i.e. the freezing pressure of He) they become solid and conditions are considered quasi-hydrostatic as the sample can experience shear stresses. Solid pressure transmitting media, as alkali halides, offers several advantages (Dewaele et al., 2012). The softness reduces the non-hydrostatic stresses, and the high compressibility make it useful also as pressure calibrant. They usually are chemically inert during laser heating experiments, reducing the possibility of contamination. Finally, the simple cubic structure results in a limited number of diffraction peaks on diffraction patterns. During laser heating experiments, the shear stresses induced by the presence of a solid pressure medium is released after a high temperature cycle. As all the experiments performed in this project were coupling high pressure and high temperature, KCl was used as the pressure transmitting medium. The high melting point in fact makes it particularly useful also as thermal insulators in laser heated experiments. Plates with variable thickness were manufactured by compressing KCl grains to the desired thickness and cut, with the femto-second laser, into disks with different diameters.

2.1.3 Pressure calibrant

The determination of pressure conditions is a critical point in high pressure experiments (Decker et al., 1972). In DAC in particular, the correlation between the force applied on the piston and the pressure applied on the sample can't simply be used to constrain the actual pressure of the sample. Diamonds deformation in response to pressure is different as pressure increase (Hemley et al., 1997; Merkel et al., 1999) and membranes can permanently expand after multiple uses, changing its response to gas injection. Thus an internal pressure gauge is required. Typically, luminescence gauges such as ruby fluorescence (Datchi et al., 1997; Mao et al., 1986) or X-ray gauges, with well calibrated equation of state relations, are positioned close to the sample and used as internal pressure scales. Using X-ray gauges (Dewaele et al., 2004; Mao et al., 1978) consists in evaluating the change in the volume of a standard material with a well constrained equation of state. Their use is particularly indicated during X-ray diffraction experiments, as both sample and pressure standard can be measured. Several metals (e.g. rhenium, gold, molybdenum, platinum) have been calibrated as pressure standards (Dewaele et al., 2004; Dorogokupets and Oganov, 2007; Fei et al., 2007). Lately also alkali halides have started to gain

attention as their characteristic high pressure behaviour make them suitable to be used not only as pressure transmitting mediums but also as pressure calibrants. Notably, when the sample is sandwiched within KCl, we have access to the cell parameters of both the sample and pressure standard at the same time, diminishing the pressure gradients issues in the sample chamber.

KCl is stable with a cubic rock-salt (B1) structure at low pressures and undergoes a phase transition to cesium-chloride (B2) structure at 2 GPa. A sudden increment of the melting temperature, from 1600 K at 1 GPa to 3200 K at 20 GPa, is associated to the structural transition (Boehler et al., 1996; Pistorius, 1965), thus making KCl suitable for high temperature experiments. The use of X-ray gauges holds some intrinsic uncertainties. Pressure is calculated with the experimentally determined cell parameters and a known equation of state that correlates the variation of volume with pressure. However, it is important to remember that also the equations of state for pressure calibrants were previously determined with an experimental dataset, using another pressure standard as a reference, as only with shock experiments absolute pressures can be determined. Many pressure calibrants are cross referenced and the consistency within each other is accurately evaluated (Dewaele et al., 2012, 2008b, 2004; Fei et al., 2007; Sata et al., 2002). It is also important to take into account the possible differences when comparing data sets from multiple authors. In the present project, KCl was used as the pressure calibrant. With the volumes determined experimentally, pressures have been calculated using the EoS proposed by Dewaele and co-authors (2012). The EoS combine an ambient temperature part obtained by fitting P-V data to Rydberg-Vinet EoS (Vinet et al., 1987) using a ruby gauge with the calibration of (Dorogokupets and Oganov, 2007) and a thermal part calculated by molecular dynamic simulations. The equation reads:

$$P(V,T)=3K_0\left(\frac{V}{V_0}\right)^{-\frac{2}{3}}\left(1-\left(\frac{V}{V_0}\right)^{\frac{1}{3}}\right)\exp\left[\frac{3}{2}\left(K'_0-1\right)\left(1-\left(\frac{V}{V_0}\right)^{\frac{1}{3}}\right)\right]+\underline{\alpha K_T}\,(T-300)$$

Where V_0, K_0 and K'_0 are respectively the ambient pressure volume, the bulk modulus and its pressure derivative. Their values are 54.5 ($Å^3$/formula unit), 17.2 GPa and 5.89.

One of the key parameters required in our experiments is the determination of pressure under high temperature. During laser heating experiments, KCl is in contact with both the sample and the diamonds. The two are experiencing different temperatures. The sample is under high temperatures, being heated by the lasers, while the diamond, an excellent heat conductor, is kept at ambient conditions (295 K) by the water cooling on the cell. Accordingly the temperature of the KCl is assumed to be a midpoint between the sample and the anvil surfaces (Figure 2.2) and as in Campbell et al. (2009) was calculated as:

$$T_{KCl}=\frac{3T_{meas}+295}{4}\pm\frac{T_{meas}+295}{2}$$

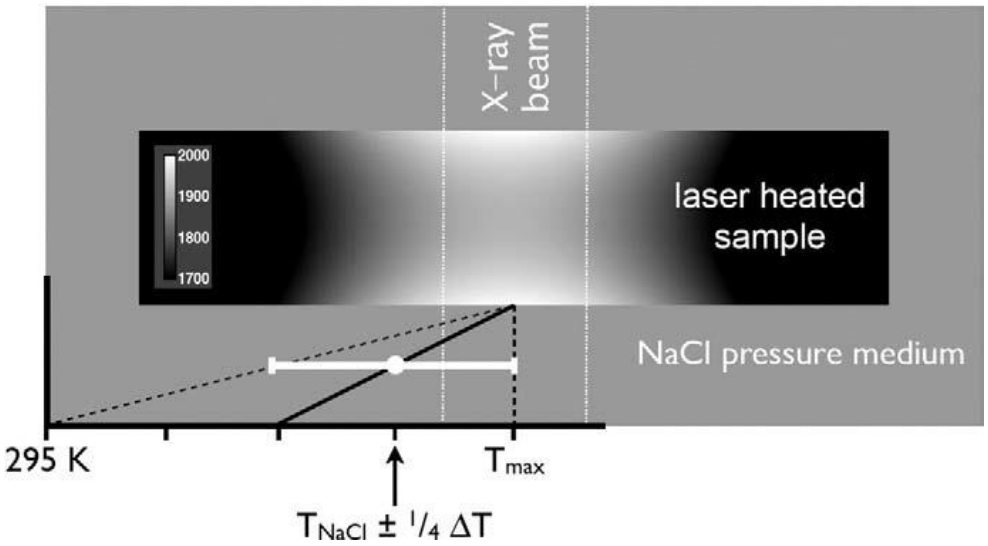

Figure 2.2: From Campbell et al. (2009), heating distribution in diamond anvil cell experiments. Temperature profile across the insulator is assumed as linear and a mean temperature between the one at the surface of the sample and the surface of the diamond is considered.

The errors on the measured temperature were also used to define the errors on pressure related to the temperature of KCl. For each data point the temperature was calculated as $T_{KCl} = (3*T_{measured} + 295)/4 \pm (T_{measured} - 295)/2$, where $(T_{measured} - 295)/2$ represents the error on temperature, defined as dT. When calculating the pressure (P) through the equation of state, two additional values are computed (dP1 and dP2), using $T_{KCl} \pm$ dT as value of the temperature. The final error on pressure (dP) is then (dP1 - dP2)/2. The average error on pressure is < 2 GPa, for T < 2000 K; 2 < dP <3 for 2000 K < T < 3000 K and dP < 3.5 GPa for 3000 K < T < 3500 K.

The behaviour during compression and laser heating of the present configuration, is consistent for every run. Accordingly pressure and temperature conditions inside the cell are reproducible. This represent a great advantage for experiments with techniques without *in situ* determination of the pressure during heating (e.g. experiments with X-ray absorption spectroscopy) as the data collected with another technique where the pressure calibrant is always measured with the sample, can be used as a reference. This procedure was applied in our recent publication (Morard et al., 2018). In this work, we determined the melting curve of iron using X-ray absorption spectroscopy. In the absence of diffraction it is not possible to have a pressure gauge at high temperature. The reproducibility of the conditions guaranteed by the configuration allowed to use the data from Miozzi et al. (2018) as a reference for the pressure at high temperature.

2.1.4 Laser heating

Two ways are commonly used to heat a sample into a diamond anvil cell: resistive heating and laser heating. The latter was the one employed for this study. Compared to resistive heating it allows to reach much higher temperatures. Up to now, the higher conditions reached combining pressure and temperature were reported to be ~ 5700 K at 360 GPa, by Tateno et al. (2010). Laser heating consists in

focussing two high power lasers on the surfaces of the sample, usually on the two sides. In the set up used for this study, the transverse mode structure of the lasers was usually purely Gaussian and with high quality of the beam. During heating the sample can be visualized, and spectroscopic and X-ray diffraction measurement can be performed. During the experiment the two lasers heat the same portion of the sample from both sides, guaranteeing homogeneous temperature along all the thickness of the sample. An even thermal insulation is required, thus needing the thermal insulator to have the same thickness on the two sides. For this reason, the laser cut of KCl disks from the same plate represents an important upgrade for the experiments, ensuring an excellent reproducibility of the sample geometry. Other advantages (low thermal conductivity and high melting point) are coming with the use of alkali salts (Dewaele et al., 2012; Morard et al., 2011). Details about the used laser heating set up and temperature measurements will be provided in the next chapter.

2.2 Manufacturing of the starting materials

The starting materials used during the present work were homogeneous thin layer of non-stoichiometric material. They were manufactured in two different ways, physical vapour deposition (PVD) and ultra-rapid quench (URQ). PVD, is a surface treatment widely use to make thin film or micrometric deposition, usually for mechanical, optical or electronic functions. Employing deposition techniques to prepare Earth related materials is a recent development. After starting to produce multilayers depositions in targets for shock compression (Torchio et al., 2016), the technique was extended to the manufacturing of samples for diamond anvil cell experiments (Hirose et al., 2017a; Morard et al., 2017). The process of sputter deposition includes the presence of targets and a substrate, where the material is going to accumulate (a glass slide for our experiments) (Figure 2.3). Targets are disks of several cm made by the pure elements that need to be deposited to obtain the desired bulk composition. A maximum of four targets can be used simultaneously, they occupy the top part of a chamber and each one is mounted on a magnetron. Its basis is composed of a rotating plate. Starting the deposition process, the chamber is filled with an argon plasma. When Ar^+ ions hit the surface of one of the targets, a plume of material is released toward the bottom and get sputtered on the substrate. The amount of elements deposited depend on current intensity on each magnetron. Accordingly, in multi elemental deposition (as Si-C and Fe-Si-C in this project), the amount of each element is defined by the intensity of the current and the time of sputtering, with the latter also influencing the thickness of the deposition. Thus, finding the correct "recipe" to make the desired starting composition and desired thickness, requires time and extensive

testing. Due to the early start of this project in the frame of the ERC PlanetDive, most of the used deposition were manufactured by Dephis (http://www.dephis.com). Only a couple of compositions were realized in the newly installed deposition laboratory at IMPMC. Post deposition chemical characterization is usually done by surface (i.e. SDL, done by Dephis) and chemical analyses (i.e. SEM and EMPA). Chemical characterization of carbon enriched samples is challenging. Carbon, due to its light weight is difficult to quantify with standard analyses and requires special attention.

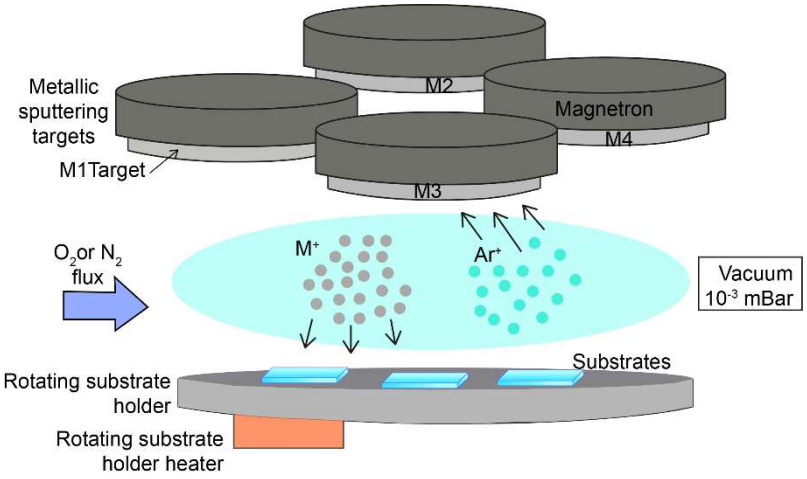

Figure 2.3: Scheme of a Physical Vapour Deposition machine, now available at IMPMC.

PVD samples represent an upgrade for diamond anvil cells experiments. The deposited layer has constant thickness and homogeneous grain size and distribution of the chemical elements. Furthermore, the low rugosity of the surface induces a good coupling with the lasers, resulting in a uniform heating across all the heating spot. The grains composing the starting material are at the nanometric scale, confirmed by SEM and diffraction analyses.

PVD deposition is a non-equilibrium process. Samples at ambient conditions often present an amorphous diffraction pattern. Upon heating, elements re-organise in a crystalline structure. The high amount of material deposited, compared to the need for a DAC loading, guarantee for the evenness of the starting materials used in each run. In contrast, working with starting materials made by powder mixtures, it is difficult to determine if the loaded material has the right proportion of chemical elements. PVD samples handling should be performed with a special care. To prepare DAC size samples, part of the film is detached from the glass substrate by the mean of a needle. If part of the glass slide remains attached to the deposited film, it could lead to SiO_2 contamination. Furthermore, unprecise handling of the samples, for example touching the surface and without gloves can determine carbon contamination.

Ultra-rapid quench samples were synthetized at ICMPE (Institute de Chimie et des Matériaux de Paris-est, Paris, France) as part of the ongoing collaboration between IMPMC and ICMPE to manufacture samples. The technique consists in obtaining homogeneous liquid Fe-alloys by induction melting in a water-cooled Cu crucible under He atmosphere. The alloys are then re-melted and ejected through a pressurized quartz nozzle on a rotating Cu-base wheel under 1 bar He atmosphere, to obtain ribbon

specimens of ~25 μm thickness and 20–30 mm width. This technique is called planar flow casting technique (PFC).

The starting materials used for PFC are usually stoichiometric compound. In particular for the Fe-Si-C samples Fe (Neyco F-12734), Si (Wacker) and Fe3C (Neyco FC-76857/1), were used. This type of samples were previously employed for several other studies (Edmund et al., 2019; Mashino et al., 2019; Morard et al., 2011). Due to the thickness of the ribbon, samples manufactured with this technique were first compressed between two bigger diamonds (~600 μm) to obtain the required thickness (usually between 7 and 10 microns) then loaded into the cell. The composition of the starting material was measured by EPMA (detailed in the following paragraphs) and was found to agree with the given nominal composition.

Several compositions, changing the amount of elements present in the sample, were used as starting material, both in the Si-C and Fe-Si-C systems. In Table 2 a list of all the starting composition is provided, together with the sample name and manufacturing technique. Detailed compositions measured by EPMA will be given in a following paragraphs, together with detailed on the analytical microprobe technique.

Table 2: List of all the nominal compositions required for the starting materials and respective manufacturing ways. Details about the chemical composition measured with EMPA will be provided in the next paragraphs.

	C (at %)	Si (at %)	Fe (at %)	Sample Name	Technique
	75	25	/	$Si_{25}C_{75}$	PVD
Si-C	45	65	/	SiC_{45}	PVD
	25	75	/	SiC_{25}	PVD
	10	20	70	$FeSi_{20}C_{10}$	PVD
Fe-Si-C	20	10	70	$FeSi_{10}C_{20}$	PVD
	3	3	94	$FeSi_3C_3$	URQ
	5	6	89	$FeSi_6C_5$	PVD

2.3 In situ high pressure and high temperature experiments

2.3.1 X-ray diffraction

X-rays are electromagnetic waves with a wavelength of the same order of magnitude as the interatomic distances in condensed matter. As a consequence, the interaction of X-ray with the electrons produces a diffraction phenomenon. In addition, when X-rays interact with a crystalline sample, interference phenomena can occur. The analysis of the resulting interference pattern lead to a characterization of the

microscopical structural properties of the sample. In the framework of the far field approximation the scattered amplitude from a solid with a volume V is written as:

$$A = \int_V dV \rho_e(r) exp(2i\pi(k - k') \cdot r)$$

In this expression $\rho_e(r)$ represents the local electron density, k and k' are the wave numbers of the incoming and scattered radiation. In a crystal, the atoms are arranged in a periodic way and a base can be defined in the forms {a, b, c}, and a translation vector (direct lattice) T=ua + vb + wc (u,v,w integer) will leave unchanged the electronic density. This electronic density can be expressed as:

$$\rho_e(r) = \sum_h \rho_{e,h} e^{2i\pi h \cdot r}$$

where h is defined as h=ha*+kb*+lc* (h,k,l are integer) and {a*,b*,c*} is the base of the reciprocal lattice defined as:

$$\begin{cases} a^* = \frac{1}{2\pi v} bxc \\ b^* = \frac{1}{2\pi v} cxa \\ c^* = \frac{1}{2\pi v} axb \end{cases}$$

where v is the volume of the parallelepiped formed by the vector a, b and c; v=|a·(b x c)|. The vector h, is perpendicular to the planes (hkl) and its modulus is given by |h|=1/d_{hkl}, where d_{hkl} is the distance between two planes of the lattice. Combining the two equations for V and $\rho_e(r)$ to have a nonzero amplitude, we can obtain in the hypothesis of elastic scattering (i.e. |k|=|k'|) the diffraction condition: $2kh = |h|^2$ .This is the vectorial expression of the Bragg's law, that can be equivalently expressed as:

$$2d_{h,k,l} \sin\theta = n\lambda$$

The angle θ is the half of the so-called diffraction angle which represents the total deviation of the X-ray beam due to the diffraction process. λ is the wavelength of the X-ray and k=1/λ. The Bragg's law provides information on the inter-planar distances (d_{hkl}) and the relative positions of the planes, these information permit to characterise the structure of the primitive cell.

2.3.2 X-ray sources

X-rays can be generated by laboratory sources, such as X-ray tubes, or in large facilities as synchrotrons light sources. In a synchrotron, electrons bunches are first inserted into a linear accelerator (LINAC), then injected in a booster and accelerated, from few hundreds MeV to the maximum energy of the storage ring. The storage ring is thus filled with the accelerated bunches kept in motion into a vacuum chamber. Storage rings are composed by different magnetic elements, dipole, quadrupole and hexapoles have the role of focusing bunches, while bending magnets and undulators create the conditions for the particles to emit electromagnetic radiations. Due to the Bremsstrahlung phenomenon, when particles with electrical charge and velocity close to the speed of light, interact with a strong magnetic field, they emit phonons on a tangential trajectory. Bending magnets, with their uniform magnetic field, change the trajectory of the particles and keep them circling in the ring. Undulators instead, consists of a pair of meters long slits facing each other and made by a concatenation of small magnets. Each pairs of magnets induce an oscillation of the electrons in phase with the other and produce constructive interferences. Varying the gap between the slits induce a change in the peaks structure for certain energies.

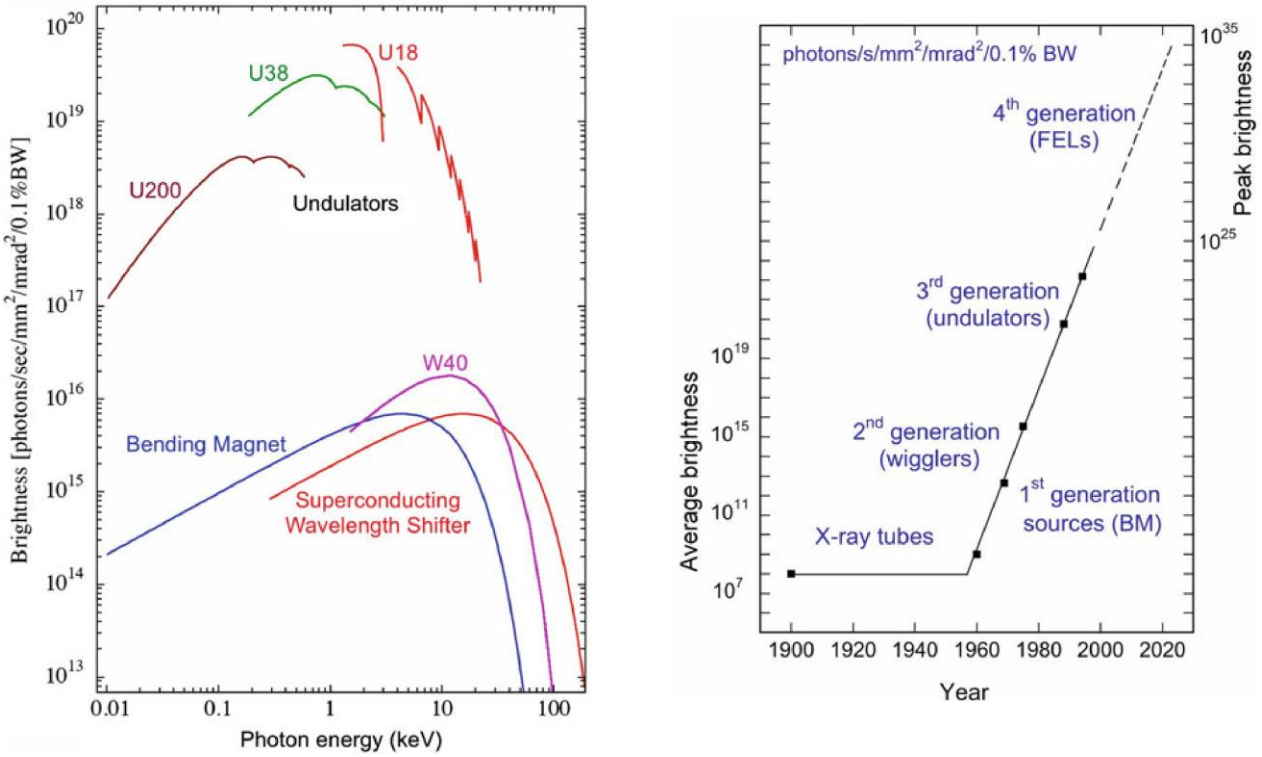

Figure 2.4: Comparison of the brilliance that is possible to obtain with different sources and different magnetic elements.as a function of energy. Image from Balerna and Mobilio (2015).

The quality of the emitted beam is defined by flux and brilliance. Flux represents the number of photons per second per unit bandwidth, passing through a defined area. Brilliance is the distribution of the flux in space and angular range. As visible in Figure 2.4, from Balerna and Mobilio (2015) the brilliance provided by undulators is 10000 times the one from bending magnets, thus making this radiation the

more suitable for studies at extreme conditions. In addition, Figure 2.4 also display the difference in brilliance between a lab source (X-ray tube) and a synchrotron source.

The choice of an optimized X-ray source as a function of the analytical purposes if of primary importance (Chavanne et al., 1998). For DAC, in particular, the beam should be intense and highly focused due to the limited sample's dimensions (10-25 μm for Mbar experiments) and the presence of highly absorbing diamond windows. Furthermore, the limited X-ray aperture of the cell imposes a high photons flux at high X-ray energies (Mezouar et al., 2005). Having a high intensity beam contributes to reduce the acquisition time, with patterns collected in seconds at dedicated beamlines. The impact of the source on the quality of the beam is visible in Figure 2.5. The two graphs display the intensity of the beam in a wide energy range for two different insertion devices installed at the ESRF, ID30 previously used up to 2004, and ID27 available from 2005 to 2018. The first (ID30) consisted in a pair undulator + wiggler. The second (ID 27) is equipped with undulators operative in the last decade (details in Mezouar et al., 2005). The phased undulators on ID27 provides higher flux intensity for energies below 40 KeV. At higher energy, it reproduces the peaks structure previously observed for low energies.

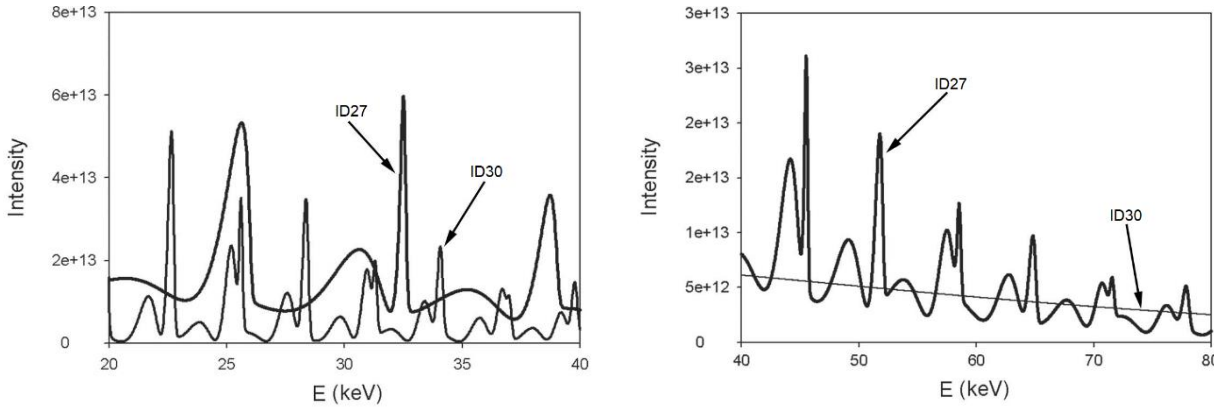

Figure 2.5: Top left and right from (Mezouar et al., 2005) comparison of the intensity at different energies for the high pressure beamline before and after the upgrade.

The electro-magnetic radiation emitted by the specific source (i.e. undulator, bending magnet) is conveyed toward the beamlines, where optical elements (monochromatic, Kirkpatrick Baez focusing mirrors) optimize the beam to satisfy the experimental needs (wavelength selection is performed by the first one, and focusing by the second one). Stability of the position and focus of the beam are of particular importance on extreme conditions beamlines due to the small dimension of the samples. Furthermore, monochromatism is needed to fulfil the Bragg law and determine the d spacing from angle dispersive collections.

2.3.3 Extreme conditions beamlines

Extreme conditions beamlines, like ID27 at the ESRF and P02.2 at Petra III, couple a beam with all the characteristics described above, with the possibility of heating the sample. Heating is achieved using solid-state fibre lasers with either crystals of Nd: YAG (Nd^{3+}- doped yttrium aluminium garnet) or Nd: YLF (Nd^{3+} - doped yttrium lithium fluoride) emitting in continuous way in the infrared domain (λ = 1.064 μm) with a purely Gaussian TEM_{00} transverse mode. The two lasers are focused one on each side of the sample and positioned in order to heat on the same spot.

Temperatures in laser hated DAC are measured via spectroradiometric method (Giampaoli et al., 2018; Mezouar et al., 2017; Schultz et al., 2005). It consists in collecting the thermal radiation emitted by the sample when it absorbs the laser, and disperse it with a spectrometer working in a small range (~500-800 nm) then fit it to a Plank law, using the grey body approximation (Benedetti and Loubeyre, 2004; Schultz et al., 2005). Alternatively the Wien approximation can be used, where a linear relation is established between Wien approximation and $1/\lambda$. A curve fit of the linear function Wien = C_0 + C_1 + $(1/\lambda)$ can be done when radiative spectra is plotted against $1/\lambda$. Temperature then can be calculated from C_1 and the other parameters (i.e. emissivity, volume) of the Wien equation can be determined from C_0.

Thermal radiation emitted by the sample, is collected with specific optics and conveyed toward a spectrometer that was previously calibrated. The collecting optics can be either reflective, where mirrors are used and are free of chromatic aberration, or refractive that instead rely on the use of lenses. The response of the optical system is determined through a calibration with a tungsten lamp and used to correct the recorded emission spectrum from the apparatus function. Light is conveyed to a spectrometer where the presence of pinholes select the hotspot area where the temperatures are measured. Details on the used spectrometers will be provided in the following part, relative to each synchrotron beamline. The advantages and differences related to the use of the two different type of optics have often been a source of debate in the high pressure community, especially in the frame of evaluating the accuracy of temperature measures (Benedetti and Loubeyre, 2004; Boehler, 2000; Boehler et al., 1990; Giampaoli et al., 2018; Mezouar et al., 2017; Schultz et al., 2005). Consequently we invite the reader to refer to the literature above for the discussion on the topic.

ID 27, ESRF (European Synchrotron Radiation Facility)

On beamline ID27, at the European Synchrotron Radiation Facility, lasers enter in the cell with an angle of ~10°. Figure 2.6 offers an overview of the set up available on the beamline (a) and the details on the cell environment (b). Thermal radiation from the sample is collected, together with the image, via two Schwarzschild reflective objectives designed to minimize chromatic aberrations (Schultz et al., 2005). The signal is magnified and transferred to a 300 mm Acton spectrometer equipped with a Pixis 100 CCD camera (e.g. Petitgirard et al., 2014) from Princeton instruments. The spectrometer, thanks to a 50 μm hole, probes an area of 2 μm in diameter on the sample. The radiation emitted from the center of the

hotspot defines a region of interest on the CCD, then integrated to give the light intensity as a function of wavelength. The pinholes are used to align the entrance of the spectrometer with the X-ray beam, and then the two lasers. This procedure is a guarantee to probe with the X-rays the same region heated with the laser and probed for the temperature.

Numerical temperature uncertainties can be estimated from the errors on the fitting procedure. However ± 150 K were always assumed in order to take in account the possible uncertainties such as temperature gradients, change in the emissivity of the samples with pressure and temperature fluctuations with time. Axial temperature gradients are related to the thickness of the sample and estimated to be ~100 K for a similar sample geometry (Campbell et al., 2009, 2007). For the experiments, lasers were defocused to an area sensibly larger than the X-ray spot, hence making the radial gradient negligible. Temperatures could be measured on the upstream and downstream side independently. As the downstream mirror is not X-ray transparent, on ID27 the upstream temperature only was measured during diffraction acquisition.

A monochromatic beam with an energy of 33 KeV ($\lambda = 0.3738$Å, iodine k-edge), is focused on a sample area of less than 3 x 3 μm^2 (full width at half maximum). Two successive pinholes are used to clean the X-ray beam by cutting the tails. The small and focused beam is suitable for experiments at extreme pressures (P > 150 GPa), as shown by the absence of Re diffraction peaks for experiments performed in a ~25 µm hole. Diffraction patterns were collected on a MAR 365 CCD detector. The distance and orientation of the image plate are usually calibrated with a cerium dioxide standard (CeO_2) from NIST (SRM 674b), subsequently integrated to obtain an intensity over angle plot with the program Dioptas (Prescher and Prakapenka, 2015). Exposure time usually varied between 5 and 10 seconds.

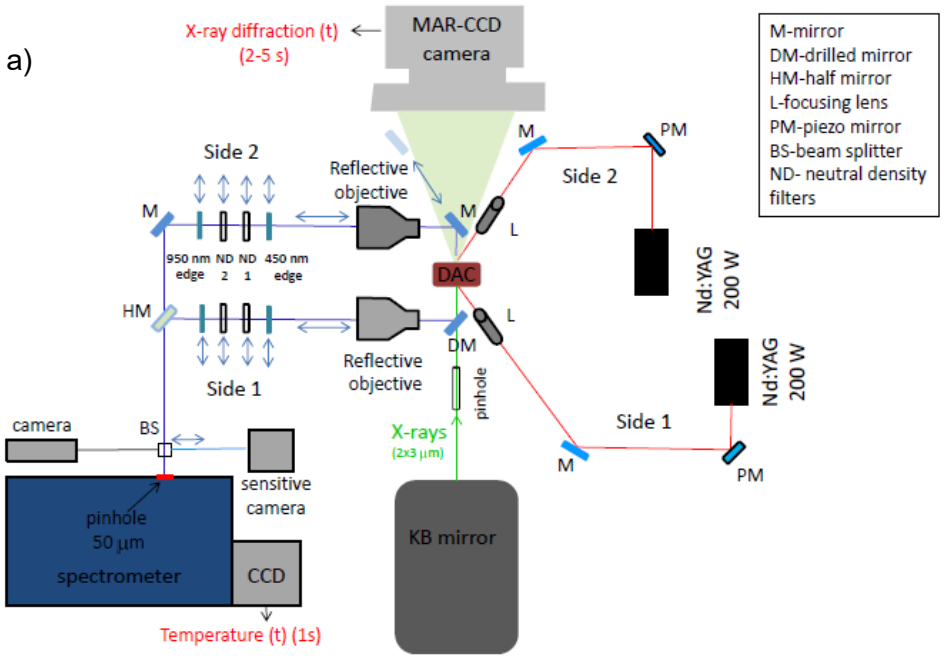

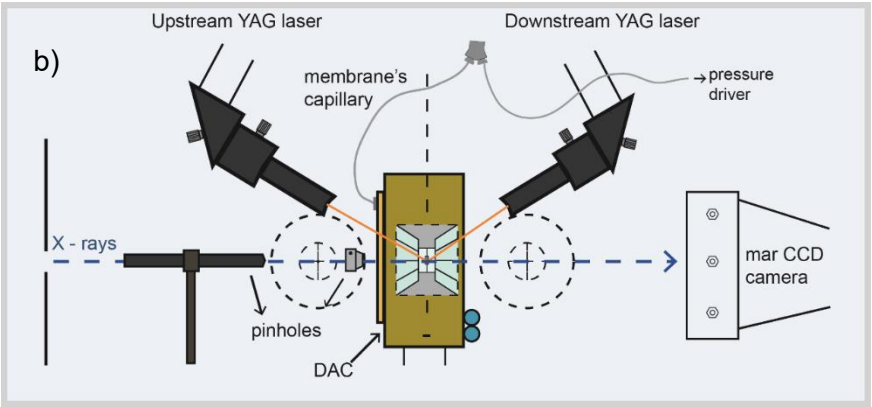

Figure 2.6: a) schematic view of beamline ID27 at the ESRF, from Anzellini (2014). In light red the path of the two YAG lasers, in blue the optical path followed by the thermal radiation, in green the X-rays. b) Side view of the cell environment in the set up. The two elements represented with dashed lines are the two reflective optics.

P02.2 at Petra III, DESY (Deutsches Elektronen Synchrotron)

On this beamline two different laser geometries are available: off axis and on-axis. The thermal radiation from the sample is collected via refractive optics and guided to the entrance slit of the spectrograph, a Shamrock with an ICCD Istar detector. On P02.2, pinholes are used to select a specific area of the hotspot where the temperature will be probed on both sides. The presence of an X-ray transparent carbon mirror on the downstream side allows to measure both sides during X-ray acquisition. The optical system response is calibrated with a tungsten lamp. The spectra are background corrected and used to calculate the temperature, fitting the curve with a Planck law, with the software T-rex, by Clemens Prescher. Errors on the temperature values are ±150 K as a result of the uncertainties coming from temperature gradients, heating instabilities and accuracy of the grey body approximation. Experiments were performed with a monochromatic beam focused to an energy of 42.7 KeV by a set of KB mirrors, with a FWHM (full width at half maximum) of 2 x 2 µm (Liermann et al., 2015). Diffraction are collected on a Perkin Elmer flat panel calibrated for distance with the diffraction of cerium dioxide standard. The detector acquired a background image before each pattern acquisition determining a delay in the acquisition time and improving the quality of the collected patterns. Dioptas (Prescher and Prakapenka, 2015) was used to obtain an intensity over angle plot.

2.3.4 Melting criterion

In diffraction patterns the angular position of the peaks is related through the Bragg law to the structure of the unit cell and permits the determination of the phases present in the sample. In Figure 2.7 an example of a collected image with the corresponding diffraction pattern. Diffraction patterns are scaled over an intensity, thus making it possible to make a quantification of the phase proportion. To extract the information of interest from a diffraction pattern several approaches can be used (i.e. Le Bail, Rietveld). Here in particular we will focus on the Le Bail (Le Bail, 2005; Le Bail et al., 1988), used to refine the cell parameters. The Le Bail method is defined as a whole diffraction pattern fitting technique. It is an iterative method where a least square minimization is performed, until the calculated pattern is consistent with the observed one. In the parameters taken in account for the fit, there are also unit cell parameters, peaks width and peaks shape, refined to the best value to match the observed pattern. For this work all the refinement were done with PDIndexer (http://pmsl.planet.sci.kobe-u.ac.jp).

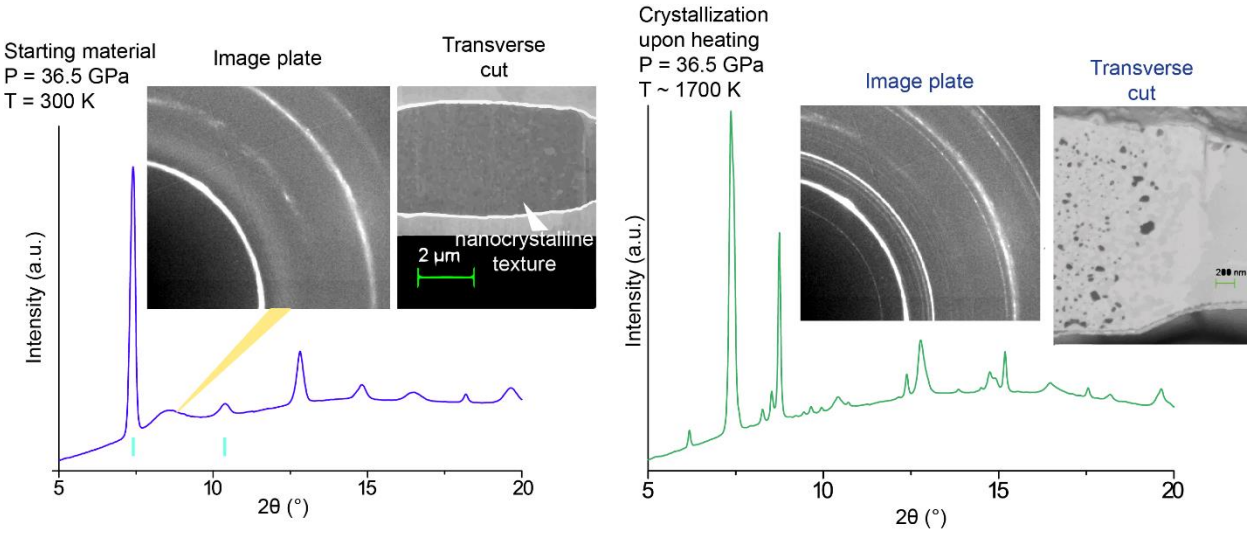

Figure 2.7: Diffraction patter, Cake image showing the diffraction lines from a crystalline solid with the corresponding diffraction pattern as intensity over 2 Theta. Orange corresponds to the pressure medium (KCl), light blue to FeSi and in blue Fe_7C_3. The high quality of the diffractions patterns consent the individuation of low intensity peaks.

Determining a melting temperature in diamond anvil cell experiments has often been a controversial topic. The appearance of diffuse scattering has been extensively used as melting diagnostic in XRD experiments (Andrault et al., 2006; Fiquet et al., 2010; Fischer et al., 2013; Lord et al., 2014; Morard et al., 2017, 2011) (Figure 2.8) . However its validity was questioned when experiments performed with a different diagnostic (i.e. XANES-X-ray near edge absorption spectroscopy) on pure Fe (Aquilanti et al., 2015), revealed lower melting temperatures than using X-ray diffraction (Anzellini et al., 2013). This controversy was recently addressed again by Morard and co-authors (2018) who retrieved a melting curve in agreement with Anzellini et al. (2013) using XANES. The agreement of the two melting curve obtained with different techniques provide an additional validation to the use of diffuse scattering as melting criterion in XRD experiments.

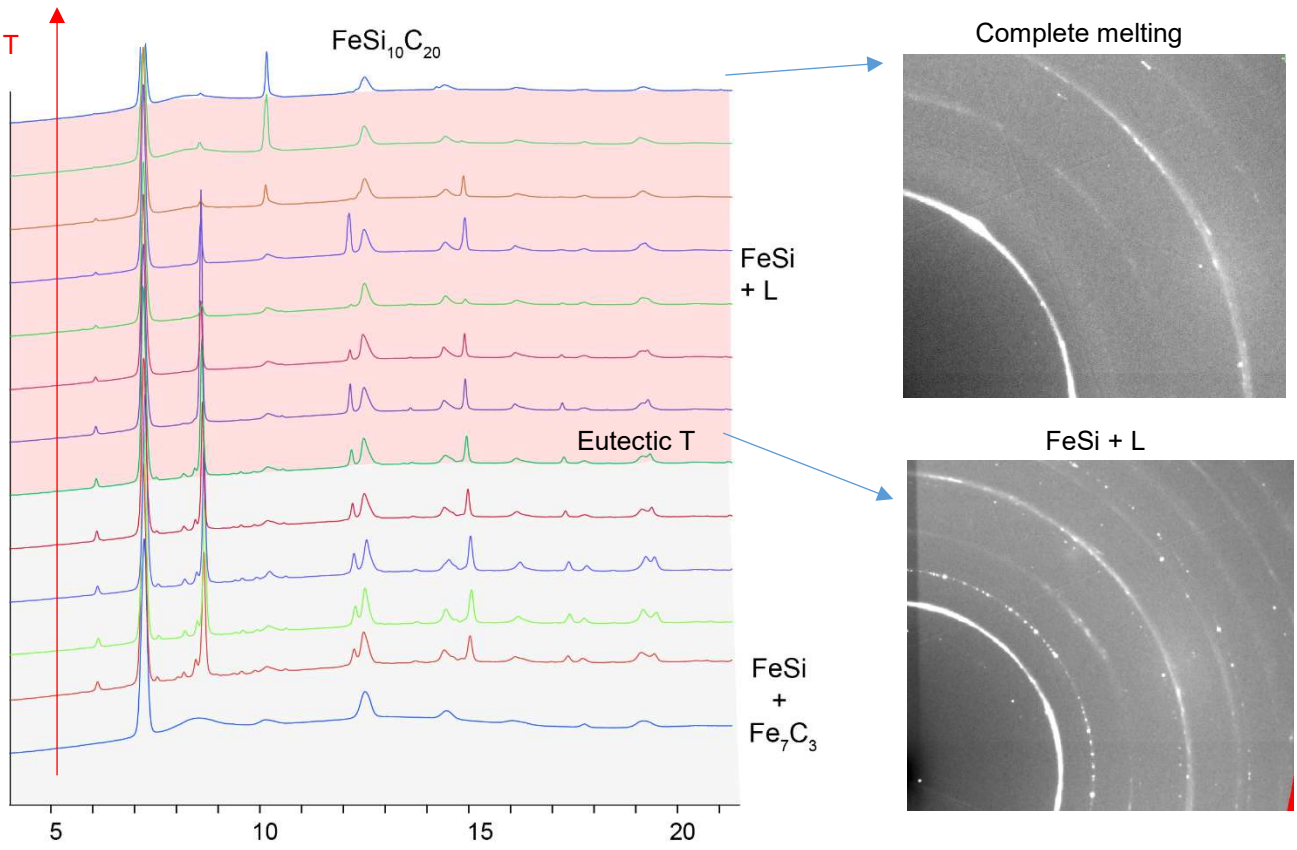

Figure 2.8: Sequence of diffraction patterns collected during a heating cycle. The starting material, amorphous at ambient temperature, recrystallize upon heating until the eutectic temperature is reached and one phase is lost. At this temperature on the image plate only the ring corresponding to the sample and the pressure medium are visible and as well the peaks on the diffraction patter correspond to this two phases. When melt occurs diffuse scattering is visible on the image plate and peaks of the sample are replaced by the bump typical of the amorphous and the only visible peaks are those of KCl. The last solid is characterized by the presence of a peak at $2\theta = 10°$ disappearing upon melting. The conservation of the diffuse scattering signal also in the quench attest the presence of a glass.

2.4 Samples recovery and preparation for electron microscopy

After laser heating experiment the sample was recovered in order to cut a transverse section of the heating spots and perform textural and chemical analyses. The procedure to prepare the samples is illustrated in Figure 2.9. The experimental chamber is cut out from the gasket with the femto-second laser and stick on a thin glass slide with carbon glue. The disk is positioned in order to have part of the hotspot, usually visible with a standard microscope, above the border of a glass. The first raw polishing is performed with an ion beam milling machine, to expose the central part of the hotspot. After polishing, samples are mounted on a hand-made copper support. As the thin glass slide is particularly fragile once it is glued on a support it should be the same for all the successive steps.

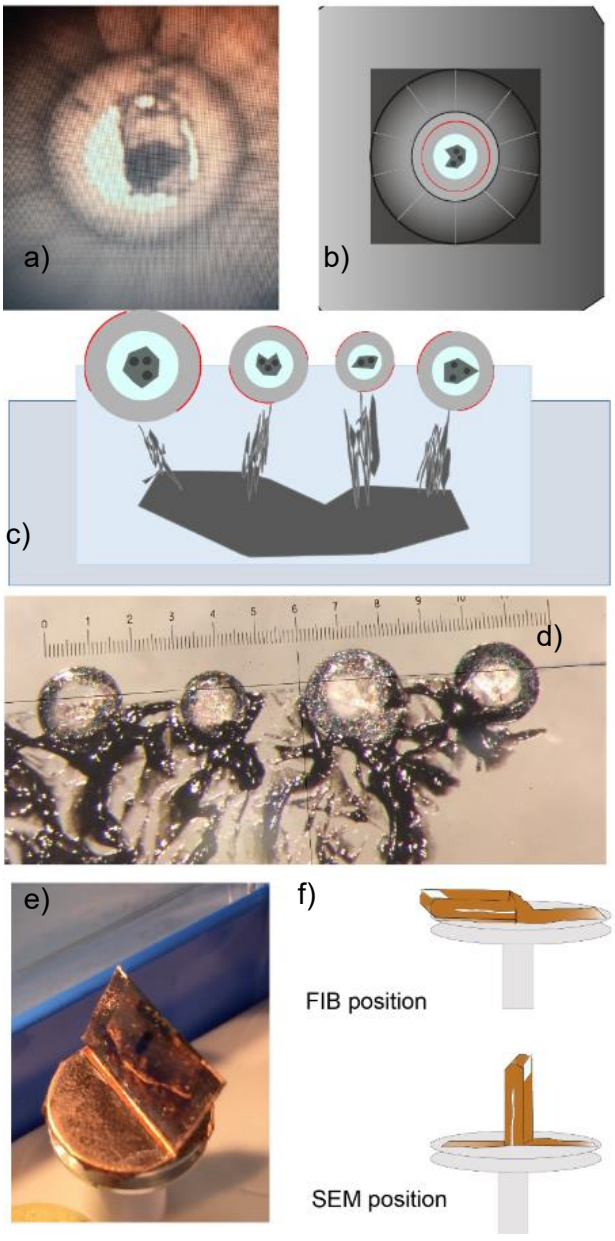

Figure 2.9: a) Picture of the sample chamber taken with an optical microscope. The sample, in the middle with elongated shaped is surrounded by the pressure medium. The laser heating spot is visible as the dark circle in the bottom part; b) schematic view of the gasket with trace of the cut to extract the experimental chamber. In light blue KCl, in light grey the sample and the dark spot correspond to the laser spots; c) schematic view of the experimental chambers attached to the glass slide and positioned; d) image of step c taken at the optical microscope; e) picture of the glass slide mounted on the ambivalent support; f, g) schematic view of the support in the two working position. For FIB, where samples should be flat and for SEM where instead samples need to be vertical.

Therefore such support should be suitable for the different configurations required by the instruments. In particular samples need to be flat for the focused ion beam (FIB) fine polishing and instead vertical for electron microscopy.

2.4.1 Focused Ion Beam

The FIB technology has been developed in the ’80 (Melngailis, 1987). However, using ions gun to thin specimens was already an acquired technique (Holland et al., 1971). Gallium ions are accelerated up to the desired current (usually lower than 10nA) and send toward the sample. The widely accepted model for ions-solid interaction is the collision cascade model for which the energy is transferred toward a series of binaries collision that provide enough energy to sputter the atoms and consequently mill the samples (Sigmund, 1987; Volkert and Minor, 2007). Modern instruments often couple a FIB column with a SEM column (FIB SEM crossbeam) (Figure 2.10a), providing the possibility of milling and imaging at the same time. The column positioned with an angle as a respect to the vertical is the ion gun. For the milling to be effective the surface to be polished should be parallel to the direction of the ions. The quality of the obtained polishing depend on the current used for the beam. As a rule, higher current (i.e. 10 or 5 nA) requires less time and are normally used to expose and identify the region of interest (ROI). Raw polishing can affect the topography of the sample producing some imperfections that are irrelevant to the determination of the ROI, but can become an issue during the analyses (Figure 2.10b). For this reason, once the ROI is localized a fine polishing with low current (i.e. 1 nA, 500 pA or 100 pA) is performed to obtain a flat surface (Figure 2.10c), ideal for the following analyses.

a)

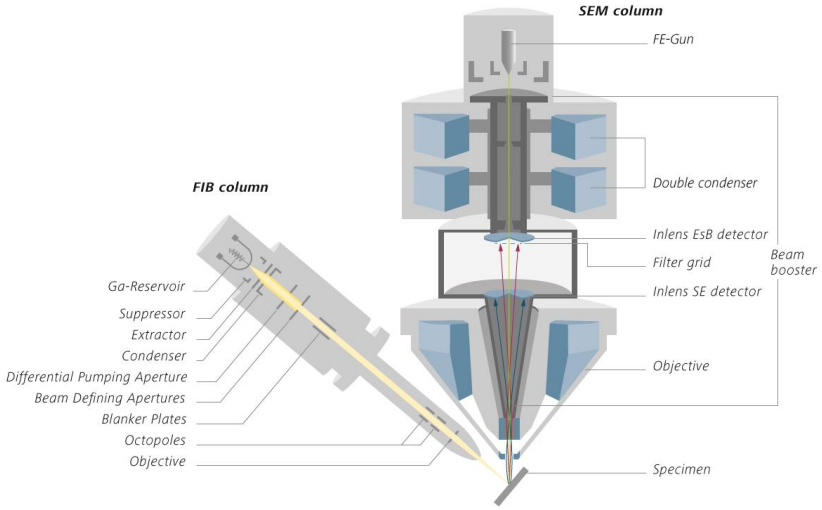

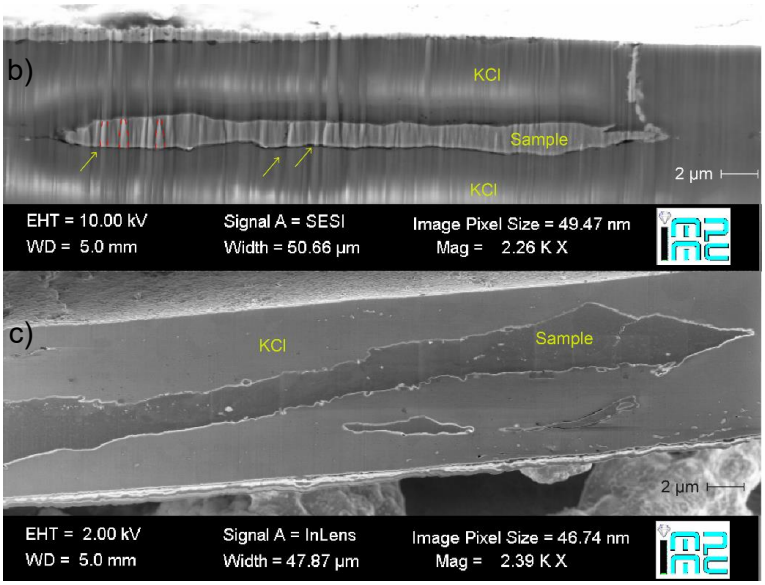

Figure 2.10: a) scheme of the FIB SEM cross beam from Zeiss available at IMPMC. b) Transverse section of a diamond anvil cell sample after polishing with a 10 nA beam. Surface marks left by the polishing are highlighted by red lines and yellow arrows; c) transverse section of a sample after polishing with 500 pA current.

The usual ROI is the center of the heating spot. During the experiment, heating usually produces an increase of the grain size and a loss of homogeneity in the grain distribution. If the sample has been molten the shape will change and display a melting pool expanding from the center of the hot spot toward the top and the bottom. Sometimes, this melt pool is detached from the rest of the sample. In Figure 2.11 four different heating spot are shown: a) represents a particular case as the sample in the center is extremely dispersed; b) melting pool expand from the center of the heating spot; c) melting point symmetrically distributed from the center d) heating spot where melting wasn't reached. The latter is well representative of the heating-induced textural changes into the sample. In both b and d) is possible to perceive the homogeneous grain size of the starting material on the sides.

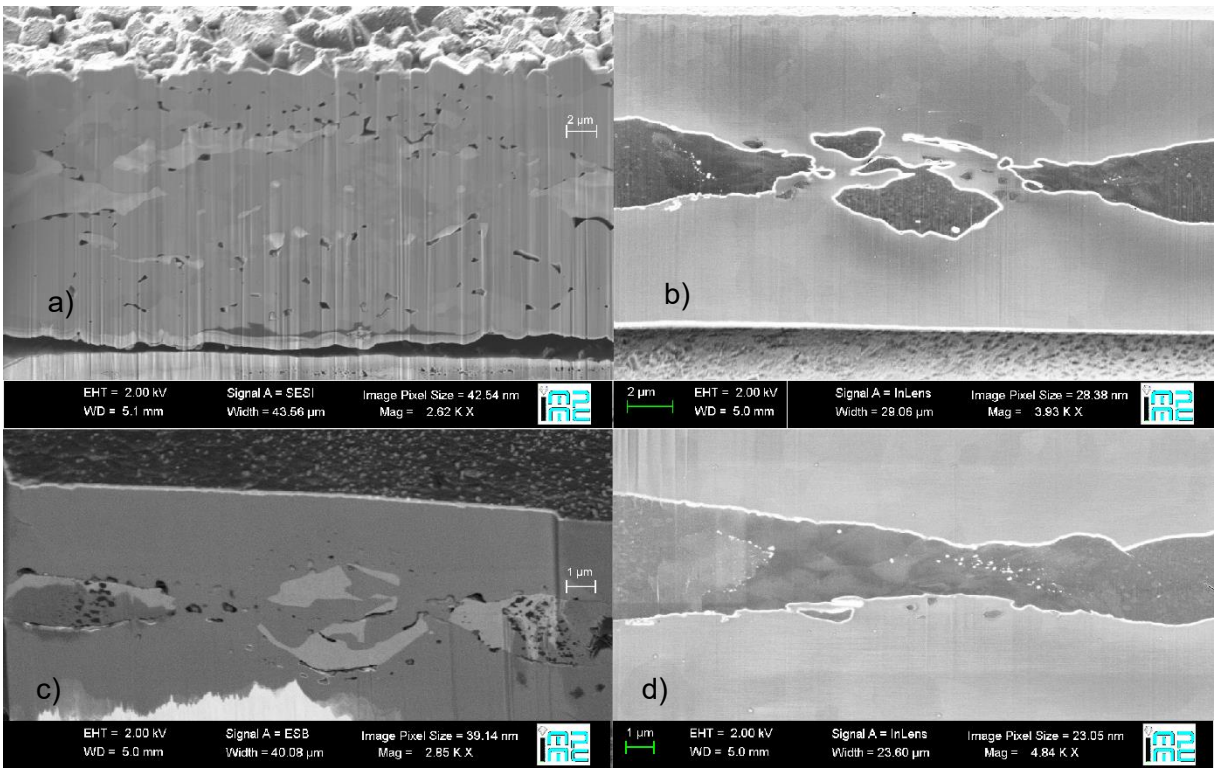

Figure 2.11: Transverse cut of different heating spots: a, b, c) typical textures for molten samples, corresponding to diffuse scattering in X-ray diffraction; d) subsolidus heating spot, complete melting is not attained, however the increase in the grain size attest the heating.

2.5 Electron microscopy analytical techniques

2.5.1 Scanning electron microscope (SEM)

Scanning electron microscopy is a widely used analytical technique (e.g. Bogner et al., 2007; Hawkes, 2004; McMullan, 1995), applied in many domains of Earth sciences (e.g. Chen et al., 2015), to obtain high quality images on different aspects of the sample (i.e. chemistry, topography). In the SEM, electrons are generated by an electron gun and accelerated to an energy between 0.1 and 30 KeV into the column, equipped with electron lenses and scan coils. Emerging from the column the beam interacts with the sample, with a certain penetration depth, and generate different types of signals, collected by detectors. Detectors are built to convert signals into intensity change (Everhart and Thornley, 1960). The differences in intensity reflect different properties of the sample that are function of the detector being used and consequently the type of collected signal (Figure 2.12).

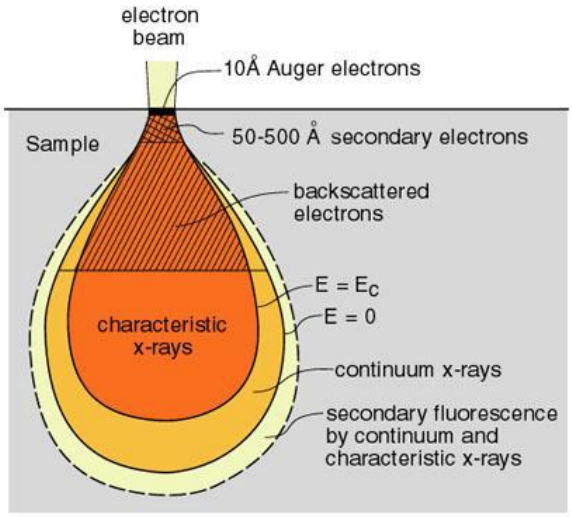

Figure 2.12: Volume regions and emitted signal during electron beam sample interaction.
Image from (https://www2.nau.edu/micro-analysis/wordpress/index.php/signals/).

Electrons elastic and inelastic scattering are studied with the SEM. Elastic scattering results in the emission of backscattered electrons (BSE) reflected from deeper portions of the sample (Napchan, 2001). The intensity of the detected signal is tightly related to the atomic number (Z) of the sample. Atoms with high Z are stronger scatterers compared to atoms with low Z, accordingly a higher number of BSE will reach the detector. The volume of interaction depth and the trajectories of the emitted electrons depend on the acceleration-voltage of the incoming beam (Figure 2.13) and the elemental composition of the sample. The effects of sample's chemistry are well visible in Figure 2.13b and c, where the BSE trajectories obtained for a carbon sample are sensibly less than those for a silicon sample (Goldstein et al., 2018; Maletz et al., 2005). For example, carbon and silicon have low Z compared to iron hence their appearance can be identified by the presence of dark patches in the transverse cut of the sample (Figure 2.11c).

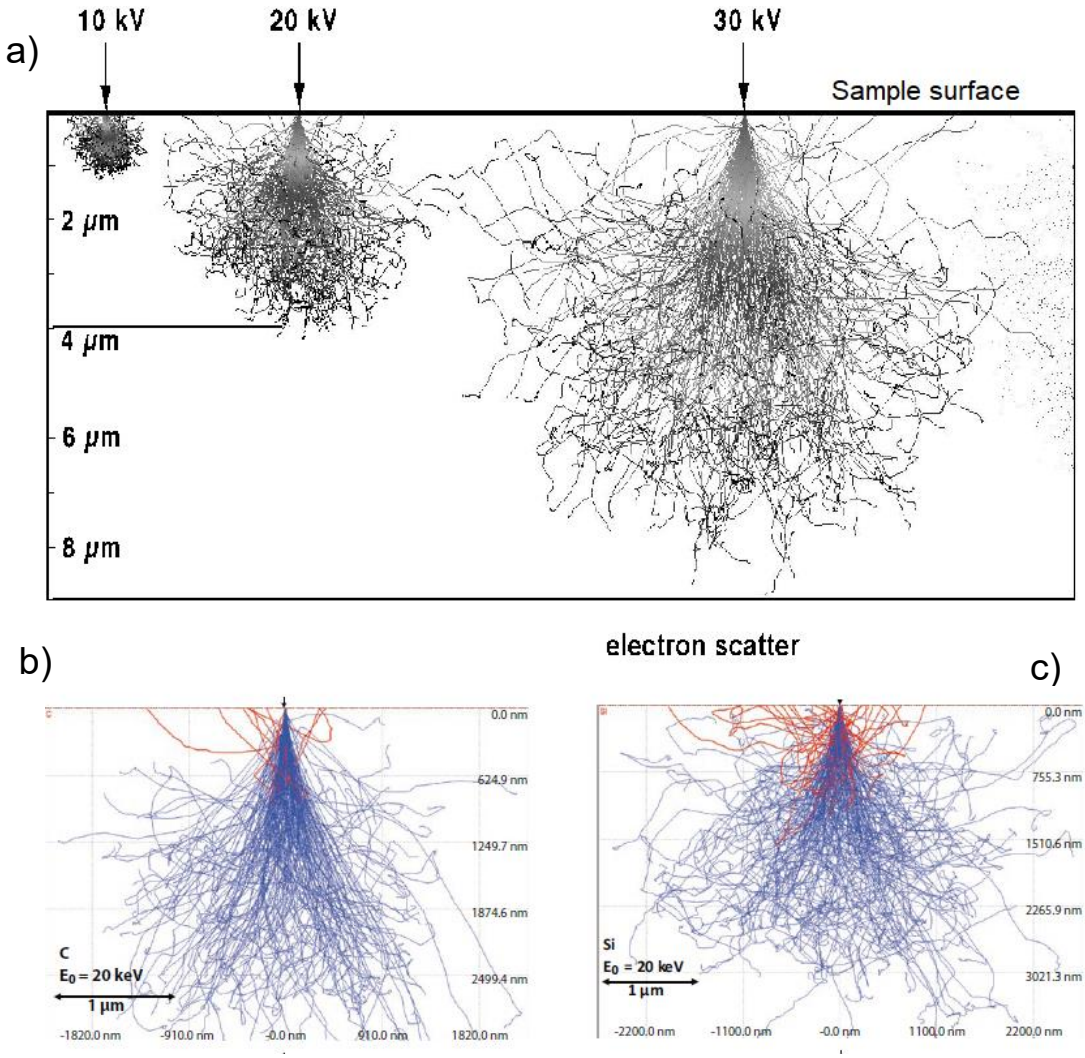

Figure 2.13: a) Monte Carlo simulations of electron scattering generated from the interaction of an electron beam with a carbon sample. The penetration depth and the volume of interaction are function of the electron beam voltage. Image elaborated from (Maletz et al., 2005) b, c) Monte Carlo simulations of the trajectories of electrons scattering into samples with different composition. In red the backscattered electrons, in blue those that are absorbed by the samples images from (Goldstein et al., 2018).

Secondary electrons (SE) are produced by inelastic interaction between incoming electrons and the sample surface. SE are emitted with an energy ≤ 50 eV from a depth range of 5-50 nm (Chen et al., 2015; Seiler, 1983). Coming from a superficial region of the sample, the number of emitted SE is influenced by the orientation of the sample surface hence allowing to image topographical features (Figure 2.14). The SE detector is positioned close to the sample, with an angle in respect to the primary electron beam.

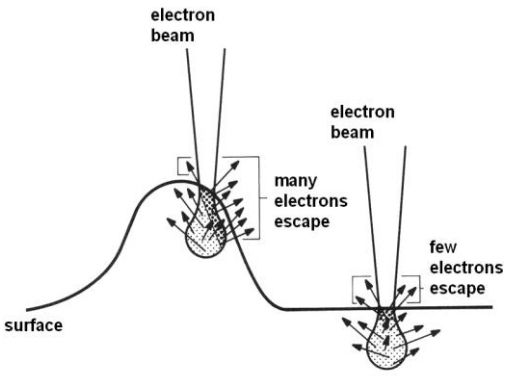

Figure 2.14: Effect of topography on the emission of secondary electrons, image from © ETH Zürich and F. Krumeich.

During electron sample interaction, generated x-rays could be collected and separated by energy level in an Energy Dispersive detector, and be used to retrieve qualitative and semi-quantitative chemical analyses of the sample (Chen et al., 2015). Each element emits energy at characteristic values corresponding to the transition energy between energy levels in the electron shell. We used such technique to perform preliminary chemical mapping and element identification in our samples prior microprobe analysis.

In this study the SEM-FEG Zeiss Ultra55 available at the IMPMC laboratory, Sorbonne University was used to obtain backscattered and secondary electron images of the samples. Furthermore, chemical mapping with the EDX detector were performed. It should be noted that the dimension of the samples and chemical features plus the chemistry of the sample itself, made it challenging to obtain precise chemical mapping. Nevertheless, enrichment zones were observed.

2.5.2 Electron Micro Probe Analyser (EMPA)

In the EMPA electrons created from a source are accelerated into a column via electron lenses and scan coil, before hitting the sample (Figure 2.15). Chemical species are discriminated through X-ray wavelength dispersive spectroscopy (WDX) instead of energy dispersive (EDX). The principle rely on employing analytical crystals with precise lattice spacing (d-spacing) and hence select only specific wavelengths through the application of the Bragg law. Instruments are equipped with several crystals having different lattice spacing. With this configuration the spectrometers can normally reach all the elemental wavelengths of interest above boron that represents the lower detection limit.

As the sample and the take-off angle of the X-rays are fixed, in order to satisfy the Bragg law for all the wavelengths of interest, the sample, analyser crystal and detector move on the Rowland circle so as to have the X-rays efficiently focused. X-rays with the specific wavelengths to pass through the analyser crystals are conveyed to the detector, usually of the proportional counter type. The intensity of the X-rays is counted and the count rate is compared to those of a standard with a known abundance.

Analyses for the present study were performed at service Camparis, in Sorbonne University, where a Cameca SXFive is available. The microprobe is equipped with 5 spectrometers with multiple analyser crystals that enable a good coverage of all the possible wavelengths. Obtaining reliable quantitative analyses on the transverse cut of the samples was a challenge, due to the small size and the very specific chemical composition.

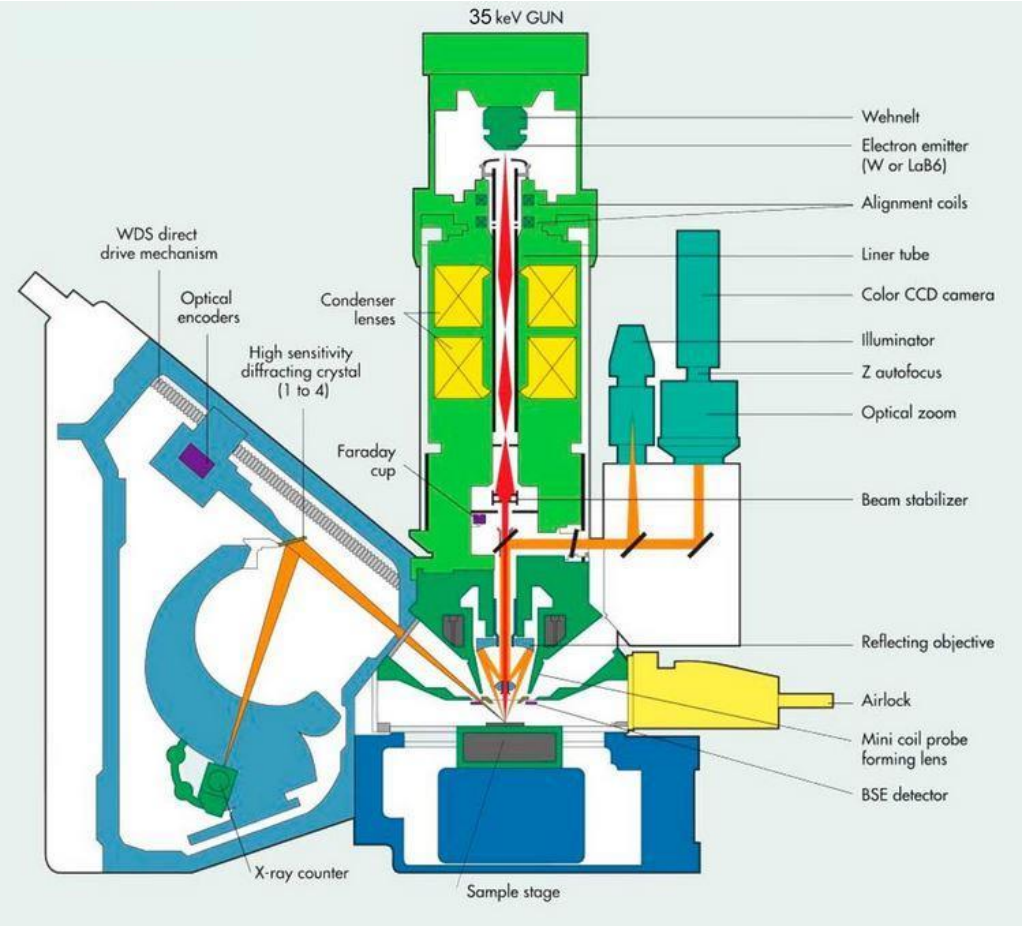

Figure 2.15: Image of the Cameca SXFive microprobe available at service Camparis, Sorbonne University. Image from http://camparis.ecceterra.fr. Vertical and in green colour the electron column with the gun and lenses, on the left side one of the spectrometers, with the diffracting crystal and the detector.

Our samples required to establish a procedure for carbon analyses in iron alloys samples. The faced issues regarded: i) carbon contamination; ii) low X-ray emission intensity; iii) interference with other chemical species; iv) selection of the reference materials and v) orientation of the sample.

Carbon contamination consists in the deposition on the specimen surface of carbon resulting from the cracking of organic molecules by the electron beam. This is recognisable by carbon counts increase while doing several analyses on the same spot. The most common solution adopted is the use of a nitrogen cooled cold fingers and an oxygen flux. The first, inserted in the chamber near the impact point of the beam, should capture volatiles organic molecules thus improving the vacuum. The flux instead create a reactive atmosphere around the measurement position removing the carbon and avoiding

deposition on the sample surface. The efficiency of these solutions is proved by the absence of increasing carbon content with time during repeated measurements.

Low X-ray intensity is the results of the low atomic weight of carbon. The amount of back-scattered electrons reaching the sample depends on the atomic number of the element. As visible in Figure 2.13b, the trajectories computed for a carbon sample are way lower compares to silicon and consequently also iron.

The presence of higher Z elements change the absorption behaviour of the system and need to be also taken in account. High Z element can absorb part of the radiation emitted by carbon leading to an underestimation of the content in the sample. For example, using a SiC standard and determining the composition of Si-C starting material gives results with a total closing at 100 wt%. Whereas analyses made on a standard containing also iron will underestimate the amount of carbon. The response of the system when both iron and carbon are present need to be well characterized and for different possible content of the two elements.

Accordingly several Fe-C standards were used: natural Fe_3C (loan by the mineralogy collection of MNHN), synthetic Fe_3C and synthetic Fe_7C_3. The synthetic iron carbides were synthetized at high pressure and temperature with large volume presses (by Julien Siebert and Yoichi Nakajima). Pure Fe was used as a calibrant and reference for the carbon background contamination (around 0.5 wt% C). Through an iterative procedure each standard was used to calibrate different carbon content and after the response of the machine was tested on another standard. With this procedure the composition of almost all the starting material was determined and the values are listed in Table 3. When the analyses are made on transverse cut of DAC samples, it is necessary to be careful with the orientation of the surface in respect to the analyser crystal that is going to be used.

The different tests made at Camparis analysis facility to solve the different presented issues were only finalized in the last months, and several samples recovered from synchrotron runs were unfortunately lost. Iron carbides samples are known for being not easy to keep pristine during storage. Even if kept under vacuum, after few months the surface will start to react and form odd structures on the surface and changing the texture in the sample as visible in Figure 2.16. At first, the sample was cut by FIB and no sign of reactions or particular textures (a), after three months all the exposed surface had reacted producing bubbles (b). The alteration also corresponds to a change in the texture of the inner part of the sample. Part of the solid material seem to have dissolved leaving behind a kind of fibrous net, only small parts of the original sample are still visible (c). At the present state, results were obtained for the starting materials and are listed in Table 3. Comparing the atomic % in the starting material with the target composition provided to the manufacturer (Table 2) a silicon enrichment of ~ 10 at% is present in the samples with higher light elements content.

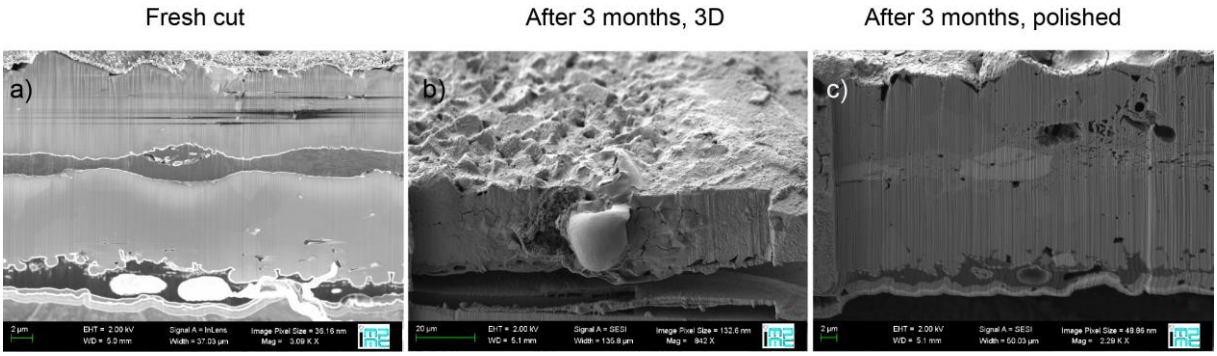

Figure 2.16: Example of alteration on Fe-C samples during storage under vacuum.

Table 3: Results of the microprobe analyses on the Fe-Si-C starting materials. The values for FeSi20C10 were extrapolated according to the measures on the other samples. *composition only estimated. Not determined with microprobe analyses.

Fe (wt %)	Si (wt %)	C (wt %)	Total	Sample	Fe (at %)	Si (at %)	C (at %)
96.77 (0.40)	1.91 (0.12)	1.0 (0.19)	100.3	$FeSi_3C_3$	91.97	3.60	4.41
81.53 (0.49)	17.67 (0.38)	2.12 (0.37)	101.31	$FeSi_6C_5$	64.43	27.77	7.79
78.98 (0.35)	16.17 (0.15)	5.50 (0.21)	100.66	$FeSi_{10}C_{20}$	57.77	23.51	18.70
78*	20*	2*	100*	$FeSi_{20}C_{10}$	61.38	31.30	7.32

2.6 Equations of state and thermal models

There are several formalisms linking the variation of volume to that of pressure (isothermal equation of state), each with its own assumption and mathematical development (Anderson and Lee, 1995; e.g. Angel, 2000; Angel et al., 2017, 2014; Duffy, T, Wang, 1998; Kroll et al., 2012; Poirier and Tarantola, 1998). Here we employed a Birch-Murnaghan equation of state, that is a "finite strain EoS", in which the strain energy of a solid undergoing compression is expressed as a Taylor series in the finite Eulerian strain f_E, where $f_E = \frac{1}{2}\left[\left(\frac{V_0}{V}\right)^{\frac{2}{3}} - 1\right]$ (Angel, 2000). The expansion to the third order in the finite strain yield to the relation:

$$P = \frac{3}{2} K_0 \left[\left(\frac{V_0}{V}\right)^{\frac{7}{3}} - \left(\frac{V_0}{V}\right)^{\frac{5}{3}}\right]\left\{1 + \frac{3}{4}\left[K_0' - 4\right]\left[\left(\frac{V_0}{V}\right)^{\frac{2}{3}} - 1\right]\right\}$$

V is the volume, V_0 and K_0 are respectively the volume and bulk modulus at ambient pressure and reference temperature (here 300 K) and K_0' the first pressure derivative of the bulk modulus ($\partial K/\partial P$). A second formalism largely used for equation of state of solids is the one by Vinet, derived from interatomic potentials and designed to better represent materials under very high compression (Vinet et al., 1987, 1986), which gives:

$$P = 3K_0 \frac{(1-f_V)}{f_V^2} \exp\left(\frac{3}{2}\left(K_0' - 1\right)(1-f_V)\right)$$

where $f_V = \left(\frac{V}{V_0}\right)^{\frac{1}{3}}$.

As those equations of state are both considered to satisfactorily describe the compression of solid materials over the pressure range of our interest, we decided to fit our data with both, and then choose the one giving less residuals.

The thermal pressure EoS model, in which the volumes explicitly and independently depends on both P and T, describes the high temperature behaviour of compressed materials. This approach requires the determination of the pressure at reference T condition, i.e. 300 K isotherm in our case P(V,300K), and then thermal pressure with increasing temperature along isochors P_{th}(V,T). Consequently the pressure at a given temperature is defined as:

$$P(V,T) = P(V,300K) + P_{th}(V,T)$$

To calculate the second term, two main thermal pressure EoS are used in literature, the Mie Grüneisen Debye and the Thermal Pressure model (Kroll et al., 2012). The Mie Grüneisen Debye (MGD) model relies on a Debye-like approach, where the thermal-induced lattice vibrations are modelled as a series

of harmonic oscillators. The vibrational energy of the lattice is expressed as a function of the temperature T normalized to the characteristic Debye temperature θ_D and written as:

$$E(T,\theta_D)=9nRT\left(\frac{T}{\theta_D}\right)^3\int_0^{\frac{\theta_D}{T}}\frac{t^3dt}{e^t-1}$$

where n is the number of atoms per formula unit, R the gas constant. The Debye temperature

$$\theta_D = \theta_0 \exp\left[\frac{\left(\gamma_0-\gamma(V)\right)}{q}\right]$$

is a function of the Grüneisen parameter (γ) given by

$$\gamma(V) = \gamma_0 \left(\frac{V}{V_0}\right)^q$$

where q corresponds to the logarithmic volume dependence of $\gamma(V)$. γ and θ_D only depend on the volume and are constant along isochors. The vibrational energy, together with the Grüneisen parameter and the volume, define the thermal pressure, with the E_c and T_c being energy and temperature at reference conditions:

$$P_{th} = \frac{\gamma(V)}{V}\left[E(T,\theta_D)-E_c(T_c,\theta_D)\right]$$

In summary, in the MGD model, parameters that control the thermal pressure, and hence allow the description of the thermal state of the system, are only three: the Debye temperature, the Grüneisen parameter, and *q* (see Angel et al., 2018 and references therein).

The second approach is the Thermal Pressure (TP) model. In this model the slope of an isochor in the P-T space is written as:

$$\left(\frac{\partial P}{\partial T}\right)_V = \alpha_V K_0$$

(Anderson, 1984; Angel et al., 2018; Poirier, 1991) with α_V being the thermal expansion. Consequently, during an isochoric heating thermal pressure can be written as:

$$P_{th}= \int_{T_0}^{T}\alpha_V K_0 \partial T$$

The product $\alpha_V K_0$ is usually assumed to be constant along an isochor, as isochors are linear for T above the Debye temperature. (Holland and Powell, 2011) also defined an approximation for the integral of P_{th}, explicitly introducing the dependence upon the Einstein function to account for the decrease to 0 as temperature decreases to 0 K (Angel et al., 2018; Holland and Powell, 2011).

$$\xi = \frac{u^2 e^u}{(e^u - 1)^2}$$

with $u = \theta_E/T$ and θ_E being the Einstein temperature. Following Holland and Powell (2011) P_{th} can then be written as:

$$P_{th} = \alpha_{V0} K_0 \left(\frac{\theta_E}{\xi_0}\right)\left(\frac{1}{\exp\left(\frac{\theta_E}{T}\right)-1} - \frac{1}{\exp\left(\frac{\theta_E}{T_0}\right)-1}\right)$$

with $\xi(T_0)$ as in the thermal expansion equation from (Kroll et al., 2012).

$$\xi(T_0) = \frac{\left(\frac{\theta_E}{T_0}\right)^2 \exp\left(\frac{\theta_E}{T_0}\right)}{\left[\exp\left(\frac{\theta_E}{T_0}\right)-1\right]^2}$$

The Einstein temperature (θ_E) can be assessed from the measured entropy. In particular, for end-members the value of $\theta_E = 10363/(S/n + 6.44)$, with S being the molar entropy and n the numbers of atoms (Holland & Powell, 2011). Alternatively, the Einstein temperature can be calculated from the Debye temperature, employing the relation ($\theta_E = \theta_D * 0.806$). In the Thermal Pressure model, thermal pressure only depends on two parameters: the coefficient of thermal expansion (α_v) and the Einstein temperature (θ_E) (which is usually fixed).

Both the MGD and the TP thermal model were used to fit our data. Indeed MGD is one of the most common parameterization to represent the P-V-T relations of a solid material under extreme conditions, and has already been used for the B3 structure by (Nisr et al., 2017). On the other hand, TP is typically used for rigid structures and recent studies (e.g. Angel et al., 2018; Milani et al., 2017). These works demonstrate that TP provides a reliable and trustworthy thermal model especially for compounds that, as SiC, have properties similar to diamond. However, it should be noted that assuming the product $\alpha_V K_0$ constant along an isochor is an approximation and, as such, it might not be always adequate (Jackson and Rigden, 1996). A discussion about the results and which model better matches our experimental data set will be presented with the results.

Chapter 3

On the Si-C binary system

3.1 State of the art on silicon carbide

At ambient conditions SiC consists in series of stacked Si4C tetrahedra and many polytypes with different structures (e.g. cubic, hexagonal, rhombohedral) are stable (e.g. Daviau and Lee, 2018; Dobrzhinetskaya et al., 2018). The cubic (3C) and hexagonal (6H) SiC were the most studied polytypes. They show the higher symmetry and electrons mobility. Furthermore, they represent the two polytypes more commonly retrieved on Earth and in meteorites. In all the experimental runs performed in this study, SiC is stable with the cubic phase, accordingly the following paragraph will focus on the 3C polytype. 3C SiC is stable at ambient conditions as a cubic zinc-blende structure (β-tin or B3), characterized by a face centred lattice where Si and C atoms are in tetrahedral coordination (Figure 3.1a). This structure transforms into a rock-salt (or B1) structure at high pressure (Figure 3.1b). Such transition was identified in the pioneering work on SiC performed via ab-initio calculations by Chang and Cohen (1987) with the aim of studying the structural phase stability at high pressure and the basic properties of 3C SiC such as the evolution of the cell parameters with pressure and the equation of state. The authors also identified a phase transition from the cubic zinc-blende to a cubic rock-salt structure.

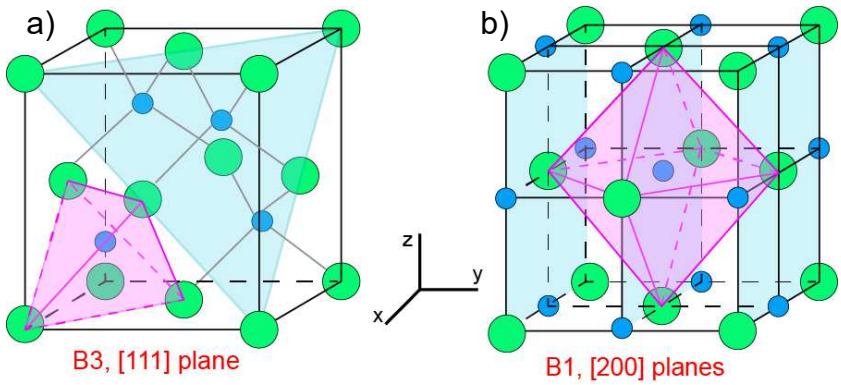

Figure 3.1: Zinc-blende to rock-salt phase transition of SiC. In light pink the coordination of the atoms, in light blue the planes responsible for the most intense peak in diffraction patterns.

Initially SiC was widely studied in the frame of material sciences. Its hardness and good thermal properties make it suitable to be used as abrasive, structural element for furnaces and semiconductor. The possibility for this compound to be the main component of a planetary interior, significantly extended the range of pressure and temperature at which characterization was required. The proposed studies thus further focused on the determination of the phase diagram and the equation of state under extreme conditions. For planetary application, mapping the evolution of the phase transition with pressure and temperature (i.e. the Clapeyron slope) and the phase diagram is fundamental do determine

the mineralogical and dynamical properties of planetary interiors. In addition, volume determination enable the calculation of reliable planetary models and mass radius plot.

However, application to exoplanets interior is recent and performing experiments at extreme conditions is challenging. Experimental studies devoted to the application to planetary interiors were first focused on the pressure range of the zinc-blende structure and the phase transition, neglecting the high pressure phase (Daviau and Lee, 2017a; Kidokoro et al., 2017; Nisr et al., 2017). Only one work overcame the phase transition and determined the volumes at ambient temperature of the high pressure phase (Kidokoro et al., 2017).

3.1.1 Phase transition

The phase transition in SiC has been an object of great interest since the work of Chang and Cohen (1987). Determining the transition pressure and evolution had been a challenge, for both experiments and computations methods and the results were relatively scattered.

In the experimental study of Yoshida et al. (1993) performed with static compression experiments coupling diamond anvil cell and synchrotron X-ray diffraction, the transition was observed at 100 GPa and associated to an important volume reduction (20.3%). The obtained pressure is sensibly higher than the 60 GPa predicted by calculations (Chang and Cohen, 1987). Few years later Karch (1996) performed a first principle study on both cubic and hexagonal SiC. In agreement with previous computations, and not the experimental study of Yoshida et al. (1993), the transition was calculated to be at ~67 GPa. Shimojo and co-authos (2000) with molecular dynamic simulations instead retrieved a transition pressure (140 GPa) higher than both experiments and previous computations. Varshney et al. (2015) then proposed 90 GPa after computing all the elastic and thermodynamic properties of cubic B3 and B1 silicon carbide.

The inconsistencies in the pressure determination of the phase transition were addressed again by Catti (2001) employing a different calculations methodology. The outcome of their work agreed with the pressure retrieved by previous computational studies (i.e. 60 GPa) and propose a new mechanism for transition including an orthorhombic P*mm*2 intermediate phase. The same transition pressure was obtained by Lee and Yao (2015) and Lu et al. (2008) with another different computational method. The transitions mechanism of Catti (2001) was afterwards supported by the results on phonons obtained by Zhuravlev et al. (2013) in their study on a single crystal of cubic SiC by the means of different techniques (i.e. X-ray diffraction, Brillouin and Raman spectroscopy). However, as the experiments were performed only up to 65 GPa this work doesn't provide any new insight on the transition pressure.

The topic of SiC phase transition was experimentally addressed again in recent years by Daviau and Lee (2017b) and Kidokoro et al. (2017) from now on referred to as D&L and KDK. In both studies experiments were performed coupling laser heated diamond anvil cells with *in situ* X-ray diffraction.

Different SiC powders were used as starting materials: D&L a B3 SiC powder from Alpha Aesar and KDK a 6H fine grained powder from GoodFellow. Samples heating however required an absorber for the YAG laser to be used. In KDK pellets of compressed powder were gold-coated and the coating used as both laser absorber and pressure calibrant. Instead there is no mention in D&L about the use of an absorber or the type of source for laser radiation. A CO_2 laser might have been used to actually heat SiC powder.

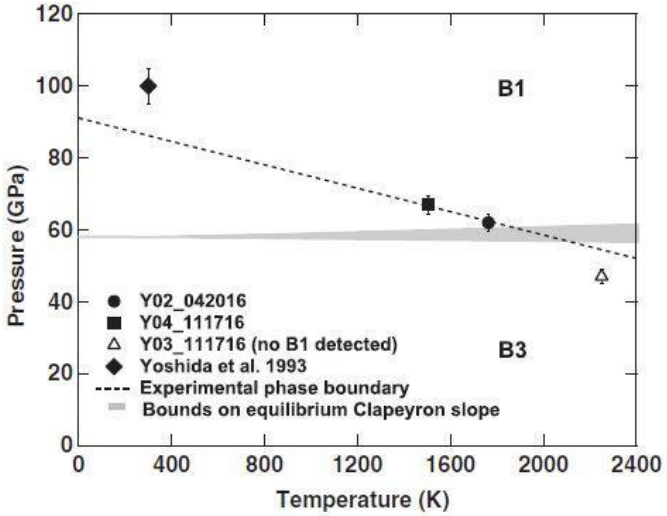

Figure 3.2: From Daviau and Lee (2017b), a) collected experimental data plotted with the determined Clapeyron slope. The filled symbols between 60 and 80 GPa display B3 B1 coexistence. The symbols at 100 GPa is a point from Yoshida et al. (1993). The open symbol display only stable B3. Dashed line represents the experimentally determined Clapeyron slope. In grey and filled the one calculated from equilibrium.

As pressure calibrant D&L always used neon while KDK opted for solid pressure medium NaCl, KCl as well as SiO_2. D&L performed three experimental runs, two displaying the coexistence of the two structures, advocating for a negative and steep Clapeyron slope ($\Delta P/\Delta T$) (-26.4 ± 19 MPa/K) of the transition that was observed at ~ 66 GPa and 1500 K, Figure 3.2) with a 17.5% volume reduction.

The results of KDK instead place the phase transition at ~80 GPa. The authors never observed any coexistence of the two phases. But used the occurrence of the last stable B3 and the first stable B1 to constrain the pressure range of the transition. The Clapeyron slope was defined after a rescaling in pressure of the calculations from Catti (2001) and estimated to be -4 MPa/K at 2000 K (Figure 3.3).

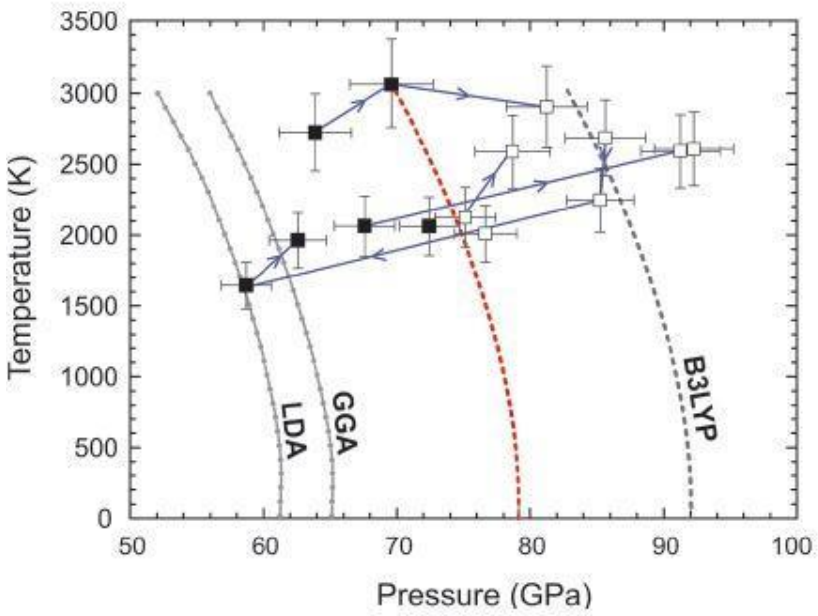

Figure 3.3: From Kidokoro et al. (2017) performed experimental run, as temperature on pressure. Symbols represent the experimental data, solid lines the transition determined with calculations. Black broken line previous calculation from Catti (2001) and in red a re-scaling in agreement with the experimental data.

3.1.2 Phase diagram

At ambient pressure SiC has been proven to melt incongruently with solid graphite + Si-rich liquid (Dolloff, 1960) but a discrepancy is present in the melting temperatures determined with calculations and experiments ~ 2840 K vs 3100 K. The main controversy on SiC melting at high pressure is whether or not it melts congruently (Sokolov et al., 2012; Togaya and Sugiyama, 1998). This topic was recently investigated by Turkevich et al. (2016) and Daviau and Lee (2017a). The first determined with thermodynamic modelling the isobaric Si-C phase diagram between 0.1 and 8 GPa. On the other hand Daviau and Lee (2017a) coupled laser heated diamond anvil cells and *in situ* X-ray diffraction with electron microscopy study of recovered samples. Their results are shown in Figure 3.4. The appearance of carbon was taken as a reference for the beginning of decomposition. However the authors never observed the complete disappearance of SiC peaks or the appearance of pure silicon, neither at high temperature, nor in the quench. Hence it is difficult to confirm the completion of the decomposition process.

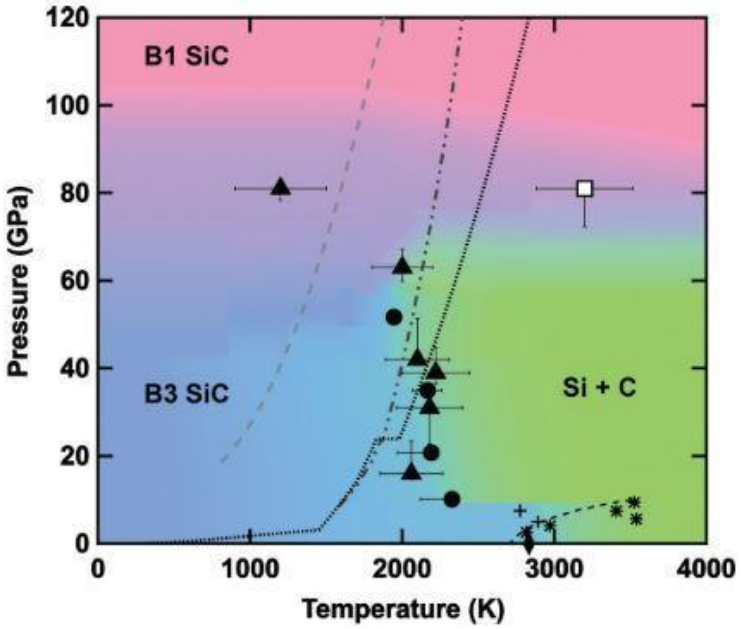

Figure 3.4: Phase diagram proposed by Daviau and Lee (2017a). Circles represent the first appearance of diamond diffraction peaks, taken as a reference for the onset of decomposition. Triangles where differences in the absorption are observed and the square corresponds to SiC B1 phase, were no evidences of decomposition were observed. Colour shading stand for the phases' regions of stability.

3.1.3 Equations of state and thermal model

The equation of state for the low pressure structure B3 at ambient temperature was obtained via computations and experiments, by several authors. Early works already attest the hardness of SiC, with a bulk modulus higher than 200 GPa. In particular, Yoshida and co-authors (1993) fitted their experimental data and obtained $K_0 = 260 \pm 9$ GPa and $K_0' = 2.9 \pm 0.3$. Zhuravlev and co-authors (2015) determined experimentally the thermodynamic and elastic properties of cubic SiC by Brillouin and single crystal XRD. The obtained solution, with $K_0 = 218 \pm 1$ GPa and $K_0' = 3.75 \pm 4$, with a V_0 of 82.96 $Å^3$ has a lower bulk modulus that Yoshida and co-authors (1993). However, differences can be attributed to a trade-off between K_0 and K_0'.

More recently, the high temperature behaviour started being investigated too. Wang et al. (2016) coupled large volume press experiments with synchrotron energy dispersive X-ray diffraction to determine the equation of state and thermal model of the B3 phase. With the results of the experiments, collected up to 8 GPa, the EoS was determined ($K_0 = 237 \pm 2$ GPa, K' fixed to 4 and $V_0 = 82.85 \pm 1$ $Å^3$) in agreement with the results from previous authors. The thermodynamic quantities were calculated with two different approaches (i.e. a modified high-T Birch Murnaghan and a Thermal Pressure model).

The high pressure and high temperature behaviour of SiC B3 was investigated also by Nisr et al. (2017). Experiments were performed in laser heated diamond anvil cells with angle dispersive X-ray diffraction. P-V-T data were collected up to ~ 70 GPa and pressure was determined using gold as pressure calibrant with neon as the pressure medium. As several equations of state are available for gold the authors

determined one set of parameters for each gold EoS, for both the 3C and the 6H polymorphs. The 300 K parameters were obtained with the Birch Murnaghan or Vinet equation of state (K_0=243 GPa; K_0'=2.68; V_0=82.8 Å^3). The Mie Grüneisen Debye parametrization was used for the thermal model. In the latter only q was determined with the collected data set, while the Debye temperature (θ_D) and gamma0 (γ_0) were fixed to values from literature. The choice of the EoS for Au, produce a change in the value of q in the order of a unit. Moreover, q displays a negative value when the gold EoS proposed by Fei et al. (2007) is used. The different EoS have also a direct relation with changes in the thermal pressure and the coefficient of thermal expansion α.

Finally Kidokoro et al. (2017) used the volumes obtained for the high pressure structure (up to 90 GPa) to first determine the equation of state at ambient temperature of the high pressure phase B1. With a second order Birch-Murnaghan EoS the parameters were determined to be: K_0 = 235 ± 9 GPa and V_0 = 10.21 cm^3/mol, in agreement with previous calculations (Durandurdu, 2004; Karch, 1996).

3.2 Experimental results on SiC

Early studies on SiC focused on determining the physical and thermal properties in a pressure range consistent with material science applications. Nevertheless, recent developments pointing toward SiC as a possible planet building material requires an accurate determination of such properties at pressure and temperatures consistent with planetary interiors. With a reliable thermal equation of state also for the high pressure phase, models of planetary interiors are expected to be more accurate. With some hope to estimate the thermal evolution as well as the dynamic of the planet. However, despite the attention given to SiC, an experimental characterization of the high pressure phase properties at high pressure and temperature was still missing. Furthermore, investigating the potential effects of structural transition in a planetary mantle, requires a more accurate evaluation of the transition in the P-T space than those available in literature.

The high quality of the diffraction patterns obtained from PVD samples allowed us to improve the P-T mapping of the phase transition and collect data up to extreme pressures without giving up on the quality of the diffraction patterns. Ultimately the non-stoichiometry of the starting material allowed us to characterize phase diagrams for Si enriched, as well as C enriched compositions. The following results represents the first extensive characterization of the main properties of SiC high pressure structure.

The samples used for this study were made with PVD depositions, with three different stoichiometry, as listed in Table 2. Data were collected in a pressure range between 20-200 GPa and temperature comprised between 300-4000 K. Two samples were enriched in carbon (SiC_{75} and SiC_{65}) and one in silicon (SiC_{25}), in order to map the entire binary phase diagram. In the low pressure range the loaded samples were large enough to make several heating spots on one loading and for each composition several runs were performed.

All the experiments were carried out at the ESRF on beamline ID27. The nonstoichiometric nature of the samples resulted in the systematic disproportionation of the starting material into SiC + C or + Si, during the first phases of heating. Hence enabling us to study the properties of the stoichiometric compound and the Si-C binary phase relations. At ambient temperature KCl peaks were only visible on the diffraction patterns due to the nanocrystalline nature of samples from PVD. SiC diffraction peaks indeed start being detectable after initial heating and recrystallization during the lasers alignment procedure. Upon the highest temperatures, the well-defined diffraction lines obtained from recrystallized amorphous material could potentially become spotty. We used new positions for each heating runs so as to record diffraction on high quality samples with fine grain size. The obtained results were used to constrain the B3-B1 phase transition, determine the thermal EoS for both the low and high pressure structure and finally investigate the Si-C phase diagram.

3.2.1 Experimental determination of the zinc-blende to rock-salt phase transition

The zinc-blende to rock-salt is a cubic to cubic phase transition, driven by a change in the coordination of the atoms (Figure 3.1). The B3 SiC diffraction pattern is characterized by four reflections, 111, 200, 220, and, at higher angle, 311, sometimes merged with the 211 reflection from KCl. At low pressure, the most intense reflection is the 111. After the phase transition to the B1 structure, the 111 reflection shifts closer to the 110 of KCl and almost merges with it. The 200 becomes the most intense reflection (Figure 3.5 and Figure 3.7).

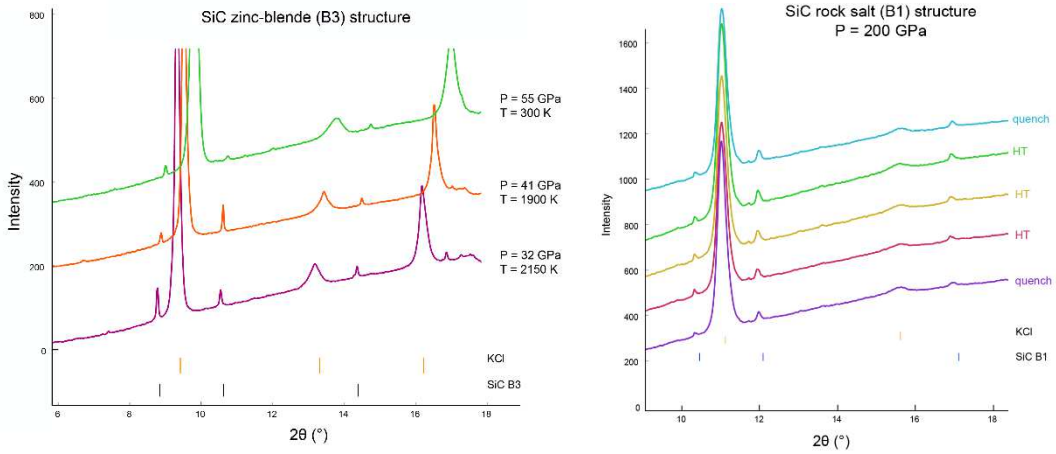

Figure 3.5: Diffraction patterns of SiC low pressure phase, with a zinc blende structure a) and the high pressure rock-salt structure b).

The large pressure temperature range explored during the experiments, and the high number of collected data points enabled to narrow the range of B3-B1 transition. The collection of several diffraction patterns showing the coexistence between the two phases unambiguously place the transition at 66 ± 2 GPa at room temperature and between 65 and 70 GPa at high temperature (Figure 3.6). The Clapeyron slope, with a value of - 0.001 GPa, is almost vertical. The data points showing coexistence are coming from different experimental runs, thus guaranteeing the reproducibility of the experiment and the validity of our observations.

The volume reduction (~10 %) is significant, with the cell parameters that depending on the actual temperature, vary from a = 4.09–4.10 Å (±0.002) (V = 68.80–69.06 (±0.1) Å^3) to a = 3.85–3.88 (±0.004) Å (V = 57.4–58.6 (±0.2) Å^3). However smaller than the values reported in literature (e.g. 20.3% from Yoshida et al. (1993) and 17 % from Daviau and Lee (2017b).

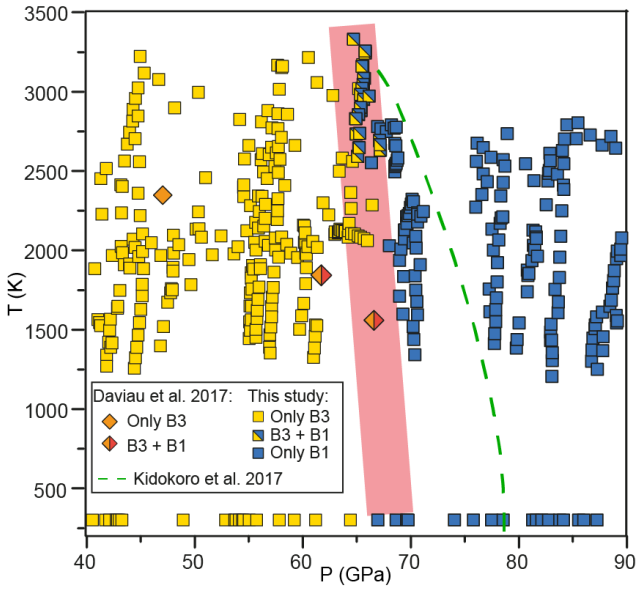

Figure 3.6: Data from this study at P =40–90 GPa and T = 300– 3,500 K. SiC B3, B1, and B3-B1 coexistence are reported in different colours; the phase transition region is highlighted by the light red band. Diamonds illustrate the data from Daviau and Lee (2017b). The green dashed line is the slope showed in Kidokoro et al. (2017) obtained after a rescaling in pressure of results by Catti (2001).

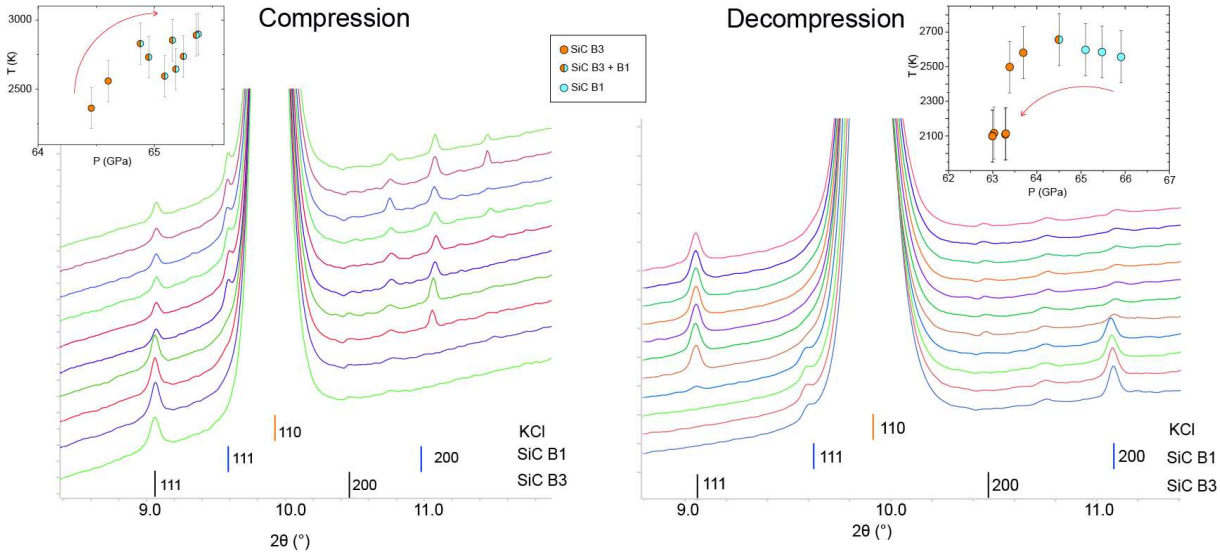

Figure 3.7: Diffraction patterns collected on SiC_{75} along selected pressure-temperature paths (displayed in the insers) show- in the phase transition from the zinc-blende structure to the rock-salt structure upon compression (left) and decompression (right). Reflections for SiC B3, B1, C, and KCl are labelled.

As mentioned before, the pressure domain of the SiC (B3-B1) phase transition has always been a matter of debate. Despite the effort made recently to provide a unique solution, discrepancies have still been observed. A sum of all the results on the phase transition is shown in Figure 3.8. Excluding dynamic

compression experiments that plot sensibly higher in pressure, the other results define a pressure range for the transition comprised between 60 and 80 GPa. The lower and higher boundaries are defined by Daviau and Lee (2017a) and Kidokoro et al. (2017) respectively. The range for the transition pressure is similar to the one deduced from theoretical studies at 0 K.

This discrepancies between our study and the previous ones might be the results of the different type of starting materials. The amorphous structure of PVD starting material in our study, makes our sample more reactive and help to avoid metastable phases. Also, different compression and decompression ramps were performed at high temperature through the phase transition. Finally, the number of data points (more than 20 points around the phase transition, from 1500 to 3500 K) presented here makes us confident about the position of phase boundary in the SiC phase diagram.

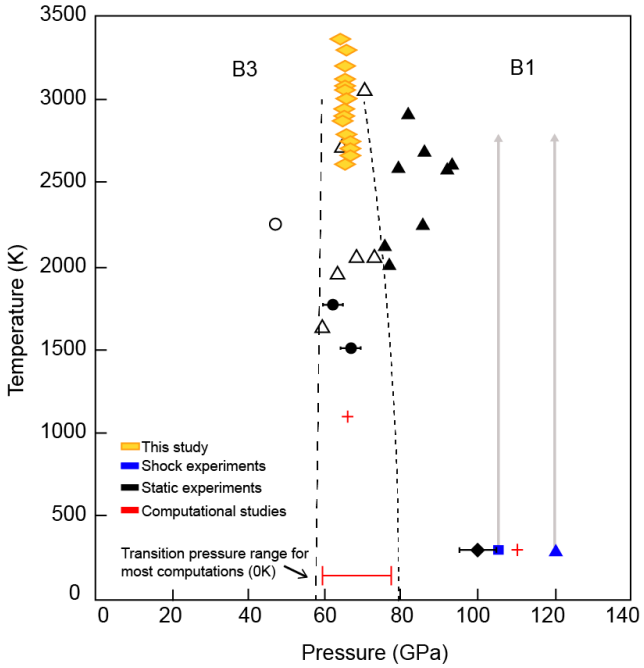

Figure 3.8: Revised from Daviau and Lee (2018). Pressure over temperature representation of the existing data on the SiC B3 to B1 phase transition. Results obtained with both static and dynamic compression, as well as computational study are shown.

3.2.2 Equations of state and thermal models

Pressure volume and temperature data were collected in a pressure and temperature range between 25 and 205 GPa and 300 – 4000 K (Figure 3.9).

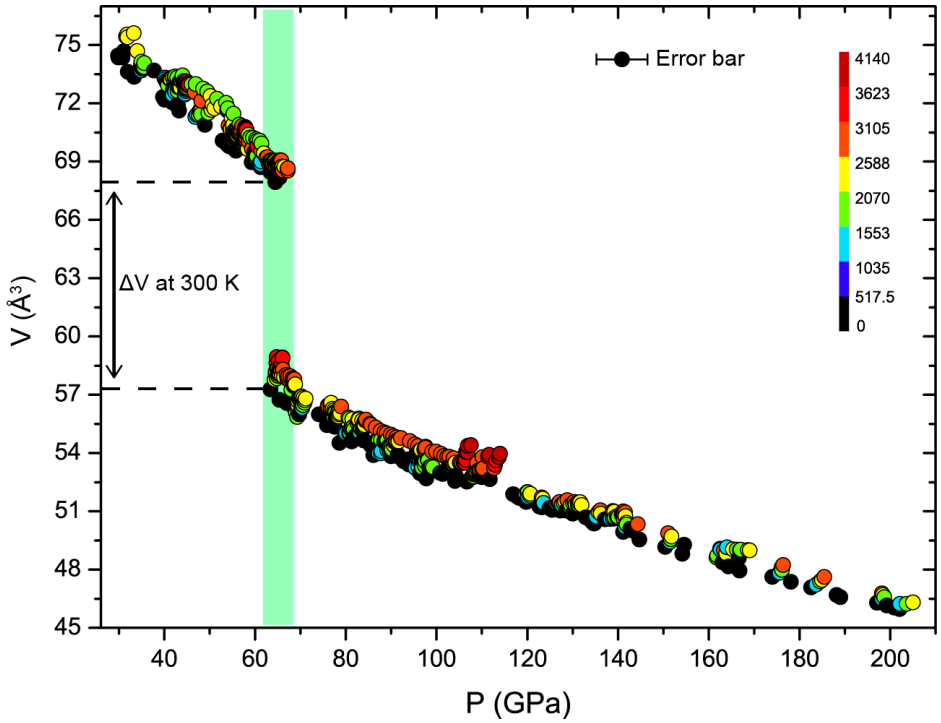

Figure 3.9: Collected data points for both SiC B3 and B1 structures. Volume, pressure, as well as temperature are shown. The green band highlight the transition zone.

The absence of data at pressures lower than 25 GPa is justified by the low melting temperature of KCl pressure medium. The data show a good pressure-temperature distribution at higher pressure. The runs performed to constrain the phase transition explains the high concentration of points around 60 GPa. For each phase the ambient temperature data were used to determine the equation of state at 300 K. The obtained parameters were then employed in the refinement of the thermal model.

Equations of state at ambient temperature

The data taken at ambient temperature were refined with both the Birch Murnaghan (BM), already used in literature to refine the data of the B3 structure, and the Vinet, designed to better represent materials under high compression (Vinet et al., 1987, 1986).

The results obtained from the fit of the B3 data are shown in Table 4 and Figure 3.10, together with the parameters determined in previous literature works. The use of two different models does not affect the refinement, as the obtained values of the parameters are in agreement within the error bar. When refining also the V_0, the absence of points below 25 GPa determines an uncertainty on the evolution of the curve at low pressure, thus affecting the bending and consequently the values of K_0 and K_0'. Accordingly, V_0 was fixed to the value determined by Nisr and co-authors (2017).

Table 4: P-V Equations of state fit results for both the low pressure (B3) structure. Data from previous experimental works are also shown.

	Zinc blende structure				
	This study		Yoshida et al. 1993	Zhuravlev et al. 2013	Nisr et al. 2017
EoS	BM	Vinet	BM	BM	Vinet
V_0 (Å^3)	82.80*	82.80*	82.92	82.96	82.80
K_0 (GPa)	224 (5)	222 (5)	260	218	243
K_0'	4.1 (0.3)	4.3 (0.4)	2.9	3.75	2.68

*Value from Nisr et al. (2017)

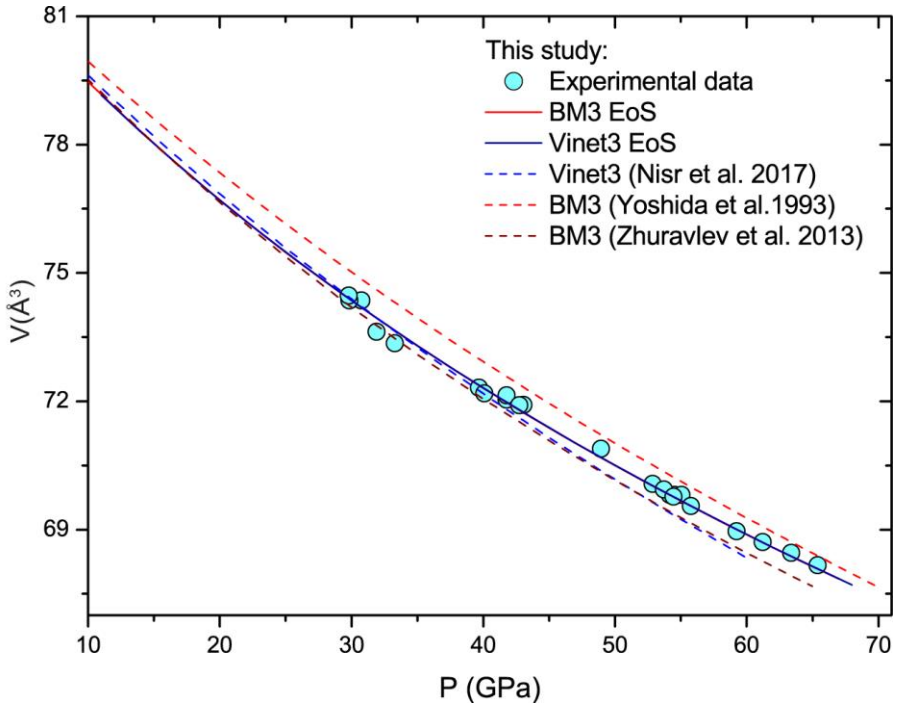

Figure 3.10: P-V data at 300 K for SiC B3 structure. The EoS obtained in this study with both models is compared with equations from literature.

The observed difference between our dataset and previous EoS is highlighted in Figure 3.10. Discrepancies are coming from the use of a different V_0, and from difference for data points over 50 GPa. However, the bulk modulus obtained from this study is lower than those determined on powders by previous XRD works (Nisr et al., 2017; Yoshida et al., 1993) but is in agreement with the data reported by (Zhuravlev et al. (2013) on SiC single crystal obtained combining XRD and Brillouin. The value of K_0' retrieved in this study is higher of those determined in the aforementioned works. The difference is not a consequence of the trade-off between parameters during the EoS refinement, but it can instead be a consequence of a shift in pressure between our data and those of Nisr et al. (2017) and

Zhuravlev et al. (2013) in the high pressure range (~45-65 GPa). Such discrepancies could be related to the different used pressure medium and related hydrostaticity, or the type of pressure calibrant (ruby for example is known for not always displaying a hydrostatic behaviour above 50 GPa). In Yoshida et al. (1993), the absence of sample heating prevents the release of the stresses during compression and points toward the non hydrostaticity as the responsible for the observed shift of the volumes.

The following data represent the first dataset collected on SiC rock- salt structure at pressures above 1 Mbar. The results from the refinement of the ambient temperature equation of state are shown in Table 5 and Figure 3.11, together with other available data from literature (Kidokoro et al., 2017).

Table 5: P-V Equations of state fit for the high pressure (B1) structure. Data from previous experimental works are also shown.

	Rock salt structure		
	This study		Kidokoro et al. 2017
EoS	BM	Vinet	BM
V_0 (Å^3)	66.3 (0.1)	66.3 (1.4)	67.5
K_0 (GPa)	323 (3)	324 (2)	235
K_0'	3.1 (0.43)	3.3 (0.52)	4

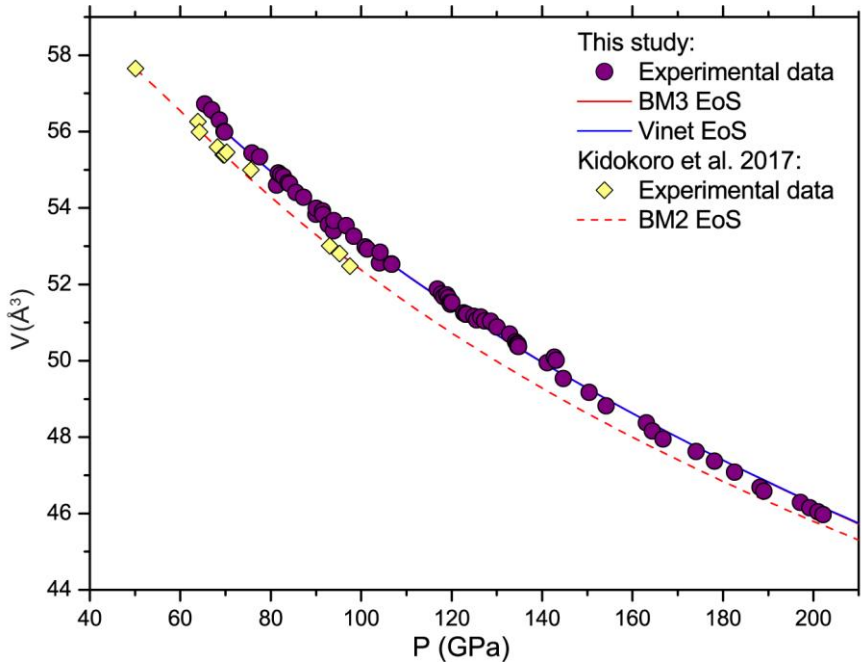

Figure 3.11: P-V data at 300 K for SiC B1 structure. The EoS fitted with both the Birch Murnaghan and Vinet model are shown together with the equation from literature. Errors are within the symbols.

The three parameters were refined with the chosen equation of state. The values obtained using the two different formalisms (Vinet and BM3) are in agreement within each other, and we cannot indicate any preferred EoS to fit the high pressure data at ambient temperature. Compared to the low pressure structure the EoS display a substantial increment in the value of K_0 (224 GPa for the B3 vs the 323 GPa of the B1) and a lower K_0' (4.1 for the B3 vs 3.1 for the B1). An increment in the value of the bulk modulus is a common outcome of the B3 to B1 phase transitions, as it often display an important reduction of the volume, driven by the change in coordination of the atoms and consistent with the observations done on other semiconductors (e.g. Ves et al., 1990; Zhao et al., 2015).

The only other EoS available for the high pressure structure, is the equation of state proposed by Kidokoro et al. (2017). Their second order Birch Murnaghan fit, results in a lower K_0 (235 GPa vs 323 GPa) and a higher initial volume, as shown in Figure 3.11. The K' fixed to 4 however hamper the possibility of a consistent comparison, as the value of K' can strongly affect the bending of the EoS. The use of a second order EoS is consistent with the narrow pressure range examined by the authors and the available data points, however it might lead to underestimation of the evolution in pressure. A second order birch Murnaghan EoS (V_0 = 70.34 Å^3, K_0 = 209 and K_0' = 4) fails to reproduce the pressure evolution of the present data (Figure 3.12), hence requiring a higher order EoS.

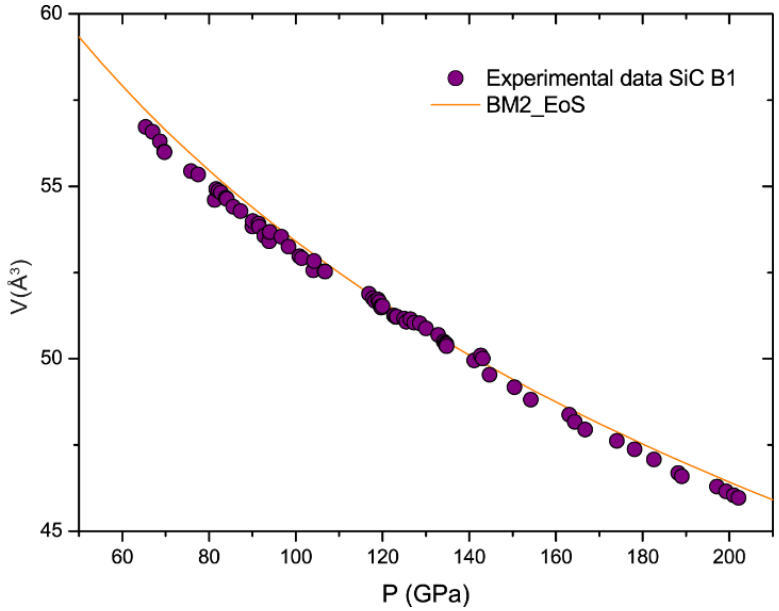

Figure 3.12: P-V data for SiC B1 structure fitted with a 2nd order BM EoS.

Au and KCl pressure determinations should be consistent with the same ruby scale, thus making it difficult to invoke the pressure scales as a possible source for the observed systematic shift in pressure between our data and Kidokoro et al. (2017).

Thermal models

The fits were performed with both the Mie Grüneisen Debye (MGD) and the Thermal Pressure (TP) models. The wide pressure range examined for this study, the presence of high temperature data and the simple structure of SiC make this exercise ideal to test the capabilities of the Thermal Pressure model for high pressures and to evaluate if such a formalism is a reliable alternative to the Mie Grüneisen Debye for all the pressure conditions. During the first phase of the refinement, in order to make an estimate of the parameters for the thermal model, the values from the BM3 EoS at 300 K were used as a reference. Afterwards an iterative procedure was followed, unlocking the parameters one by one and looking for a new solution for every step. The validity of the obtained solutions was estimated from the errors on the obtained values, the plot of the calculated volume over those experimentally determined, the residuals in pressure (P_{obs}-P_{calc}/P_{obs}) graph as well as the pressure evolution of the isotherms.

Data for the zinc-blende structure were collected at pressures between 25 and 65 GPa and temperature between 300 and 2500 K. The results obtained from the fit with the Mie Grüneisen Debye and the Thermal Pressure models are displayed in Table 6 and Table 7 respectively. In analogy with the 300 K EoS, the initial volume was kept fixed to the value from Nisr et al. (2017) and the values proposed by the authors for the Debye temperature and $gamma_0$ were used. Cycles of refinement done with all the parameters free except the V_0, could not converge to a realistic solution for the values of the thermal model. We added more constrains and choose to refine only K_0, K_0' and q. The obtained compressibility (228 ± 7 GPa) is in good agreement with the one determined at 300 K, while the first derivative is slightly lower (3.9 ± 0.3 vs 4.1 ± 0.3). The only parameter refined for the thermal model (q) has a value of -1.3. A negative value of q implies that the Grüneisen parameter increases with compression. Although quite an unusual behaviour, this was already reported by Nisr et al. (2017) for one of the pressure scales they used. Most likely, the negative value of q does not have a physical meaning, and simply is a numerical consequence of a fit performed over relatively limited pressure range with points showing some scatter, in particular at high temperature.

Table 6: Values of the thermal equation of state for the zinc-blende structure, fitted with the Mie Grüneisen Debye model. Parameters kept fixt are marked with an asterisk

Number of data points	V_0 (Å^3)	K_0 (GPa)	K_0'	T Debye (K)	Gamma $_0$	q
105	82.80*	228 (7)	3.9 (0.3)	1200*	1.06*	-1.3 (0.5)

Fit to the data with the TP model (Table 7 and Figure 3.13), yields better residuals in pressure. The value of the Einstein temperature was fixed to that calculated from the Debye temperature of the MGD model ($\theta_E = \theta_D * 0.806$). The obtained parameters for the zinc – blende B3 structure are $K_0 = 224 \pm 2$ GPa, $K_0' = 4.08 \pm 0.2$ with $\alpha_V = 0.62\ 10^{-5} \pm 0.1\ K^{-1}$. The latter is lower than previous experimental determination by Nisr et al. (2017), but is close to the values derived from calculations by Varshney et al. (2015). The

compressibility and pressure derivative have the same values as in the Birch – Murnaghan 300 K EoS-with smaller errors on the parameters, while the values found with the thermal MGD model are slightly different. The isotherms well reproduce the thermal behaviour of the data set.

Table 7: Values of the thermal equation of state for the zinc-blende structure, fitted with the Thermal Pressure model. Parameters kept fixt are marked with an asterisk

Number of data points	V_0 (Å^3)	K_0 (GPa)	K_0'	T Einstein (K)	Alpha (10^{-5} K^{-1})
105	82.80*	224 (2)	4.1 (0.17)	976.2*	0.62 (0.11)*

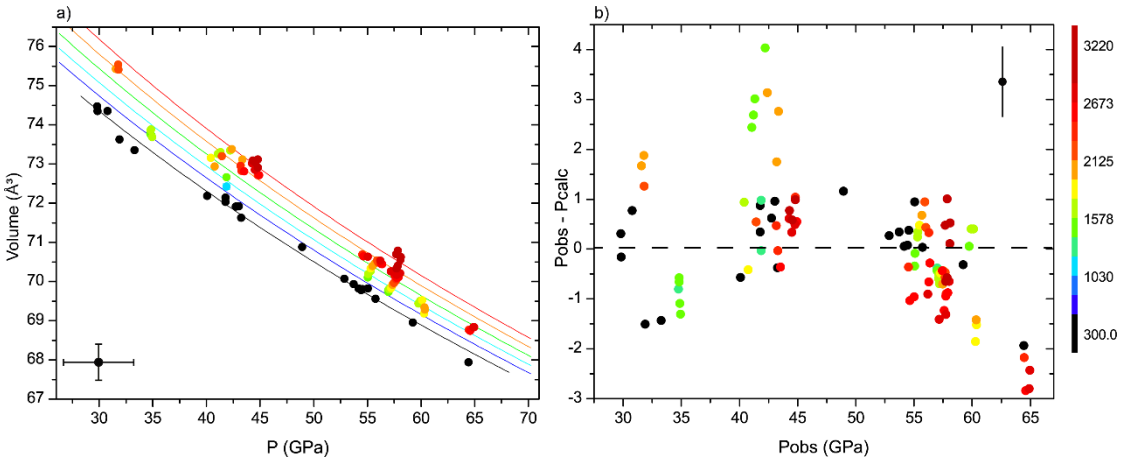

Figure 3.13: Results obtained fitting the zinc blende structure with the Thermal Pressure model: a) experimental data points and isotherms; b) Pressure residuals of the fit. On the right the temperature scale.

The thermal model for the rock-salt structure was refined with 348 data points, distributed in a pressure range between 65 and 205 GPa and temperatures between 300 and 3000 K. The only fixed parameter was the Debye temperature, kept to the value reported by Varshney et al. (2015). The results obtained with the MGD thermal model are presented in Table 8 while those obtained with the TP are shown in Table 9. The best fit solution with the MGD model yields $V_0 = 65.90 \pm 0.04$ Å^3, $K_0 = 340 \pm 10$ GPa and $K_0' = 3.06 \pm 0.06$, with a Debye temperature of 1200 K, $\gamma_0 = 0.50 \pm 0.05$ and $q = 1.6 \pm 0.5$, with $\chi 2 = 2.46$. As for the 300 K EoS the obtained compressibility is approximately 100 GPa higher than the low pressure structure. Such high value for the bulk modulus bring SiC closer to diamond ($K_0 = 444$ (Angel et al., 2015; Dewaele et al., 2008a; Occelli et al., 2003)). The convergence of the fit was investigated both refining the Debye temperature and keeping it fixed. Considering the solution with fixed θ_D, the obtained value of γ_0 is lower (0.5 vs. 1.06) than the one from previous computational work (i.e. Varshney et al., 2015). We also investigated the correlation between the parameters of the thermal model and how the different values would affect γ. Several refinements were performed individually fixing or refining θ_D, γ_0, and q. Using the relation $\gamma(V) = \gamma_0(V/V_0)^q$, we systematically obtained a value between 0.3 and 0.4, thus excluding the fixed value of θ_D as a possible source of ambiguity in the fit. The results for the MGD refinement are shown in Figure 3.14. SiC B1 display a low thermal expansion over the whole

pressure range with the isotherms obtained with the model that fit well the experimental data. The pressure residuals comprised between ± 5 GPa over a pressure range higher than 140 GPa attest the high quality of the fit.

Table 8: Values of the thermal equation of state for the rock-salt structure, fitted with the Mie Grüneisen Debye model. Parameters kept fixt are marked with an asterisk

Number of data points	V_0 (Å^3)	K_0 (GPa)	K_0'	T Debye (K)	Gamma $_0$	*q*
348	65.8 (0.04)	339 (10)	3.06 (0.06)	1200*	0.50 (0.05)	1.67 (0.5)

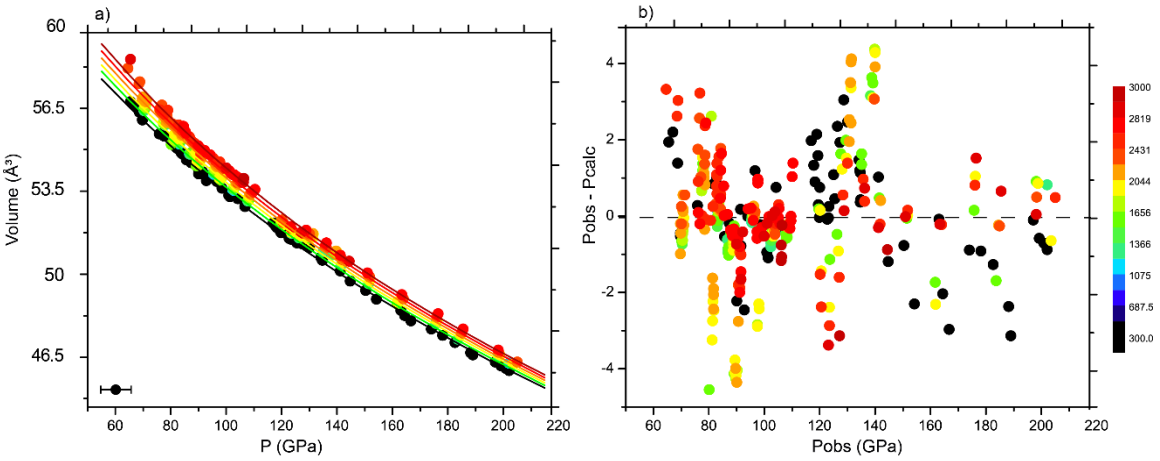

Figure 3.14: Results obtained fitting our data for the B1 structure with the MGD thermal model: a) experimental points and isotherms from 300 to 3000K; b) pressure residuals for the fit. On the right the temperature scale

An analogue procedure was followed to refine the Thermal Pressure model. The Einstein temperature (θ_E), calculated from the Debye temperature, was kept fixed during all the refinement cycles. Results are shown in Table 9 and plotted in Figure 3.15. The obtained values are $V_0 = 65.9 \pm 0.04$ Å^3, $K_0 = 339 \pm 2$ GPa, K' = 3.03 ± 0.02 and $\alpha = 0.58 \pm 0.01$ K^{-1} 10^{-5}. V_0, K_0 and K' are the same as for the MGD model within error bars, and $\chi^2 = 2.67$. Several different tests were carried out to assess the reliability of the determined solution. The low thermal expansion is consistent with the collected experimental data and fall within the range of values derived from theoretical models (Varshney et al., 2015) which also predicted a significant decrease across the transition from the B3 to the B1 structure. Refined V_0, K_0 and K' show a reasonable agreement, i.e. almost within error bars, with parameters determined at ambient temperature and the parameters obtained with the two models are consistent within each other.

Table 9: Values of the thermal equation of state for the rock-salt structure, fitted with the Thermal Pressure model. Parameters kept fixt are marked with an asterisk

Number of data points	V_0 (Å^3)	K_0 (GPa)	K_0'	T Einstein (K)	Alpha (10^{-5} K^{-1})
348	65.9 (0.04)	339 (2)	3.03 (0.02)	976.2*	0.56 (0.01)

The TP model, as well as the MGD, assume αK_T to be constant (e.g. Anderson and Lee, 1995). We tested the validity of the assumption by calculating alpha*bulk modulus and plotting them as a function of pressure and temperature. Our results doesn't show any trend, with a scatter of less than 10 % over the entire pressure range, thus guaranteeing for the validity of the used model.

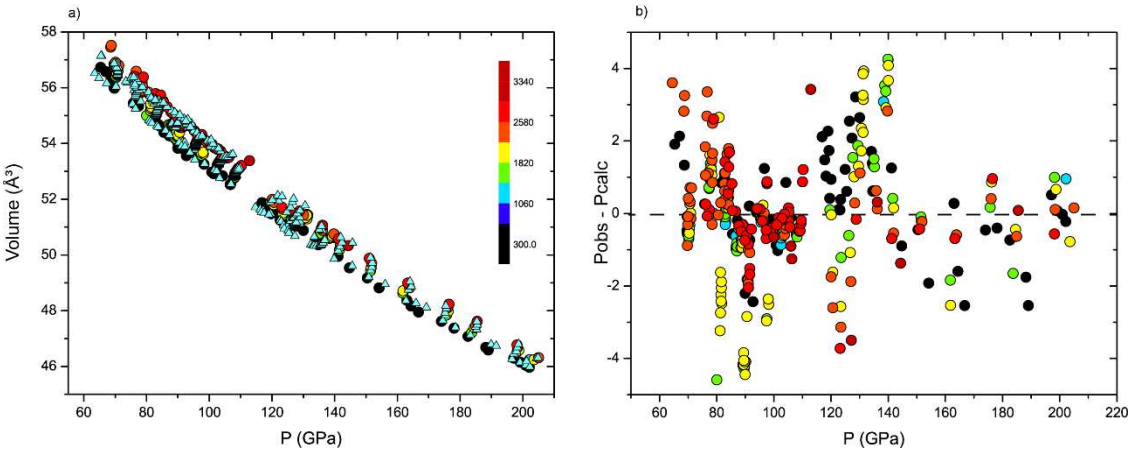

Figure 3.15: Results from the refinement of the SiC rock-salt structure with the Thermal Pressure model a) Volume on pressure graph, comparing the experimental data (circles) collected from room to high temperature, and the points re-calculated by the model (light blue triangles). The proposed model well reproduce the experimental data along all the investigated pressure range. b) Plot of the pressure residuals obtained with the Thermal Pressure model, different colours stand for different temperatures.

These results represent the first assessment of the rock-salt structure thermal behaviour by means of experiments, preventing any comparison with other experimental data. We think that the extended investigated P-T range, the quality of the data set and the reliability of the equation of state allow us to use these results for exoplanets modelling (Chapter 5).

3.2.3 Phase diagram

The non-stoichiometric compounds chosen as starting material provide the ideal frame to characterize the silicon-rich and carbon-rich sides of the phase diagram. The obtained phase diagram is presented in Figure 3.16c.

During the high temperature runs with the silicon enriched samples, several other peaks were observed on the diffraction pattern together with SiC and KCl. Following the work of Anzellini et al. (submitted) such peaks were indexed as Si VII, a phase stable in the examined pressure range with a orthorhombic *P63=mmc* structure (see Figure 3.16a). On the Si-rich side of the diagram, we have been able to determine the melting temperature at 2100 K and 60 GPa for the sample SiC_{25}, based on the disappearance of the solid diffraction peaks and a simultaneous plateau in the temperature versus laser power curve. Due to the low Z of the material, however we could not detect the appearance of diffuse scattering. Our melting criterion, thus possibly leads to overestimating of the melting temperature. As no other signature of melting were observed, we assumed the initial composition of the sample (77.48 at % Si and 22 at % C) to be close to the eutectic. As all the diffraction peaks were indexed on the

pressure range investigated, we can exclude the appearance of intermediate compounds on the Si-rich side of the phase diagram.

On the C-rich side no melting was detected in the whole examined pressure range for T up to 3500 K (Figure 3.16b). This could be related to the difference of melting temperature of the two end members, Si and C. Diamond has indeed a very high melting temperature (triple point graphite diamond liquid at 4000K and 15 GPa (Correa et al., 2006)), much larger than that of Si. Such difference in the melting temperature can have strong implications for planetary dynamics through melt production for any small Si enrichment, whereas the two phase assemblage (i.e. SiC + C) can stay solid in C-rich systems. Overall, the resulting phase diagram is in agreement with the phase diagrams proposed by Wilson and Militzer (2014). In addition, our results are in disagreement with theoretical works suggesting the stability of compounds with intermediate stoichiometry SiC_2 around 25 GPa (Andrew et al., 2012).

Concerning the phase diagram proposed by Daviau and Lee (2017a), the authors used the appearance of C diffraction peaks as a reference for the beginning of SiC decomposition. However, they actually never observe Si appearance and SiC disappearance on the diffraction patterns, necessary conditions to actually prove that decomposition had happen. Following their observations it would be more appropriate to define an exsolution of C from SiC rather than decomposition. The present data set does not offer any support to this argument, as we always see coexistence of C or Si with SiC, due to the intrinsic nature of our samples. We can however state that in all the examined P-T conditions, we have never witnessed the disappearance of SiC from the diffraction patterns, thus denying the argument of a complete decomposition Figure 3.16c.

The extremely high melting point of diamond makes it difficult to determine the behaviour on the carbon rich side of the graph. But it was instead possible to determine a melting point on the silicon rich side. Hypothetically Si-C phase diagram (see Figures 3.16c and 5.4) might look like the binary Fe-C (see Figure 4.20). On the silicon rich side Si + SiC coexist at lower temperature upon the first melting. We assume the presence of an eutectic in the silicon rich side Figure 3.16 (d,c), where Si is in equilibrium with a liquid on the high Si content side of the diagram, and SiC + L on the high carbon content side. With increasing the carbon content, diamond would be the stable phase coexisting with SiC at subsolidus. With increasing temperature, the higher melting temperature of diamond compared to SiC would determine the conditions for the existence of a C + L field. A peritectic point, where the reaction SiC+ L = C takes place, would connect the SiC + L to the C + L field. The relevancy of the phase diagram to exoplanets interior will be discussed in chapter 5.

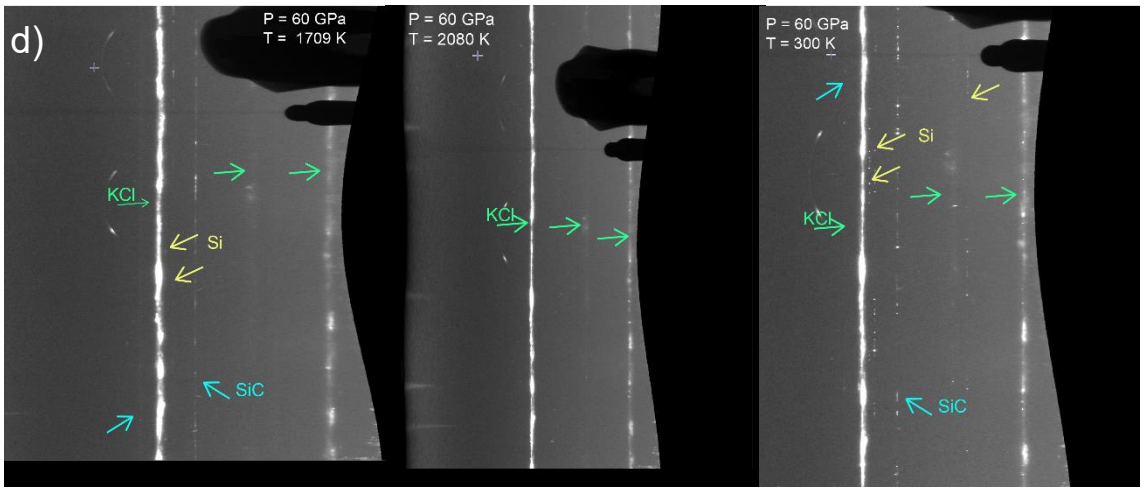

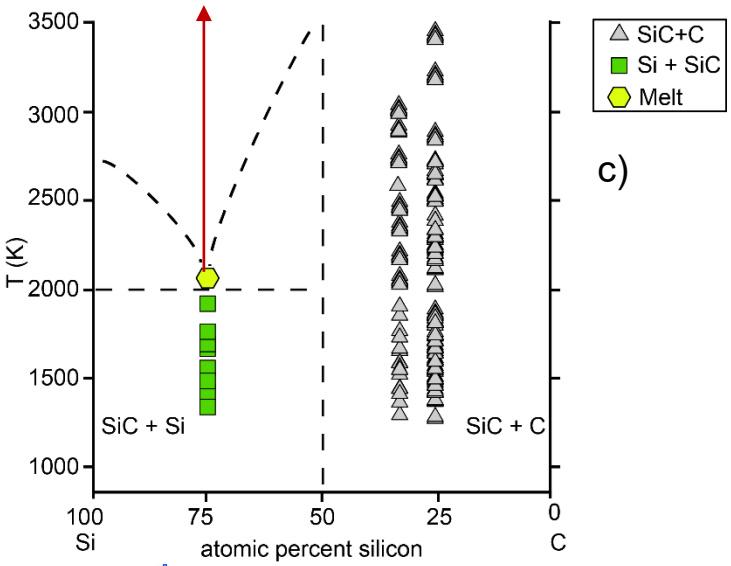

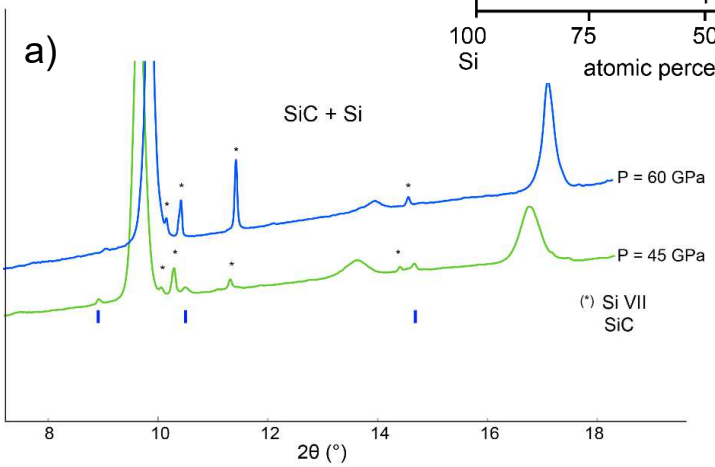

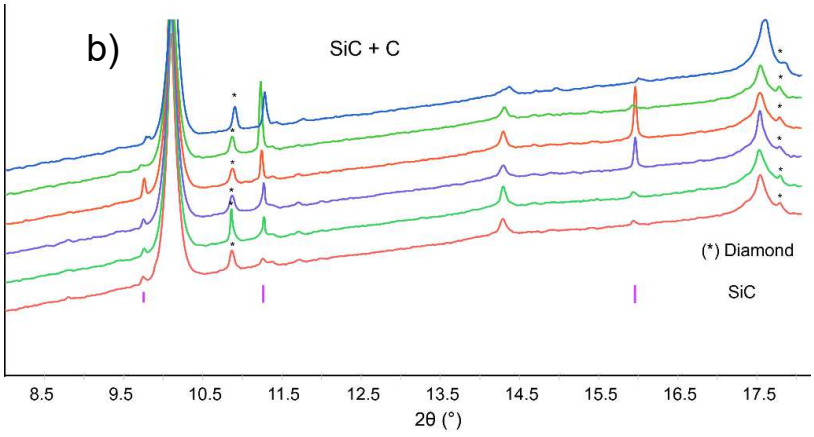

Figure 3.16: a), b) Diffraction patterns as intensity (in arbitrary unit) over angle for SiC + Si and SiC + C. c) Phase diagram obtained with the experimental data at P = 60 GPa. d) Examples of cake images collected for a SiC25 sample, at the same pressure and three different temperatures, before melting (left), above melting (center) and upon temperature quench.

Chapter 4

On the ternary Fe-Si-C phase diagram

4.1 State of the art on the Fe-Si-C system

The Fe-Si-C ternary system has been investigated with application to metallurgy and material sciences, where carbon and silicon doped iron is defined as grey iron and has properties that make it suitable to be the main component of mechanical systems. The bulk of the work specifically carried out on the Fe-Si-C system had several objectives, all related to the employment of such alloys in metallurgy. Attention was mostly given to thermodynamic properties and phase stability of the iron rich corner of the diagram, and the compositional evolution of the eutectic at ambient conditions ((SGTE), 2012; Lacaze and Sundman, 1991; Miettinen, 1998) (Figure 4.1a). Solubility of carbon in molten Si and the phase between a Fe-Si melt and SiC at high temperature (i.e. 1523 and 1723 K respectively) were also investigated (Kawanishi et al., 2009). Lately Narumi et al. (2014) expanded the study of the phase diagram to high temperatures, evaluating solubility of carbon in the Fe-Si-C system while identifying efficient SiC growing procedures (Figure 4.1b).

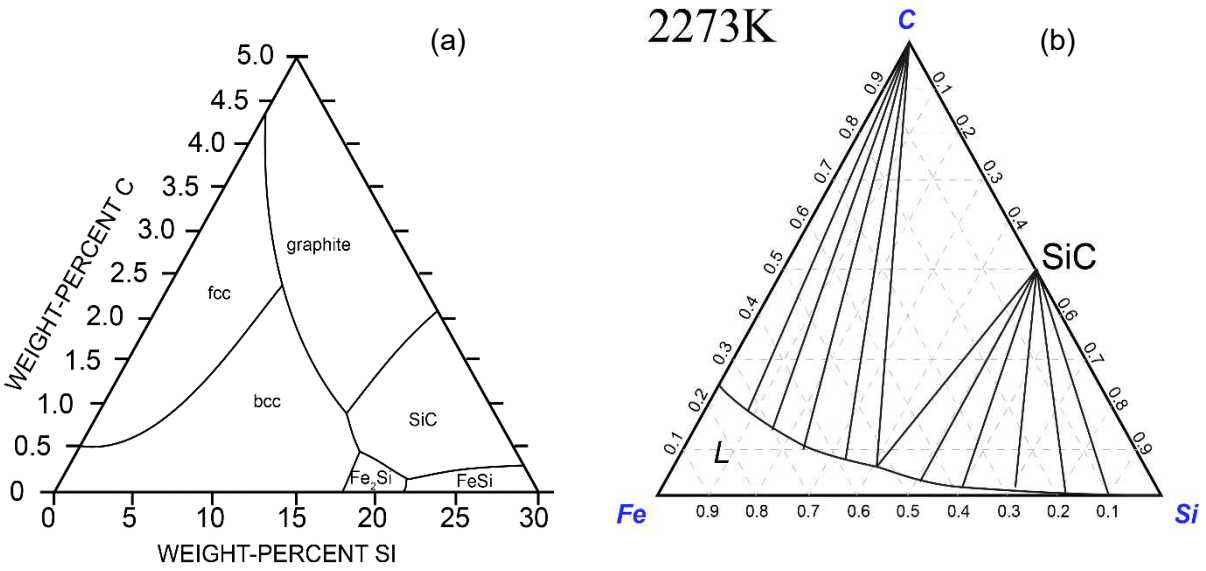

Figure 4.1: Ternary phase diagrams as in Lacaze & Sundman 1991 (a) and Narumi et al. 2014 (b). a) Projection of the calculations of the stable diagram at ambient conditions. b) Carbon solubility in the Fe-Si-C system at high temperature.

At low pressure SiC has been proven to be a commonly occurring phase, along with iron, FeSi and Fe_2Si, while iron carbides were unlikely. The results of the cited study highlight the wide range of possible element solubility in the phases forming in the ternary system. However, the pressure and temperature conditions investigated do not provide any insight on the evolution of the ternary systems at planetary interior conditions.

In planetary sciences, the ternary Fe-Si-C system represents a good proxy for planetary cores. Low amount of carbon and silicon have been already assumed to be present in the Earth's core (e.g. Badro et al., 2014; Y. Li et al., 2018; Vočadlo, 2015) and studying a wider range of composition is a good way to account for the potential variability of rocky exoplanets. On the Earth, iron silicide inclusions in equilibrium with SiC and Si have been retrieved in multiple geological contexts thus validating the possibility of stabilizing ultra-reduced species also in oxidised planets. Furthermore the evidence was supported by the experimental work done on the stability of moissanite (Schmidt et al., 2014). Here the authors stabilized, at 2 and 10 GPa, a FeSiC alloy in a Mg-Si-Fe-C-O system and traced its chemical equilibrium and stability field in term of T and fO_2 (Figure 1.6). The presence of Mg and O in the starting material, as well as the fixed P condition hamper the possibility of using this study as a reference for the HP-HT behaviour of the ternary Fe-Si-C. Nevertheless the data are of great interest for planetary interior.

The lack of knowledge about the properties of the ternary Fe-Si-C system at conditions relevant to exoplanets interiors is partially compensated by the extensive characterization performed on Fe-C and Fe-Si binary systems, due to their importance for the Earth.

4.1.1 Fe-C binary system

The high pressure and high temperature properties of Fe-C binary system have been investigated by multiple authors, and by the mean of experiments and calculations. The two intermediate compounds are Fe_3C and Fe_7C_3. The first occurs with an orthorhombic *Pnma* structure which undergoes several magnetic transitions: with increasing pressure and temperature from a stable ferromagnetic, at ambient conditions, to a paramagnetic and finally a nonmagnetic phase. There is a general agreement for the first transition to take place at ~ 10 GPa while the second occurs at ~ 60 GPa (e.g. Prescher et al., 2012).

Fe_7C_3 has been reported with three possible structures. A hexagonal $P6_3mc$ (e.g. Herbstein and Snyman, 1967) and two orthorhombic structures, *Pnma* and *Pbca* (e.g. Litasov et al., 2014; Prescher et al., 2015, 2012; Vocadlo et al., 2002) have been proposed. As for Fe_3C, the existence of magnetic and spin transitions in Fe_7C_3 were assessed through shear and elastic softening (e.g. Chen et al., 2014; Jiachao Liu et al., 2016) as well by discontinuities observed in the high pressure behaviour. At high pressure and temperature (Jin Liu et al., 2016) observed a decomposition of Fe_3C in Fe_7C_3 + Fe (hcp), in agreement with previous works (e.g. Fei and Brosh, 2014; Nakajima et al., 2009).

Fundamental to the determination of the ternary system properties, is the determination of the temperature and composition of the eutectic point in the binary system. The eutectic temperature has been investigated by Morard et al. (2017), also providing an estimate of the eutectic composition using Rietveld refinement of recrystallized phase. The eutectic composition was investigated by Lord et al. (2009) and Fei and Brosh (2014). However the results show some discrepancies. We addressed the topic in a study in collaboration with Izumi Mashino recently published (Mashino et al., 2019). LH DAC experiments were performed at high pressure and temperature and the carbon content of the eutectic

liquid was measured with an electron microprobe analyser. A Fe + Fe_3C phase assemblage was observed to be stable up to 255 GPa (Figure 4.2). Above 255 GPa the recovered sample displayed Fe + Fe_7C_3 (Figure 4.3). The microprobe analyses show a constant carbon content of 4 (± 0.20) wt % in the eutectic liquid and place the solubility limit of carbon in iron to 1 (± 0.30) wt% .

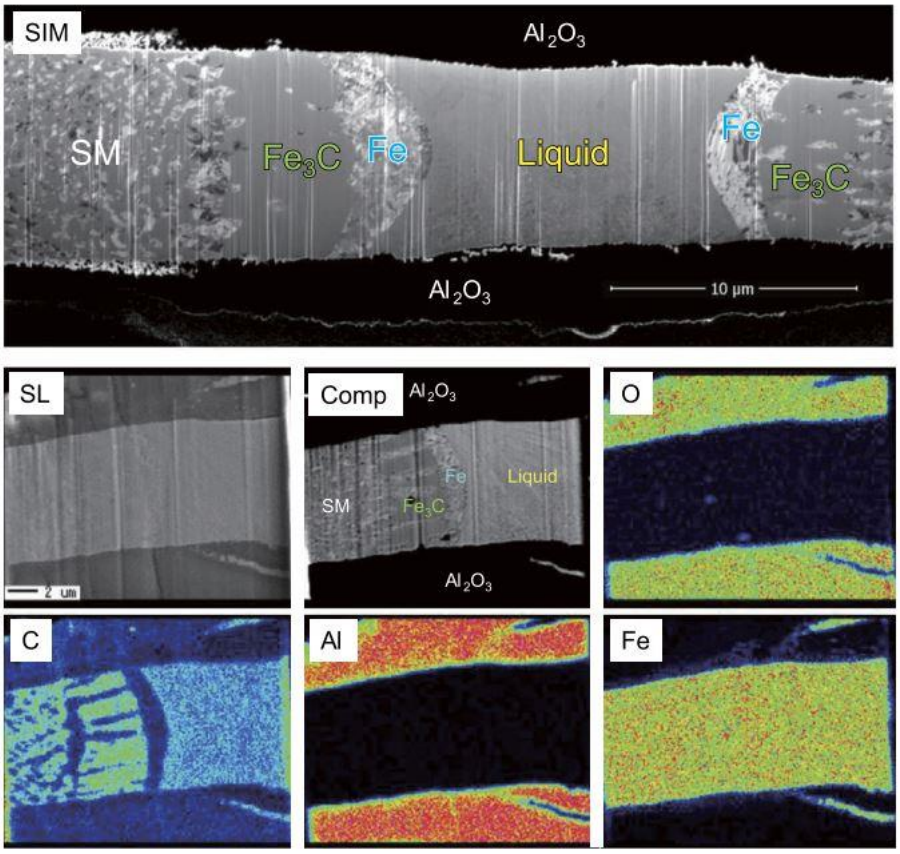

Figure 4.2: From Mashino et al. (2019). Melting textures of a quenched sample and composite X-ray maps for oxygen, carbon, aluminium, and iron at 40 GPa. SIM, scanning ion microscope image; SL, secondary electron image; Comp, backscattered image. Homogeneous quenched liquid is found at the center surrounded by solid layers of Fe and Fe_3C.

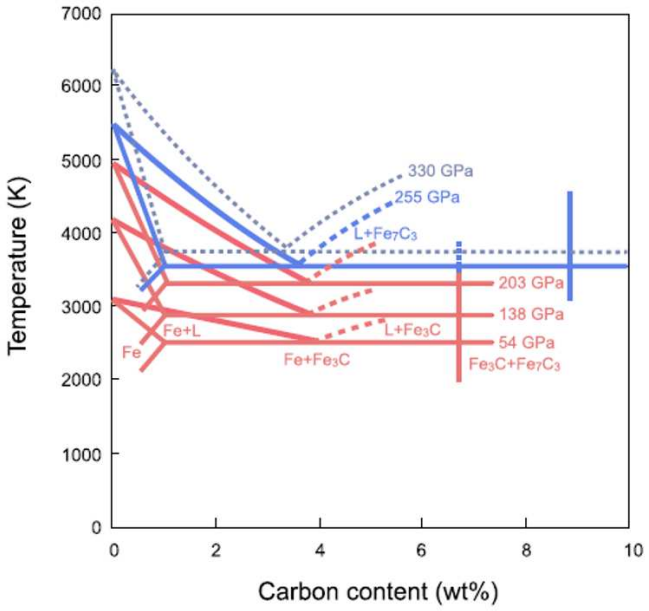

Figure 4.3: From Mashino et al. (2019). Binary X-T phase diagram showing the evolution in pressure of the eutectic composition.

4.1.2 Fe-Si binary system

The binary Fe-Si system has been widely studied as a function of pressure, temperature and silicon content (Figure 4.4). The phase diagram is characterised by a wide range of possible structures, stable for different Si content and at different temperatures. With increasing silicon content, one has hcp Fe with silicon in solution, followed by a cubic B2 structure stabilized in a field of coexistence. At 50 GPa the FeSi cubic structure is stable for ~ 33 at % Si and up to 50 at %. Further solubility of silicon in pure iron increase with increasing pressure (Fischer et al., 2013).

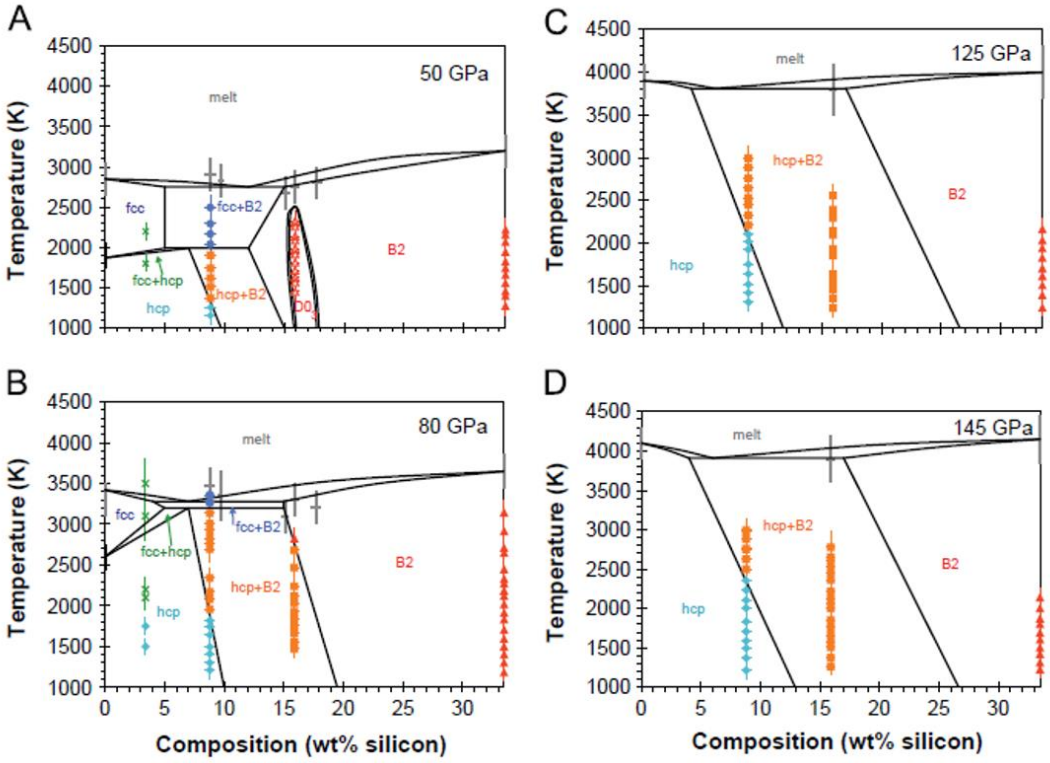

Figure 4.4: From Fischer et al. (2013). Composition–temperature phase diagrams in the Fe–FeSi system at different pressures.

The eutectic melting temperature was estimated by Fischer and co-authors (2013). The silicon content of the eutectic composition was determined by Ozawa et al. (2016) and decreases with pressure. At 50 GPa the eutectic liquid contain 13 at % Si and decreases to 2 at % at 120 GPa (Figure 4.5).

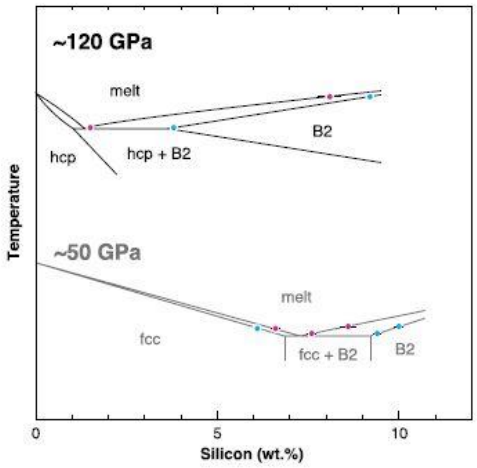

Figure 4.5: From Ozawa et al. (2016). Evolution of the silicon content at the eutectic in the Fe-Si system with pressure.

A correlation has been observed between the silicon content in FeSi and the volume displayed by the structure. The correlations between volume and silicon content in FeSi has been discussed in the PhD thesis of Eric Edmund (Edmund 2018) and in a recently published paper (Edmund et al., 2019). In the low silicon range, up to 8 at % of Si can be incorporated in the structure of hcp Fe without any change in the volume (Figure 4.6).

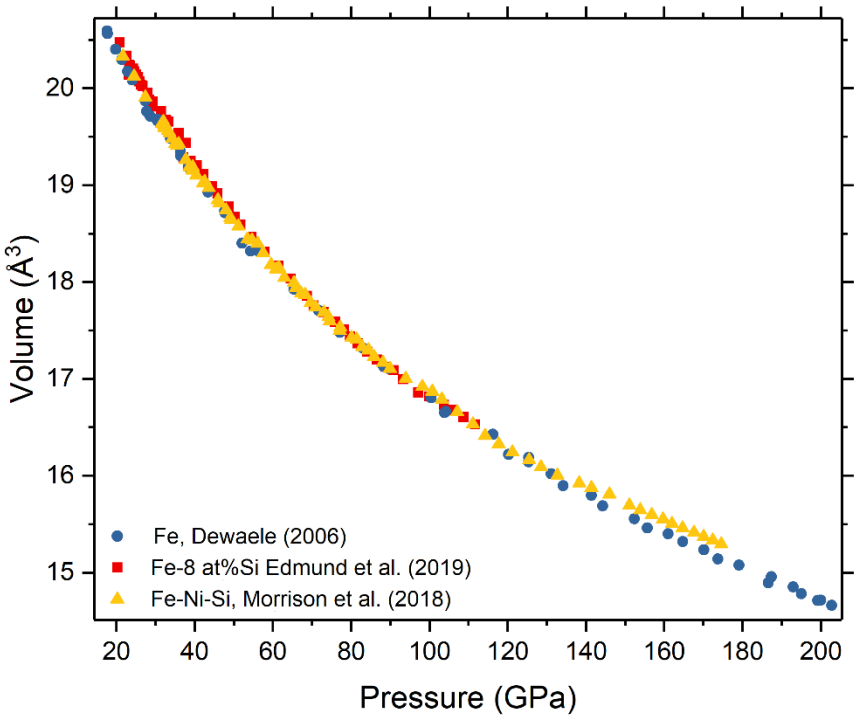

Figure 4.6: From Edmund et al. (2019). Plot of the volume over pressure data for Fe-8 at% Si, pure Fe and silicon and nickel doped iron.

Furthermore, in the stability field of cubic FeSi increasing silicon content is associated with a reduction of the unit cell volume. This unexpected behaviour can be caused by Si interfering on the magnetic repulsion forces between the iron atoms in the structure (Edmund 2018).

4.2 Experimental results on the Fe-Si-C system properties at extreme conditions.

The starting materials used for these experiments were mostly manufactured by PVD deposition. Only one composition was prepared with URQ due to the low light element content required. All the samples were investigated at high pressure and high temperature and the following pressure conditions were reached: $FeSi_3C_3$ and $FeSi_{20}C_{10}$ were studied up to ~ 195 GPa and 4000 K, $FeSi_{10}C_{20}$ up to ~145 GPa and $FeSi_6C_5$ up to ~ 70 GPa.

The starting materials transform into two different mineral assemblages during the experiments. $FeSi_3C_3$ upon heating and increasing pressure displayed a dissociation in hcp Fe + Fe_3C. Conversely, samples with higher light elements content always decomposed in FeSi + Fe_7C_3. Is important to notice that hcp Fe is known for hosting light elements in the structure. A computational work demonstrates how Si can be incorporated in iron carbides (Das et al., 2017) and FeSi is known to incorporate carbon at 1 GPa and 1300 K (Vander Kaaden et al., 2016). Accordingly, a wide range of solid solutions are possible in the stable phases retrieved during the experiments and will be discussed with the results.

4.2.1 Phase diagram and melting relations

Results regarding phase stability at extreme conditions, as well as phase and melting relations, will be presented separately for each starting material.

$FeSi_3C_3$

In the investigated pressure range, the starting material, stable as Fe (hcp) at ambient temperature, decomposes in hcp Fe + Fe_3C upon heating (Figure 4.7a). No silicon or silicon-bearing compounds (i.e. SiC, FeSi) were observed, neither in the diffraction patterns, nor in the transverse cuts made on the recovered samples (Figure 4.7b). The observed sub-solidus relations are in agreement with the results of multi-anvil experiments (Fei and Brosh, 2014; Nakajima et al., 2009). In the present study, hcp Fe and Fe_3C are the stable compounds for all examined P-T conditions. The present results, even though in disagreement with the proposed decomposition of Fe_3C into in Fe_7C_3 + Fe above 157 GPa observed by Liu and coauthors (2016), are consistent with the recent study of Mashino et al. (2019) (Figure 4.3).

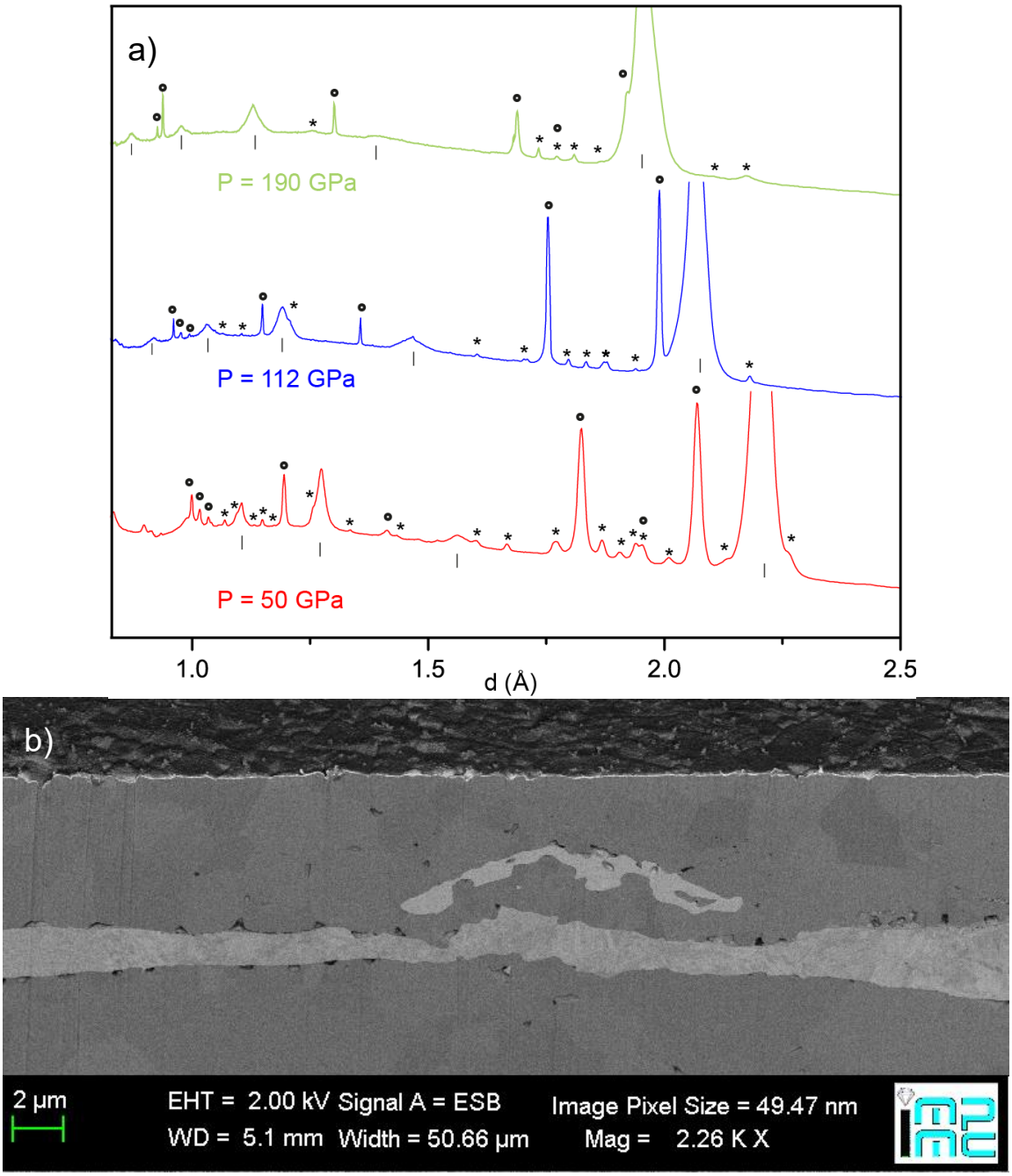

Figure 4.7: a) Diffraction patterns collected on $FeSi_3C_3$ showing the coexistence of hcp Fe and Fe_3C. Intensity in arbitrary units is plotted over d-spacings. Stars represent peaks indexed as Fe_3C and circles hcp Fe, KCl reflections are indicated by vertical ticks; b) Backscattered image of a laser heating spot in $FeSi_3C_3$. The textured part corresponds to solid part of the sample (typical features from solid metal as in Morard et al, 2018), whereas the homogeneous part (arc shape on top) corresponds to the liquid extracted after partial melting. The dark grey areas on both side of the sample are KCl layers used as pressure transmitting medium and pressure calibrant.

Quenched volumes of hcp Fe collected in this study are larger, over the whole pressure range, than those of pure hcp Fe from literature (e.g. Dewaele et al., 2006; Fei et al., 2016) (Figure 4.8). Such volume increase cannot be explained by the presence of silicon as highlighted in previous works on the Fe-Si-Ni system (Morrison et al., 2018) and on the Fe-Si (Edmund et al., 2019). Si shows a large solubility in hcp Fe under high pressure, up to ~18 % at Si (Fischer et al., 2012; Tateno et al., 2015). In

addition, iron hcp structure can incorporate up to 8 at % Si without change of the unit cell volume. Decomposition of the starting material into Fe_3C and Fe hcp may follow the lever rule (Figure 4.8), implying a content of Si in hcp iron lower than 3 at%, thus advocating for a conservation of the same volume as hcp Fe. Therefore a small amount of carbon should be incorporated together with silicon, in order to explain the volume increment of the hcp Fe unit cell, here after called hcp Fe (+Si, +C). Additionally, the simultaneous presence of Fe_3C with hcp Fe (+Si, +C) suggests that the solubility limit of carbon was reached. The strong effect of small amount of C on the volume of hcp Fe may be related with its interstitial position in the hcp iron cell (Caracas, 2017). Conversely, Si substituted to iron atoms and therefore does not change the cell volume (Edmund et al., 2019).

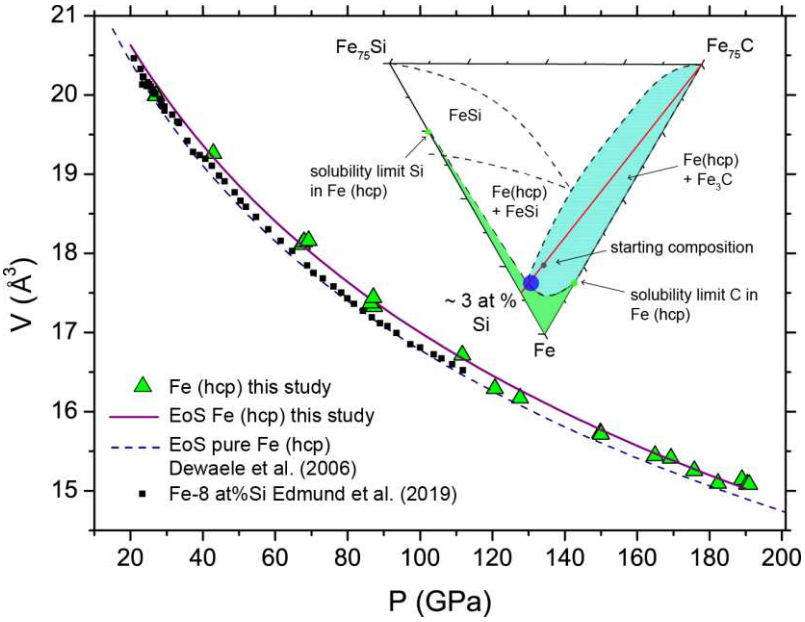

Figure 4.8: Plot of the volume as a function of pressure at T = 300 K for hcp Fe. Green triangles represent the experimental data from this study, purple line the fitted EoS, black squares the experimental data on Fe-8 at % Si from Edmund et al (2019). Black dashed line the EoS of pure Fe (hcp) from Dewaele et al. (2006). Insert: Ternary Fe-Si-C diagram showing the phase relations in the iron rich side. In red the tie line connecting the starting material and Fe_3C. In green the solubility field for Si and C in (hcp) Fe estimated at 50 GPa. The interception represents the solubility limit of light elements in iron.

The phase diagram and melting behaviour of $FeSi_3C_3$ were measured up to 190 GPa and 3500 K (Figure 4.9). At low temperature (hcp) Fe (+Si, +C) is the only stable phase, Fe_3C exsolves at higher temperature. In all this pressure range, hcp Fe (+Si, +C) was observed in coexistence with Fe_3C before melting. Then upon heating, hcp Fe (+Si, +C) crystals diffraction is observed along with diffuse scattering from the first liquid until complete melting is attained. The obtained eutectic temperatures (Figure 4.9) are lower than those for the binary Fe-Si (Fischer et al., 2013) and instead consistent with the eutectic temperatures determined reported by Morard et al., (2017). Considering the binary Fe-C and Fe-Si systems, carbon has been observed to have a strong effect on the melting temperature of pure iron (Morard et al., 2017), whereas silicon barely affect the melting (Fischer et al., 2013; Lord et al., 2010;

Morard et al., 2011). The depression of the melting curve for the ternary alloy demonstrates that carbon has a predominant effect on the melting also if it is present in lower amount compared to silicon.

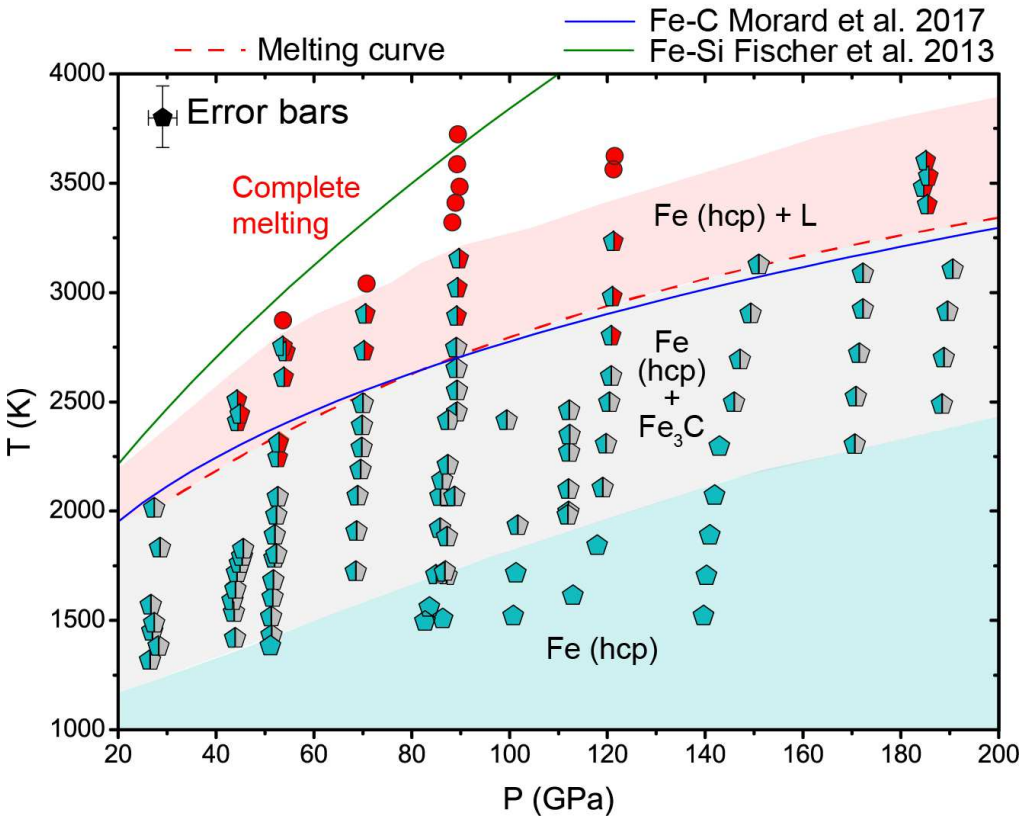

Figure 4.9: P-T diagram in the Fe-Si-C system for the composition $FeSi_3C_3$. The red dashed line represents the eutectic temperatures, above which melting occurs and (hcp) Fe is in equilibrium with a liquid. Circles represent the P-T conditions where complete melting occurred and only diffuse scattering was visible on the diffraction pattern. The melting curve is compared with those of Fe-Si (Fischer et al., 2013) and Fe-C (Morard et al., 2017).

$FeSi_{10}C_{20}$

All the collected data are shown in (Figure 4.10). As all the studied samples manufactured with PVD deposition, at ambient conditions the starting material is characterized by a signal typical of an amorphous material. Recrystallization usually starts upon the first heating, usually made when aligning the lasers. Upon heating the first phase to be visible on the image plate with the pressure medium is FeSi, stable with a cubic B2 structure. Then a small temperature increase is enough to stabilize hexagonal Fe_7C_3 (space group *P6₃mc*). The assemblage FeSi + Fe_7C_3 at low pressure has a narrow stability field in temperature, with the first melting occurring below 1750 K at 30 GPa and close to 1500 K at 20 GPa. Increasing pressure sensibly increases the temperature stability of carbides that at the higher investigated pressure are stable up to 3500K. When first melting occurs only FeSi peaks are still visible on the pattern, whereas carbides rings are not present any longer and instead there is a small increment of the background in the pattern. When the melting is complete only diffuse scattering is visible on the diffraction pattern.

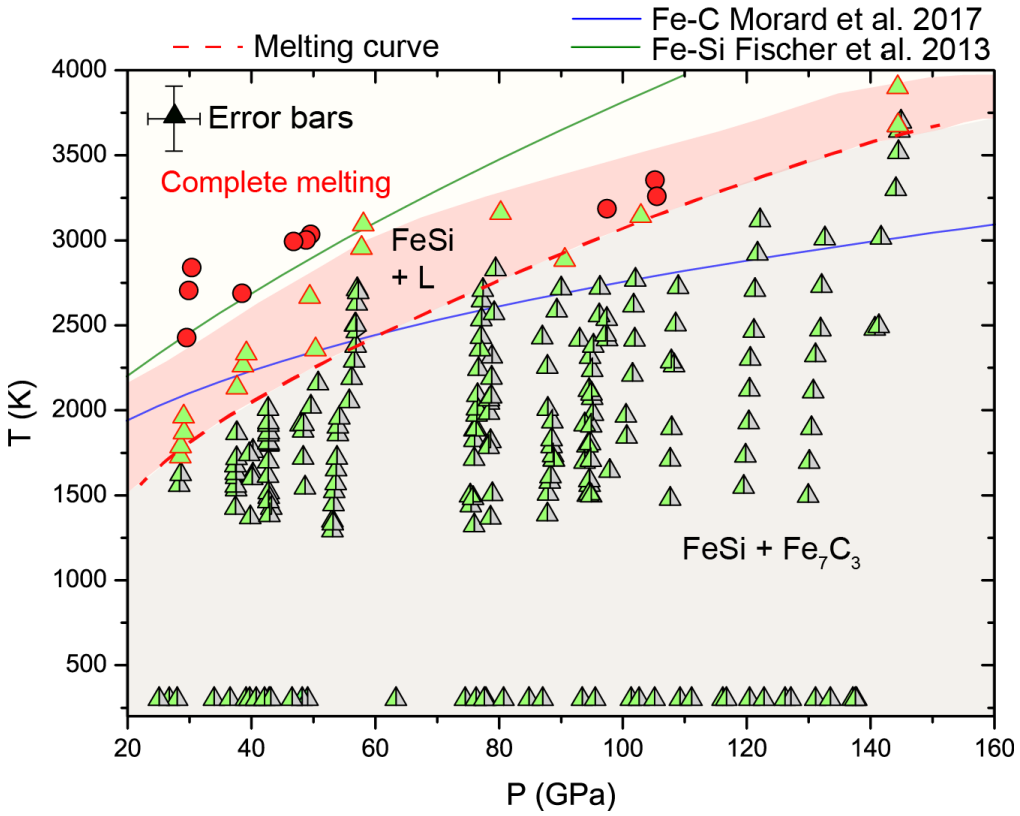

Figure 4.10: P-T diagram in the Fe-Si-C system for the composition $FeSi_{10}C_{20}$. Green triangles represent the first points above the solidus. The eutectic melting curve is shown with the red dashed line in comparison with the melting curves of Fe-Si (Fischer et al., 2013) and Fe-C (Morard et al., 2017). Red circles represent the P-T conditions where complete melting was attained.

The evolution of the melting temperature with pressure for $FeSi_{10}C_{20}$ is consistent with the melting curve Fe-Si (Fischer et al., 2013) however the presence of carbon induces a shift toward lower temperatures. The eutectic temperature of $FeSi_{10}C_{20}$ is lower than the Fe-C system up to 80 GPa and increase at higher pressures displaying a different behaviour compared to $FeSi_3C_3$.

The transverse cut of the recovered samples display the presence of a region of dark patches symmetrically distributed on both sides of the heating spot. The dark patches advocate for the presence of SiC or C (Figure 4.11a). The colour close to black is typical of low weight elements when the detector for backscattered electrons is used, because the response is function of the atomic number. Furthermore, the secondary electrons image accentuate the topographic effects in the sample (Figure 4.11b). Cones of low polished material are visible below the patches thus attesting the hardness of the overlying minerals and confirming the SiC or C (diamond) hypothesis Figure 4.11b and c.

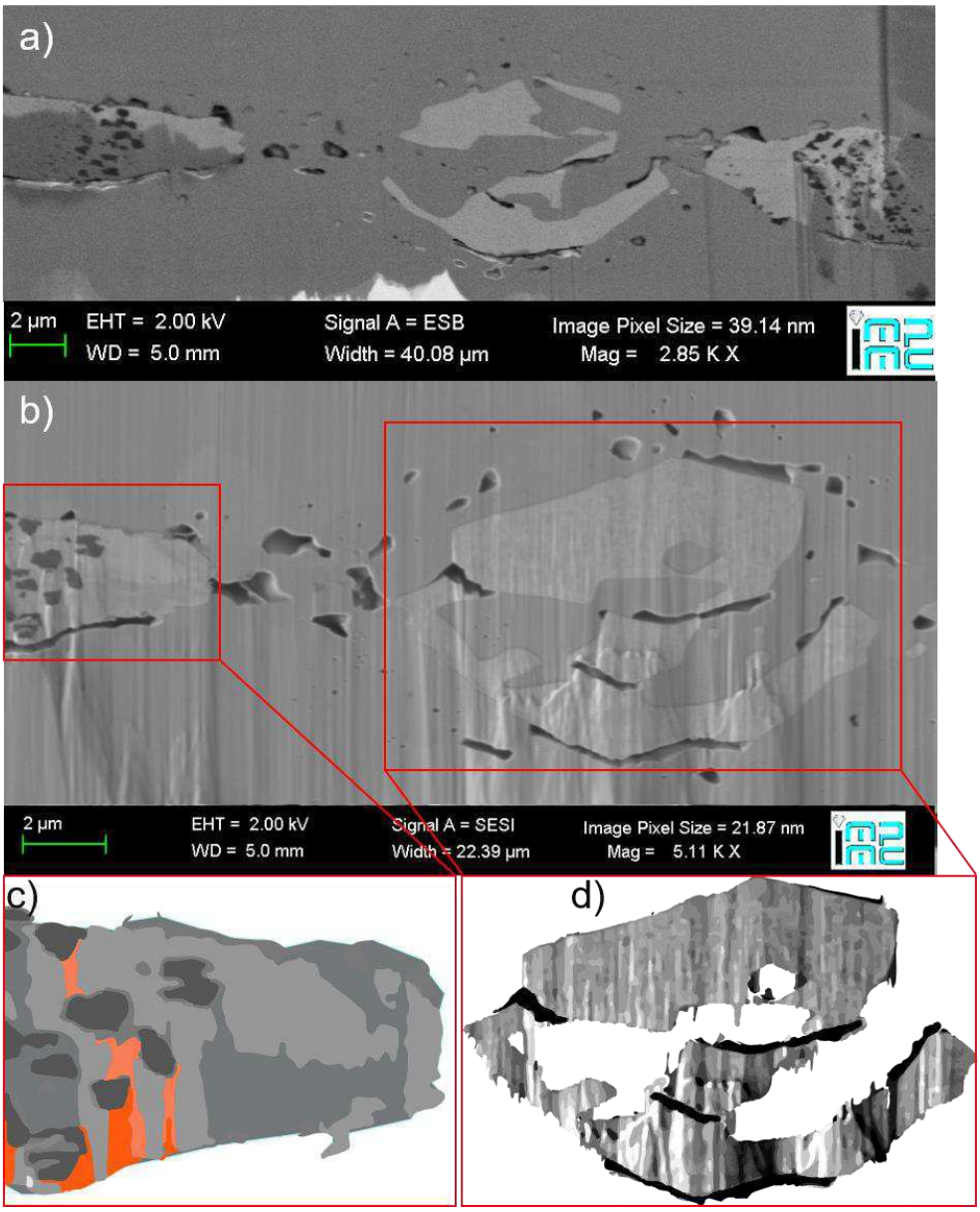

Figure 4.11: FIB transverse section of a laser heating hotspot. a) Panoramic of the heating spot with an ESB detector; b) magnification of the ROIs; c,d) Rasterization of the two regions of interest. The colour distribution reproduce the differences in the chemistry of the samples. In figure c) the red colour correspond to topographic high where the polishing was less efficient due to the shadowing effect of SiC or C. In d) detail of the melt pool. The homogeneity in the chemistry and distribution of grains size is recognisable.

SiC or C possibly result from exsolution during the heating procedure and it would not have been possible to notice from the diffraction patterns due to an overlap of the peaks with Fe_7C_3. The higher

melting temperature compared to the other phases would have prevent them to melt with the rest of the sample and thus migrate toward the external part of the heating spot.

$FeSi_{20}C_{10}$

Experimental data were collected between 20 and 200 GPa and up to 4000 K. Upon heating and up to ~ 100 GPa, FeSi with a B2 structure is the first phase to recrystallize. Increasing temperature above 100 GPa Fe_7C_3 coexists with FeSi in the whole examined pressure range (Figure 4.12). The absence of iron carbides at low pressure, supports the evidence of carbon solution in FeSi. The exsolution of iron carbides at higher pressure implies the overcome of the solubility limit that accordingly decreases with increasing pressure. All the run above 100 GPa were performed in subsolidus with a stable assemblage FeSi + Fe_7C_3. Hence we do not have experimental evidences about the melting sequence above 100 GPa. The melting temperatures are qualitatively consistent with those determined for $FeSi_{10}C_{20}$ with a shift toward higher values for the low pressure data.

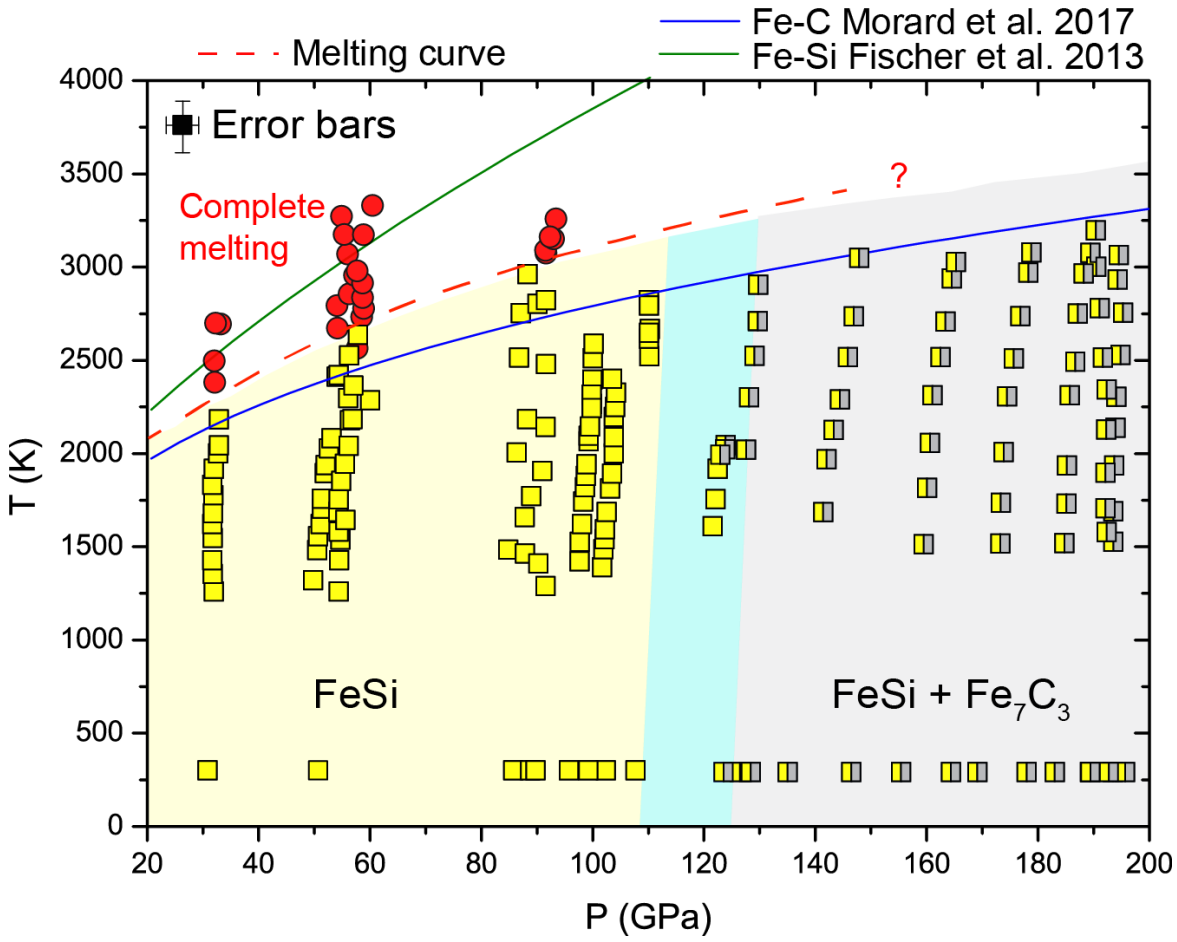

Figure 4.12: P-T diagram in the Fe-Si-C system for the composition$FeSi_{20}C_{10}$. The eutectic melting curve is shown with the red dashed line in comparison with the melting curves of Fe-Si (Fischer et al., 2013) and Fe-C (Morard et al., 2017).

$FeSi_6C_5$

Data for $FeSi_6C_5$ were collected up to 120 GPa and ~ 4000 K in the subsolidus and melting regime (Figure 4.13).

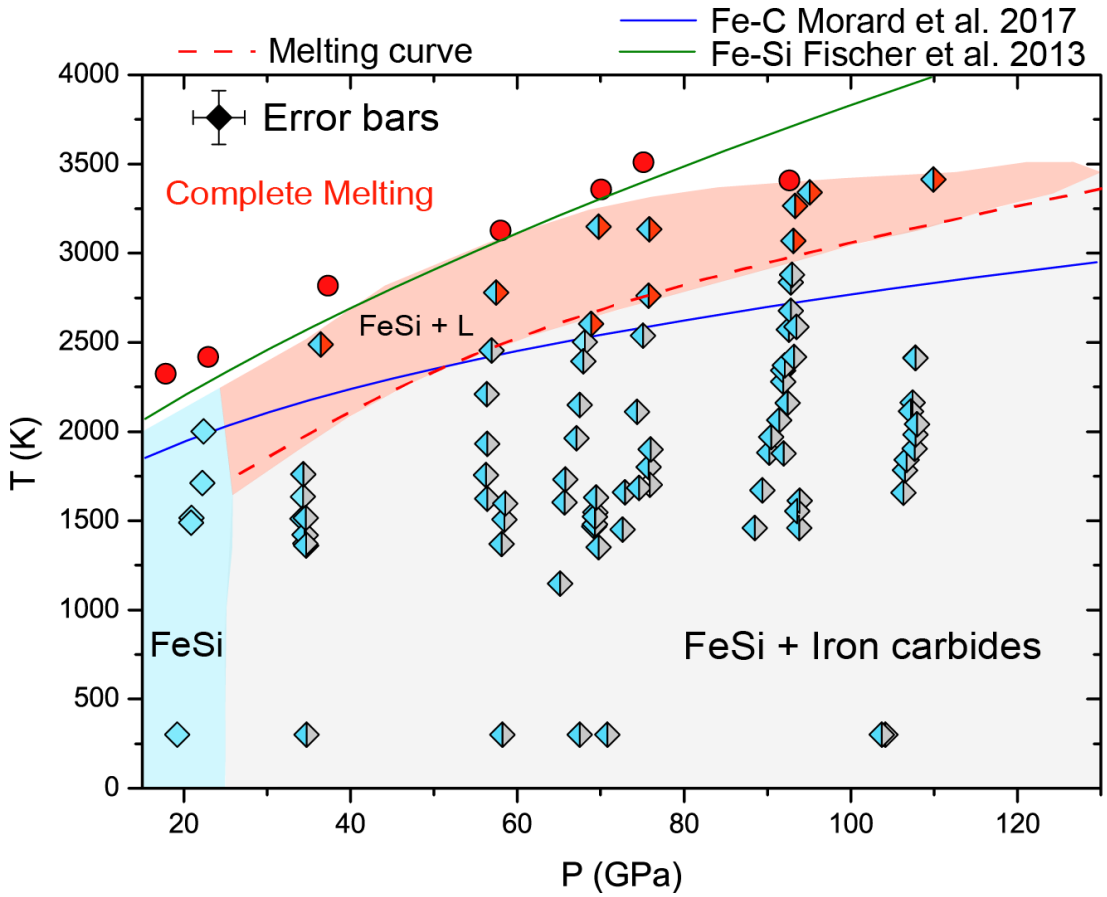

Figure 4.13: P-T diagram in the Fe-Si-C system for the composition $FeSi_6C_5$. Half red diamonds represent the P-T conditions above the solidus. The eutectic melting curve is shown with the red dashed line in comparison with the melting curves of Fe-Si (Fischer et al., 2013) and Fe-C (Morard et al., 2017).

At low pressure (i.e. 20 GPa) FeSi is the only phase visible on the diffraction patterns, stable with a cubic DO3 structure (space group *Fm-3m*), while neither iron carbides, nor pure iron peaks are visible. In absence of carbides FeSi melts at 2300 K. The stability field of the DO3 structure occupies a narrow range, at 30 GPa FeSi transit from the DO3 to a cubic B2 structure (space group *Pm-3m*) and iron carbides, indexed as hexagonal Fe_7C_3 (space group $P6_3mc$) become stable. Some patterns however present multiple additional reflections that couldn't be indexed as Fe_7C_3 and would rather be Fe_3C (space group *Pnma*) or a mixture of iron carbides + hcp iron as in the work of Jin Liu et al. (2016). The presence of silicon carbides or diamond in the observed extra peaks is excluded as no traces are observed in the transverse cut of the samples (Figure 4.14).

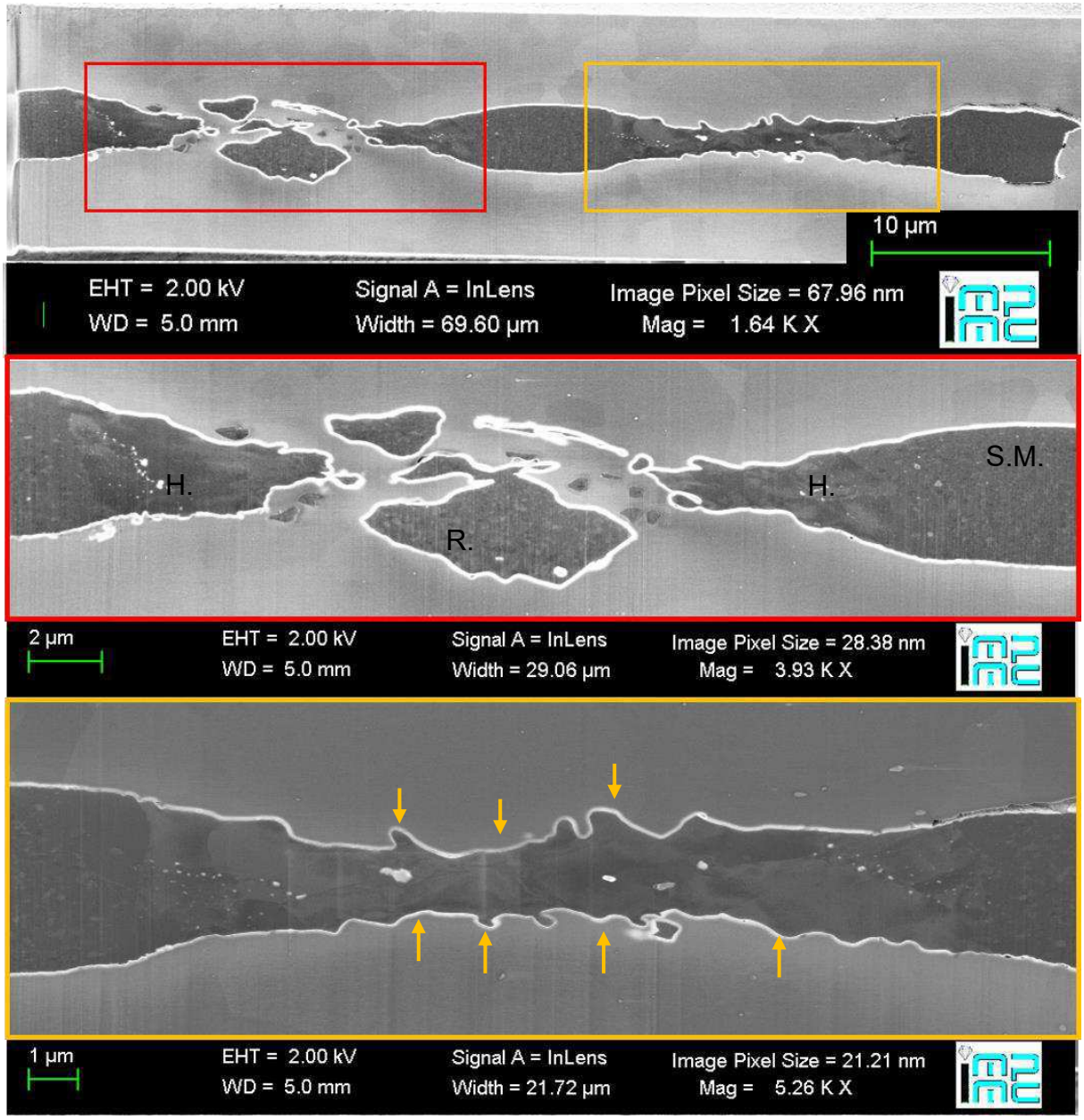

Figure 4.14: Transverse cut of a laser heated $FeSi_6C_5$ sample. Two heating spots are visible within the coloured boxes and magnified in the two lower images. The heating spot on the left went through complete melting and recrystallization at low temperature, visible for the homogeneous grain size in (R). The sample on the right did not reach complete melting. Nevertheless, typical heated textures are displayed (H). The initial homogeneity in grain size (S.M) is lost in favour of a mixture and sample boundaries display smitten features, indicated by the arrows. S.M. corresponds to a region in which the starting material is preserved and attests the quality of PVD samples. In the top image one can also notice the constant thickness of the sample, as shows in the unheated portions.

The wide range of possible stable assemblages and solid solution in the ternary compositions with a similar amount of silicon and carbon complicates the interpretation of the pattern. To provide an unambiguous characterization of the existing phases, further analyses of the collected data will be needed.

In the stability field of FeSi + Fe_7C_3, iron carbide is the first phase to melt, leaving FeSi in coexistence with a liquid (Figure 4.13). Complete melting is then attained at higher temperatures. In the stability

field of FeSi DO3 melting take place at ~2300 K. In the stability field of iron carbides, the eutectic melting curve of $FeSi_6C_5$ qualitatively follows the binary Fe-C systems. The melting temperatures are consistent with those retrieved for the other samples with a higher light elements content.

4.2.2 Discussion on the retrieved volumes

The volumes of FeSi and Fe_7C_3 obtained in all the experimental runs at ambient temperature are compared with data from literature in order to estimate the light element content and the possible presence of solutes.

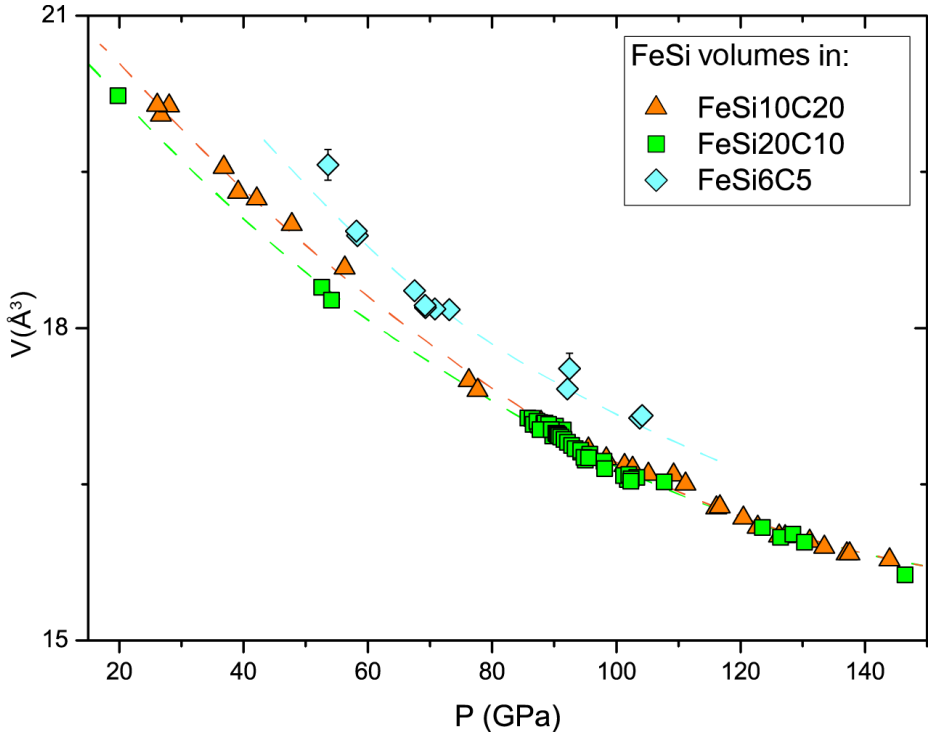

Figure 4.15: Plot of the FeSi volumes at 300K recovered in three of the studied samples. Symbols represent experimental data and lines the trend. Except where shown, error bars are within the dimension of the symbol.

Cubic FeSi is known for displaying a strong correlation between the volume of the structure and the silicon content. An increase in the silicon content goes with a reduction in the unit cell volume, due to the interference of the silicon atoms with the repulsive magnetic forces exiting between the Fe atoms (Edmund 2018).

In Figure 4.15 volumes of the cubic B2 phase only are shown. The presence of the DO3 structure at low pressure allows us to place some constrains on the Si content, which is 30 at %. Furthermore, $FeSi_6C_5$ volumes are shifted toward higher values and do not display any change in the trend in the whole pressure range. $FeSi_{10}C_{20}$ and $FeSi_{20}C_{10}$ have different volumes at low pressure. As expected according to (Edmund 2018), the sample with nominally higher silicon has a smaller volume.

The evolution in pressure of the volumes for $FeSi_{20}C_{10}$ shows a kink at ~ 100 GPa, where the volumes suddenly increase and overlap with those of $FeSi_{10}C_{20}$. Such increase can be related to a change in the

chemistry of the system. This hypothesis is supported by the correspondence in pressure between the kink and the boundary of iron carbide stability field (Figure 4.12). The exsolution of iron carbide and the relative depletion of Fe in FeSi can affect the magnetic state of the system and determine changes in the Fe atoms interaction.

The experimental data from the present study are plotted with those collected by Edmund (2018) for several FeSi alloys with different silicon content (Figure 4.16).

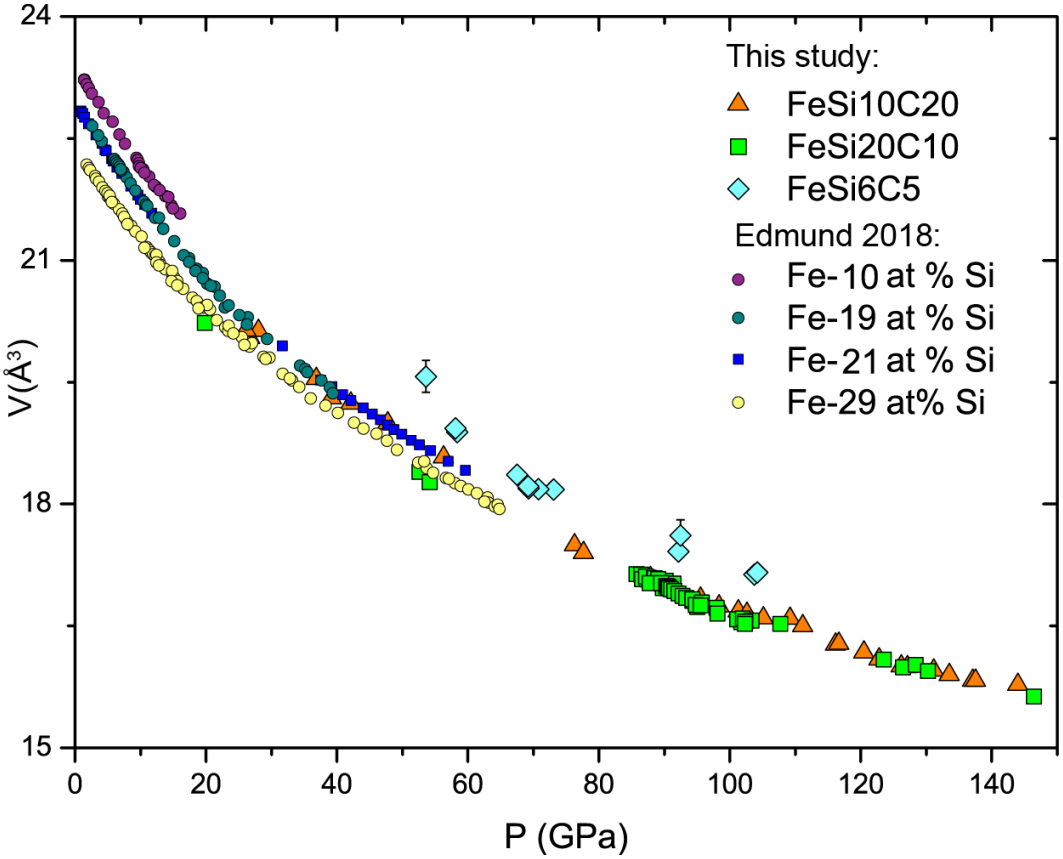

Figure 4.16: Plot of the FeSi volumes over pressure. The compositions investigated in this study are compared with those from Edmund (2018). Except where shown, error bars are within the dimension of the symbol.

The FeSi volumes collected in this study display the same trend at high pressure as volumes determined by Edmund (2018). However, in our mineral assemblage the presence of iron carbides, and carbon in solution in FeSi need to be taken in account in the evaluation of the silicon content, thus hampering the possibility of using the data from Edmund et al. (2018) for direct comparison. Applying the lever rule to the ternary phase diagram we expect a silicon content in FeSi comprised between 30 and 50 at %. Following the trend of volume reduction with increasing Si, the data should ideally display lower volumes. On the other hand, carbon incorporation has been observed to increase the volume of hcp Fe (see Figure 4.8). Consistently carbon could be in solution in both the compositions (i.e. $FeSi_{10}C_{20}$ and $FeSi_{20}C_{10}$).

In Figure 4.17 volumes of Fe_7C_3 are compared with those available from literature (Chen et al., 2012; Nakajima et al., 2011). $FeSi_{10}C_{20}$ and $FeSi_{20}C_{10}$ volumes show good agreement with those measured by (Chen et al., 2012) up to 140 GPa. Above this pressure, a change is observed in the pressure evolution of the volumes.

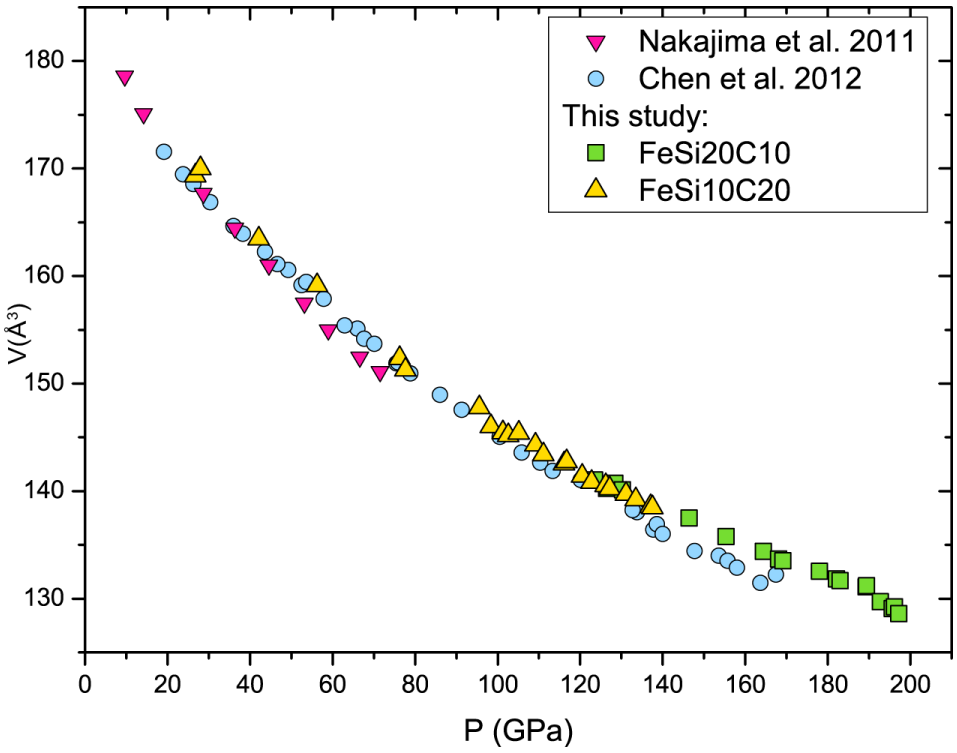

Figure 4.17: Plot of Fe_7C_3 volumes over pressure. Data from this study are plotted with those from literature. Error bars are within the dimension of symbols.

A similar drift is observed also with the data from Nakajima et al. (2011). A difference in the volumes above all the pressure range is usually attributed to pressure gradients in the cell or pressure calibration. However the magnetic effects and spin transitions typical of iron carbides should be kept in mind as they affect the volumes. A third data set on hexagonal Fe_7C_3 in the same pressure range as ours and Chen et al. (2012) would be needed to increase the statistics on the observations. Nevertheless, the consistency of the observed volumes with previous study on the pure binary Fe-C system advocate for the absence of silicon inside the structure. Moreover, according to the results of (Das et al., 2017) silicon incorporation in hexagonal Fe_7C_3 should reduce the volume of the unit cell. Such reduction is not observed in the present data set and we can exclude the presence of Si in solution.

4.2.3 Reconstruction of the ternary phase diagram

The relations established with the present results were used together with those for Fe-C and Fe-Si to reconstruct the ternary relations in the Fe-Si-C system, at a fixed pressure of 50 GPa as a function of temperature.

For low light elements content we have observed that the stable phases are hcp Fe + Fe_3C, with hcp iron hosting all the silicon and part of the carbon. The absence of SiC or diamond was confirmed by the FIB cuts on the hotspot. The temperature of the eutectic melting (i.e. 2300 K at 50 GPa) is consistent with the Fe-C binary system. To evaluate the eutectic composition a Rietveld analysis was performed on one of the patterns obtained after recrystallization at low temperature of a glass from a quenched liquid at 50 GPa. The quantity of silicon was assumed using the equal partitioning coefficient between the solid and liquid phase. The diffraction pattern of the assemblage Fe hcp (+Si, +C) + Fe_3C indicates a C content of 13 at% for the liquid in the ternary system that serves as a lower bound as some of the carbon is in hcp iron as well.

For higher light elements content, FeSi and Fe_7C_3 were observed in all the runs, with different distribution in pressure and temperature depending on the starting composition. In $FeSi_{10}C_{20}$ and $FeSi_{20}C_{10}$ the presence of a harder phase (i.e. silicon carbide or diamond) was observed in the transverse cuts of the heating spots. From the volume data, FeSi with a B2 structure, known to be stable for a wide range of silicon content was observed to host also carbon atoms. On the other hand the absence of volume changes in Fe_7C_3 seems to confirm the absence of Si in substitution in the structure.

The phase relations were first defined for the iron rich corner of the diagram. The view of the space model (Figure 4.18) shows a liquidus made by two different surfaces, ABCF and CFED obtained when the eutectic point F from the present work is connected to the two binary systems. Joining the binary and ternary eutectics, forms two eutectic valleys (i.e. BF and FD). At high temperature and 50 GPa $FeSi_3C_3$ solidus assemblage consists in hcp Fe + L hence should be part of the hcp Fe + L surface. The solubility limit on the Fe-Si and Fe-C side is defined by literature. Fe can host ~4.3 at% of carbon (Mashino et al., 2019) while the solubility limit of Si in Fe is ~ 18 at % (Fischer et al., 2013). The limit of the solubility field of both Si and C in iron lies on the iron rich side of the tie line joining Fe_3C and the starting material (Figure 4.8). Four isothermal sections were determined at temperature below the ternary eutectic (a), in correspondence of the ternary eutectic (b), at higher temperature then the ternary eutectic (c) and in correspondence to the melting temperature of pure iron (d). The temperature range between the eutectic of Fe-C and Fe-Si determine and extended field where a solid is in equilibrium with the liquid. At 2200 K (Figure 4.18a) both the Fe-C binary and the ternary system eutectics are higher in temperature. On the Fe-C side the stable subsolidus phase assemblage is Fe (hcp) + Fe_3C. On the silicon rich side instead different FeSi structures crystallize in function of the silicon content. The 2300 K isotherm (Figure 4.18b) is in correspondence with the eutectic of the ternary system and slightly

lower of the Fe-C binary eutectic that is at 2400 K. Accordingly, a narrow melt pool forms in correspondence of the ternary eutectic composition. At 2700 K (Figure 4.18c) the high eutectic temperature in the binary Fe-Si determine the isotherm to cross both the solidus and the liquidus of the system. On the carbon rich side hcp Fe + L is still present in a narrow range.

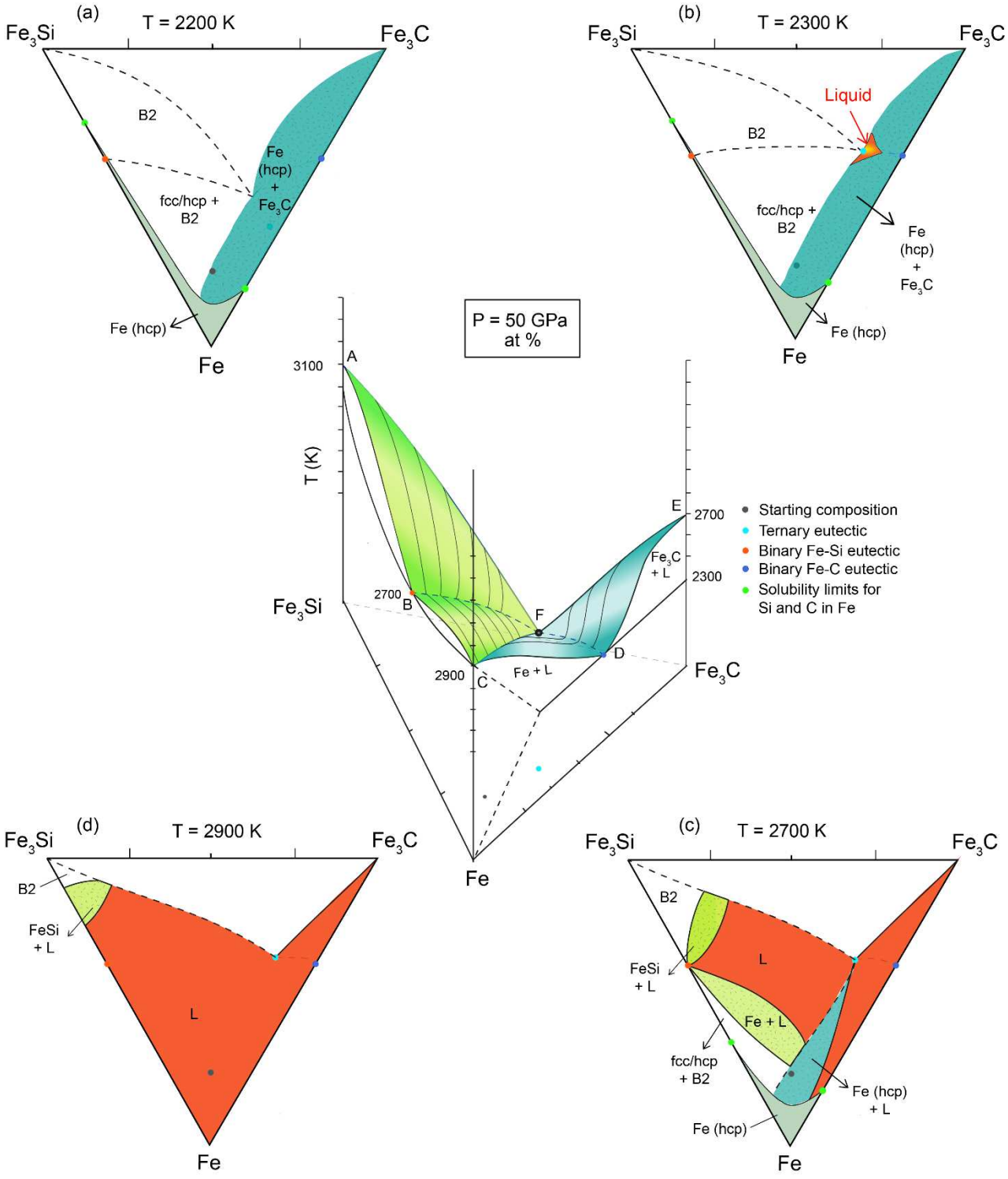

Figure 4.18: Space model of the iron corner in the Fe-Si-C ternary diagram, at the fixed pressure of 50 GPa. In the center the phase relations are shown as composition in function of the temperature. The four triangles represent isothermal sections to illustrate the phase relations below (a), in correspondence (b) and above (c and d) the ternary eutectic.

Finally, at 2900 K (Figure 4.18d) only a small compositional range display the existence of crystalline FeSi while the remaining phase diagram is characterized by liquid. In the Fe-Si system complete melting is attained only when temperature overcome 3100 K.

Increasing the light elements content stabilizes FeSi + Fe_7C_3. The subsolidus phase relations are shown in Figure 4.19. The proposed phase diagram only consider compositional space between 50 and 100 at % Fe and 0 and 50 at % Si and C. From the corner considered in the previous discussion where hcp Fe coexist with Fe_3C, moving toward the SiC side of the diagram carbon bearing phases replace pure iron. The absence of iron carbides at low pressure in $FeSi_{20}C_{10}$ indicates the presence of a solubility zone in correspondence of the FeSi corner. On the binary FeSi-Fe line, cubic FeSi is stabilized for 33 at%.

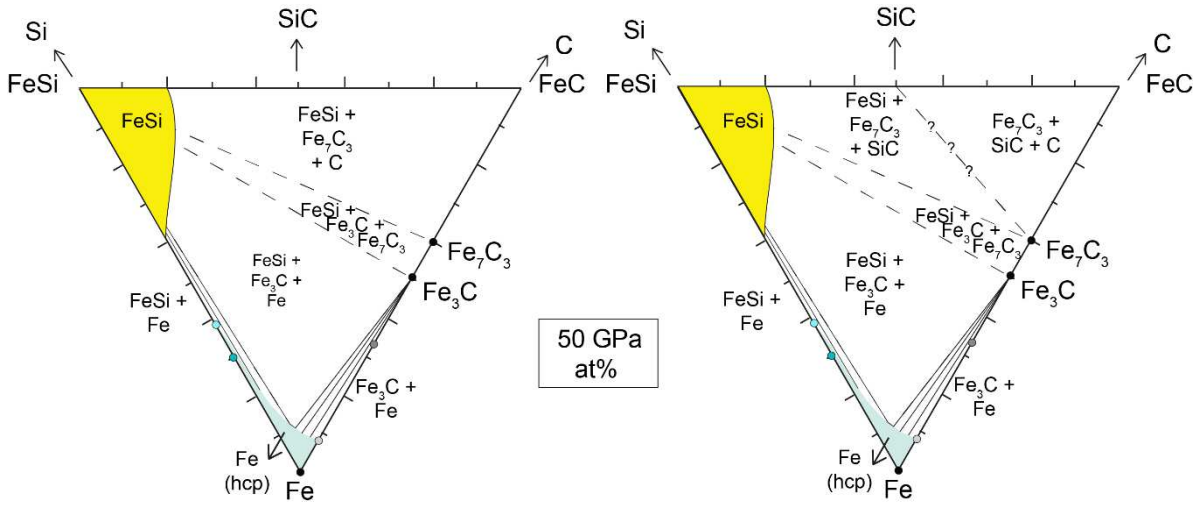

Figure 4.19: Isotherm sections of the ternary Fe-Si-C diagram below the eutectic temperature, in the subsolidus region. The two diagrams differs in the interpretation of the field with stable SiC or C,

The solubility of carbon in FeSi observed in our experiments enable to extend the field to the FeSi-FeC tie-line. For low carbon content Fe_3C is the stable carbide. It changes to Fe_7C_3 with higher carbon content. The existence of the stability field for SiC or C is confirmed by the presence of such phases in the transverse cut (Figure 4.11). As it was difficult to determine whether only carbon was present or instead there was also some silicon, both the possibilities were taken in account. If the observed spots are diamond a large stability field would exists were diamonds are in equilibrium with Fe_7C_3 and FeSi. On the other hand, the stability of SiC would require the presence of a tie line connecting the SiC side with iron carbide and determining the existence of a stability field were silicon carbide would coexist with diamond and an iron carbide.

At 50 GPa, the melting temperature retrieved for the samples with higher light element content (i.e. 2500 K) is 200 K higher than the eutectic temperature of $FeSi_3C_3$ (i.e. 2300 K). The stability of a phase with a higher carbon content and a higher melting temperature support the presence of a peritectic point, in analogy with the binary Fe-C system (Figure 4.20). A peritectic represent a point on the phase diagram where the occurring reaction consumes a solid and the liquid to produce a solid with different composition (Smallman and Ngan, 2014), as for example Fe_3C and the liquid that starts reacting together to from Fe_7C_3 (Fei and Brosh, 2014; Lord et al., 2009). In Fe-C two peritectics are assumed to exist (Figure 4.20), one entering the portion of the diagram where Fe_7C_3 is stable and a second at higher temperature and carbon content, entering the stability field of diamond. In a ternary system as the number of components increase the reaction would involve two liquids and two solids.

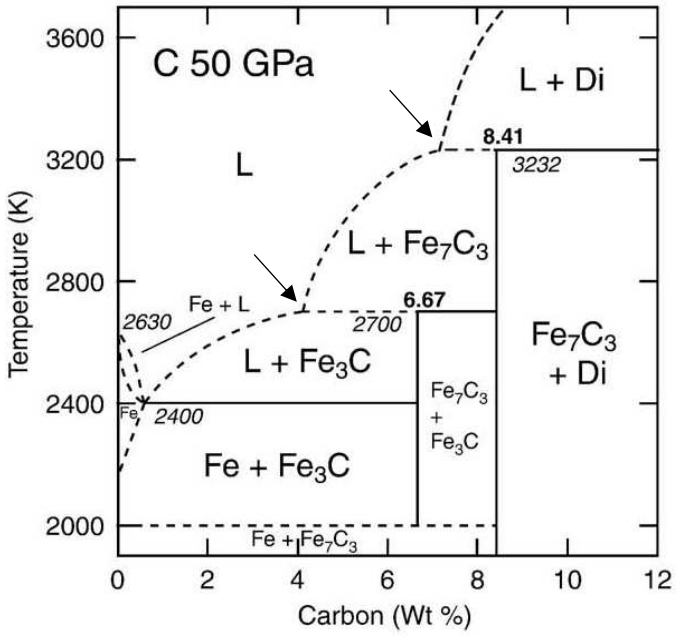

Figure 4.20: Binary Fe-C diagram at 50 GPa from Lord et al. (2009). Arrows point toward the two peritectic points.

Our work represents the first attempt to characterize the ternary Fe-Si-C system. Consequently there aren't many available references, especially regarding the existence of two peritectics and their carbon content. Accordingly the position in the Fe-C binary was used as a reference and shifted toward higher silicon content to account for the presence of Si. The main phases and the temperature relations are shown in Figure 4.21.

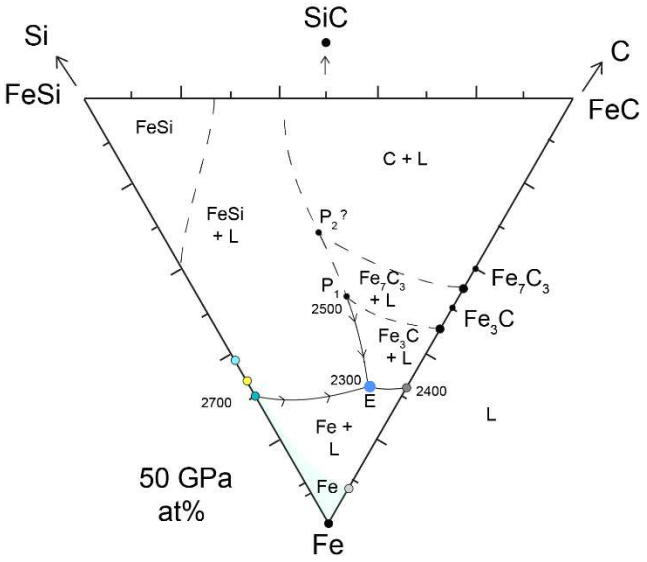

Figure 4.21: Isobaric phase diagram showing the eutectic and peritectic curves in the Fe-Si-C.

Finally, we updated the diagram proposed in Figure 4.18 with the addition of the phase relations for higher light elements content. The updated space model is shown in (Figure 4.22a). Two isothermal sections are proposed, respectively at the temperature of the ternary eutectic (b) and above the peritectic (c). The peritectic point is connected to the eutectic through a eutectic line (P1-E), representing the intersection between the liquidus surfaces of Fe-Si and Fe-C. At the eutectic temperature (i.e. 2300 K) the phase assemblage for higher Fe content is similar to the one displayed in Figure 4.18b. The close eutectic temperature of the binary Fe-C and the ternary Fe-Si-C, determine the existence of a narrow liquid portion in correspondence of the ternary eutectic surrounded by the hcp Fe + Fe_3C field of coexistence. As the section is taken at a temperature lower than the peritectic, in the carbon enriched side of the binary Fe-C, no melting is observed and the subsolidus relations are consistent with those defined in Figure 4.19. Due to the higher eutectic temperature of the binary Fe-Si and the narrow solid liquid coexistence field also on the silicon rich side of the diagram no melting is observed. Above the peritectic temperature (Figure 4.22c) the melt pool in correspondence of the eutectic increase and determines extensive melting, both in the iron rich side of the Fe-C system and in the Fe-Si system. The points representing the initial compositions (orange points in Figure 4.22) stable as FeSi + L at high temperature provide a constraint for the boundary of the FeSi + L field. The peritectic reaction include FeSi and a liquid as well as Fe_7C_3 and a second liquid with a different composition.

The wide compositional space displaying the stability of FeSi + L is supported by the results of the presented experiments, in which FeSi +L is the stable solidus assemblage. If the ternary diagram reproduce the features of the binary Fe-C, above the first peritectic and for higher carbon content we expect Fe_7C_3 to be stable in coexistence with diamond or SiC. The existence of this field is potentially confirmed by the retrieval in the transverse cut of the recovered samples of a low Z and hard phase (Figure 4.11). The presence of ultra-reduced phases (i.e. SiC or diamond) in the iron side of the diagram,

imply an extensive presence of SiC or C in system. SiC can hypothetically form an extended immiscibility zone into the ternary Fe-Si-C system, in analogy with the Fe-Si-O (Hirose et al., 2017b), opening new scenarios in planetary evolution.

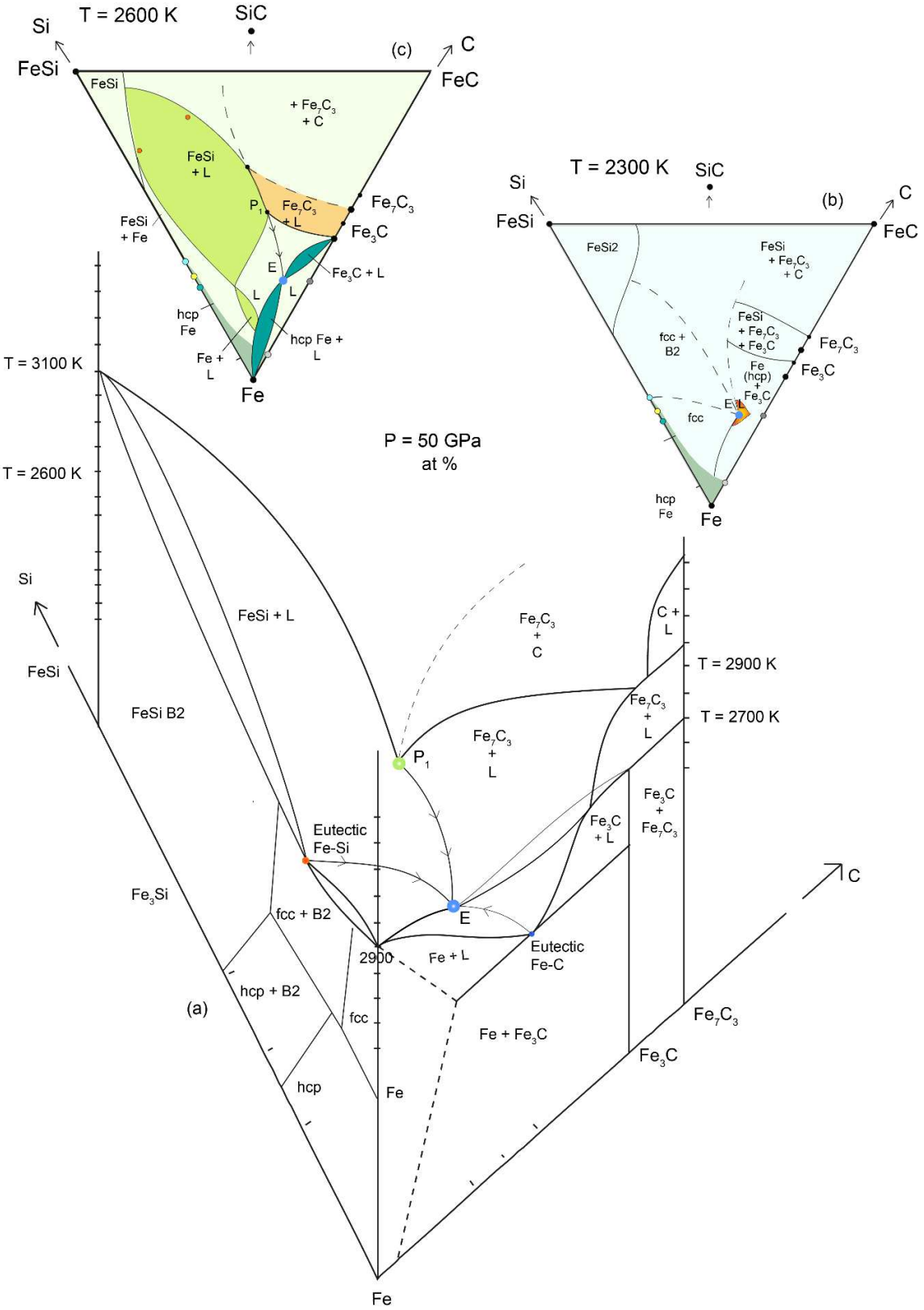

Figure 4.22: a) Updated ternary phase diagram (a) and isothermal sections at the eutectic (b) and peritectic temperatures (c).

4.2.4 Equations of state & thermal models

Determining the parameters of equations of state and thermal model is fundamental for modelling planetary interiors. P-V-T data sets for each phase were therfore fitted in order to have a first estimate of the parameters.

$FeSi_3C_3$

The P-V-T datasets, obtained for both hcp Fe (+Si, +C) and Fe_3C were fitted with a 3rd order Vinet equation of state to describe the isothermal pressure behaviour and a Mie Grüneisen Debye thermal model is proposed (details in Miozzi et al. (2018) and references therein). All refinements were performed with the EoSFit suite (Angel et al., 2014).

For hcp Fe (+Si, +C), the equation of state at ambient temperature, fitted with a third order Vinet EoS yields a bulk modulus K_0 = 150 (6) GPa, and it pressure derivative K_0'= 5.5 (2), with an initial volume V_0 = 22.8 (1) Å^3. The values for K_0 and K_0' are in relative agreement, within the error bar, with K_0 = 163.4 (8) GPa and K_0' = 5.38 (16) proposed by Dewaele et al. (2006). The difference in the V_0 (22.48 Å^3 in Dewaele) is related to the observed shift in the volume at 300 K due to carbon incorporation. It should be noticed that the two studies used the same equation of state but different pressure medium (KCl in our study and He in Dewaele et al., 2006).

For the thermal model a standard Mie Grüneisen Debye parameterization has been used (e.g. Angel et al., 2017; Duffy, T, Wang, 1998; Duffy et al., 2015; Miozzi et al., 2018), in which all the parameters have been refined from the collected experimental dataset. Values from literature were used only as initial reference points. The best-fit results are shown in Table 10 and Figure 4.23. The pressure residuals (Figure 4.23 top right insert), within ± 6 GPa, and the χ^2 equal to 1.3 account for the quality of the fit. The spacing within the isotherms displays a narrowing at high pressure, consistent with the lowering of thermal expansion with increasing pressure (Figure 4.23, bottom left insert).

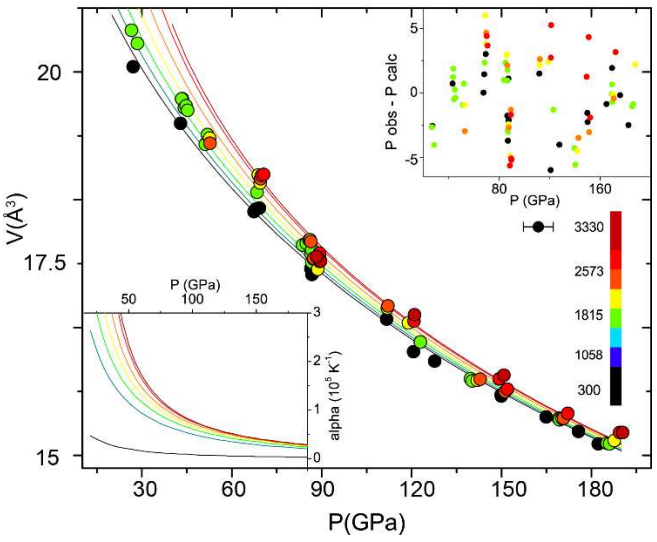

Figure 4.23: Results obtained fitting HP-HT data of (hcp) Fe with the Mie Grüneisen Debye thermal model. Upper insert: Pressure residuals for the fit. Lower insert: Value of the thermal expansion as a function of pressure and temperature.

	V_0 (Å^3)	K_0 (GPa)	K_0'	θ_D (K)	γ_0	q
Hcp Fe (+Si, +C)	23.25 ± 0.1	131 ± 10	5.8 ± 0.4	2200 ± 850	1.5 ± 0.9	3.38 ± 1.8
Fe_3C	151.4 ± 0.3	275 ± 30	3.7 ± 0.3	1720 ± 700	1.5 ± 0.5	2.6 ± 0.8

Table 10: Results from the refinement of the EoS and thermal model with a. For both Fe (hcp) (+Si, +C) and Fe_3C.

The obtained results are in disagreement with the thermal model proposed by Fei et al. (2016) as their solution, compared to our data overestimates the thermal expansion (Figure 4.24). Our data instead are in agreement with those collected by Fiquet et al. (2007) that display the same small thermal expansion.

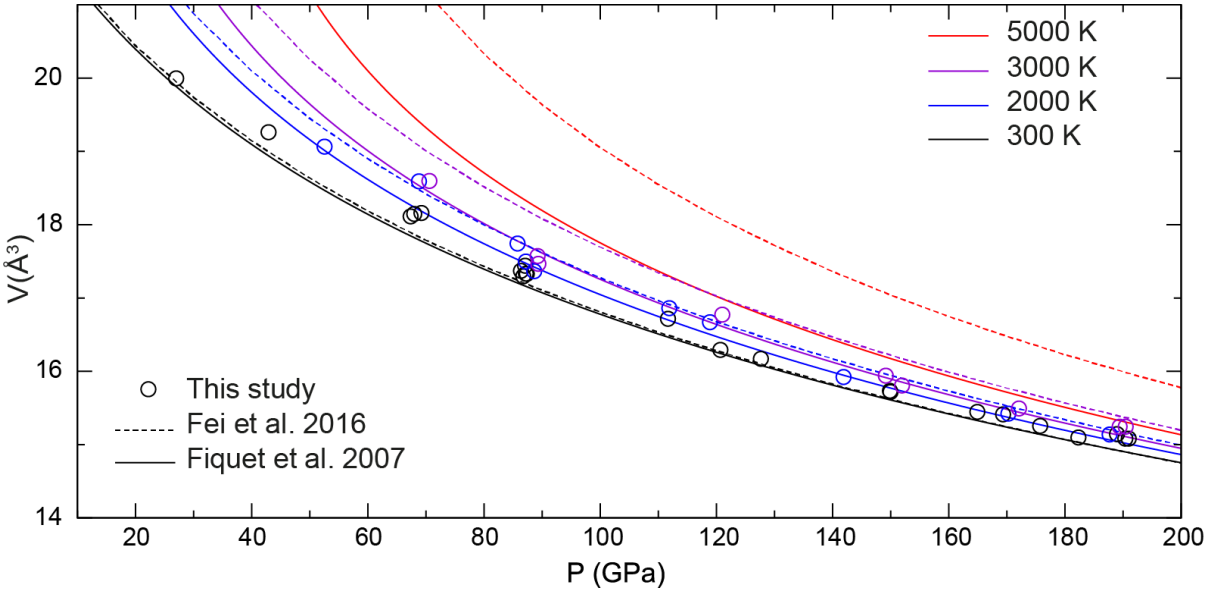

Figure 4.24: V-P plot for hcp Fe (+Si, +C) obtained in this study compared with the data from Fei et al. 2016 and Fiquet et al. 2007.

The volumes obtained for Fe_3C as a function of pressure and temperature are shown in Figure 4.25, together with the pressure variation of the a, b and c cell parameters at 300K and 1800 K. The 300 K compression curve is consistent with previous studies in the same pressure range (e.g. Sata et al., 2010) and the low pressure trend is in good agreement with data collected in large volume experiments (e.g. Litasov et al., 2013). No sudden reduction of the volume is visible in our dataset, but the cell parameters (Figure 4.25a and b) displays an inversion between b and a axis at 300 K between 20 and 60 GPa. This supports the report by Ono and Mibe (2010) of a magnetic transition occurring around 60 GPa. However the data from this study below 60 GPa are too sparse to carefully monitor a discontinuity in the volume change. This topic has been widely discussed in recent literature (Ono and Mibe, 2010; Prescher et al.,

2012; Wang et al., 2016). As the collected dataset is not well adapted for such specific subject, we refer to previous work for an extensive discussion of magnetic transition in Fe_3C.

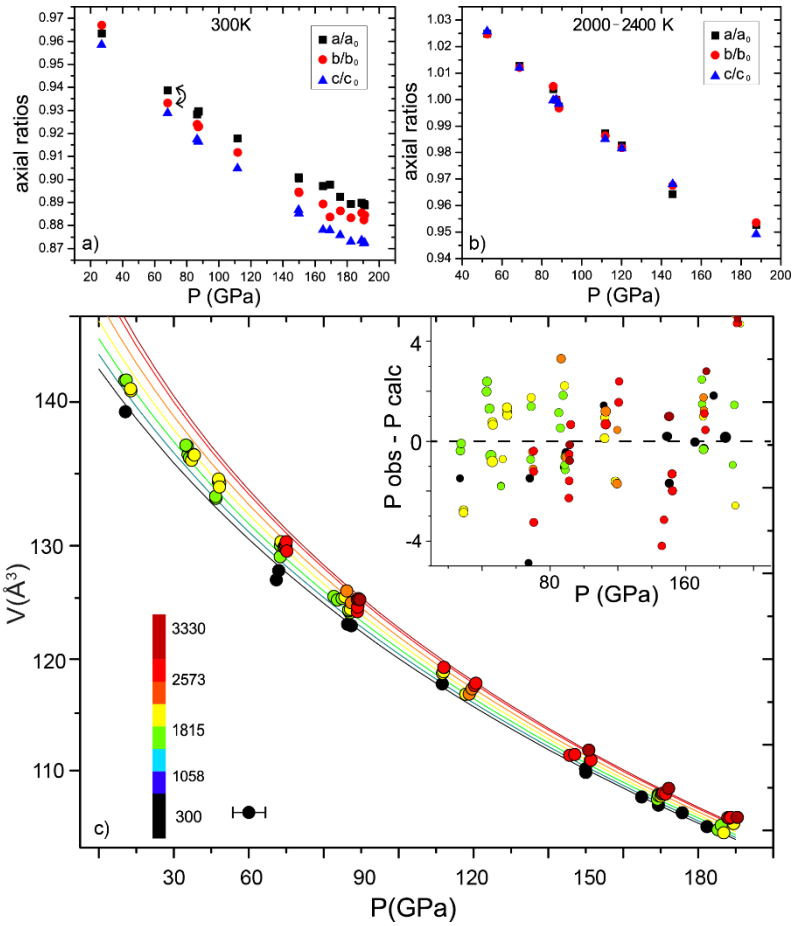

Figure 4.25: a) Fe_3C axial ratios for a, b and c at 300K. At 60 GPa. b) Axial ratios for a, b and c at high temperature. C) Results obtained fitting the Fe_3C data with the Mie Grüneisen Debye thermal model. In the insert the pressure residuals for the fit. Symbols represent the experimental data points collected.

The equation of state at 300 K and thermal model for Fe_3C were refined. Fitting the ambient temperature data with a Vinet EoS at the 3rd order yields a V_0 = 150 (5) Å^3 with K_0 = 295 (25) GPa and the first pressure derivative K_0' = 3.6 (1). These results are consistent with Sata and coauthors (2010) for the non-magnetic phase. In addition, V_0 and K_0 are also comparable within the error bars with those obtained employing computational methods and two different equations of state, Birch Murnaghan (Vocadlo et al., 2002) and Vinet (Mookherjee, 2011). The experimentally determined K' however, is always lower (3.4 here compared to 4.3 in Vocadlo et al. (2002) and 4.9 for Mookherjee (2011). The parameters of the thermal model were all refined from our experimental data, with reasonable pressure residuals (± 4 GPa) (Figure 4.25 insert). The values for the best-fit solution are shown in Table 10. Differences in the values of V_0 and K_0 between the 300 K EoS and the thermal model is most likely a consequence of the presence of more high temperature points between 30 and 60 GPa, which significantly improves the fit. The obtained Debye temperature is higher than the values obtained by Litasov and coauthors (2013) and other previous authors. However those values were determined for the low pressure ferromagnetic and paramagnetic phases in a P-T range much smaller than the one examined in this study.

$FeSi_{10}C_{20}$

FeSi

The initial volume was fixed to the value retrieved by Edmund (2018). The amorphous character of the starting material prevent refining the volumes before heating. Both the Birch Murnaghan and the Vinet formalisms at the third order were used and the results are in agreement within the errors. With a Birch Murnaghan EoS at the third order, we obtained K_0 = 109 (1) GPa and K_0' = 6.1 (2). The parameters were used as a reference for the thermal model fit. The P-V-T data were fitted with a Mie Grüneisen Debye thermal model, keeping V_0 fixed to the value used for the 300 K. The results are shown in Figure 4.26, where the collected data are shown with the isotherms re-calculated with the obtained thermal model. The residuals in pressure are between 8 and -8 (Figure 4.26 insert).

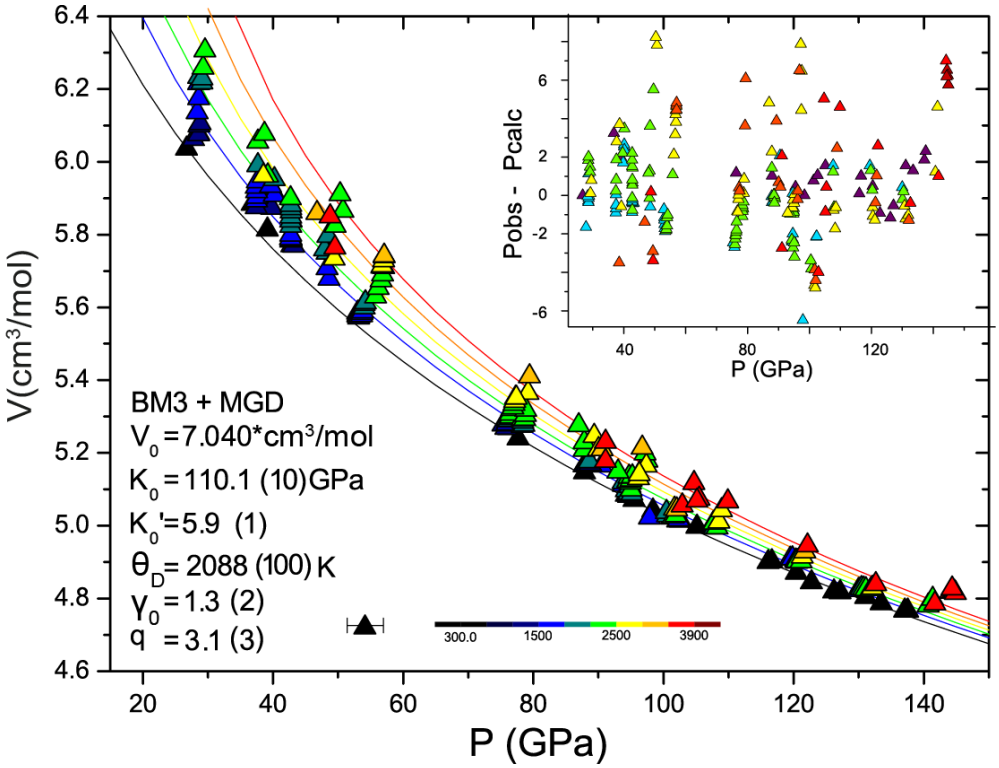

Figure 4.26: P-V-T data for FeSi in $FeSi_{10}C_{20}$ as volume on pressure and temperature in the colour scale. Refinement of the MGD thermal model with only the volume fixed. The insert on the top right displays the pressure residuals for the selected model.

The fit reproduces nicely the temperature variation of the volumes at high pressure. At low pressure however, the distribution of the isotherms might underestimate the thermal expansion of the material. The refined thermal parameters are different from those obtained by Fischer (2014) employing the same thermal model. Such difference can be ascribed to the different approach used for the fit. While we decided to refine all the parameters with the present data set, Fisher and co-authors refined only γ_0 and kept θ_D and q fixed to reference values.

As the value of Debye temperature in our model is higher compared to those previously obtained, we did a refinement keeping θ_D fixed to 450 K, in order to study the variability of the other parameters. The

results (Figure 4.27) then display an underestimation of the thermal expansion at high pressure. The isotherms that are shifted toward lower volumes compared to the experimental data. Using a purely vibrational model as the MGD as a matter of fact excludes the electronic contribution to the thermal pressure, often taken into account when iron is involved (Dewaele et al., 2006; Edmund et al., 2019; Fei et al., 2016).

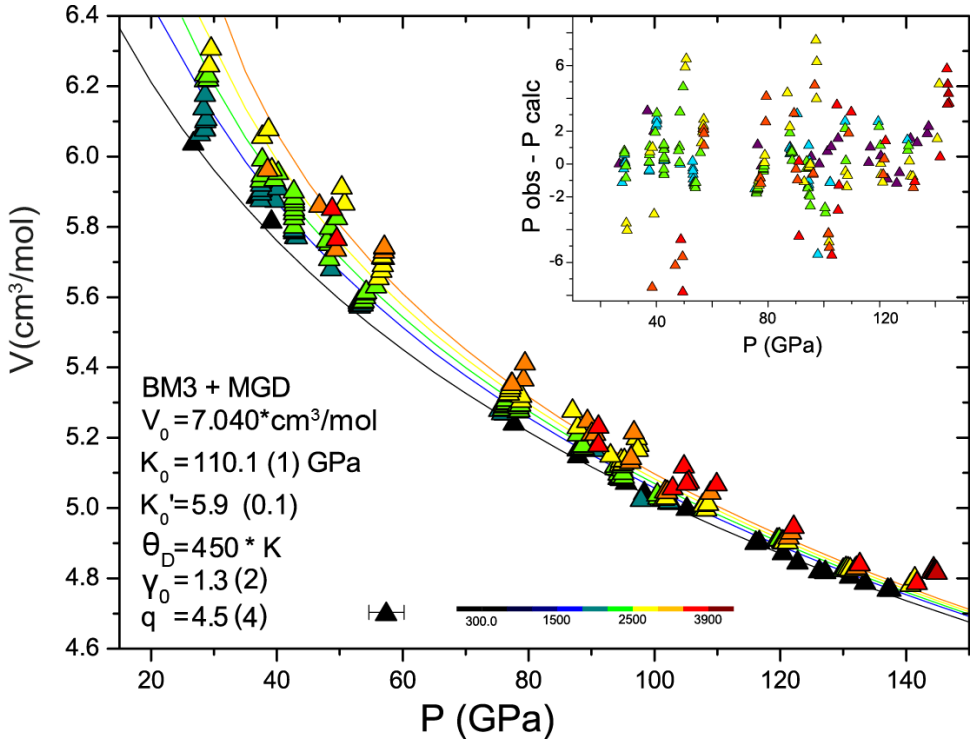

Figure 4.27: Refinement of the MGD thermal model with the Debye temperature fixed to the literature values Fe_7C_3.

In the P-V-T data set two clusters can be recognised from the evolution of the volume in pressure. In the range between 20 and 60 GPa the compound is stiffer, and shows a softening in the range between 60 and 160 GPa (Figure 4.28a). The same behaviour is visible in the evolution of the axial ratio a/c. The pressure dependence of the axial ratio a/c is high in the low pressure range and become smaller above 60 GPa (Figure 4.28b). This effect on the compressibility and axial ratio has been predicted by calculation (Mookherjee, 2011) and observed in experiments (Chen et al., 2012; Prescher et al., 2015), as the consequence of a ferromagnetic to non-magnetic spin transition.

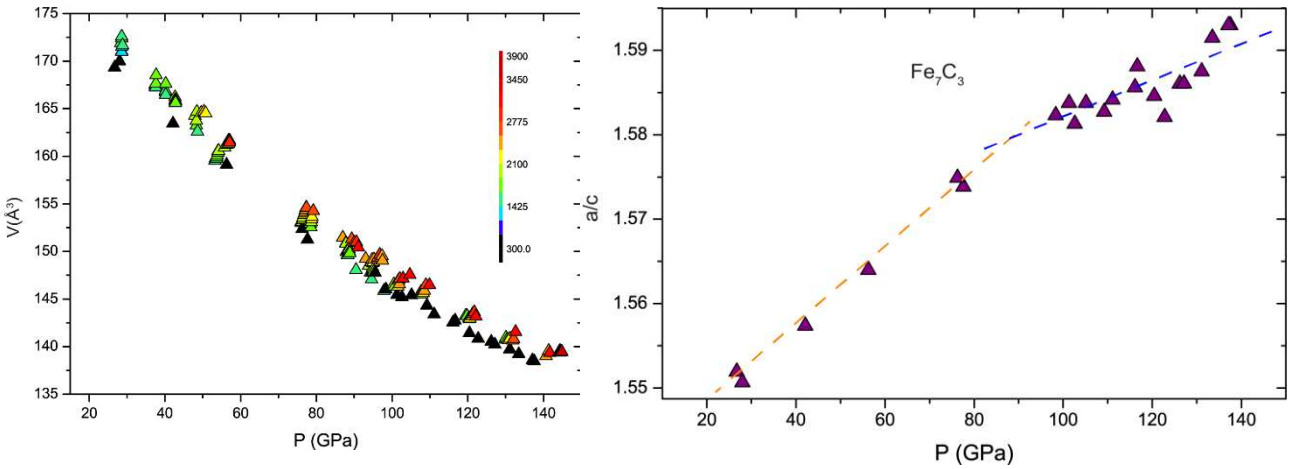

Figure 4.28: a) P-V-T data for Fe_7C_3 as volume over pressure. b) axial ratio a/c at 300 K as a function of pressure.

The presence of two magnetic phases requires the determination of two different EoS. In this study the thermal model was determined only for the non-magnetic phase which is the most relevant for application to planetary interiors. Between 20 and 60 GPa the scarce distribution in pressure and the absence of high temperature data hamper the possibility of determining a reliable model. In the high pressure range, data were fitted with a Thermal Pressure model. For the refinement the initial volume was fixed to the value determined by Chen et al. (2012) and the Einstein temperature was calculated from the Debye temperature proposed by Litasov et al. (2014) for the paramagnetic phase, as no data are available about temperature behaviour of the non-magnetic phase. The obtained results are shown in Figure 4.29.

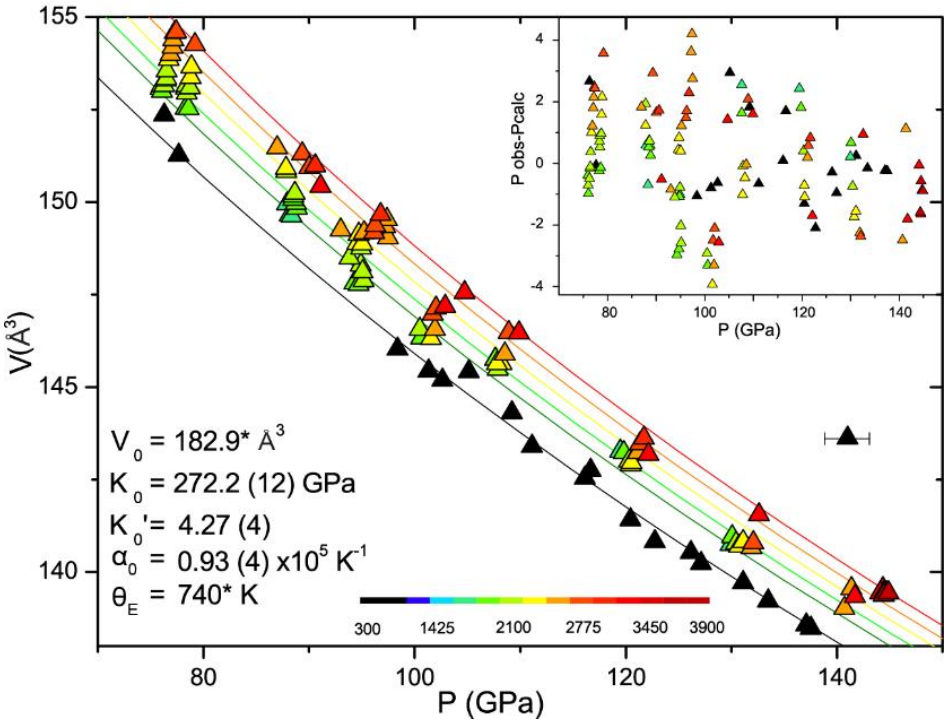

Figure 4.29: P-V-T data for Fe_7C_3 fitted with the Thermal Pressure equation of state. Triangles correspond to the collected experimental data. Lines the calculated isotherms. Up right insert the pressure residuals for the fit. Asterisks denote the parameters of the fit that were fixed from literature.

The obtained K_0 and K_0' are qualitatively in agreement with those determined by experiments (Chen et al., 2012) and computations (Mookherjee et al., 2011). The experimental EoS retrieved by Chen and co-authors (2012) display a higher K_0 (307 GPa) and lower K_0' (3.2), thus the difference with the present data can be consider an effect of the correlation between the parameters. Furthermore, in our study the value K_0 and K_0' obtained with the 300 K Eos were refined simultaneously to the parameters of the thermal models. Conversely, the EoS obtained from computation has a higher K_0 (291 GPa) and also a higher K_0' (4.5) thus making it difficult to attribute the shift to a trade-off between parameters.

Refining the Einstein temperature with the current thermal model resulted in a θ_E of ~ 2500 K and the coefficient of thermal expansion (α_0) = $0.0131 \cdot 10^5 K^{-1}$. Such low value is almost certainly a mathematical artefact from the fit. Iron carbides are known to exhibit a reduction of the thermal expansion due to an Invar behaviour above the high pressure discontinuity, however is unlikely for the reduction to have this magnitude. Accordingly the value of the Einstein temperature was kept fixed during the whole procedure.

$FeSi_{20}C_{10}$

In Figure 4.30 the data collected for FeSi and Fe_7C_3 are shown. The presence of carbon in solution in FeSi at low pressure requires the use of two different equations. As the distribution of the data between 40 and 120 GPa is not optimal to refine an equation of state or a thermal model, only the high pressure will be analysed.

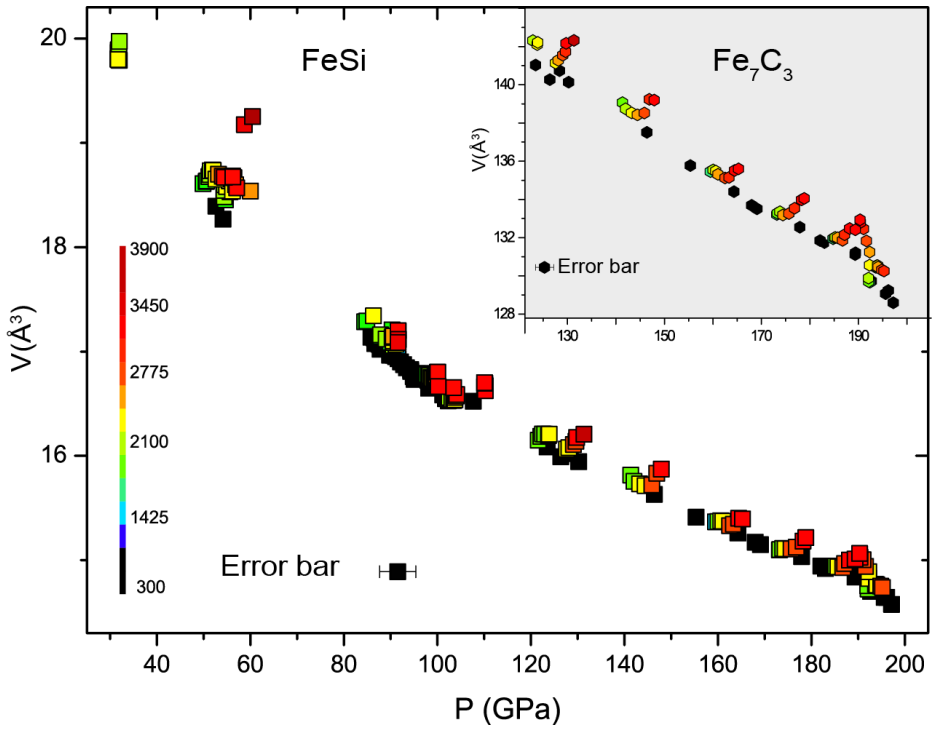

Figure 4.30: Collected P-V-T data plotted as volume over pressure. In the main window FeSi, in the upper insert Fe_7C_3. Colour coding corresponds to temperature. Errors on volumes are of the size of symbols.

FeSi

The data at ambient temperature and above 100 GPa were fitted with a 3rd order Birch Murnaghan equation of state. The initial volume was set to the value of 22 $Å^3$ and refined only when the least square was converging on a solution. V_0 was blocked also during the refinement of the thermal model, while K_0 and K_0' were assessed with α_0 and θ_E of the Thermal Pressure model.

The results of the fit are shown in Figure 4.31. The refined K_0 and K_0', 173.3 GPa and 5.16 respectively, are consistent with the values proposed in previous work on FeSi (Edmund 2018). The isotherms at higher temperature struggle to properly address the thermal expansion of the experimental data. The issue related to the thermal expansion is also deducible from the plot of the pressure residuals, where the data at high temperature lie all in the region above the zero without any symmetrical distribution.

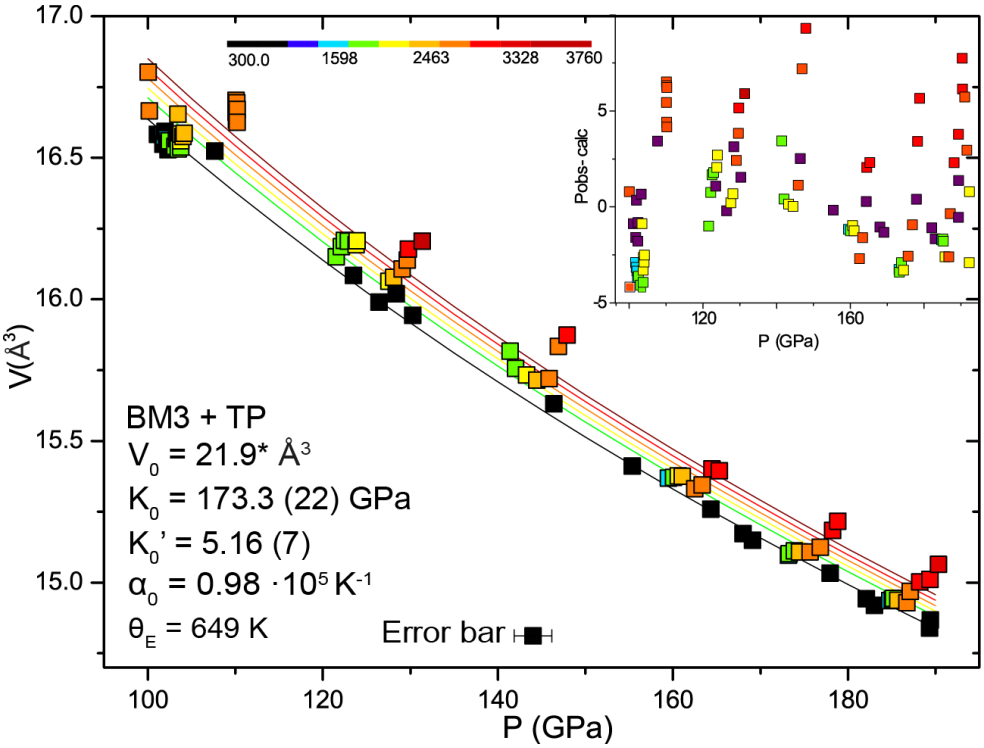

Figure 4.31: Collected P-V-T for FeSi in $FeSi_{20}C_{10}$, data plotted with the isotherms calculated from the solution obtained with the Thermal Pressure model. Upper insert: pressure residuals from the fit. Errors on volumes are of the size of symbols.

It should be noted that not much is known about the compositional evolution of FeSi and whether or not part of the carbon is still in the structure after Fe_7C_3 exsolution. However, the distribution of the data points at intermediate temperature raise some question about the possibility of having a systematic error in the fit of the diffraction patterns.

Fe_7C_3

To overcome the absence of points at low pressure, V_0 of Fe_7C_3 was fixed to the value found for $FeSi_{10}C_{20}$ (i.e. 182.9 Å^3). Data were refined with a 3rd order Birch Murnaghan and the Thermal pressure model using the same iterative procedure as for the other samples. The Einstein temperature was first fixed to 740 K then refined when the fit gained some accuracy. Fe_7C_3 should already be in the stability field of the non-magnetic phase, as it exsolves only above 100 GPa.

Results are shown in Figure 4.32. With a fixed V_0, the values obtained for K_0 and K_0' are in agreement within the error bars with those determined for Fe_7C_3 in $FeSi_{10}C_{20}$. The higher K_0 is compensated by a smaller K_0' and overall the EoS got the trend of the experimental data.

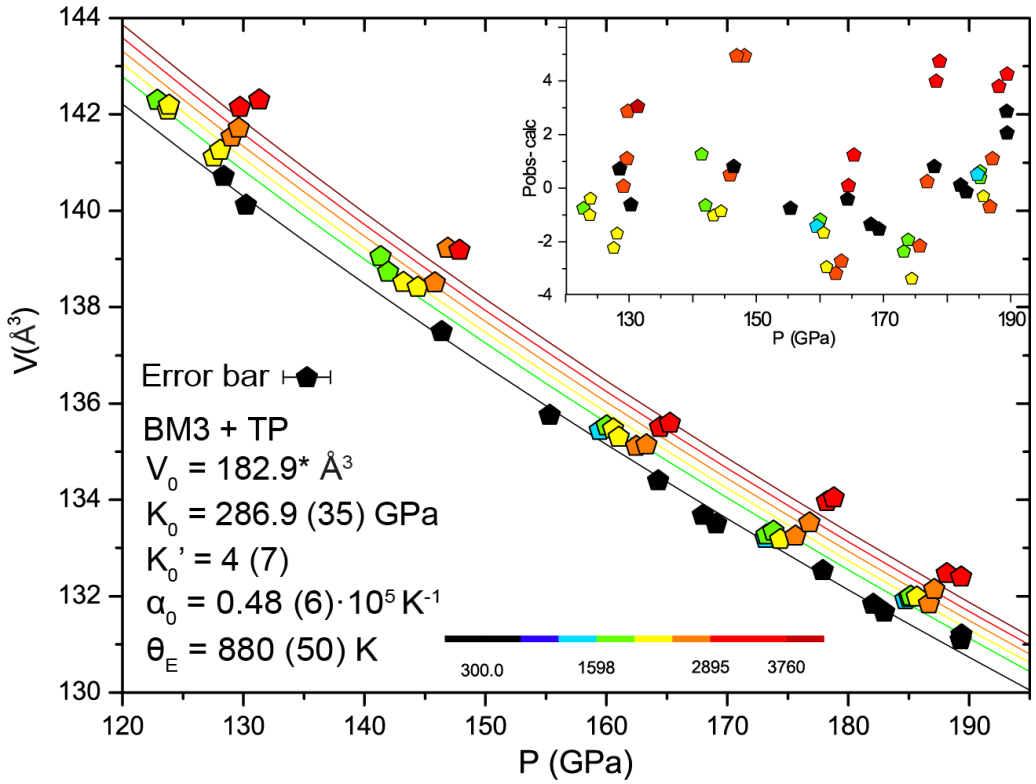

Figure 4.32: Collected P-V-T data plotted over the isotherms calculated with the Thermal Pressure model. Value of the parameters are at the bottom left. Top right insert: plot of the pressure residuals from the fit.

The obtained θ_E is in agreement within the error bars with the starting value. The coefficient of thermal expansion instead display a low value. As for FeSi the distribution of the isotherms is not consistent with the collected experimental points but underestimate the volumes at high temperature for most of the data. This low value of α_0 is probably a mathematical artefact of the fit, coming from the differences in the distribution of the points in each of the HP-HT clusters.

The distribution of Fe_7C_3 (Figure 4.32) exhibits a strong resemblance to that of FeSi (Figure 4.31). Hence is unlikely for it to be related to specific local phenomena in FeSi or Fe_7C_3 and also exclude the possibility of a systematic bias during the diffraction pattern fit of the phases. More likely the cause is to be found in the determination of the unit cell parameters of the pressure medium, thus possibly leading to an underestimation of pressure.

$FeSi_6C_5$

Data for $FeSi_6C_5$ were collected up to 120 GPa and ~ 4000 K in the subsolidus and up to the melting regime. The collected volumes at both 300 K and high temperature do not show precise and well defined trend but instead form clusters of points. It is thus difficult to identify the evolution at high temperature (Figure 4.33). The scatter of the points at 300 K and the absence of data at lower pressure, makes it impossible to refine any isothermal equation of state.

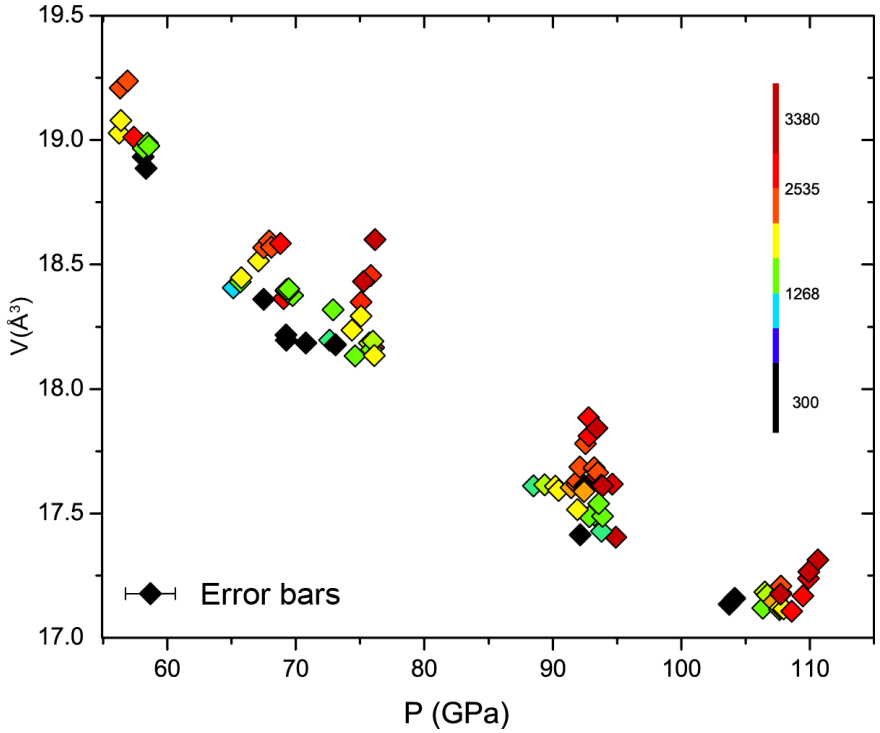

Figure 4.33: Collected data set for FeSi as volume over pressure, collected in the sample $FeSi_6C_5$.

Chapter 5

Application to exoplanets interiors

The results of all the experiments performed provide for the first time a characterization of the ternary Fe-Si-C system up to pressures of 200 GPa and temperature of 4000 K. Based on the melting temperatures obtained for the different starting materials, we propose the existence of an eutectic point at low temperature with high carbon and low silicon content, and a peritectic at higher temperature and enriched in light elements. The established phase relations (Figue 4.22) display how FeSi is stable in a wide compositional range and can incorporate several atomic % of carbon. Carbon incorporation is likely to increase the volume of the unit cell, conversely to silicon addition that instead triggers a reduction of the volume. Whether the phenomena is a direct result of the interaction of silicon with the magnetic properties of iron is still to be investigated. For the studied compositions with high light elements content, FeSi is the stable phase above the solidus. For $FeSi_3C_3$ starting composition, hcp Fe is the phase stable across the solidus and it has been observed to incorporate carbon, as well as silicon. Furthermore, carbon incorporation is responsible for an increase of the unit cell volume (Figure 4.8).

Above the solubility limit of carbon in iron, Fe_3C is stable for low light elements content and Fe_7C_3 for high light elements content. No evidences were found to support the non-stoichiometry of the compound or the presence of Si in solution (e.g. Das et al., 2017; Zhu et al., 2019). In the compositional space, the two phases are expected to coexist with FeSi in a narrow field but this was not observed in our experiments. The retrieval of a phase with low Z in the transverse cut of the recovered samples advocates for the presence of silicon carbide or diamond, potentially signing the presence of an immiscibility gap for higher light element content.

Concerning the Si-C binary system our results accurately locate the pressure of the phase transition B1-B3 at 66 ± 2 GPa and revise the estimate for the volume jump (~10%), found to be lower than what has been previously proposed. The parameters of the thermal equation of state were obtained for the low pressure structure B3, already present in literature and for the first time also for the high pressure structure B1, using data collected up to 200 GPa and 4000 K. Finally, we were able to observe the presence of a eutectic point in the silicon rich side of the binary phase diagram. SiC is often considered as candidate to be the major component of the mantle in carbon enriched exoplanets. As such, having a precise knowledge of the evolution of the structure and properties with pressure and temperature is needed to increase the accuracy of interior models.

The results on the ternary system offer an overview on how compositional variations would affect the crystallization process of a Fe-Si-C core and the outcomes in terms of structures and dynamic hence the likelihood of starting a dynamo and a magnetic field. Using as a reference the results of the experiments,

the phase diagram can be considered as made by four main compositional zones, shown in Figure 5.1 described in the new paragraphs from a phenomenological point of view.

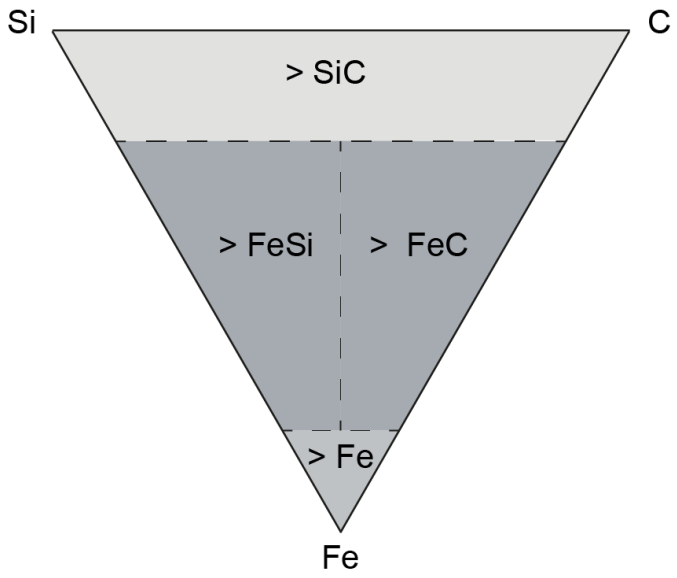

Figure 5.1: Schematic view of the ternary Fe-Si-C diagram with the distinction in main compositional domains.

5.1 Estimate of the solidification processes in a Fe-Si-C core.

The presence of a metallic core and its main characteristics (composition and thermal evolution) deeply affect the properties of a planet. It determines the possibility to start a dynamo hence to trigger the presence of a magnetic field. The presence of convection, thermal or compositional, in a metallic core, is the necessary condition to have a dynamo action (Breuer et al., 2015; Stevenson, 2001). If the core is entirely liquid, thermal convection can happen when the outgoing thermal flux exceed the heat flux along the adiabat. Heat flux is a function of the sum between thermal conductivity and thermal expansivity thus related to the properties of the liquid. In addition, for thermal convection to be effective also mantle conductivity should be considered, as it needs to remove heat at a higher rate than the thermal flux from the core (Breuer et al., 2015; Williams and Nimmo, 2004). If the rate of heat removal is lower than the critical flow, a stratified and thermally stable core will be obtained and heat released only by conduction.

Compositional convection will take place when a buoyant chemical component is released, typically during solidification of a denser inner core, like in the Earth. Therefore, it is strongly influenced by the chemistry of the system, in particular the amount of light elements and the type of crystallization process. The latter depends from the relative slopes of the adiabat $(dT/dP)_{ad}$, the melting curve $(dT/dP)_{liq}$ as well as the density of the solid and liquid phases (Breuer et al., 2015; Stevenson, 2001; Williams and Nimmo, 2004; Williams, 2009). Using the phase relations established in the present data set, it is possible to estimate the core solidification processes occurring in the ternary diagram for different compositions (Figure 5.2). In the chosen crystallization scenario we assume melting to display a monotonic behaviour with a positive slope and it crosses the adiabat at a depth corresponding to the center of the planet.

In the Fe-rich corner, the first phase to crystallize is hcp Fe (+Si, + C). The light elements partitioning coefficient between solid and liquid determine an enrichment of light element in the liquid phase and accordingly the forming crystals can sink and accumulate toward the bottom, thus forming a solid inner core. Solidification will deplete the liquid in iron and further increase its light elements content. During crystallization a boundary of liquid with different composition separates the solid inner core from the remaining liquid and compositional convection starts in the outer part of the core to homogenize the composition (e.g. Breuer et al., 2015; Williams, 2009). Cooling progresses until the adiabat crosses the melting curve at the eutectic temperature, thus crystallizing a second phase and consuming all the residual liquid. This process, usually referred to as bottom up crystallization, is the one proposed for the formation of the Earth's core (Williams, 2009). The presence of compositional convection in the outer layer is an important energy source to activate the dynamo.

In the FeSi side of the diagram, the differences in the stable phases might induce extremely different behaviours. With higher silicon in the initial liquid, the first solidifying phase is FeSi, potentially hosting small amount of carbon in the structure. Light elements partition equally between liquid metals and solid silicides. As a consequence, the density contrast between the formed crystal and the remaining liquid is not sufficient to affect the buoyancy (i.e. to have them sinking or floating upward). Therefore it is likely to create a mushy zone at the base of the core where crystals are in suspension in the liquid.

The eutectic in the binary Fe-Si system shifts toward higher silicon content with increasing pressure (Figure 4.5). Accordingly the silicon content in the solid and the density of crystals increase along the cooling path. The dynamical implication of this process is strongly related to the evolution of the system that requires more constraints as it also depends on other parameters (such as viscosity). For instance, one possibility for the core is to evolve as layers of crystals in suspension in a liquid and with a compositional gradient. During cooling of the system, each layer can progressively solidify a second solid phase from the remaining liquid and produce a stratified core. The solidification regime would be different if we assume the possibility of mixing between the forming layers. In such case, the growing crystals, due to density increment, would sink below those previously formed and equilibrate with the composition of the fluid. The density difference between the solid and the liquid is still not enough to have the crystals upwelling, instead they will be confined in the bottom part inside a mushy zone. The remaining liquid core can undergo compositional convection as the results of the chemical differences between the main liquid and the one at the boundary with the bottom layer. Solidification of crystals in the mushy zone will proceed until the adiabat reach the eutectic melting temperature and a solid layer will be formed.

The Fe-C side of the system represents a different case from the previous two. Carbides would be the first phase to form in the center of the planet and the coefficient of partitioning between liquid and solid may be relatively high. Accordingly the forming solids will be enriched in carbon with respect to the

liquid. When the adiabat crosses the melting temperature, crystals are formed and the low density induced by the presence of light elements will have them rising upwards, toward the core mantle boundary. As the temperature would be still above the liquidus, crystals melt again enriching the liquid in light elements, while the liquid at the bottom is still depleted. This process of crystallization and dissolution at the core mantle boundary proceeds until the liquidus is crossed and iron carbides start solidifying. The lower density of the crystal keeps them floating and accumulating on the core side of the core-mantle boundary. The thickness of the top layer will increase with cooling, until the eutectic temperature is reached and a second phase will crystallize. During all the process, the density difference between the bottom and the top liquid, respectively depleted and enriched in light elements, set the boundaries for compositional convection to happen. This process is usually referred to as top-down crystallization and has been proposed as one of the possible mechanisms for the formations of Mercury's core (Williams, 2009).

Finally, with the liquidus field of SiC likely to occupy a large portion of the Fe-Si-C ternary, an analogy with the Fe-Si-O system can be made regarding the solidification paths and implications (Helffrich et al., 2018; Hirose et al., 2017a).

All the proposed scenarios for core solidification from a ternary Fe-Si-C alloy result in cores with different structures and thermal behaviours. According to the phenomenological description provided, while a Fe core and Fe-C core would represent quite standard solidification style, already proposed for the Earth and other solar system's planets (Breuer et al., 2015; Williams, 2009) a core with a higher silicon content would represent the most interesting case.

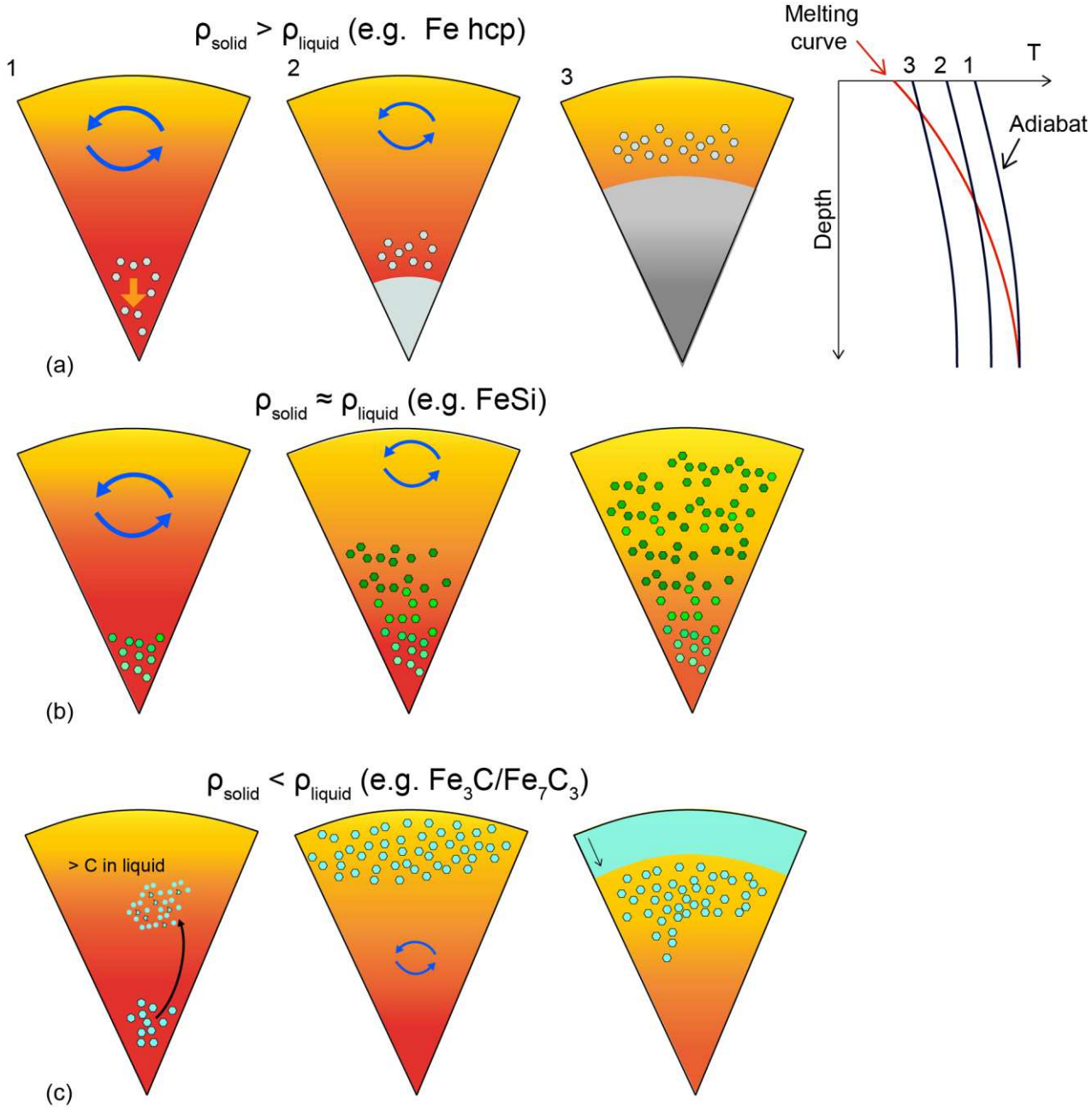

Figure 5.2: Crystallization scenarios in the Fe-Si-C system and corresponding relationship between the adiabat (black lines) and a hypothetical melting curve (red line) evaluated for three time steps. a) Bottom up crystallization. When crystals start forming the remaining liquid is enriched in light elements and drives compositional convection. b) FeSi crystals forms in the bottom part and due to the low density contrast rest suspended in a mushy zone. c) Floating crystals equilibrate with the liquid while rising upward. The carbon enriched liquid generate a density contrast with the depleted bottom layer. Eventually crystals will solidify and accrete at the CMB producing a solid iron carbides layer.

The state of the core is a critical parameter to evaluate. At the current state exoplanets models are build assuming a core made by pure iron (Dorn et al., 2018, 2017; Howe et al., 2014; Valencia et al., 2006b) neglecting light elements incorporations. This assumption potentially lead to an overestimation of core density and underestimation of the planetary radius (Dorn et al., 2015; Wagner et al., 2011). In the next years, an increase of the accuracy in the planets mass and radius measurement is expected. Furthermore, compositions and ages of the host star will be determined. The improvements in this field of observations, should correspond to an increment in the accuracy of the available models for planetary interiors evolving toward more complex compositions.

Including compositional variation of planetary cores represent an improvement for planetary interiors modelling. Knowledge about the chemistry of the system is a key for calculating more accurate mass radius plot. The existing link between the composition and solidification process of the core, coupled with the determination of the planetary system age may provide an estimate about the core state and the eventual presence of an active dynamo. Properties of iron in binary and ternary alloys with light elements come from the work done for the Earth's core (Badro et al., 2015, 2014; e.g. Edmund et al., 2019; Hirose et al., 2017a; Mashino et al., 2019; Prescher et al., 2015; Tateno et al., 2018, 2015) where low light element content is considered to satisfy the cosmochemical constrains and also on Mercury's core (e.g. Vander Kaaden et al., 2016). However, to cover all the possible compositions for models higher light element content should also be considered. The possible incorporation of high Si content in planetary cores would induce changes in the estimate of the mantle composition and consequently dynamic. Currently the Fe/Si and Mg/Si value of the host stars, are used as a reference for the composition of the planetary mantles, as they condensate at similar temperature and small distance from the star and are assumed to not differentiate in the core (Dorn et al., 2015; Hinkel and Unterborn, 2018; Valencia, 2013). Variation in the Mg/Si content of a mantle, if Si is included in the core, has important consequence on the dynamic and habitability of a planet and requires careful estimation (Unterborn et al., 2014; Unterborn and Panero, 2017).

As first application we assumed the composition of the Earth's core to be made by a FeSiC alloy, with the carbon content limited to a maximum of 4 at % (Dasgupta, 2013). The thermal equation of state determined for hcp Fe (+Si, +C) in $FeSi_3C_3$ was used for instance to extrapolate volumes at pressures corresponding to the Earth's inner core. Using the PREM (Dziewonski and Anderson, 1981) as a reference, we calculated the densities of the compound for the highest and lower possible carbon content, a four different temperatures. The results were also compared with densities of pure Fe determined at 300 K and 5500 K, as well as the densities for $Fe_{94}Si_3C_3$ computed by Li et al. (2018). Results are shown in Figure 5.3. The obtained density values at 300 K and 360 GPa are as expected lower than pure iron and in qualitative agreement with those predicted for an alloy with intermediate composition ($Fe_{94}Si_3C_3$) by recent computational work (Li et al., 2018). Conversely to the density calculated for $Fe_{94}Si_3C_3$ at 6000 K that match the one of the PREM. The low thermal expansion obtained from our experimental

results does not permit to match the values of the PREM model for an inner core containing 3 at% Si and up to 4 at% C for all conceivable temperatures.

A different estimate of volume variation with pressure can lead to the observed outcome as it affect density and consequently the value of the thermal expansion. The low amount of the two light elements and the different positions they occupy in hcp Fe iron, shown in paragraph 4.2.1, induce a configurational disorder that might be difficult to account for with calculations. Thus leading to an overestimation of the thermal expansion compared to the one experimentally determined. In Figure 5.3 the densities of pure iron at 300 K and 5500 K are also shown.

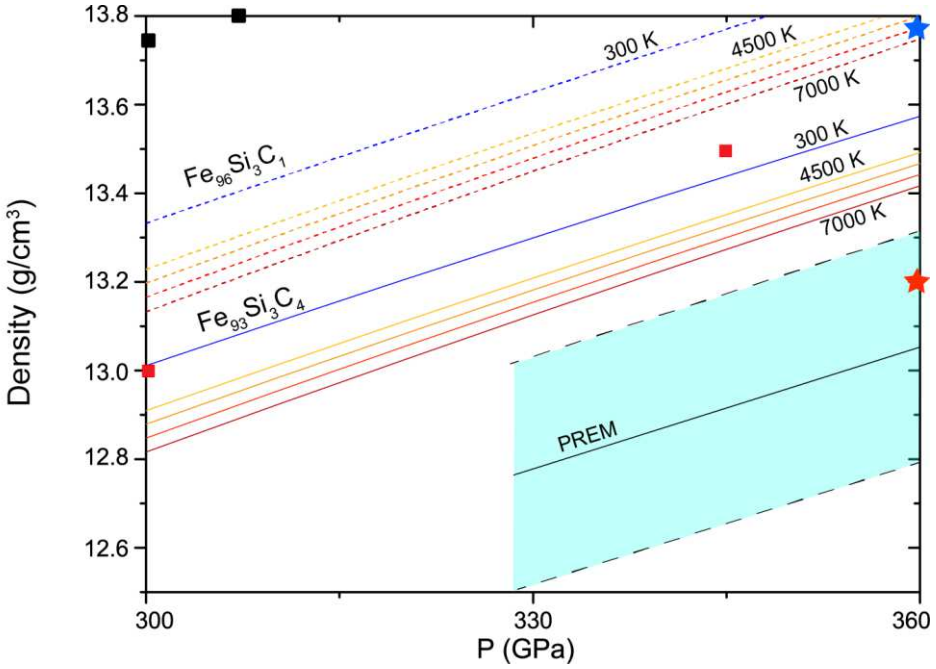

Figure 5.3: From Miozzi et al. (in prep). Densities as a function of pressure for different hcp Fe-Si-C alloys. Solid and dashed lines are respectively for the highest and lowest carbon content (numbers are given in at %). Colour code is used for different isotherms, specifically 300, 4500, 5000, 6000 and 7000 K. Stars stand for the densities calculated by Li et al. (2018) for a $Fe_{94}Si_3C_3$ alloy at 360 GPa and 300 (in blue) and 6000 (red) K respectively. Squares stand for the density of pure iron at 300 K (in black) and 5500 K (in red) by Fei et al. 2016.

5.2 SiC as main component of a planetary mantle

Our first approach to exoplanets modelling is to discuss a synthetic planet made by a SiC rich mantle and a pure iron core. The latter is indeed an underestimation of core's complexity, as previously discussed, it is however necessary in order to have a reference on the properties of simple systems. Furthermore it is consistent with the current models of planetary interior, all done considering a pure iron core (e.g. Dorn et al., 2017; Wang et al., 2019).

Before the discovery of 55 Cancri e, silicon carbide had never been considered as possible main constituent of planetary interiors. The discovery of SiC grains with extra-terrestrial origin confirmed the possibility for reduced phases to be stabilized around specific stars (Zinner, 2007) and small inclusions also attest of this possibility in terrestrial contexts (e.g. Nazzareni et al., 2019). The solar system with its oxidizing nature did not support the existence of high amount of SiC. For this reason silicon carbide has often been considered as an "exotic" phase and its physical properties at high pressure and high temperature have never been investigated. The discovery of 55 Cancri e draw attention toward carbides and at the same time underlined the necessity of further investigation on this compound, in order to build reliable models of planetary interiors. The experimental study performed in this project provides for the first time a detailed characterization of SiC stability field, phase diagram and elastic properties.

The non-stoichiometry of the starting materials allows us to describe the binary Si-C phase diagram, shown in Figure 5.4, therefore to test the different dynamic scenarios associated to carbon or silicon enrichment in magma ocean. The differences within the solidus and liquidus temperatures in a silicon enriched versus carbon enriched system would be reflected in the crystallization mechanism. For a system with extensive crystallization, the expression relating viscosity with the crystal fraction has a maximum packing crystal fraction (Φ_m) parameter (viscosity is infinite when it is reached, as proposed by (Solomatov, 2007)). The crystal fraction in relation to Φ_m, is often use as a reference for the viscosity of the magma ocean.

At the initial stage the heat flow from the core induces thermal convection in the liquid magma ocean. In a convective magma ocean with low viscosity the melting curve is assumed to be steeper than the adiabat. When the two curves cross, the first crystals solidify at the bottom. When crystals start to nucleate and grow, the rate of the process, the density contrast between the solid and liquid phase and ultimately the temperature profile would determine the crystallization regime (Dumberry and Rivoldini, 2015; Solomatov, 2007). In the case of a denser solid phase, crystals sink and concentrate at the bottom of the layer. With cooling, the shift of the adiabat toward lower temperatures determines an increase of the solid layer thickness, thus reducing the volume stirred by thermal convection. Conversely, crystals with a lower density are buoyant and upwell with the convective regime potentially undergoing chemical equilibration, if the adiabat cross the liquidus at shallow depth. The possibility of having equilibration will also depend on the dissolution rate and the viscosity of the liquid.

Assuming a composition in the Si-C binary system to be the main component of a magma ocean, the differences visible in the phase diagram between the silicon and carbon rich side, would lead to extremely different crystallization paths and thermal evolution.

In the Si rich side, at the left of the eutectic, the first phase to solidify would be Si (Figure 5.4). The higher density of the crystals compared to the remaining liquid indicates a bottom up solidification style. Denser solid Si particles sink and form a bottom layer of increasing thickness, depleting the liquid in Si, until the adiabat reach the solidus temperature and also SiC start to crystallize.

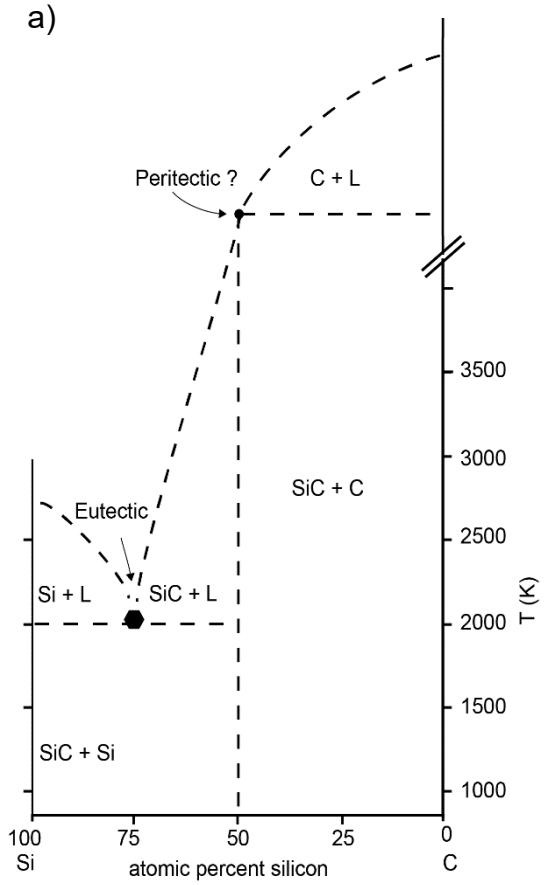

Figure 5.4: Binary Si-C phase diagram at 60 GPa determined in chapter 2. For higher carbon content the phase relations are extrapolated to higher temperature following the experiments of Turkevich et al. (2016).

Conversely, in the carbon rich side of the phase diagram, core will crystallize with a top down style. Due to the lower density, the newly formed crystals float toward the top and accrete as a graphite layer and compositional convection starts in the remaining liquid. During cooling, if the graphite layer become thick enough diamonds can form at the bottom and get eroded and involved in convection. Furthermore, the thermal evolution would be consistently different as diamonds start crystallizing at higher temperature than silicon. Finally, the crystallization process taking place if SiC is the first phase to crystallize, would be analogous to the process described for FeSi in the previous paragraph due to the similar density between the crystals and the remaining Si-rich liquid.

In a SiC mantle the B3-B1 phase transition determines the presence of a discontinuity that potentially affect the dynamic behaviour. In general, the presence of an endothermic phase transition can locally control the thermal state and dynamics of the mantle, for example with a layered convection (Christensen, 1995; Christensen and Yuen, 1985; Tackley et al., 1993). The interaction of the phase transition with the thermal flow is dictated by the magnitude of the Clapeyron slope and the density contrast between the phases (Tackley et al., 1993). The presence of a steep and negative Clapeyron slope associated to an important volume reduction, such as that of the SiC B3 B1 transition, makes it a good candidate to act as a thermal boundary and to induce two convective cells (Nisr et al., 2017). This idea finds support in the partial permeability to the thermal flow displayed by the 660 km discontinuity in the Earth mantle for example,

characterized by a density increase of 5% (Shearer and Flanagan, 1999). In a SiC mantle the phase transition yields a 10 % density change. Accordingly, the impact on the thermal state of the mantle is also expected to be important with a reduction of the thermal flow across the phase boundary, and the creation of two different convective cells (Figure 5.5).

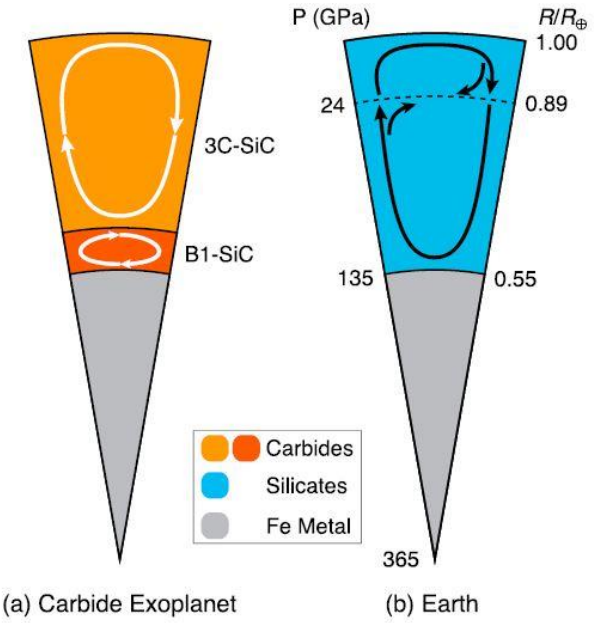

Figure 5.5: From Nisr et al. (2017), possible internal structure and dynamic for a carbide type planet (on the left side) compared with the one of the Earth (on the right side).

Furthermore, an estimate of the convection vigour using the Rayleigh number (defined as $Ra_H = \frac{\rho^2 g \alpha_V d^5 A}{K \eta k}$ where ρ is the initial density, g the gravitational acceleration, α_V the coefficient of thermal expansion, d the distance, A the heat production per unit mass, K the coefficient of thermal conductivity, η the dynamic viscosity and k the thermal diffusivity) suggests a low intensity convection, due to the high thermal conductivity compared to silicates (Li et al., 1998). Nevertheless, the uncertainties about the evolution of the parameters at high pressure in the equation deny the possibility of making precise estimates.

Using the Clapeyron slope and density jump determined in chapter 2, we numerically estimate the dynamic of a SiC mantle. Some parameters needed to estimate the Rayleigh are unfortunately unknown which number limits the possibility of running complex models. We thus decided to investigate how different values of viscosity jump and activation volume would affect the dynamic of such planet. Accordingly we map the onset of mantle convection for different initial temperatures. In collaboration with Antoine Rozel (ETH, Zurich) numerical simulations were performed for a planet of one Earth mass, with the B3-B1 transition occurring at 1830 km. The thermodynamic parameters determined in this

study and rheological data from Carter Jr. et al. (1984) were used and all the details regarding computations are provided in Appendix A.

Figure 5.6 summarises all the simulations results. Values of activation volume between 2×10^{-6} to 6×10^{-6} m^3/mol together with a viscosity jump from 0.1 to 100 were explored for three different mantle temperatures. For each temperature convection only start for low activation volume ($3 \cdot 10^{-6}$ to $6 \cdot 10^{-6}$ m^3/mol) compared to Earth material that has a common value ranging from $10\text{-}30 \cdot 10^{-6} m^3$/mol (Green and Borch, 1987; Karato and Jung, 2003). The viscosity jump seems to have little impact on convection as the boundary curves are vertical.

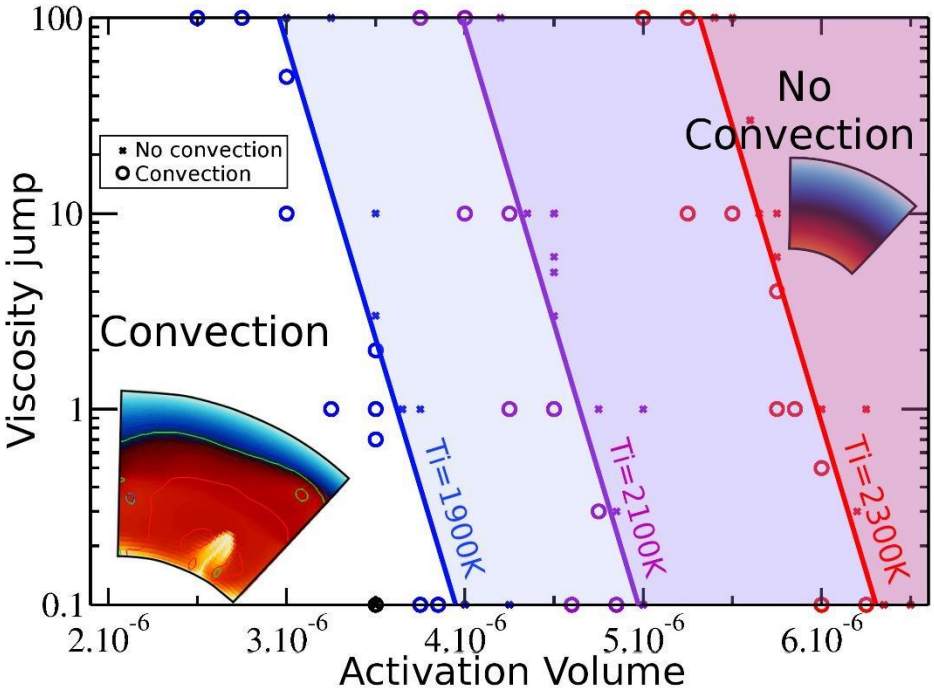

Figure 5.6: From Miozzi et al. (2018). Map of the onset of convection in all numerical simulations. Open circles show simulation in which convection started, and crosses show when convection never started. Blue, purple and red data represent cases with initial mantle potential temperature of 1900, 2100 and 2300 K respectively. Thick lines represent the regime boundary between convection and diffusion. The 2-D images show two examples of temperature field with convection (bottom left) or not (top right) in our computational domain. The isocontours show viscosities of η =1019 pa.s (red), η =1021 pa.s (green), and η =1023 pa.s (blue).

On the other hand, the onset of convection strongly depends on the activation volume of the non-Newtonian rheology and on the initial temperature after a potential magma ocean crystallisation. The activation volumes required for convection have been found to be lower by a factor 2 to 10 than typical values for Earth material. This result is very different from what is commonly accepted for the early Earth which certainly underwent solid-state convection right after its magma ocean stage. This fundamental difference in behaviour seems to be a consequence of the strong rheology of silicon carbide. Further investigation is clearly needed here for the sake of robustness.

After characterizing possible mechanisms of formation for a SiC mantle and the resulting geodynamics, it is important to determine how it affects the exoplanet's observables (i.e. mass and radius) thus establishing the link between mineral physics and astronomy. In collaboration with Caroline Dorn

(University of Zurich) the equations of state determined for the B3 and B1 structure of SiC, were used to model the mass radius curves for two different carbon rich exoplanets compositions. Results are shown in Figure 5.7 and details about the calculations are in Appendix B. Similar models have already been proposed in the past, usually plotting mass-radius relations for archetypal planets made entirely by one element (i.e., carbon or iron) or one compound (i.e., $MgSiO_3$, SiC, and H_2O) as in (Duffy et al., 2015). Here instead, we present the mass-radius curves for several idealized carbon-rich differentiated planets in which a pure iron core is assumed (EoS from Bouchet et al. (2013)) as Fe is considered one of the most abundant elements also for this type of planets.

In the first model of an Earth-like planet, the iron core makes up a third of the planet mass. In the second the proportions of Fe and SiC are chosen so as the bulk composition of the planet match the solar Fe/Si abundances (solar Fe/Si; Lodders (2003)). Extrapolations have been limited to 3.5 times the mass of the Earth for the 1/3 Fe core planet and 2.5 times the mass of the Earth for the solar Fe/Si ratio planet. As expected, the addition of iron to SiC contribute to increase the average density of the planet, with the curve for the solar Fe/Si plotting sensibly below the Earth-like curve. On the other hand, the Earth-like SiC planet displays an intermediate density between pure SiC and the solar Fe/Si, and is close to the M/R plot of the Earth. This modelling confirms that it is impossible (or difficult) to discriminate between

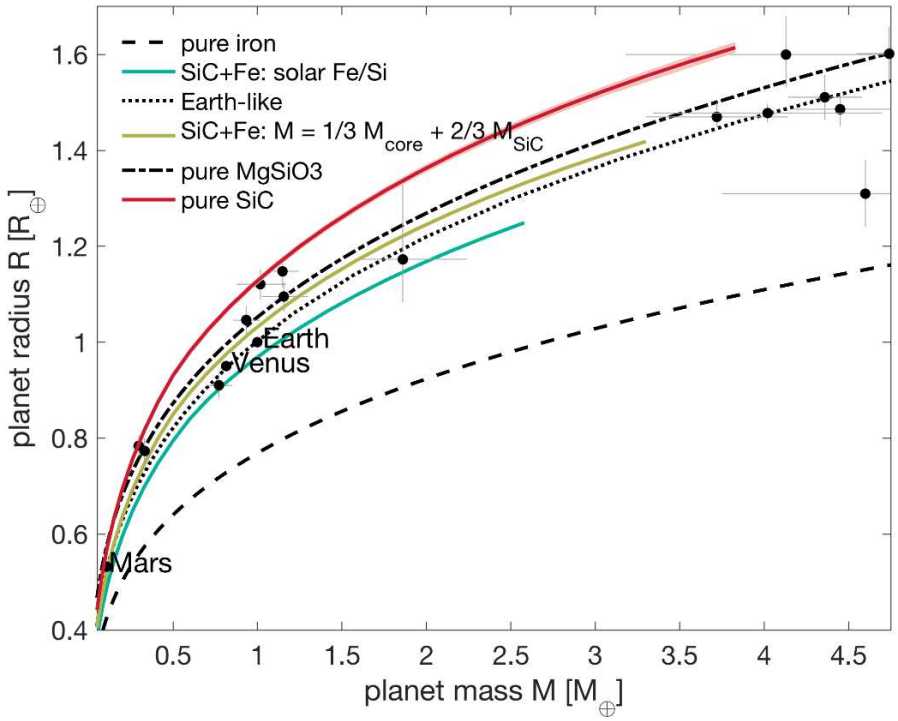

Figure 5.7: From Miozzi et al. (2018). Mass radius relations for different idealized exoplanet interiors together with the standard comparison curves (pure Fe, $MgSiO_3$ and Earth-like). We propose several C-rich end-members: a pure SiC planet, an core + SiC mantle planet with mass proportions similar to the Earth's core and mantle, and finally, an iron core + SiC mantle planet with a bulk ratio of Fe/Si that matches solar abundances. The black dots show the measured masses and radii for solar system planets and some observed exoplanets.

Earth-like planets and carbon rich exoplanets, from the sole mass-radius systematics. We stress the need for additional constraints to be used for better identification of the nature of such planets.

The resemblance of the plots, despite the different mantle compositions, confirms the strong correlation between the presence and characteristic of a core and the computed mass and radius, thus highlight the potential underestimation of exoplanets diversity if only average density keep being use as a reference.

It is important to notice that our carbon rich idealized planet is unlikely to occur in nature as Mg and O are expected to be present in exoplanets (Carter-Bond et al., 2012). Mg-O free end-members are important to provide limits on the bulk density and interpret possible interiors of observed exoplanets. However, neglecting Mg and O underestimate the mineralogical complexity of the forming planet, the potential effect on dynamic and ultimately habitability. Hypothetically, a planet forming from a Fe-Si-C-Mg-O enriched nebula will have an iron enriched core, alloyed with Si and/or C and/or O and a magnesium richer mantle with the residual light elements. The interaction between the cooling core and the mantle then would be different depending on the composition and physical state of the two layers at the core mantle boundary. On the core side, in the higher Si-C and Fe-C compositional domain (Figure 5.1), crystallization of low density phases would determine the presence of a solid layer at the interface. On the other hand, for the Fe-Si and Fe enriched compositional domains a liquid would be present on the core side of the core mantle boundary. On the mantle side assuming a Mg, C, Si, O composition oxygen fugacity would be the main discriminant for the chemistry and the physical state as it determine the equilibrium between oxidising and reducing phases. The solid liquid partition coefficient will then play a fundamental role in core mantle interactions. The effects of different carbon content on the dynamic of a planet were discussed in a general sense by Unterborn et al. (2014). The calculated models point out the importance of knowing the stable mineral phases and their properties to determine the habitability of a planet, thus highlighting the importance of oxygen fugacity.

A first study performed by Hakim et al. (2019) on starting compositions consistent with carbon enriched small planetesimals retrieve an oxygen fugacity corresponding to (IW-0.3 < log fO_2 < IW-1.2). Accordingly the experimental products only display the formation of graphite only as reduced phase.

On the other hand, highly reducing phases such as silicon carbides, FeSiC alloys and FeSi have been retrieved in terrestrial and extra-terrestrial contexts (e.g. Golubkova et al., 2016; Nazzareni et al., 2019; Zinner, 2007). Hence with the existence of specific conditions, naturally occurring reaction can lead to the formation of reduced phases in oxidised environment (Dorfman et al., 2018; Schmidt et al., 2014).

Considering the variability of the observed exoplanets compositions, constraining the mineral properties of all the possible forming phases become fundamental to improve the calculated models. The phase stability and relations in complex multiphase systems need to be addressed at conditions representative of super Earth's interior and not only small planetary bodies.

Chapter 6

Conclusions

Following the debate about the potential existence of carbon enriched planets, we approached the topic from an experimental point of view studying two representative systems, the binary Si-C and the ternary Fe-Si-C. We used synchrotron X-ray diffraction coupled with laser heated diamond anvil cell to perform experiments in the P-T range between 20-200 GPa and 300-4000 K. Recovered samples were analysed by electron microscopy techniques for a textural and mineralogical study. For each system, three or more different stoichiometries were investigated.

We have performed measurements on several alloys in the Fe-Si-C compositional space. Increasing the amount of light elements in the starting material induces a change in mineralogical assemblage stable at high pressure and high temperature. From hcp Fe + Fe_3C for low light elements content, it evolves to FeSi + Fe_7C_3 + SiC/C for higher light elements content, with SiC/C identified with SEM analyses made on the recovered samples. The P-V data at ambient temperature obtained for all the samples were compared with those from pure Fe and the Fe-Si and Fe-C binary systems. Hcp Fe in $FeSi_3C_3$ was observed to host both Si (~ 3 at %) and C (1-4 at %), with carbon occupying interstitial positions compared to silicon that is expected in substitution. FeSi was also observed to host carbon. In $FeSi_{20}C_{10}$ incorporation is attested by the exsolution of carbides only at high pressure, and a similar behaviour is observed for $FeSi_6C_5$, where carbides exsolves at low pressure. It is however difficult to say if FeSi host carbon in $FeSi_{10}C_{20}$. FeSi B2 volumes change as a function Si content in the sample. As carbon is also present in the structure, deconvolution between Si and C effects is not (yet) possible with our dataset. The P-V data obtained for Fe_3C and Fe_7C_3 are in overall agreement with those obtained in literature (Chen et al., 2012; Litasov et al., 2013; Nakajima et al., 2011), thus potentially excluding large incorporation of silicon in Fe_7C_3.

At the pressure of 50 GPa the melting temperature of $FeSi_3C_3$ (2300 K) is lower than the temperature measures for the other samples, advocating for the presence of a peritectic in analogy with the prediction of Lord et al. (2009) on the binary Fe-C system. All the obtained data were analysed together as so to define for the first time the evolution in temperature of the ternary FeSiC. We thus provide insights about possible core's composition and crystallisation processes for carbon rich exoplanets cores.

The axial compressibility of Fe_3C was measured and shows an inversion at 60 GPa, consistent with the magnetic transition supported by Ono and Mibe (2010). The proposed thermal EoS represent the first determination of the EoS for Fe_3C in such a wide pressure range. The axial ratio a/c determined for Fe_7C_3 shows a bending that is consistent with that observed by Chen et al. (2012) and Prescher et al.

(2015). The thermal EoS of this non-magnetic phase refined with the P-V-T data for $FeSi_{10}C_{20}$ up to 140 GPa represents first determinations as well.

The P-V-T data collected for hcp Fe (+Si, +C) show a smaller thermal expansion compared to the thermal EoS proposed by Fei et al. (2016). An overestimation of the thermal expansion determines an underestimation of the density also affecting the extrapolations at higher pressures. For $FeSi_3C_3$ also, its densities extrapolated at high pressure by ab initio calculation (Li et al., 2018) display a lower density compared to our experimental data. This difference may arise from difficulties for computation to reproduce the configurational disorder deriving from the low light elements content in the structure. Finally, we had difficulties with the P-V-T data of FeSi to find a reliable parametrisation to describe the high pressure and temperature behaviour of iron and iron alloys.

In the Si-C system, we propose an accurate mapping of the P-T phases, with the collection of multiple coexistence points of the zinc-blende and rock-salt structures. These points unambiguously locate the transition in pressure and temperature, establishing the Clapeyron slope. The extension of the P-T mapping and the favourable provided by our specific PVD samples place our work as the experimental reference for the B3-B1 transition in SiC. The trend is in agreement with the equilibrium calculations of Daviau and Lee (2017b) and observed in Kidokoro et al. (2017), although pressures differ in the latter. With the P-V-T dataset, we determined the thermal equation of state for the low pressure B3 structure, and propose for the first time the thermal equation of state for the high pressure B1 structure of SiC, needed to compute mass radius plots of synthetic planets. The parameters, obtained with a Thermal Pressure model (Angel et al., 2017 and references therein) confirms the ability of such model to describe the behaviour for such rigid compounds. Finally we prove the existence of an eutectic point at higher silicon content, unlike what was predicted by Turkevich et al. (2016). We also confirm the stability of SiC up to 4000 K at 60 GPa, in contrast with Daviau and Lee,2(017a) that predicted a decomposition of SiC into Si + C. These results are important for modelling planetary interiors not only in term of mass and radius but also dynamics. The mass radius curve for a carbon enriched planet made by an iron core occupying 1/3 of the mass and a SiC mantle plot on the curve corresponding to the Earth.

The overlap of the mass radius curve for a carbon enriched planet with the one of an Earth-like planet highlights the difficulty to distinguish them from the M/R plot. Hence, using such plot to interpret the data coming from astrophysical observations can lead to an underestimation of the variability of exoplanets interiors. Elemental abundances of the planetary systems are thus needed and this also includes a better understanding of the correlation between relative bulk elemental abundances of planets and their host stars (Wang et al., 2019 and references therein).

An effort should be done to improve the available models by increasing the variability of the considered chemical species. This is valid especially for planetary cores, where composition strongly affects the mass radius plot and the evolution of the planet. In this frame, our results on the Fe-Si-C system provide

a comprehensive study of the ternary phase diagram placing major constrains useful to estimate the potential composition of a core and its crystallisation process. Our data increase the variability of planetary cores that is possible to model thus including two light elements that together with iron are considered as important building block of planetary systems. Despite the revision downward on the C/O for many carbon enriched composition (Teske et al., 2013), carbon needs to be taken in consideration as a possible light element in planetary cores, as well as silicon, in order to address the potential variability of exoplanets interior. The starting composition has a fundamental role in determining the chemical make-up as well as the dynamical processes taking place in the forming core, which have strong implications for having a dynamo operating, hence a magnetic field. As magnetic fields stop atmospheres from being blown off planets (a scenario that is invoked for Mars for instance), the core composition is needed to evaluate the potential habitability of the planet surface. Finally, considering the number of future missions and the way higher number of discovered exoplanets, there will be the need of selecting targets were to focus the investigative effort. Accordingly being able to clearly identify planets not suitable for further investigation with a method of "negative feedback" is important as well.

Perspectives

The first fundamental requirements for better constraining our experimental dataset will be to accurately measure the chemical composition of the stable mineralogical assemblages for the different starting materials at variable P-T conditions in the Fe-Si-C system. The phenomenological description performed here needs the support of accurate compositions, so as to parametrize a complete and consistent thermodynamic model. During the limited time of my PhD, we struggled to determine a protocol allowing carbon measurements in diamond anvil cell samples. In the last months, we finally established a suitable protocol with the support of Camparis analytical platform, as highlighted by the composition determined on the starting materials. In the next months, we will work to extend this protocol to diamond anvil cell samples. Following the P-T conditions of *in situ* experiments, we will repeat these experiments with the laser heating system available at IMPMC and directly proceed with the cut and analysis of the samples. Furthermore, TEM analyses will be taken in consideration to discern the exact nature of the observed black spot.

The second step will be to apply the obtained dataset to the diversity of exoplanets interiors. In collaboration with Caroline Dorn from the University of Zurich, we expect to apply the complete data set to exoplanets interior. It will be interesting to determine the variability of core size in function of the composition and how it affect the mass radius curve.

Regarding carbon enriched exoplanets, the Fe-Si-C system is mainly representative of planetary cores. The absence of Mg and O makes our modelled synthetic planet an endmember, an archetypal planet useful to constrain the bulk density. From the experimental point of view, we choose to start with the smallest number of variable and increase the complexity of the system step by step. The uncertainties

related to the evolution in pressure and temperature of the ternary Fe-Si-C phase diagram, as well as the lack of high pressure studies on SiC (it is important to notice that all the recent papers published on SiC (Daviau and Lee, 2017b, 2017a; Kidokoro et al., 2017; Nisr et al., 2017), were published during the first year of this project) required to start from simple systems. The addition of magnesium as well as oxygen will increase the complexity of the system.

As we mentioned, the amount of oxygen available in the system (i.e. oxygen fugacity) is of fundamental importance for planetary evolution. The use of non-equilibrium PVD deposition of compounds in the Fe-Si-C-Mg-O and performing a high pressure and temperature study as for Fe-Si-C, will provide the solubility limits between elements, determine the phase relations and establish the quantity of carbon and oxygen in term of C/O ratio. Investigating different composition would potentially give the possibility of determining the threshold that separate the formation of carbonates and carbides. A similar study was already carried out at pressures below 5 GPa by Takahashi et al. (2013), in a multi anvil press. Extending this work to higher pressures and mapping the compositional space to establish how the composition of the metallic phase change in function of pressure related to the oxidation state of the system would be primordial for carbon-rich planetary interiors. The possibility to form a large amount of reduced phases would be quite interesting in term of application to exoplanets interior.

For example, the possibility of stabilizing reducing phases like Fe_7C_3 and diamond has been already observed by (Dorfman et al., 2018) in the experimental study related to Earth lower mantle, with the evaluation the interaction of a subducting carbonate assemblage with pure iron. In an assemblage made by an iron foil sandwiched into carbonates crystals, the redox coupling between iron and the carbonate leads to the breakdown of carbonate and produces a mixture of iron carbide, diamond, oxide and a calcium carbonate.

Finally, the most recent efforts are directed to detect and analyse exoplanets atmospheres. It will be important to predict the expected atmosphere compositions for different planetary interiors, in order to have references to use for the interpretation of future observations. However, the possibility of forming and maintaining an atmosphere is tightly linked with the properties of the interior. From the characteristics of the core, potentially forming a magnetic field, to the existence of tectonics that recycle elements from the surface to the interior. It makes sense to start with Earth-like planets, since our curiosity toward detecting an analogue of the Earth, but end-member composition are important as well. It is thus priority to constrain and investigate, through experiments and computations, those factors that affect habitability the most.

References

(SGTE), 2012. Ternary System C-Fe-Si, in: Ternary Steel Systems: Phase Diagrams and Phase Transition Data. Springer Berlin Heidelberg, Berlin, Heidelberg, pp. 189–201. https://doi.org/10.1007/978-3-540-88142-1_69

Adibekyan, V., 2019. Heavy Metal Rules. I. Exoplanet Incidence and Metallicity. Geosciences 9, 105. https://doi.org/10.3390/geosciences9030105

Ali-Dib, M., Mousis, O., Petit, J.-M., Lunine, J.I., 2014. Carbon-Rich Planet Formation in a Solar Composition Disk. Astrophys. J. 785, 125. https://doi.org/10.1088/0004-637X/785/2/125

An Astrobiology Strategy for the Search for Life in the Universe, 2019. . National Academies Press, Washington, D.C. https://doi.org/10.17226/25252

Anders, E., Grevesse, N., 1989. Abundances of the elements: Meteoritic and solar. Geochim. Cosmochim. Acta 53, 197–214. https://doi.org/10.1016/0016-7037(89)90286-X

Anders, E., Zinner, E., 1993. Interstellar Grains in Primitive Meteorites: Diamond, Silicon Carbide, and Graphite. Meteoritics 28, 490–514. https://doi.org/10.1111/j.1945-5100.1993.tb00274.x

Anderson, O.L., 1984. A universal thermal equation-of-state. J. Geodyn. 1, 185–214. https://doi.org/10.1016/0264-3707(84)90027-9

Anderson, O.L., Lee, P.A., 1995. Equations of state of solids for geophysics and ceramic science. Oxford University Press on Demand.

Andrault, D., Morard, G., Bolfan-Casanova, N., Ohtaka, O., Fukui, H., Arima, H., Guignot, N., Funakoshi, K., Lazor, P., Mezouar, M., 2006. Study of partial melting at high-pressure using in situ X-ray diffraction. High Press. Res. 26, 267–276. https://doi.org/10.1080/08957950600897013

Andrew, R.C., Braun, M., Chetty, N., 2012. A theoretical investigation of the stability of crystalline silicon dicarbide. Comput. Mater. Sci. 55, 186–191. https://doi.org/10.1016/j.commatsci.2011.10.040

Angel, R.J., 2000. Equations of State. Rev. Mineral. geochemistry 35–59. https://doi.org/10.1007/978-3-642-01014-9

Angel, R.J., Alvaro, M., Miletich, R., Nestola, F., 2017. A simple and generalised P–T–V EoS for continuous phase transitions, implemented in EosFit and applied to quartz. Contrib. to Mineral. Petrol. 172, 29. https://doi.org/10.1007/s00410-017-1349-x

Angel, R.J., Alvaro, M., Nestola, F., 2018. 40 years of mineral elasticity: a critical review and a new

parameterisation of equations of state for mantle olivines and diamond inclusions. Phys. Chem. Miner. 45, 95–113. https://doi.org/10.1007/s00269-017-0900-7

Angel, R.J., Alvaro, M., Nestola, F., Mazzucchelli, M.L., 2015. Diamond thermoelastic properties and implications for determining the pressure of formation of diamond-inclusion systems. Russ. Geol. Geophys. 56, 211–220. https://doi.org/10.1016/j.rgg.2015.01.014

Angel, R.J., Gonzalez-Platas, J., Alvaro, M., 2014. EosFit7c and a Fortran module (library) for equation of state calculations. Zeitschrift fur Krist. 229, 405–419. https://doi.org/10.1515/zkri-2013-1711

Anzellini, S., Dewaele, A., Mezouar, M., Loubeyre, P., Morard, G., 2013. Melting of Iron at Earth's Inner Core Boundary Based on Fast X-ray Diffraction. Science (80-.). 340, 464–466. https://doi.org/10.1126/science.1233514

Anzellini, S., Wharmby, M.T., Miozzi, F., Kleppe, A., Daisenberger, D., Wilhelm, H., n.d. Quasi-hydrostatic equation of state of Si up to 1 Mbar at ambient temperature. Submitted to Phys. Rev. B.

Aquilanti, G., Trapananti, A., Karandikar, A., Kantor, I., Marini, C., Mathon, O., Pascarelli, S., Boehler, R., 2015. Melting of iron determined by X-ray absorption spectroscopy to 100 GPa. Proc. Natl. Acad. Sci. 112, 12042–12045. https://doi.org/10.1073/pnas.1502363112

Asplund, M., Grevesse, N., Sauval, A.J., 2005. Cosmic Abundances as Records of Stellar Evolution and Nucleosynthesis in honor of The Solar Chemical Composition. ASP Conf. Ser. 336.

Asplund, M., Grevesse, N., Sauval, A.J., Scott, P., 2009. The Chemical Composition of the Sun. Annu. Rev. Astron. Astrophys. 47, 481–522. https://doi.org/10.1146/annurev.astro.46.060407.145222

Badro, J., Brodholt, J.P., Piet, H., Siebert, J., Ryerson, F.J., 2015. Core formation and core composition from coupled geochemical and geophysical constraints. Proc. Natl. Acad. Sci. 112, 12310–12314. https://doi.org/10.1073/pnas.1505672112

Badro, J., Cote, A.S., Brodholt, J.P., 2014. A seismologically consistent compositional model of Earth's core. Proc. Natl. Acad. Sci. 111, 7542–7545. https://doi.org/10.1073/pnas.1316708111

Balerna, A., Mobilio, S., 2015. Introduction to Synchrotron Radiation, in: Synchrotron Radiation. Springer Berlin Heidelberg, Berlin, Heidelberg, pp. 3–28. https://doi.org/10.1007/978-3-642-55315-8_1

Baraffe, I., Chabrier, G., Fortney, J., Sotin, C., 2014. Planetary Internal Structures. Protostars Planets VI. https://doi.org/10.2458/azu_uapress_9780816531240-ch033

Benedetti, L.R., Loubeyre, P., 2004. Temperature gradients, wavelength-dependent emissivity, and accuracy of high and very-high temperatures measured in the laser-heated diamond cell. High

Press. Res. 24, 423–445. https://doi.org/10.1080/08957950412331331718

Bernatowicz, T., Fraundorf, G., Ming, T., Anders, E., Wopenka, B., Zinner, E., Fraundorf, P., 1987. Evidence for interstellar SiC in the Murray carbonaceous meteorite. Nature 330, 728–730. https://doi.org/10.1038/330728a0

Bernatowicz, T.J., Walker, R.M., 1997. Ancient Stardust in the Laboratory. Phys. Today 50, 26–32. https://doi.org/10.1063/1.882049

Boehler, R., 2000. Laser heating in the diamond cell: Techniques and applications. Hyperfine Interact. 128, 307–321. https://doi.org/10.1023/A:1012648019016

Boehler, R., De Hantsetters, K., 2004. New anvil designs in diamond-cells. High Press. Res. 24, 391–396. https://doi.org/10.1080/08957950412331323924

Boehler, R., Ross, M., Boercker, D.B., 1996. High-pressure melting curves of alkali halides. Phys. Rev. B 53, 556–563. https://doi.org/10.1103/PhysRevB.53.556

Boehler, R., von Bargen, N., Chopelas, A., 1990. Melting, thermal expansion, and phase transitions of iron at high pressures. J. Geophys. Res. 95, 21731. https://doi.org/10.1029/JB095iB13p21731

Bogner, A., Jouneau, P.-H., Thollet, G., Basset, D., Gauthier, C., 2007. A history of scanning electron microscopy developments: Towards “wet-STEM” imaging. Micron 38, 390–401. https://doi.org/10.1016/j.micron.2006.06.008

Bond, J.C., Lauretta, D.S., Tinney, C.G., Butler, R.P., Marcy, G.W., Jones, H.R.A., Carter, B.D., O’Toole, S.J., Bailey, J., 2008. Beyond the Iron Peak: r - and s -Process Elemental Abundances in Stars with Planets. Astrophys. J. 682, 1234–1247. https://doi.org/10.1086/589236

Bond, J.C., O’Brien, D.P., Lauretta, D.S., 2010. THE COMPOSITIONAL DIVERSITY OF EXTRASOLAR TERRESTRIAL PLANETS. I. IN SITU SIMULATIONS. Astrophys. J. 715, 1050–1070. https://doi.org/10.1088/0004-637X/715/2/1050

Bond, J.C., Tinney, C.G., Butler, R.P., Jones, H.R.A., Marcy, G.W., Penny, A.J., Carter, B.D., 2006. The abundance distribution of stars with planets. Mon. Not. R. Astron. Soc. 370, 163–173. https://doi.org/10.1111/j.1365-2966.2006.10459.x

Borucki, W.J., Koch, D., Basri, G., Batalha, N., Brown, T., Caldwell, D., Caldwell, J., Christensen-Dalsgaard, J., Cochran, W.D., DeVore, E., Dunham, E.W., Dupree, A.K., Gautier, T.N., Geary, J.C., Gilliland, R., Gould, A., Howell, S.B., Jenkins, J.M., Kondo, Y., Latham, D.W., Marcy, G.W., Meibom, S., Kjeldsen, H., Lissauer, J.J., Monet, D.G., Morrison, D., Sasselov, D., Tarter, J., Boss, A., Brownlee, D., Owen, T., Buzasi, D., Charbonneau, D., Doyle, L., Fortney, J., Ford, E.B., Holman, M.J., Seager, S., Steffen, J.H., Welsh, W.F., Rowe, J., Anderson, H., Buchhave, L.,

Ciardi, D., Walkowicz, L., Sherry, W., Horch, E., Isaacson, H., Everett, M.E., Fischer, D., Torres, G., Johnson, J.A., Endl, M., MacQueen, P., Bryson, S.T., Dotson, J., Haas, M., Kolodziejczak, J., Van Cleve, J., Chandrasekaran, H., Twicken, J.D., Quintana, E. V., Clarke, B.D., Allen, C., Li, J., Wu, H., Tenenbaum, P., Verner, E., Bruhweiler, F., Barnes, J., Prsa, A., 2010. Kepler Planet-Detection Mission: Introduction and First Results. Science (80-.). 327, 977–980. https://doi.org/10.1126/science.1185402

Borucki, W.J., Koch, D.G., Basri, G., Batalha, N., Boss, A., Brown, T.M., Caldwell, D., Christensen-Dalsgaard, J., Cochran, W.D., Devore, E., Dunham, E.W., Dupree, A.K., Gautier, T.N., Geary, J.C., Gilliland, R., Gould, A., Howell, S.B., Jenkins, J.M., Kjeldsen, H., Latham, D.W., Lissauer, J.J., Marcy, G.W., Monet, D.G., Sasselov, D., Tarter, J., Charbonneau, D., Doyle, L., Ford, E.B., Fortney, J., Holman, M.J., Seager, S., Steffen, J.H., Welsh, W.F., Allen, C., Bryson, S.T., Buchhave, L., Chandrasekaran, H., Christiansen, J.L., Ciardi, D., Clarke, B.D., Dotson, J.L., Endl, M., Fischer, D., Fressin, F., Haas, M., Horch, E., Howard, A., Isaacson, H., Kolodziejczak, J., Li, J., Macqueen, P., Meibom, S., Prsa, A., Quintana, E. V., Rowe, J., Sherry, W., Tenenbaum, P., Torres, G., Twicken, J.D., Van Cleve, J., Walkowicz, L., Wu, H., 2011. Characteristics of Kepler planetary candidates based on the first data set. Astrophys. J. 728. https://doi.org/10.1088/0004-637X/728/2/117

Borucki, W.J., Summers, A.L., 1984. The photometric method of detecting other planetary systems. Icarus 58, 121–134. https://doi.org/10.1016/0019-1035(84)90102-7

Bouchet, J., Mazevet, S., Morard, G., Guyot, F., Musella, R., 2013. Ab initio equation of state of iron up to 1500 GPa. Phys. Rev. B - Condens. Matter Mater. Phys. 87, 1–8. https://doi.org/10.1103/PhysRevB.87.094102

Breuer, D., Rueckriemen, T., Spohn, T., 2015. Iron snow, crystal floats, and inner-core growth: modes of core solidification and implications for dynamos in terrestrial planets and moons. Prog. Earth Planet. Sci. 2, 39. https://doi.org/10.1186/s40645-015-0069-y

Buchhave, L.A., Bizzarro, M., Latham, D.W., Sasselov, D., Cochran, W.D., Endl, M., Isaacson, H., Juncher, D., Marcy, G.W., 2014. Three regimes of extrasolar planet radius inferred from host star metallicities. Nature 509, 593–595. https://doi.org/10.1038/nature13254

Buchhave, L.A., Latham, D.W., Johansen, A., Bizzarro, M., Torres, G., Rowe, J.F., Batalha, N.M., Borucki, W.J., Brugamyer, E., Caldwell, C., Bryson, S.T., Ciardi, D.R., Cochran, W.D., Endl, M., Esquerdo, G.A., Ford, E.B., Geary, J.C., Gilliland, R.L., Hansen, T., Isaacson, H., Laird, J.B., Lucas, P.W., Marcy, G.W., Morse, J.A., Robertson, P., Shporer, A., Stefanik, R.P., Still, M., Quinn, S.N., 2012. An abundance of small exoplanets around stars with a wide range of metallicities. Nature 486, 375–377. https://doi.org/10.1038/nature11121

Burrows, A., Hubeny, I., Budaj, J., Hubbard, W.B., 2007. Possible Solutions to the Radius Anomalies of Transiting Giant Planets. Astrophys. J. 661, 502–514. https://doi.org/10.1086/514326

Cameron, A.G.W., 2001. From interstellar gas to the Earth-Moon system. Meteorit. Planet. Sci. 36, 9–22. https://doi.org/10.1111/j.1945-5100.2001.tb01806.x

Campbell, A.J., Danielson, L., Righter, K., Seagle, C.T., Wang, Y., Prakapenka, V.B., 2009. High pressure effects on the iron-iron oxide and nickel-nickel oxide oxygen fugacity buffers. Earth Planet. Sci. Lett. 286, 556–564. https://doi.org/10.1016/j.epsl.2009.07.022

Campbell, A.J., Seagle, C.T., Heinz, D.L., Shen, G., Prakapenka, V.B., 2007. Partial melting in the iron–sulfur system at high pressure: A synchrotron X-ray diffraction study. Phys. Earth Planet. Inter. 162, 119–128. https://doi.org/10.1016/j.pepi.2007.04.001

Caracas, R., 2017. The influence of carbon on the seismic properties of solid iron. Geophys. Res. Lett. 44, 128–134. https://doi.org/10.1002/2016GL071109

Carter-Bond, J.C., O'Brien, D.P., Raymond, S.N., 2012. THE COMPOSITIONAL DIVERSITY OF EXTRASOLAR TERRESTRIAL PLANETS. II. MIGRATION SIMULATIONS. Astrophys. J. 760, 44. https://doi.org/10.1088/0004-637X/760/1/44

Carter Jr., C.H., Davis, R.F., Bentley, J., 1984. Kinetics and mechanisms of high-temperature creep in silicon carbide. 1: Reaction-bonded. J. Amer. Ceram. Soc. 67, 409–417.

Catti, M., 2001. Orthorhombic intermediate state in the zinc blende to rocksalt transformation path of SiC at high pressure. Phys. Rev. Lett. 87, 035504. https://doi.org/10.1103/PhysRevLett.87.035504

Chang, K.J., Cohen, M.L., 1987. Ab initio pseudopotential study of structural and high-pressure properties of SiC. Phys. Rev. B 35, 8196–8201. https://doi.org/10.1103/PhysRevB.35.8196

Chavanne, J., Elleaume, P., Van Vaerenbergh, P., 1998. The ESRF insertion devices. J. Synchrotron Radiat. 5, 196–201. https://doi.org/10.1107/S0909049597012855

Chen, B., Gao, L., Lavina, B., Dera, P., Alp, E.E., Zhao, J., Li, J., 2012. Magneto-elastic coupling in compressed Fe 7 C 3 supports carbon in Earth's inner core. Geophys. Res. Lett. 39, 2–5. https://doi.org/10.1029/2012GL052875

Chen, B., Li, Z., Zhang, D., Liu, J., Hu, M.Y., Zhao, J., Bi, W., Alp, E.E., Xiao, Y., Chow, P., Li, J., 2014. Hidden carbon in Earth's inner core revealed by shear softening in dense Fe 7 C 3. Proc. Natl. Acad. Sci. 111, 17755–17758. https://doi.org/10.1073/pnas.1411154111

Chen, L., Xu, J., Chen, J., 2015. Applications of scanning electron microscopy in earth sciences. Sci. China Earth Sci. 58, 1768–1778. https://doi.org/10.1007/s11430-015-5172-9

Christensen, U., 1995. Effects of Phase Transitions on Mantle Convection. Annu. Rev. Earth Planet. Sci. 23, 65–87. https://doi.org/10.1146/annurev.ea.23.050195.000433

Christensen, U.R., Yuen, D.A., 1985. Layered convection induced by phase transitions. J. Geophys. Res. 90, 10291. https://doi.org/10.1029/JB090iB12p10291

Clayton, D.D., 1988. Isotopic anomalies - Chemical memory of Galactic evolution. Astrophys. J. 334, 191. https://doi.org/10.1086/166829

Correa, A.A., Bonev, S.A., Galli, G., 2006. Carbon under extreme conditions: Phase boundaries and electronic properties from first-principles theory. Proc. Natl. Acad. Sci. 103, 1204–1208. https://doi.org/10.1073/pnas.0510489103

Das, T., Chatterjee, S., Ghosh, S., Saha-Dasgupta, T., 2017. First-principles prediction of Si-doped Fe carbide as one of the possible constituents of Earth's inner core. Geophys. Res. Lett. 44, 8776–8784. https://doi.org/10.1002/2017GL073545

Dasgupta, R., 2013. Ingassing, Storage, and Outgassing of Terrestrial Carbon through Geologic Time. Rev. Mineral. Geochemistry 75, 183–229. https://doi.org/10.2138/rmg.2013.75.7

Datchi, F., LeToullec, R., Loubeyre, P., 1997. Improved calibration of the SrB4O7:Sm2+optical pressure gauge: Advantages at very high pressures and high temperatures. J. Appl. Phys. 81, 3333–3339. https://doi.org/10.1063/1.365025

Daviau, K., Lee, K., 2018. High-Pressure, High-Temperature Behavior of Silicon Carbide: A Review. Crystals 8, 217. https://doi.org/10.3390/cryst8050217

Daviau, K., Lee, K.K.M., 2017a. Decomposition of silicon carbide at high pressures and temperatures. Phys. Rev. B 96, 174102. https://doi.org/10.1103/PhysRevB.96.174102

Daviau, K., Lee, K.K.M., 2017b. Zinc-blende to rocksalt transition in SiC in a laser-heated diamond-anvil cell. Phys. Rev. B 95, 1–6. https://doi.org/10.1103/PhysRevB.95.134108

Decker, D.L., Bassett, W.A., Merrill, L., Hall, H.T., Barnett, J.D., 1972. High Pressure Calibration: A Critical Review. J. Phys. Chem. Ref. Data 1, 773–836. https://doi.org/10.1063/1.3253105

Delgado Mena, E., Israelian, G., González Hernández, J.I., Bond, J.C., Santos, N.C., Udry, S., Mayor, M., 2010. CHEMICAL CLUES ON THE FORMATION OF PLANETARY SYSTEMS: C/O VERSUS Mg/Si FOR HARPS GTO SAMPLE. Astrophys. J. 725, 2349–2358. https://doi.org/10.1088/0004-637X/725/2/2349

Dewaele, A., Belonoshko, A.B., Garbarino, G., Occelli, F., Bouvier, P., Hanfland, M., Mezouar, M., 2012. High-pressure–high-temperature equation of state of KCl and KBr. Phys. Rev. B 85, 214105. https://doi.org/10.1103/PhysRevB.85.214105

Dewaele, A., Datchi, F., Loubeyre, P., Mezouar, M., 2008a. High pressure–high temperature equations of state of neon and diamond. Phys. Rev. B 77, 094106. https://doi.org/10.1103/PhysRevB.77.094106

Dewaele, A., Loubeyre, P., Mezouar, M., 2004. Equations of state of six metals above 94 GPa. Phys. Rev. B - Condens. Matter Mater. Phys. 70, 1–8. https://doi.org/10.1103/PhysRevB.70.094112

Dewaele, A., Loubeyre, P., Occelli, F., Marie, O., Mezouar, M., 2018. Toroidal diamond anvil cell for detailed measurements under extreme static pressures. Nat. Commun. 9, 2913. https://doi.org/10.1038/s41467-018-05294-2

Dewaele, A., Loubeyre, P., Occelli, F., Mezouar, M., Dorogokupets, P.I., Torrent, M., 2006. Quasihydrostatic Equation of State of Iron above 2 Mbar. Phys. Rev. Lett. 97, 215504. https://doi.org/10.1103/PhysRevLett.97.215504

Dewaele, A., Torrent, M., Loubeyre, P., Mezouar, M., 2008b. Compression curves of transition metals in the Mbar range: Experiments and projector augmented-wave calculations. Phys. Rev. B - Condens. Matter Mater. Phys. 78, 1–13. https://doi.org/10.1103/PhysRevB.78.104102

Di Pierro, S., Gnos, E., Grobety, B.H., Armbruster, T., Bernasconi, S.M., Ulmer, P., 2003. Rock-forming moissanite (natural α-silicon carbide). Am. Mineral. 88, 1817–1821. https://doi.org/10.2138/am-2003-11-1223

Dobrzhinetskaya, L., Mukhin, P., Wang, Q., Wirth, R., O'Bannon, E., Zhao, W., Eppelbaum, L., Sokhonchuk, T., 2018. Moissanite (SiC) with metal-silicide and silicon inclusions from tuff of Israel: Raman spectroscopy and electron microscope studies. Lithos 310–311, 355–368. https://doi.org/10.1016/j.lithos.2017.04.001

Dolloff, R.T., 1960. Research study to determine the phase equilibrium relations of selected metal carbides at high temperatures, Wadd Technical Report.

Dong, C., Jin, M., Lingam, M., Airapetian, V.S., Ma, Y., van der Holst, B., 2018. Atmospheric escape from the TRAPPIST-1 planets and implications for habitability. Proc. Natl. Acad. Sci. 115, 260–265. https://doi.org/10.1073/pnas.1708010115

Dong, C., Lingam, M., Ma, Y., Cohen, O., 2017. Is Proxima Centauri b Habitable? A Study of Atmospheric Loss. Astrophys. J. 837, L26. https://doi.org/10.3847/2041-8213/aa6438

Dorfman, S.M., Badro, J., Nabiei, F., Prakapenka, V.B., Cantoni, M., Gillet, P., 2018. Carbonate stability in the reduced lower mantle. Earth Planet. Sci. Lett. 489, 84–91. https://doi.org/10.1016/j.epsl.2018.02.035

Dorn, C., Khan, A., Heng, K., Alibert, Y., Connolly, J.A.D., Benz, W., Tackley, P., 2015. Can we

constrain interior structure of rocky exoplanets from mass and radius measurements? Astron. Astrophys. 83. https://doi.org/10.1051/0004-6361/201424915

Dorn, C., Noack, L., Rozel, A.B., 2018. Outgassing on stagnant-lid super-Earths. Astron. Astrophys. 614, A18. https://doi.org/10.1051/0004-6361/201731513

Dorn, C., Venturini, J., Khan, A., Heng, K., Alibert, Y., Helled, R., Rivoldini, A., Benz, W., 2017. A generalized Bayesian inference method for constraining the interiors of super Earths and sub-Neptunes. Astron. Astrophys. 597, A37. https://doi.org/10.1051/0004-6361/201628708

Dorogokupets, P.I., Oganov, A.R., 2007. Ruby, metals, and MgO as alternative pressure scales: A semiempirical description of shock-wave, ultrasonic, x-ray, and thermochemical data at high temperatures and pressures. Phys. Rev. B - Condens. Matter Mater. Phys. 75, 1–16. https://doi.org/10.1103/PhysRevB.75.024115

Dressing, C.D., Charbonneau, D., Dumusque, X., Gettel, S., Pepe, F., Collier Cameron, A., Latham, D.W., Molinari, E., Udry, S., Affer, L., Bonomo, A.S., Buchhave, L.A., Cosentino, R., Figueira, P., Fiorenzano, A.F.M., Harutyunyan, A., Haywood, R.D., Johnson, J.A., Lopez-Morales, M., Lovis, C., Malavolta, L., Mayor, M., Micela, G., Motalebi, F., Nascimbeni, V., Phillips, D.F., Piotto, G., Pollacco, D., Queloz, D., Rice, K., Sasselov, D., Ségransan, D., Sozzetti, A., Szentgyorgyi, A., Watson, C., 2015. THE MASS OF Kepler-93b AND THE COMPOSITION OF TERRESTRIAL PLANETS. Astrophys. J. 800, 135. https://doi.org/10.1088/0004-637X/800/2/135

Dubrovinskaia, N., Dubrovinsky, L., Solopova, N.A., Abakumov, A., Turner, S., Hanfland, M., Bykova, E., Bykov, M., Prescher, C., Prakapenka, V.B., Petitgirard, S., Chuvashova, I., Gasharova, B., Mathis, Y.-L., Ershov, P., Snigireva, I., Snigirev, A., 2016. Terapascal static pressure generation with ultrahigh yield strength nanodiamond. Sci. Adv. 2, e1600341. https://doi.org/10.1126/sciadv.1600341

Duffy, T, Wang, Y., 1998. Pressure-Volume-Temperature Equations of state. Rev. Mineral. Geochemistry 37, 425–457.

Duffy, T., 2015. Mineralogy of Super-Earth Planets, Treatise on Geophysics. Elsevier B.V. https://doi.org/10.1016/B978-0-444-53802-4.00053-1

Duffy, T., Madhusudhan, N., Lee, K.K.M., 2015. 2.07 - Mineralogy of Super-Earth Planets, Treatise on Geophysics (Second Edition). Elsevier B.V. https://doi.org/https://doi.org/10.1016/B978-0-444-53802-4.00053-1

Dumberry, M., Rivoldini, A., 2015. Mercury's inner core size and core-crystallization regime. Icarus 248, 254–268. https://doi.org/10.1016/j.icarus.2014.10.038

Durandurdu, M., 2004. Pressure-induced phase transition of SiC. J. Phys. Condens. Matter 16, 4411–4417. https://doi.org/10.1088/0953-8984/16/25/002

Dziewonski, A.M., Anderson, D.L., 1981. Preliminary reference Earth model. Phys. Earth Planet. Inter. 25, 297–356. https://doi.org/10.1016/0031-9201(81)90046-7

Edmund, E., Antonangeli, D., Decremps, F., Miozzi, F., Morard, G., Boulard, E., Clark, A.N., Ayrinhac, S., Gauthier, M., Morand, M., Mezouar, M., 2019. Velocity-Density Systematics of Fe-5wt%Si: Constraints on Si Content in the Earth's Inner Core. J. Geophys. Res. Solid Earth. https://doi.org/10.1029/2018JB016904

Elkins-Tanton, L.T., Seager, S., 2008. Coreless Terrestrial Exoplanets. Astrophys. J. 688, 628. https://doi.org/10.1086/592316

Endl, M., Robertson, P., Cochran, W.D., MacQueen, P.J., Brugamyer, E.J., Caldwell, C., Wittenmyer, R.A., Barnes, S.I., Gullikson, K., 2012. REVISITING ρ 1 CANCRI e: A NEW MASS DETERMINATION OF THE TRANSITING SUPER-EARTH. Astrophys. J. 759, 19. https://doi.org/10.1088/0004-637X/759/1/19

Everhart, T.E., Thornley, R.F.M., 1960. Wide-band detector for micro-microampere low-energy electron currents. J. Sci. Instrum. 37, 246–248. https://doi.org/10.1088/0950-7671/37/7/307

Fei, Y., Brosh, E., 2014. Experimental study and thermodynamic calculations of phase relations in the Fe–C system at high pressure. Earth Planet. Sci. Lett. 408, 155–162. https://doi.org/10.1016/j.epsl.2014.09.044

Fei, Y., Murphy, C., Shibazaki, Y., Shahar, A., Huang, H., 2016. Thermal equation of state of hcp-iron: Constraint on the density deficit of Earth's solid inner core. Geophys. Res. Lett. 43, 6837–6843. https://doi.org/10.1002/2016GL069456

Fei, Y., Ricolleau, A., Frank, M., Mibe, K., Shen, G., Prakapenka, V., 2007. Toward an internally consistent pressure scale. Proc. Natl. Acad. Sci. 104, 9182–9186. https://doi.org/10.1073/pnas.0609013104

Fiquet, G., Auzende, A.L., Siebert, J., Corgne, A., Bureau, H., Ozawa, H., Garbarino, G., 2010. Melting of peridotite to 140 gigapascals. Science (80-.). 329, 1516–1518. https://doi.org/10.1126/science.1192448

Fiquet, G., Badro, J., Azuende, A., Gregoryanz, E., Siebert, J., Matas, J., Guignot, N., 2007. A New Thermal Equation of State for Iron at Megabar Pressure, in: AGU Fall Meeting Abstracts.

Fischer, D.A., Valenti, J., 2005. The Planet-Metallicity Correlation. Astrophys. J. 622, 1102–1117. https://doi.org/10.1086/428383

Fischer, R.A., 2014. Equations of State in the Fe-FeSi system at high pressures and temperatures. J. Geophys. Res. Solid Earth 2810–2827. https://doi.org/10.1002/2013JB010898.Received

Fischer, R.A., Campbell, A.J., Caracas, R., Reaman, D.M., Dera, P., Prakapenka, V.B., 2012. Equation of state and phase diagram of Fe–16Si alloy as a candidate component of Earth's core. Earth Planet. Sci. Lett. 357–358, 268–276. https://doi.org/10.1016/j.epsl.2012.09.022

Fischer, R.A., Campbell, A.J., Reaman, D.M., Miller, N.A., Heinz, D.L., Dera, P., Prakapenka, V.B., 2013. Phase relations in the Fe-FeSi system at high pressures and temperatures. Earth Planet. Sci. Lett. 373, 54–64. https://doi.org/10.1016/j.epsl.2013.04.035

Fortney, J.J., 2012. on the Carbon-To-Oxygen Ratio Measurement in Nearby Sun-Like Stars: Implications for Planet Formation and the Determination of Stellar Abundances. Astrophys. J. 747, L27. https://doi.org/10.1088/2041-8205/747/2/L27

Fressin, F., Torres, G., Charbonneau, D., Bryson, S.T., Christiansen, J., Dressing, C.D., Jenkins, J.M., Walkowicz, L.M., Batalha, N.M., 2013. THE FALSE POSITIVE RATE OF KEPLER AND THE OCCURRENCE OF PLANETS. Astrophys. J. 766, 81. https://doi.org/10.1088/0004-637X/766/2/81

Gaidos, E., Conrad, C.P., Manga, M., Hernlund, J., 2010. THERMODYNAMIC LIMITS ON MAGNETODYNAMOS IN ROCKY EXOPLANETS. Astrophys. J. 718, 596–609. https://doi.org/10.1088/0004-637X/718/2/596

Gallino, R., Busso, M., Picchio, G., Raiteri, C.M., 1990. On the astrophysical interpretation of isotope anomalies in meteoritic SiC grains. Nature 348, 298–302. https://doi.org/10.1038/348298a0

Giampaoli, R., Kantor, I., Mezouar, M., Boccato, S., Rosa, A.D., Torchio, R., Garbarino, G., Mathon, O., 2018. Measurement of temperature in the laser heated diamond anvil cell : comparison between reflective and refractive optics. High Press. Res. 0, 1–20. https://doi.org/10.1080/08957959.2018.1480017

Gillon, M., Demory, B.-O., Benneke, B., Valencia, D., Deming, D., Seager, S., Lovis, C., Mayor, M., Pepe, F., Queloz, D., Ségransan, D., Udry, S., 2012. Improved precision on the radius of the nearby super-Earth 55 Cnc e. Astron. Astrophys. 539, A28. https://doi.org/10.1051/0004-6361/201118309

Goldstein, J.I., Newbury, D.E., Michael, J.R., Ritchie, N.W.M., Scott, J.H.J., Joy, D.C., 2018. Scanning Electron Microscopy and X-Ray Microanalysis. Springer New York, New York, NY. https://doi.org/10.1007/978-1-4939-6676-9

Golubkova, A., Schmidt, M.W., Connolly, J.A.D., 2016. Ultra-reducing conditions in average mantle peridotites and in podiform chromitites: a thermodynamic model for moissanite (SiC) formation.

Contrib. to Mineral. Petrol. 171, 41. https://doi.org/10.1007/s00410-016-1253-9

Green, H.W., Borch, R.S., 1987. The pressure dependence of creep. Acta Metall. 35, 1301–1305. https://doi.org/10.1016/0001-6160(87)90011-3

Hakim, K., Spaargaren, R., Grewal, D.S., Rohrbach, A., Berndt, J., Dominik, C., van Westrenen, W., 2019. Mineralogy, Structure, and Habitability of Carbon-Enriched Rocky Exoplanets: A Laboratory Approach. Astrobiology 19, ast.2018.1930. https://doi.org/10.1089/ast.2018.1930

Hawkes, P., 2004. Recent advances in electron optics and electron microscopy. Ann. la Fond. Louis Broglie 29, 837–855.

Helffrich, G., Ballmer, M.D., Hirose, K., 2018. Core-Exsolved SiO 2 Dispersal in the Earth's Mantle. J. Geophys. Res. Solid Earth 123, 176–188. https://doi.org/10.1002/2017JB014865

Hemley, R.J., Mao, H.K., Shen, G., Badro, J., Gillet, P., Hanfland, M., D, H., 1997. X-ray Imaging of Stress and Strain of Diamond, Iron, and Tungsten at Megabar Pressures. Science (80-.). 276, 1242–1245. https://doi.org/10.1126/science.276.5316.1242

Henning, T., Semenov, D., 2013. Chemistry in protoplanetary disks. Chem. Rev. 113, 9016–9042. https://doi.org/10.1021/cr400128p

Herbstein, F.H., Snyman, J.A., 1967. Identification of Eckstrom-Adcock Iron Carbide as Fe,C,. Inorg. Chem. 1422, 1963–1965.

Hinkel, N.R., Unterborn, C.T., 2018. The Star–Planet Connection. I. Using Stellar Composition to Observationally Constrain Planetary Mineralogy for the 10 Closest Stars. Astrophys. J. 853, 83. https://doi.org/10.3847/1538-4357/aaa5b4

Hirose, K., Morard, G., Sinmyo, R., Umemoto, K., Hernlund, J., Helffrich, G., Labrosse, S., 2017a. Crystallization of silicon dioxide and compositional evolution of the Earth's core. Nature 543, 99–102. https://doi.org/10.1038/nature21367

Hirose, K., Morard, G., Sinmyo, R., Umemoto, K., Hernlund, J., Helffrich, G., Labrosse, S., 2017b. Crystallization of silicon dioxide and compositional evolution of the Earth's core. Nature 543, 99–102. https://doi.org/10.1038/nature21367

Holland, L., Hurley, R.E., Laurenson, L., 1971. The operation of a glow discharge ion gun used for specimen thinning. J. Phys. E. 4, 198–200. https://doi.org/10.1088/0022-3735/4/3/011

Holland, T.J.B., Powell, R., 2011. An improved and extended internally consistent thermodynamic dataset for phases of petrological interest, involving a new equation of state for solids. J. Metamorph. Geol. 29, 333–383. https://doi.org/10.1111/j.1525-1314.2010.00923.x

Hoppe, P., Rubin, M., Altwegg, K., 2018. Presolar Isotopic Signatures in Meteorites and Comets: New Insights from the Rosetta Mission to Comet 67P/Churyumov–Gerasimenko. Space Sci. Rev. 214, 106. https://doi.org/10.1007/s11214-018-0540-3

Howe, A.R., Burrows, A., Verne, W., 2014. MASS-RADIUS RELATIONS AND CORE-ENVELOPE DECOMPOSITIONS OF SUPER-EARTHS AND SUB-NEPTUNES. Astrophys. J. 787, 173. https://doi.org/10.1088/0004-637X/787/2/173

Huss, G.R., Lewis, R.S., 1995. Presolar diamond, SiC, and graphite in primitive chondrites: Abundances as a function of meteorite class and petrologic type. Geochim. Cosmochim. Acta 59, 115–160. https://doi.org/10.1016/0016-7037(94)00376-W

Jackson, I., Rigden, S.M., 1996. Analysis of P-V-T data: constraints on the thermoelastic properties of high-pressure minerals. Phys. Earth Planet. Inter. 96, 85–112. https://doi.org/10.1016/0031-9201(96)03143-3

Jamieson, J.C., Lawson, A.W., Nachtrieb, N.D., 1959. New device for obtaining X-ray diffraction patterns from substances exposed to high pressure. Rev. Sci. Instrum. 30, 1016–1019. https://doi.org/10.1063/1.1716408

Jepps, N.W., Page, T.F., 1983. Polytypic transformations in silicon carbide. Prog. Cryst. Growth Charact. 7, 259–307. https://doi.org/10.1016/0146-3535(83)90034-5

Karato, S.-I., Jung, H., 2003. Effects of pressure on high-temperature dislocation creep in olivine. Philos. Mag. 83, 401–414. https://doi.org/10.1080/0141861021000025829

Karato, S., Rama Murthy, V., 1997. Core formation and chemical equilibrium in the Earth—I. Physical considerations. Phys. Earth Planet. Inter. 100, 61–79. https://doi.org/10.1016/S0031-9201(96)03232-3

Karch, K. et al., 1996. First-principles study of thermal properties of 3C SiC 220, 448–450.

Kawanishi, S., Yoshikawa, T., Tanaka, T., 2009. Equilibrium Phase Relationship between SiC and a Liquid Phase in the Fe-Si-C System at 1523–1723 K. Mater. Trans. 50, 806–813. https://doi.org/10.2320/matertrans.MRA2008404

Kidokoro, Y., Umemoto, K., Hirose, K., Ohishi, Y., 2017. Phase transition in SiC from zinc-blende to rock-salt structure and implications for carbon-rich extrasolar planets. Am. Mineral. 102, 2230–2234. https://doi.org/10.2138/am-2017-6033

Klotz, S., Chervin, J.C., Munsch, P., Le Marchand, G., 2009. Hydrostatic limits of 11 pressure transmitting media. J. Phys. D. Appl. Phys. 42. https://doi.org/10.1515/zatw.2004.010

Kroll, H., Kirfel, A., Heinemann, R., 2012. Volume thermal expansion and related thermophysical

parameters in the Mg, Fe olivine solid-solution series. Eur. J. Mineral. 26, 607–621. https://doi.org/10.1127/0935-1221/2014/0026-2398

Lacaze, J., Sundman, B., 1991. An assessment of the Fe-C-Si system. Metall. Trans. A 22, 2211–2223. https://doi.org/10.1007/BF02664987

Lammer, H., Bredehöft, J.H., Coustenis, A., Khodachenko, M.L., Kaltenegger, L., Grasset, O., Prieur, D., Raulin, F., Ehrenfreund, P., Yamauchi, M., Wahlund, J.-E., Grießmeier, J.-M., Stangl, G., Cockell, C.S., Kulikov, Y.N., Grenfell, J.L., Rauer, H., 2009. What makes a planet habitable? Astron. Astrophys. Rev. 17, 181–249. https://doi.org/10.1007/s00159-009-0019-z

Larimer, J.W., 1975. The effect of C O ratio on the condensation of planetary material. Geochim. Cosmochim. Acta 39, 389–392. https://doi.org/10.1016/0016-7037(75)90204-5

Le Bail, A., 2005. Whole powder pattern decomposition methods and applications: A retrospection. Powder Diffr. 20, 316–326. https://doi.org/10.1154/1.2135315

Le Bail, A., Duroy, H., Fourquet, J.L., 1988. Ab-initio structure determination of LiSbWO6 by X-ray powder diffraction. Mater. Res. Bull. 23, 447–452. https://doi.org/10.1016/0025-5408(88)90019-0

Lee, W.H., Yao, X.H., 2015. First principle investigation of phase transition and thermodynamic properties of SiC. Comput. Mater. Sci. 106, 76–82. https://doi.org/10.1016/j.commatsci.2015.04.044

Leung, I., Guo, W., Friedman, I., Gleason, J., 1990. Natural occurrence of silicon carbide in a diamondiferous kimberlite from Fuxian. Nature 346, 352–354. https://doi.org/10.1038/346352a0

Li, J., Porter, L., Yip, S., 1998. Atomistic modeling of finite-temperature properties of crystalline β-SiC. J. Nucl. Mater. 255, 139–152. https://doi.org/10.1016/S0022-3115(98)00034-8

Li, Ji, C., Yang, W., Wang, J., Yang, K., Xu, R., Liu, W., Cai, Z., Chen, J., Mao, H., 2018. Diamond anvil cell behavior up to 4 Mbar. Proc. Natl. Acad. Sci. 115, 1713–1717. https://doi.org/10.1073/pnas.1721425115

Li, Y., Vočadlo, L., Brodholt, J.P., 2018. The elastic properties of hcp -Fe alloys under the conditions of the Earth's inner core. Earth Planet. Sci. Lett. 493, 118–127. https://doi.org/10.1016/j.epsl.2018.04.013

Liermann, H.-P., Konôpková, Z., Morgenroth, W., Glazyrin, K., Bednarčik, J., McBride, E.E., Petitgirard, S., Delitz, J.T., Wendt, M., Bican, Y., Ehnes, A., Schwark, I., Rothkirch, A., Tischer, M., Heuer, J., Schulte-Schrepping, H., Kracht, T., Franz, H., 2015. The Extreme Conditions Beamline P02.2 and the Extreme Conditions Science Infrastructure at PETRA III. J. Synchrotron

Radiat. 22, 908–924. https://doi.org/10.1107/S1600577515005937

Lissauer, J.J., De Pater, I., 2013. Fundamental planetary science: physics, chemistry and habitability. Cambridge University Press.

Litasov, K.D., Sharygin, I.S., Dorogokupets, P.I., Shatskiy, A., Gavryushkin, P.N., Sokolova, T.S., Ohtani, E., Li, J., Funakoshi, K., 2013. Thermal equation of state and thermodynamic properties of iron carbide Fe3C to 31 GPa and 1473 K. J. Geophys. Res. Solid Earth 118, 5274–5284. https://doi.org/10.1002/2013JB010270

Litasov, K.D., Sharygin, I.S., Shatskii, a. F., Gavryushkin, P.N., Dorogokupets, P.I., Sokolova, T.S., Ohtani, E., Dymshits, a. M., Alifirova, T. a., 2014. P-V-T equations of state for iron carbides Fe3C and Fe7C3 and their relationships under the conditions of the Earth's mantle and core. Dokl. Earth Sci. 453, 1269–1273. https://doi.org/10.1134/S1028334X13120192

Liu, J., Li, J., Ikuta, D., 2016. Elastic softening in Fe 7 C 3 with implications for Earth's deep carbon reservoirs. J. Geophys. Res. Solid Earth 121, 1514–1524. https://doi.org/10.1002/2015JB012701

Liu, J., Lin, J.F., Prakapenka, V.B., Prescher, C., Yoshino, T., 2016. Phase relations of Fe3C and Fe7C3up to 185 GPa and 5200 K: Implication for the stability of iron carbide in the Earth's core. Geophys. Res. Lett. 43, 12,415-12,422. https://doi.org/10.1002/2016GL071353

Lodders, K., 2003. Solar System Abundances and Condensation Temperatures of the Elements. Astrophys. J. 1220–1247. https://doi.org/10.1086/375492

Lord, O.T., Walter, M.J., Dasgupta, R., Walker, D., Clark, S.M., 2009. Melting in the Fe-C system to 70 GPa. Earth Planet. Sci. Lett. 284, 157–167. https://doi.org/10.1016/j.epsl.2009.04.017

Lord, O.T., Walter, M.J., Dobson, D.P., Armstrong, L., Clark, S.M., Kleppe, A., 2010. The FeSi phase diagram to 150 GPa. J. Geophys. Res. Solid Earth 115, 1–9. https://doi.org/10.1029/2009JB006528

Lord, O.T., Wann, E.T.H., Hunt, S.A., Walker, A.M., Santangeli, J., Walter, M.J., Dobson, D.P., Wood, I.G., Vočadlo, L., Morard, G., Mezouar, M., 2014. The NiSi melting curve to 70GPa. Phys. Earth Planet. Inter. 233, 13–23. https://doi.org/10.1016/j.pepi.2014.05.005

Lu, Y.-P., He, D.-W., Zhu, J., Yang, X.-D., 2008. First-principles study of pressure-induced phase transition in silicon carbide. Phys. B Condens. Matter 403, 3543–3546. https://doi.org/10.1016/j.physb.2008.05.028

Madhusudhan, N., Harrington, J., Stevenson, K.B., Nymeyer, S., Campo, C.J., Wheatley, P.J., Deming, D., Blecic, J., Hardy, R. a, Lust, N.B., Anderson, D.R., Collier-Cameron, A., Britt, C.B.T., Bowman, W.C., Hebb, L., Hellier, C., Maxted, P.F.L., Pollacco, D., West, R.G., 2011. A high C/O

ratio and weak thermal inversion in the atmosphere of exoplanet WASP-12b. Nature 469, 64–67. https://doi.org/10.1038/nature09602

Madhusudhan, N., Lee, K.K.M., Mousis, O., 2012. A POSSIBLE CARBON-RICH INTERIOR IN SUPER-EARTH 55 Cancri e. Astrophys. J. 759, L40. https://doi.org/10.1088/2041-8205/759/2/L40

Maletz, J., Steiner, M., Fatka, O., 2005. Middle Cambrian pterobranchs and the Question: What is a graptolite? Lethaia 38, 73–85. https://doi.org/10.1080/00241160510013204

Mao, H.K., Bell, P.M., Shaner, J.W., Steinberg, D.J., 1978. Specific volume measurements of Cu, Mo, Pd, and Ag and calibration of the ruby R1 fluorescence pressure gauge from 0.06 to 1 Mbar. J. Appl. Phys. 49, 3276–3283. https://doi.org/10.1063/1.325277

Mao, H.K., Xu, J., Bell, P.M., 1986. Calibration of the ruby pressure gauge to 800 kbar under quasi-hydrostatic conditions. J. Geophys. Res. 91, 4673. https://doi.org/10.1029/JB091iB05p04673

Mashino, I., Miozzi, F., Hirose, K., Morard, G., Sinmyo, R., 2019. Melting experiments on the Fe–C binary system up to 255 GPa: Constraints on the carbon content in the Earth's core. Earth Planet. Sci. Lett. 515, 135–144. https://doi.org/10.1016/j.epsl.2019.03.020

Mason, B., 1967. Extraterrestrial Mineralogy1. Am. Mineral. 52, 307–325.

Mathez, E.A., Fogel, R.A., Hutcheon, I.D., Marshintsev, V.K., 1995. Carbon isotopic composition and origin of SiC from kimberlites of Yakutia, Russia. Geochim. Cosmochim. Acta 59, 781–791. https://doi.org/10.1016/0016-7037(95)00002-H

Mayor, M., Queloz, D., 1995. A Jupiter-mass companion to a solar-type star. Nature 378, 355–359. https://doi.org/10.1038/378355a0

McMullan, D., 1995. Scanning electron microscopy 1928–1965. Scanning 17, 175–185. https://doi.org/10.1002/sca.4950170309

Melngailis, J., 1987. Focused ion beam technology and applications. J. Vac. Sci. Technol. B Microelectron. Nanom. Struct. 5, 469. https://doi.org/10.1116/1.583937

Merkel, S., Hemley, R.J., Mao, H.K., 1999. Finite-element modeling of diamond deformation at multimegabar pressures. Appl. Phys. Lett. 74, 656–658. https://doi.org/10.1063/1.123031

Mezouar, M., Crichton, W.A., Bauchau, S., Thurel, F., Witsch, H., Torrecillas, F., Blattmann, G., Marion, P., Dabin, Y., Chavanne, J., Hignette, O., Morawe, C., Borel, C., 2005. Development of a new state-of-the-art beamline optimized for monochromatic single-crystal and powder X-ray diffraction under extreme conditions at the ESRF. J. Synchrotron Radiat. 12, 659–664. https://doi.org/10.1107/S0909049505023216

Mezouar, M., Giampaoli, R., Garbarino, G., Kantor, I., Dewaele, A., Weck, G., Boccato, S., Svitlyk, V., Rosa, A.D., Torchio, R., Mathon, O., Hignette, O., 2017. Methodology for in situ synchrotron X-ray studies in the laser-heated diamond anvil cell. High Press. Res. 0, 1–11. https://doi.org/10.1080/08957959.2017.1306626

Miettinen, J., 1998. Reassessed thermodynamic solution phase data for ternary Fe-Si-C system. Calphad 22, 231–256. https://doi.org/10.1016/S0364-5916(98)00026-1

Milani, S., Angel, R.J., Scandolo, L., Mazzucchelli, M.L., Ballaran, T.B., Klemme, S., Domeneghetti, M.C., Miletich, R., Scheidl, K.S., Derzsi, M., Tokár, K., Prencipe, M., Alvaro, M., Nestola, F., 2017. Thermo-elastic behavior of grossular garnet at high pressures and temperatures. Am. Mineral. 102, 851–859. https://doi.org/10.2138/am-2017-5855

Ming, T., Anders, E., Hoppe, P., Zinner, E., 1989. Meteoritic silicon carbide and its stellar sources; implications for galactic chemical evolution. Nature 339, 351–354. https://doi.org/10.1038/339351a0

Ming, T., Anders, E., Zinner, E., 1988. Noble Gases, C, N and Si Isotopes in Interstellar SiC from the Murchison Carbonaceous Chondrite. Lunar Planet. Sci. 1177–1178. https://doi.org/1988LPICo.650...25M

Miozzi, F., Morard, G., Antonangeli, D., Clark, A.N., Mezouar, M., Dorn, C., Rozel, A., Fiquet, G., 2018. Equation of State of SiC at Extreme Conditions: New Insight Into the Interior of Carbon-Rich Exoplanets. J. Geophys. Res. Planets 19, 2295–2309. https://doi.org/10.1029/2018JE005582

Mookherjee, M., 2011. Elasticity and anisotropy of Fe3C at high pressures. Am. Mineral. 96, 1530–1536. https://doi.org/10.2138/am.2011.3917

Mookherjee, M., Nakajima, Y., Steinle-Neumann, G., Glazyrin, K., Wu, X., Dubrovinsky, L., McCammon, C., Chumakov, A., 2011. High-pressure behavior of iron carbide (Fe 7 C 3) at inner core conditions. J. Geophys. Res. 116, B04201. https://doi.org/10.1029/2010JB007819

Morard, G., Andrault, D., Antonangeli, D., Nakajima, Y., Auzende, A.L., Boulard, E., Cervera, S., Clark, A., Lord, O.T., Siebert, J., Svitlyk, V., Garbarino, G., Mezouar, M., 2017. Fe–FeO and Fe–Fe3C melting relations at Earth's core–mantle boundary conditions: Implications for a volatile-rich or oxygen-rich core. Earth Planet. Sci. Lett. 473, 94–103. https://doi.org/10.1016/j.epsl.2017.05.024

Morard, G., Andrault, D., Guignot, N., Siebert, J., Garbarino, G., Antonangeli, D., 2011. Melting of Fe-Ni-Si and Fe-Ni-S alloys at megabar pressures: Implications for the core-mantle boundary temperature. Phys. Chem. Miner. 38, 767–776. https://doi.org/10.1007/s00269-011-0449-9

Morard, G., Boccato, S., Rosa, A.D., Anzellini, S., Miozzi, F., Henry, L., Garbarino, G., Mezouar, M.,

Harmand, M., Guyot, F., Boulard, E., Kantor, I., Irifune, T., Torchio, R., 2018. Solving Controversies on the Iron Phase Diagram Under High Pressure. Geophys. Res. Lett. 45, 11,074-11,082. https://doi.org/10.1029/2018GL079950

Moriarty, J., Madhusudhan, N., Fischer, D., 2014. Chemistry in an evolving protoplanetary disk: effects on terrestrial planet composition. Astrophys. J. 787, 81. https://doi.org/10.1088/0004-637X/787/1/81

Morrison, R.A., Jackson, J.M., Sturhahn, W., Zhang, D., Greenberg, E., 2018. Equations of State and Anisotropy of Fe-Ni-Si Alloys. J. Geophys. Res. Solid Earth 123, 4647–4675. https://doi.org/10.1029/2017JB015343

Nakajima, Y., Takahashi, E., Sata, N., Nishihara, Y., Hirose, K., Funakoshi, K.I., Ohishi, Y., 2011. Thermoelastic property and high-pressure stability of Fe7C 3: Implication for iron-carbide in the Earth's core. Am. Mineral. 96, 1158–1165. https://doi.org/10.2138/am.2011.3703

Nakajima, Y., Takahashi, E., Suzuki, T., Funakoshi, K., 2009. "Carbon in the core" revisited. Phys. Earth Planet. Inter. 174, 202–211. https://doi.org/10.1016/j.pepi.2008.05.014

Napchan, E., 2001. Backscattered Electrons in the SEM. Microsc. Anal. 9–11.

Narumi, T., Kawanishi, S., Yoshikawa, T., Kusunoki, K., Kamei, K., Daikoku, H., Sakamoto, H., 2014. Thermodynamic evaluation of the C–Cr–Si, C–Ti–Si, and C–Fe–Si systems for rapid solution growth of SiC. J. Cryst. Growth 408, 25–31. https://doi.org/10.1016/j.jcrysgro.2014.08.027

Nazzareni, S., Nestola, F., Zanon, V., Bindi, L., Scricciolo, E., Petrelli, M., Zanatta, M., Mariotto, G., Giuli, G., 2019. Discovery of moissanite in a peralkaline syenite from the Azores Islands. Lithos 324–325, 68–73. https://doi.org/10.1016/j.lithos.2018.10.036

Nisr, C., Meng, Y., MacDowell, A.A., Yan, J., Prakapenka, V., Shim, S.-H., 2017. Thermal expansion of SiC at high pressure-temperature and implications for thermal convection in the deep interiors of carbide exoplanets. J. Geophys. Res. Planets 122, 124–133. https://doi.org/10.1002/2016JE005158

Nissen, P.E., 2013. The carbon-to-oxygen ratio in stars with planets. Astron. Astrophys. 552, A73. https://doi.org/10.1051/0004-6361/201321234

Nissen, P.E., Chen, Y.Q., Carigi, L., Schuster, W.J., Zhao, G., 2014. Carbon and oxygen abundances in stellar populations. Astron. Astrophys. 568, A25. https://doi.org/10.1051/0004-6361/201424184

Nittler, L.R., 2003. Presolar stardust in meteorites: recent advances and scientific frontiers. Earth Planet. Sci. Lett. 209, 259–273. https://doi.org/10.1016/S0012-821X(02)01153-6

Noack, L., Breuer, D., 2014. Plate tectonics on rocky exoplanets: Influence of initial conditions and

mantle rheology. Planet. Space Sci. 98, 41–49. https://doi.org/10.1016/j.pss.2013.06.020

O'D Alexander, C.., 1993. Presolar SiC in chondrites: How variable and how many sources? Geochim. Cosmochim. Acta 57, 2869–2888. https://doi.org/10.1016/0016-7037(93)90395-D

Öberg, K.I., Murray-Clay, R., Bergin, E.A., 2011. THE EFFECTS OF SNOWLINES ON C/O IN PLANETARY ATMOSPHERES. Astrophys. J. 743, L16. https://doi.org/10.1088/2041-8205/743/1/L16

Occelli, F., Loubeyre, P., LeToullec, R., 2003. Properties of diamond under hydrostatic pressures up to 140 GPa. Nat. Mater. 2, 151–154. https://doi.org/10.1038/nmat831

Ono, S., Mibe, K., 2010. Magnetic transition of iron carbide at high pressures. Phys. Earth Planet. Inter. 180, 1–6. https://doi.org/10.1016/j.pepi.2010.03.008

Ozawa, H., Hirose, K., Yonemitsu, K., Ohishi, Y., 2016. High-pressure melting experiments on Fe-Si alloys and implications for silicon as a light element in the core. Earth Planet. Sci. Lett. 456, 47–54. https://doi.org/10.1016/j.epsl.2016.08.042

Petigura, E.A., Marcy, G.W., Winn, J.N., Weiss, L.M., Fulton, B.J., Howard, A.W., Sinukoff, E., Isaacson, H., Morton, T.D., Johnson, J.A., 2018. The California- Kepler Survey. IV. Metal-rich Stars Host a Greater Diversity of Planets. Astron. J. 155, 89. https://doi.org/10.3847/1538-3881/aaa54c

Petitgirard, S., Salamat, A., Beck, P., Weck, G., Bouvier, P., 2014. Strategies for in situ laser heating in the diamond anvil cell at an X-ray diffraction beamline. J. Synchrotron Radiat. 21, 89–96. https://doi.org/10.1107/S1600577513027434

Pistorius, C.W.F.T., 1965. Melting curves of the potassium halides at high pressures. J. Phys. Chem. Solids 26, 1543–1548. https://doi.org/10.1016/0022-3697(65)90054-5

Poirier, J.-P., Tarantola, A., 1998. A logarithmic equation of state. Phys. Earth Planet. Inter. 109, 1–8. https://doi.org/10.1016/S0031-9201(98)00112-5

Poirier, J., 1994. Light elements in the Earth's outer core: A critical review. Phys. Earth Planet. Inter. 85, 319–337. https://doi.org/10.1016/0031-9201(94)90120-1

Poirier, J.P., 1991. Introduction to physics of the Earth's Interior Cambridge University Press. Cambridge, Engl.

Prescher, C., Dubrovinsky, L., Bykova, E., Kupenko, I., Glazyrin, K., Kantor, A., McCammon, C., Mookherjee, M., Nakajima, Y., Miyajima, N., Sinmyo, R., Cerantola, V., Dubrovinskaia, N., Prakapenka, V., Rüffer, R., Chumakov, A., Hanfland, M., 2015. High Poisson's ratio of Earth's inner core explained by carbon alloying. Nat. Geosci. 8, 220–223.

https://doi.org/10.1038/ngeo2370

Prescher, C., Dubrovinsky, L., McCammon, C., Glazyrin, K., Nakajima, Y., Kantor, A., Merlini, M., Hanfland, M., 2012. Structurally hidden magnetic transitions in Fe 3C at high pressures. Phys. Rev. B - Condens. Matter Mater. Phys. 85, 6–9. https://doi.org/10.1103/PhysRevB.85.140402

Prescher, C., Prakapenka, V.B., 2015. DIOPTAS: a program for reduction of two-dimensional X-ray diffraction data and data exploration. High Press. Res. 35, 223–230. https://doi.org/10.1080/08957959.2015.1059835

Rama Murthy, V., Karato, S., 1997. Core formation and chemical equilibrium in the Earth—II: Chemical consequences for the mantle and core. Phys. Earth Planet. Inter. 100, 81–95. https://doi.org/10.1016/S0031-9201(96)03233-5

Rogers, L.A., Seager, S., 2010. A FRAMEWORK FOR QUANTIFYING THE DEGENERACIES OF EXOPLANET INTERIOR COMPOSITIONS. Astrophys. J. 712, 974–991. https://doi.org/10.1088/0004-637X/712/2/974

Sata, N., Hirose, K., Shen, G., Nakajima, Y., Ohishi, Y., Hirao, N., 2010. Compression of FeSi, Fe<inf>3</inf>C, Fe<inf>0.95</inf>O, and FeS under the core pressures and implication for light element in the Earth's core. J. Geophys. Res. Solid Earth 115, 1–13. https://doi.org/10.1029/2009JB006975

Sata, N., Shen, G., Rivers, M.L., Sutton, S.R., 2002. Pressure-volume equation of state of the high-pressure (formula presented) phase of NaCl. Phys. Rev. B - Condens. Matter Mater. Phys. 65, 1–7. https://doi.org/10.1103/PhysRevB.65.104114

Schmidt, M.W., Gao, C., Golubkova, A., Rohrbach, A., Connolly, J.A., 2014. Natural moissanite (SiC) – a low temperature mineral formed from highly fractionated ultra-reducing COH-fluids. Prog. Earth Planet. Sci. 1, 27. https://doi.org/10.1186/s40645-014-0027-0

Schultz, E., Mezouar, M., Crichton, W., Bauchau, S., Blattmann, G., Andrault, D., Fiquet, G., Boehler, R., Rambert, N., Sitaud, B., Loubeyre, P., 2005. High Pressure–High Temperature Monochromatic X-Ray Diffraction At the Esrf. High Press. Res. 25, 71–83. https://doi.org/10.1080/08957950500076031

Seager, S., 2013. Exoplanet Habitability. Science (80-.). 340, 577–581. https://doi.org/10.1126/science.1232226

Seager, S., Kuchner, M.J., Hier-Majumder, C.A., Militzer, B., 2007. Mass-Radius Relationships for Solid Exoplanets. Astrophys. J. 669, 1279. https://doi.org/10.1086/521346

Seiler, H., 1983. Secondary electron emission in the scanning electron microscope. J. Appl. Phys. 54,

R1–R18. https://doi.org/10.1063/1.332840

Shearer, P.M., Flanagan, M.P., 1999. Seismic Velocity and Density Jumps Across the 410- and 660-Kilometer Discontinuities. Science (80-.). 285, 1545–1548. https://doi.org/10.1126/science.285.5433.1545

Shimojo, F., Ebbsjö, I., Kalia, R.K., Nakano, A., Rino, J.P., Vashishta, P., 2000. Molecular Dynamics Simulation of Structural Transformation in Silicon Carbide under Pressure. Phys. Rev. Lett. 84, 3338–3341. https://doi.org/10.1103/PhysRevLett.84.3338

Shiryaev, A.A., Griffin, W.L., Stoyanov, E., 2011. Moissanite (SiC) from kimberlites: Polytypes, trace elements, inclusions and speculations on origin. Lithos 122, 152–164. https://doi.org/10.1016/j.lithos.2010.12.011

Sigmund, P., 1987. Mechanisms and theory of physical sputtering by particle impact. Nucl. Instruments Methods Phys. Res. Sect. B Beam Interact. with Mater. Atoms 27, 1–20. https://doi.org/10.1016/0168-583X(87)90004-8

Smallman, R.E., Ngan, A.H.W., 2014. Modern Physical Metallurgy, Modern Physical Metallurgy: Eighth Edition. Elsevier. https://doi.org/10.1016/C2011-0-05565-5

Sokolov, P.S., Mukhanov, V.A., Chauveau, T., Solozhenko, V.L., 2012. On melting of silicon carbide under pressure. J. Superhard Mater. 34, 339–341. https://doi.org/10.3103/S1063457612050097

Solomatov, V., 2007. Magma Oceans and Primordial Mantle Differentiation, in: Treatise on Geophysics. Elsevier, pp. 91–119. https://doi.org/10.1016/B978-044452748-6.00141-3

Sotin, C., Grasset, O., Mocquet, A., 2007. Mass–radius curve for extrasolar Earth-like planets and ocean planets. Icarus 191, 337–351. https://doi.org/10.1016/j.icarus.2007.04.006

Sotin, C., Jackson, J.M., Seager, S., 2010. Terrestrial Planet Interiors. Exoplanets 375–395.

Spiegel, D.S., Fortney, J.J., Sotin, C., 2014. Structure of exoplanets. Proc. Natl. Acad. Sci. 111, 12622–12627. https://doi.org/10.1073/pnas.1304206111

Stassun, K.G., Oelkers, R.J., Pepper, J., Paegert, M., Lee, N. De, Torres, G., Latham, D.W., Charpinet, S., Dressing, C.D., Huber, D., Kane, S.R., Lépine, S., Mann, A., Muirhead, P.S., Rojas-Ayala, B., Silvotti, R., Fleming, S.W., Levine, A., Plavchan, P., 2018. The TESS Input Catalog and Candidate Target List. Astron. J. 156, 102. https://doi.org/10.3847/1538-3881/aad050

Stevenson, D.J., 2001. Mars' core and magnetism. Nature 412, 214–219. https://doi.org/10.1038/35084155

Tackley, P.J., Stevenson, D.J., Glatzmaier, G.A., Schubert, G., 1993. Effects of an endothermic phase

transition at 670 km depth in a spherical model of convection in the Earth's mantle. Nature 361, 699–704. https://doi.org/10.1038/361699a0

Takahashi, S., Ohtani, E., Terasaki, H., Ito, Y., Shibazaki, Y., Ishii, M., Funakoshi, K., Higo, Y., 2013. Phase relations in the carbon-saturated C–Mg–Fe–Si–O system and C and Si solubility in liquid Fe at high pressure and temperature: implications for planetary interiors. Phys. Chem. Miner. 40, 647–657. https://doi.org/10.1007/s00269-013-0600-x

Tateno, S., Hirose, K., Ohishi, Y., Tatsumi, Y., 2010. The structure of iron in earth's inner core. Science (80-.). 330, 359–361. https://doi.org/10.1126/science.1194662

Tateno, S., Hirose, K., Synmio, R., Morard, G., Hirao, N., Ohishi, Y., 2018. Melting experiments on Fe – Si – S alloys to core pressures : Silicon in the core ? Am. Mineral. 103, 742–748.

Tateno, S., Kuwayama, Y., Hirose, K., Ohishi, Y., 2015. The structure of Fe-Si alloy in Earth's inner core. Earth Planet. Sci. Lett. 418, 11–19. https://doi.org/10.1016/j.epsl.2015.02.008

Taylor, S.R., Esat, T.M., 2013. Geochemical Constraints on the Origin of the Moon, in: Earth Processes: Reading the Isotopic Code. pp. 33–46. https://doi.org/10.1029/GM095p0033

Teske, J.K., Cunha, K., Schuler, S.C., Griffith, C.A., Smith, V. V., 2013. Carbon and Oxygen Abundances in Cool Metal-Rich Exoplanet Hosts: a Case Study of the C/O Ratio of 55 Cancri. Astrophys. J. 778, 132. https://doi.org/10.1088/0004-637X/778/2/132

Thorngren, D.P., Fortney, J.J., Murray-Clay, R.A., Lopez, E.D., 2016. THE MASS–METALLICITY RELATION FOR GIANT PLANETS. Astrophys. J. 831, 64. https://doi.org/10.3847/0004-637X/831/1/64

Togaya, M., Sugiyama, S., 1998. Melting Behavior of .BETA.-SiC at High Pressure. Rev. HIGH Press. Sci. Technol. 7, 1037–1039. https://doi.org/10.4131/jshpreview.7.1037

Torchio, R., Occelli, F., Mathon, O., Sollier, A., Lescoute, E., Videau, L., Vinci, T., Benuzzi-Mounaix, A., Headspith, J., Helsby, W., Bland, S., Eakins, D., Chapman, D., Pascarelli, S., Loubeyre, P., 2016. Probing local and electronic structure in Warm Dense Matter: single pulse synchrotron x-ray absorption spectroscopy on shocked Fe. Sci. Rep. 6, 26402. https://doi.org/10.1038/srep26402

Turkevich, V.Z., Stratiichuk, D.A., Turkevich, D. V., 2016. Thermodynamic calculation of the phase diagram of the Si–C system up to 8 GPa. J. Superhard Mater. 38, 145–147. https://doi.org/10.3103/S106345761602009X

Ulmer, G.C., Grandstaff, D.E., Woermann, E., Gobbels, M., Schonitz, M., Woodland, a B., 1998. The redox stability of moissanite (SiC) compared with metal-metal oxide buffers at 1773 K and at pressures up to 90 kbar. Neues Jahrb. Fur Mineral. 172, 279–307.

https://doi.org/10.1127/njma/172/1998/279

Unterborn, C.T., Dismukes, E.E., Panero, W.R., 2016. SCALING THE EARTH: A SENSITIVITY ANALYSIS OF TERRESTRIAL EXOPLANETARY INTERIOR MODELS. Astrophys. J. 819, 32. https://doi.org/10.3847/0004-637X/819/1/32

Unterborn, C.T., Hull, S.D., Stixrude, L.P., Teske, J.K., Johnson, J.A., Panero, W.R., 2017. Stellar Chemical Clues As To The Rarity of Exoplanetary Tectonics. Draft.

Unterborn, C.T., Kabbes, J.E., Pigott, J.S., Reaman, D.M., Panero, W.R., 2014. the Role of Carbon in Extrasolar Planetary Geodynamics and Habitability. Astrophys. J. 793, 124. https://doi.org/10.1088/0004-637X/793/2/124

Unterborn, C.T., Panero, W.R., 2017. The Effects of Mg/Si on the Exoplanetary Refractory Oxygen Budget. Astrophys. J. 845, 61. https://doi.org/10.3847/1538-4357/aa7f79

Valencia, D., 2013. Composition and Internal Dynamics of Super-Earths, in: Physics and Chemistry of the Deep Earth. John Wiley & Sons, Ltd, Chichester, UK, pp. 271–294. https://doi.org/10.1002/9781118529492.ch9

Valencia, D., O'Connell, R.J., 2009. Convection scaling and subduction on Earth and super-Earths. Earth Planet. Sci. Lett. 286, 492–502. https://doi.org/10.1016/j.epsl.2009.07.015

Valencia, D., O'Connell, R.J., Sasselov, D., 2006a. Internal structure of massive terrestrial planets. Icarus 181, 545–554. https://doi.org/10.1016/j.icarus.2005.11.021

Valencia, D., O'Connell, R.J., Sasselov, D., 2006b. Internal structure of massive terrestrial planets. Icarus 181, 545–554. https://doi.org/10.1016/j.icarus.2005.11.021

Vander Kaaden, K.E., McCubbin, F.M., Kent Ross, D., Rapp, J.F., Danielson, L.R., Keller, L.P., Righter, K., 2016. Carbon solubility in Si-Fe-bearing metals during core formation on Mercury, in: Lunar Plan. Sci. Conf. XLVII.

Varshney, D., Shriya, S., Varshney, M., Singh, N., Khenata, R., 2015. Elastic and thermodynamical properties of cubic (3C) silicon carbide under high pressure and high temperature. J. Theor. Appl. Phys. 9, 221–249. https://doi.org/10.1007/s40094-015-0183-7

Ves, S., Schwarz, U., Christensen, N.E., Syassen, K., Cardona, M., 1990. Cubic ZnS under pressure: Optical-absorption edge, phase transition, and calculated equation of state. Phys. Rev. B 42, 9113–9118. https://doi.org/10.1103/PhysRevB.42.9113

Vinet, P., Ferrante, J., Rose, J.H., Smith, J.R., 1987. Compressibility of solids. Geophys. Res. Lett. 92, 9319–9325. https://doi.org/10.1029/JB092iB09p09319

Vinet, P., Ferrante, J., Smith, J.R., Rose, J.H., 1986. A universal equation of state for solids. J. Phys. C Solid State Phys. 19, L467–L473. https://doi.org/10.1088/0022-3719/19/20/001

Vočadlo, L., 2015. Earth's Core: Iron and Iron Alloys, Treatise on Geophysics. https://doi.org/10.1016/B978-0-444-53802-4.00032-4

Vocadlo, L., Brodholt, J., Dobson, D.P., Knight, K.S., Marshall, W.G., Price, G.D., Wood, I.G., 2002. The effect of ferromagnetism on the equation of state of Fe 3 C studied by first-principles calculations. Earth Planet. Sci. Lett. 203, 567–575.

Volkert, C. a, Minor, a M., 2007. Focused Ion Beam Microscopy and Micromachining. MRS Bull. 32, 389–399. https://doi.org/10.1557/mrs2007.62

Wagner, F.W., Sohl, F., Hussmann, H., Grott, M., Rauer, H., 2011. Interior structure models of solid exoplanets using material laws in the infinite pressure limit. Icarus 214, 366–376. https://doi.org/10.1016/j.icarus.2011.05.027

Walter, M.J., Trønnes, R.G., 2004. Early Earth differentiation. Earth Planet. Sci. Lett. 225, 253–269. https://doi.org/10.1016/j.epsl.2004.07.008

Wang, H.S., Liu, F., Ireland, T.R., Brasser, R., Yong, D., Lineweaver, C.H., 2019. Enhanced constraints on the interior composition and structure of terrestrial exoplanets. Mon. Not. R. Astron. Soc. 482, 2222–2233. https://doi.org/10.1093/mnras/sty2749

Wang, Y., Liu, Z.T.Y., Khare, S. V., Collins, S.A., Zhang, J., Wang, L., Zhao, Y., 2016. Thermal equation of state of silicon carbide. Appl. Phys. Lett. 108. https://doi.org/10.1063/1.4941797

Williams, J.-P., Nimmo, F., 2004. Thermal evolution of the Martian core: Implications for an early dynamo. Geology 32, 97. https://doi.org/10.1130/G19975.1

Williams, Q., 2009. Bottom-up versus top-down solidification of the cores of small solar system bodies: Constraints on paradoxical cores. Earth Planet. Sci. Lett. 284, 564–569. https://doi.org/10.1016/j.epsl.2009.05.019

Wilson, H.F., Militzer, B., 2014. Interior Phase Transformations and Mass-Radius Relationships of Silicon-Carbon Planets. Astrophys. J. 793, 34. https://doi.org/10.1088/0004-637X/793/1/34

Winn, J.N., Fabrycky, D.C., 2015. The Occurrence and Architecture of Exoplanetary Systems. Annu. Rev. Astron. Astrophys. 53, 409–447. https://doi.org/10.1146/annurev-astro-082214-122246

Wolszczan, A., Frail, D.A., 1992. A planetary system around the millisecond pulsar PSR1257 + 12. Nature 355, 145–147. https://doi.org/10.1038/355145a0

Xu, S., Wu, W., Xiao, W., Yang, J., Chen, J., Ji, S., Yican Liu, 2008. Moissanite in serpentinite from

the Dabie Mountains in China. Mineral. Mag. 72, 899–908. https://doi.org/10.1180/minmag.2008.072.4.899

Yoshida, M., Onodera, A., Ueno, M., Takemura, K., Shimomura, O., 1993. Pressure-induced phase transition in SiC. Phys. Rev. B 48, 10587–10590. https://doi.org/10.1103/PhysRevB.48.10587

Zhao, R., Wang, P., Yao, B., Hu, T., Yang, T., Xiao, B., Wang, S., Xiao, C., Zhang, M., 2015. Co effect on zinc blende–rocksalt phase transition in CdS nanocrystals. RSC Adv. 5, 17582–17587. https://doi.org/10.1039/C4RA14798G

Zhu, F., Li, J., Walker, D., Liu, J., Lai, X., Zhang, D., 2019. Origin and consequences of non-stoichiometry in iron carbide Fe7C3. Am. Mineral. 104, 325–332. https://doi.org/10.2138/am-2019-6672

Zhuravlev, K.K., Goncharov, A.F., Tkachev, S.N., Dera, P., Prakapenka, V.B., 2013. Vibrational, elastic, and structural properties of cubic silicon carbide under pressure up to 75 GPa: Implication for a primary pressure scale. J. Appl. Phys. 113. https://doi.org/10.1063/1.4795348

Zinner, E., 2007. Presolar Grains, in: Treatise on Geochemistry. Elsevier, pp. 1–33. https://doi.org/10.1016/B0-08-043751-6/01144-0

Zinner, E., Ming, T., Anders, E., 1989. Interstellar SiC in the Murchison and Murray meteorites: Isotopic composition of Ne, Xe, Si, C, and N. Geochim. Cosmochim. Acta 53, 3273–3290. https://doi.org/10.1016/0016-7037(89)90107-5

Zinner, E., Ming, T., Anders, E., 1987. Large isotopic anomalies of Si, C, N and noble gases in interstellar silicon carbide from the Murray meteorite. Nature 330, 730–732. https://doi.org/10.1038/330730a0

Zinner, E., Nittler, L.R., Gallino, R., Karakas, A.I., Lugaro, M., Straniero, O., Lattanzio, J.C., 2006. Silicon and Carbon Isotopic Ratios in AGB Stars: SiC Grain Data, Models, and the Galactic Evolution of the Si Isotopes. Astrophys. J. 650, 350–373. https://doi.org/10.1086/506957

Acknowledgments

First of all I want to thank Guillaume Morard and Guillaume Fiquet for giving me this incredible opportunity of working here and supporting me, my work, and sharing with me their knowledge and experience. Guillaume Professor Morard, thank you for always dealing my stubbornness. For putting me in the conditions of learning as much as I could from this PhD. For the countless discussions about data, science and exoplanets and of course for introducing me to the magic of synchrotron experiments, I think also the walls at IMPMC (and not only) now know that I like synchrotrons.

Thank you to Anat Shahar and James Badro for agreeing to be reviewers of this thesis and to Giovanna Tinetti, Sébastien Merkel, Chrystèle Sanloup and Pierre Beck for being part of the jury.

I would also like to thank Daniele, for being always available for discussion and ready to offer an advice, as well as introducing me to the art of diamond anvil cell loading.

My officemates Fang and Antoine and the two Silvias that dealt with my "writing mood" always encouraging me. The lady for her help and enthusiasm also during sleepless synchrotron nights and finally all the IMPMC group and my fellow geologists at Istep.

Caroline in Zurich for sharing her knowledge about exoplanets, including me in the exoplanets world and collaborating with us and Antoine on the silicon carbide work. Simone in Diamond for having me participating to some of his works. A special thanks to Matteo, Mara and the people at University of Pavia that always welcomed me as one of the family and included me in all the possible occasions. Paccio, my Eosfit guru, always ready to answer my many questions and Ross for the enlightening discussions about equations of state and thermal models. I can't forget that I wouldn't be here if it wasn't for my zen master Simone Tumiati and Carla, that first introduced me to research work and made me consider the idea of making a PhD and of course Frapie that told me about this PhD opening.

On a more personal note, thank you to Silvia, Titta, Fil and Alb for adopting me as a roommate at the "Maison can" and for the time spent together. Zuffa and Giovi for the support despite the distances and the time difference and all my other friends with whom I shared many adventures. Andre, thank you for the patience and the moral support. I would like to thank Anne and my father, Gian and especially my mother, marmot. She always encouraged me to follow my passion and taught me the value of work and if this thesis is complete is also because she came in Paris some days "so I didn't have to care about anything else than writing".

In conclusion, thank you to all the people that I surely forgot to cite and to the reader for arriving here.

Appendix A

Details on the computations for the geodynamic model of a SiC mantle

Rheology of pure Si-C has been measured by Carter et al. (1984) at upper mantle temperature conditions and atmospheric pressure and appears to be very non-Newtonian in a stress range of 100-200 MPa and a relatively low experimental strain rate of 10^{-9}-10^{-7} s^{-1}. To describe the rheology, we used a standard Arrhenius form:

$$\in_a = \frac{A}{\Delta\eta}\exp\left(\frac{E+PV}{RT}\right)\tau^{n-1}\,\tau_a$$

where $\in_a$ is the strain rate tensor, $A = B/G^n$ is a constant derived in Carter et al., (1984) ($B = 5.12\ 10^{29}$ s^{-1} and the shear modulus G = 130 GPa), E is the activation energy (found to be E = 711 kj/mol), V is the activation volume, n = 5.6 is a constant, τ_a is the deviatoric tress tensor and τ its second invariant. $\Delta\eta$ imposes the viscosity jump as it only is equal to 1 in the upper mantle and is successively takes other values in the lower mantle through our parameter study. The activation volume V results in a gradual viscosity increase with depth. For Earth materials in the dislocation creep regime, common values for V span over from 10-30 10^{-6} m^3/mol (Green and Borch, 1987; Karato and Wu, 1993; Karato and Jung, 2003), although this physical property is extremely hard to measure experimentally as the effect of pressure on deformation is small compared to temperature. The viscosity η (P,T,τ) required for our numerical simulations can be obtained using Equation 1 together with the standard definition $\tau_a = 2\,\eta\,\in_a$.

The equations of thermal compressible convection are solved using the code StagYY (Tackley, 2008) in 2D spherical annulus geometry (Hernlund and Tackley, 2008) using a 8th of annulus (see Figure 8). We solve the equations of momentum and mass conservations and implicit heat diffusion using the UMFPACK direct solver (Davis, 2004) available through PETSC toolkit (Balay et al., 1997). The finite difference approximation is performed on a staggered grid (Harlow and Welch, 1965) with radial mesh refinement in the outer and inner boundary layers. The domain is discretized by 64 times 64 cells and we use free-slip conditions at all boundaries. A tracer field is advected through the grid using a second order spatial interpolation of the velocity field on each tracer and a fourth order Runge-Kutta advection scheme throughout time. Each tracer carries temperature to avoid numerical diffusion during advection. Since the rheology is non-Newtonian, we perform Picard iterations to converge the viscosity at each time step using logarithmic under-relaxation. At each iteration, in log scale, 30% of the new stress-based viscosity is used together with 70% of the previous viscosity. Iterations are performed until the largest viscosity variations becomes smaller than 0.01 % of the viscosity itself.

The surface temperature is fixed at 300 K and the initial core temperature is 5000 K. We use a simple parameterisation for core cooling using its heat capacity and the heat flux at the base of the mantle. In the mantle, an Earth-based time-dependent radiogenic heating is assumed: $H = 18.77\ 10^{-12}\ \exp(-t/t_{hl})$

W/kg where t is time and the half-life t_{hl} = 2.43 Gyr. The choice of the initial temperature field in the mantle is very important as the topology of convection patterns (or even the onset of convection itself) is known to depend on the initial state for non-Newtonian rheologies (Solomatov, 2012; Rozel et al., 2014). This is due to the fact that the viscosity decreases with increasing stress, which makes initial stresses very important. Starting from boundary layers of homogeneous thicknesses at top and bottom, as it is usually the case in geodynamical simulations, would not provide initial stresses and thus make the onset of convection very difficult. Therefore, we impose an initial thermal state resembling a convection cell in the plate tectonics scenario in which a downwelling and an upwelling are initially imposed on the two sides of the computational domain. Boundary layers have an initial thickness of 50 km (decreasing exponentially with depth) and the magnitude of the initial upwelling and downwelling linearly decrease to 0 from its source to the opposite boundary. White noise of 400 K magnitude is added in each cell to introduce asymmetrical patterns.

The choice of the initial mantle temperature is also rather difficult to make. In the Earth evolutionary simulations often start around 1700 to 2000 K as the present day mantle potential temperature (temperature at the top of the upper mantle if there would be no lithosphere) is close to 1600 K, and it is assumed that the Earth's mantle cooled by ~200-300 K over 4 billion years (Herzberg et al., 2010; Keller and Schoene, 2018). Since giant impacts are also likely to generate magma oceans on rocky planets (Hartmann and Davis, 1975; Golabek et al., 2011), then reaching much higher temperatures, we try various initial mantle potential temperatures T_i between 1900 and 2300 K, although melting is neglected in our geodynamical estimations.

Appendix B

Details on the calculations of the mass radius plot for carbon enriched planets

In the plot in Figure 5.7 we show mass-radius curves of different idealized planetary compositions. For the C-rich planetary interiors, we assume a pure iron core surrounded by a mantle made of pure SiC. For the computation of the mass-radius relationships we solve the hydrostatic equilibrium equation that incorporates equation of state modelling.

The equation of hydrostatic equilibrium is:

$$\frac{dP(r)}{dr} = -G \cdot m(r) \cdot \rho(r) \frac{-Gm(r)\rho(r)}{r^2}$$

Where P is the pressure, r is the radius, rho the density, and G the gravitational constant. The mass contained in a spherical shell m(r) is described by:

$$\frac{dm(r)}{dr} = 4\pi r^2 \rho(r)$$

The relationship between pressure P, temperature T, and density rho is given by the Eos P(r) = *f* (ρ(r), P(r)). For the SiC-mantles, we use the hereby-determined 3rd order Birch-Murnaghan EoS (Table 1) and the Holland-Powel thermal pressure model (Table 2).

For the core, we use the EoS fit of iron in the hcp (hexagonal close-packed) structure provided by (Bouchet et al., 2013) on ab initio molecular dynamics simulations for pressures up to 1500 GPa. This EoS fit is optimal for the modelling of Earth-like exoplanets up to ten Earth masses.

Numerically, we solve equations (1) and (2), start at a central pressure and integrate outwards up to the planetary surface R, where the pressure is zero. Integrating m(r) over the planetary R yields the planetary mass M. By varying the central pressure for a given idealized interior, we essentially compute a range of M-R pairs that present the coloured curves in Figure 7.

We assume an adiabatic temperature profile for both mantle and core. The adiabat is calculated by:

$$\frac{\mathrm{dT}}{\mathrm{dP}} = \gamma * \frac{\mathrm{T}}{\mathrm{K\_S}}$$

with

$$K_S = (1 + \gamma * \alpha * T) * K\_T$$

which is related to the thermal bulk modulus K_T.

Appendix D

Example of diffraction patterns fitted with the Le Bail method.

FeSi3C3

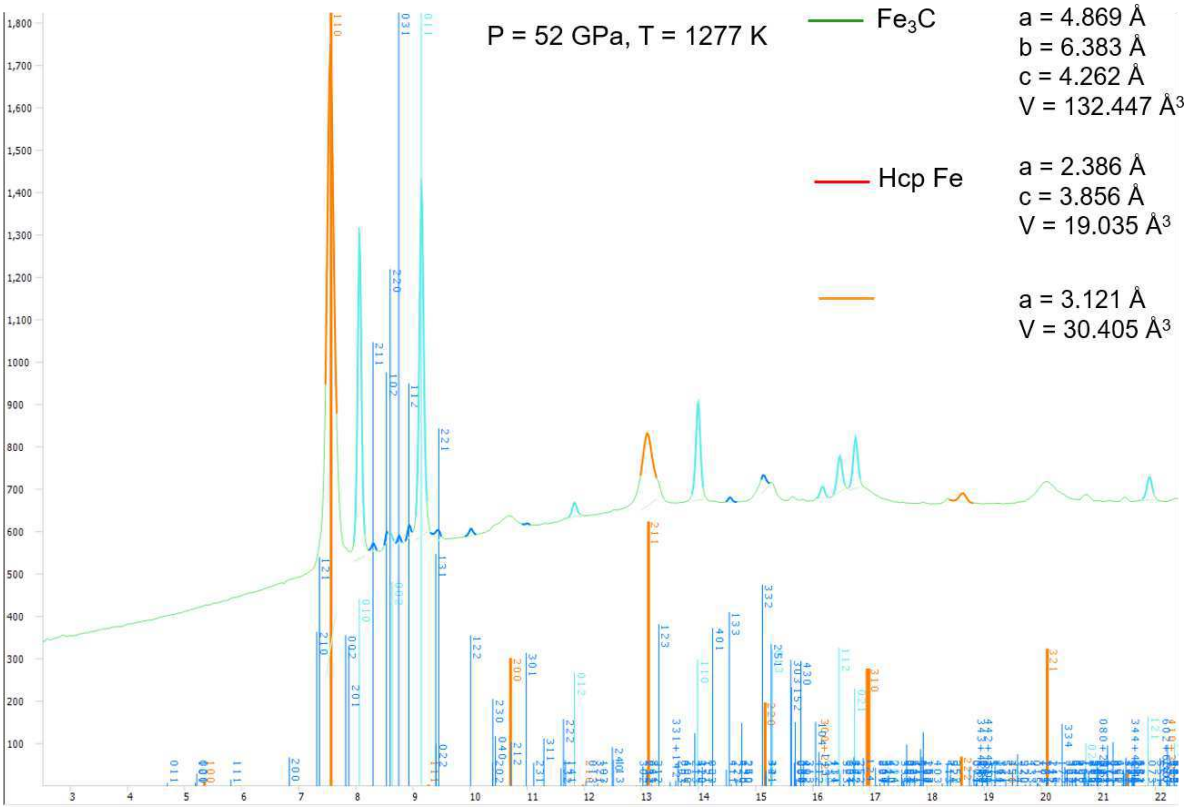

FeSi6C5

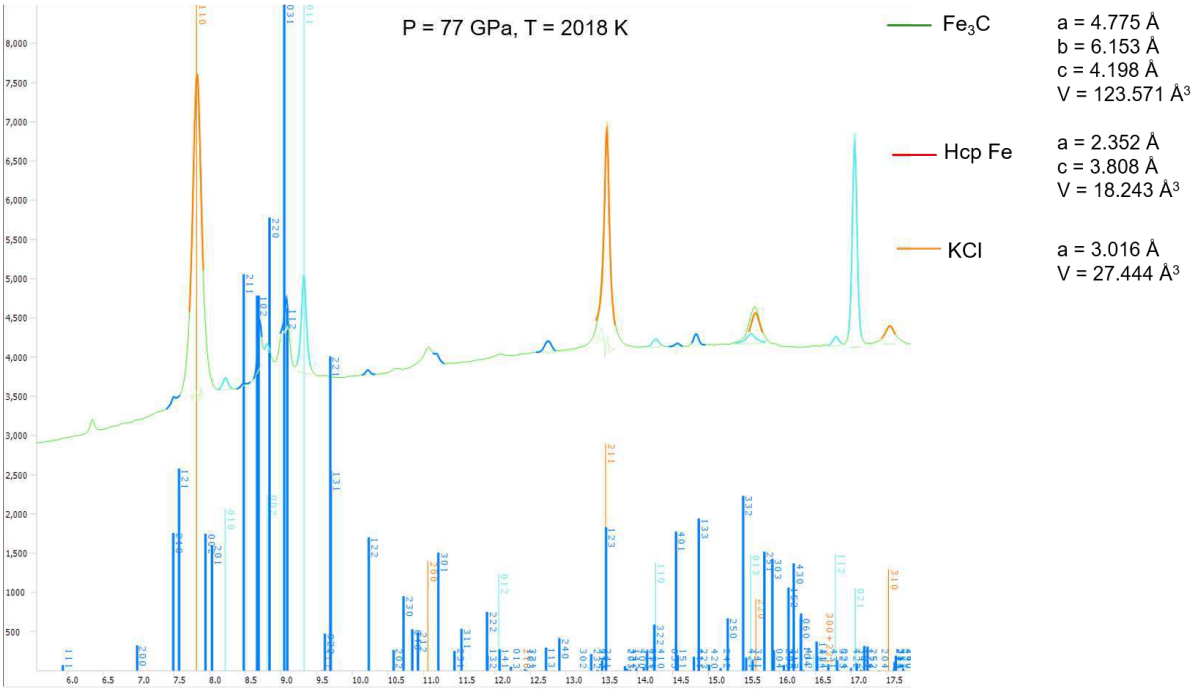

FeSi20C10_1

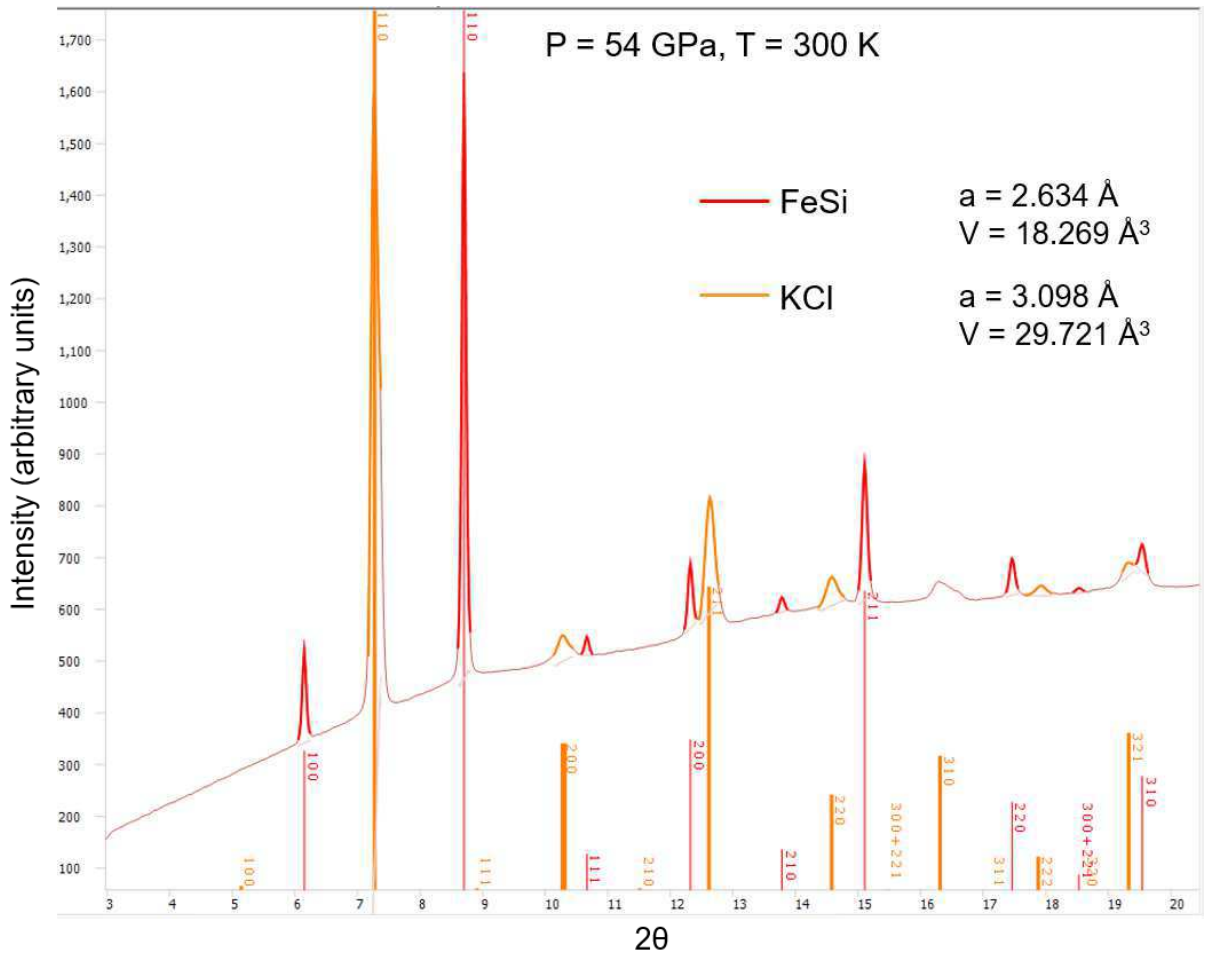

FeSi20C10_2

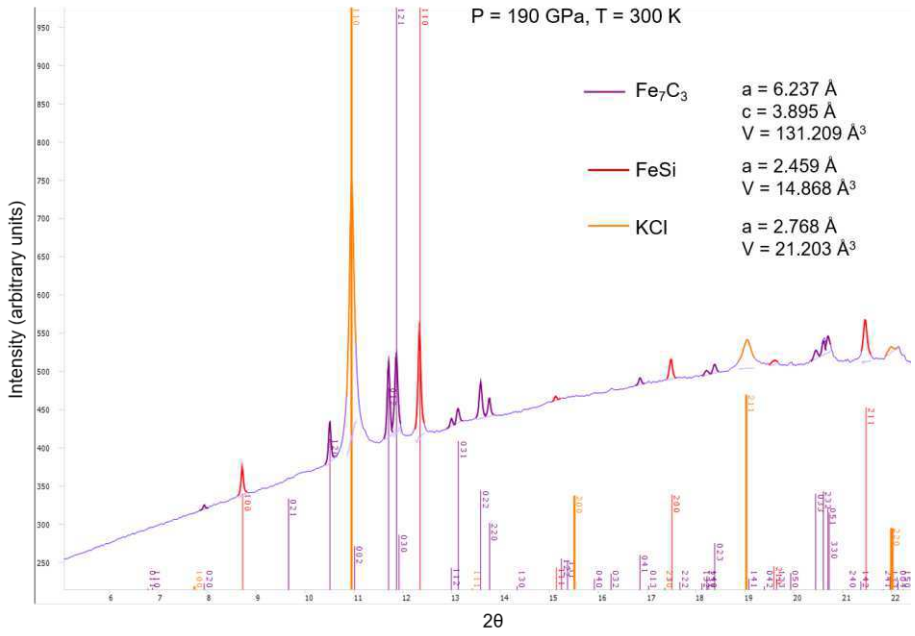

FeSi10C20

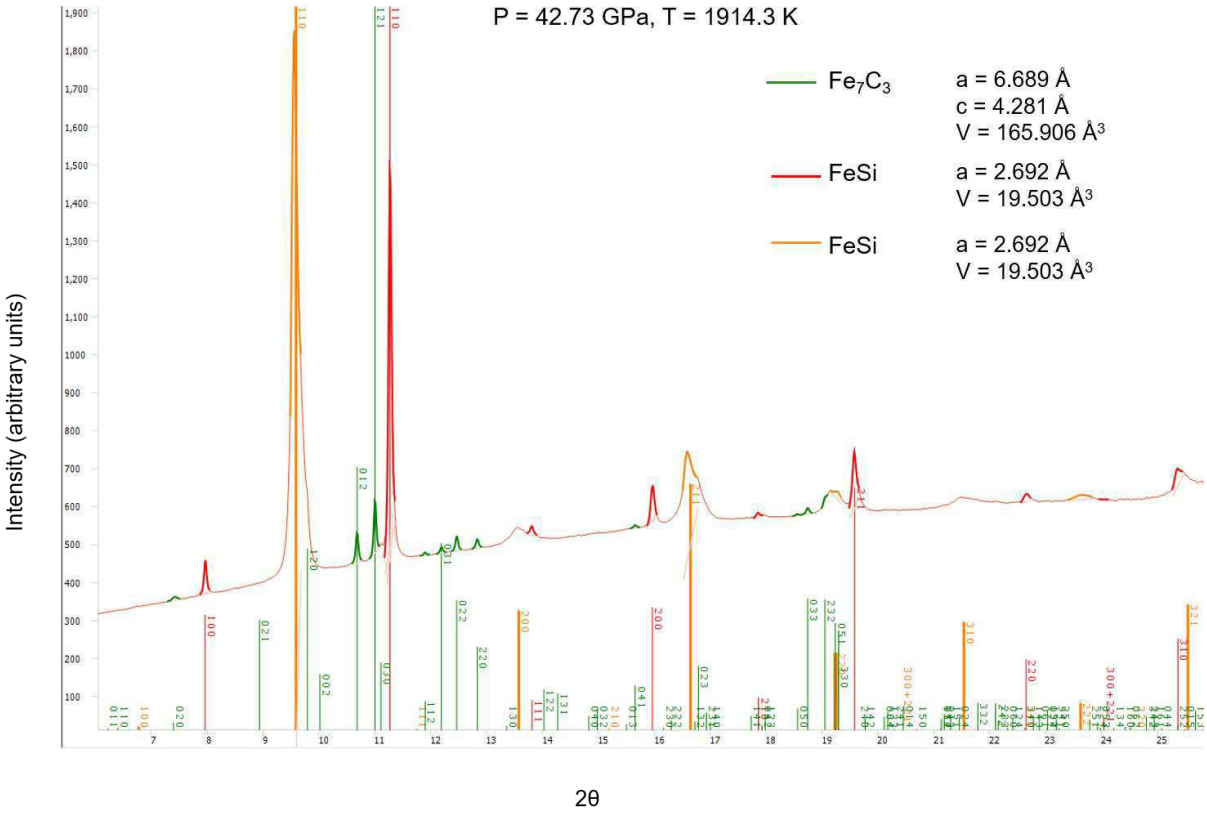
P = 42.73 GPa, T = 1914.3 K
Fe7C3
a = 6.689 Å
c = 4.281 Å
V = 165.906 Å3
FeSi
a = 2.692 Å
V = 19.503 Å3
FeSi
a = 2.692 Å
V = 19.503 Å3
Intensity (arbitrary units)
2θ

Appendix C

Co-authored papers cited in the text:

- Miozzi, F., Morard, G., Antonangeli, D., Clark, A.N., Mezouar, M., Dorn, C., Rozel, A., Fiquet, G., 2018. Equation of State of SiC at Extreme Conditions: New Insight Into the Interior of Carbon-Rich Exoplanets. J. Geophys. Res. Planets 19, 2295–2309. https://doi.org/10.1029/2018JE005582
- Morard, G., Boccato, S., Rosa, A.D., Anzellini, S., Miozzi, F., Henry, L., Garbarino, G., Mezouar, M., Harmand, M., Guyot, F., Boulard, E., Kantor, I., Irifune, T., Torchio, R., 2018. Solving Controversies on the Iron Phase Diagram Under High Pressure. Geophys. Res. Lett. 45, 11,074-11,082. https://doi.org/10.1029/2018GL079950
- Mashino, I., Miozzi, F., Hirose, K., Morard, G., Sinmyo, R., 2019. Melting experiments on the Fe–C binary system up to 255 GPa: Constraints on the carbon content in the Earth's core. Earth Planet. Sci. Lett. 515, 135–144. https://doi.org/10.1016/j.epsl.2019.03.020.
- Edmund, E., Antonangeli, D., Decremps, F., Miozzi, F., Morard, G., Boulard, E., Clark, A.N., Ayrinhac, S., Gauthier, M., Morand, M., Mezouar, M., 2019. Velocity-Density Systematics of Fe-5wt%Si: Constraints on Si Content in the Earth's Inner Core. J. Geophys. Res. Solid Earth. https://doi.org/10.1029/2018JB016904.

Journal of Geophysical Research: Planets

RESEARCH ARTICLE
10.1029/2018JE005582

Equation of State of SiC at Extreme Conditions: New Insight Into the Interior of Carbon-Rich Exoplanets

F. Miozzi[1], G. Morard[1], D. Antonangeli[1], A. N. Clark[2], M. Mezouar[3], C. Dorn[4], A. Rozel[5], and G. Fiquet[1]

[1]Institut de Minéralogie, de Physique des Matériaux, et de Cosmochimie (IMPMC), Sorbonne Université, UMR CNRS 7590, IRD, Muséum National d'Histoire Naturelle, Paris, France, [2]Department of Earth and Planetary Sciences, Northwestern University, Evanston, IL, USA, [3]European Synchrotron Radiation Facility, Grenoble, France, [4]Institute of Computational Sciences, University of Zurich, Zurich, Switzerland, [5]Institute of Geophysics, Department of Earth Sciences, ETH Zurich, Zurich, Switzerland

Key Points:
- We experimentally determined the SiC thermal equation of state up to 200 GPa and 3,500 K
- We constrain the SiC B3-B1 phase transition and expand the Si-C binary phase diagram mapping
- Carbon-enriched planets can have the same mass-radius relationship as Earth's-like planets but different dynamical behavior

Supporting Information:
- Supporting Information S1
- Data Set S1

Correspondence to:
F. Miozzi,
francesca.miozzi@upmc.fr

Citation:
Miozzi, F., Morard, G., Antonangeli, D., Clark, A. N., Mezouar, M., Dorn, C., et al. (2018). Equation of state of SiC at extreme conditions: New insight into the interior of carbon-rich exoplanets. *Journal of Geophysical Research: Planets*, *123*, 2295–2309. https://doi.org/10.1029/2018JE005582

Received 26 FEB 2018
Accepted 26 JUL 2018
Accepted article online 6 AUG 2018
Published online 6 SEP 2018

Abstract There is a direct relation between the composition of a host star and that of the planets orbiting around it. As such, the recent discovery of stars with unusual chemical composition, notably enriched in carbon instead of oxygen, supports the existence of exoplanets with a chemistry dominated by carbides instead of oxides. Accordingly, several studies have been recently conducted on the Si–C binary system at high pressure and temperature. Nonetheless, the properties of carbides at the pressure-temperature conditions of exoplanets interiors are still inadequately constrained, effectively hampering reliable planetary modeling. Here we present an in situ X-ray diffraction study of the Si–C binary system up to 200 GPa and 3,500 K, significantly enlarging the pressure range explored by previous experimental studies. The large amount of collected data allows us to properly investigate the phase diagram and to refine the Clapeyron slope of the transition line from the zinc blende to the rock salt structure. Furthermore, the pressure-volume-temperature equation of state is provided for the high-pressure phase, characterized by low compressibility and thermal expansion. Our results are used to model idealized C-rich exoplanets of end-members composition. In particular, we derived mass-radius relations and performed numerical simulations defining rheological parameters and initial conditions which lead to onset of convection in such SiC planets. We demonstrate that if restrained to silicate-rich mantle compositions, the interpretation of mass-radius relations may underestimate the interior diversity of exoplanets.

1. Introduction

1.1. Exoplanets

Exoplanets represent one of the most vibrant current research topics in space sciences. Since the first exoplanet was discovered (e.g., Mayor & Queloz, 1995), the technological progresses have greatly enhanced this field of research, largely fostered by the quest of Earth's twin planets. The Kepler space telescope (Borucki et al., 2011), the first telescope devoted to exoplanets discovery, detected and confirmed more than a thousand exoplanets. For some of them, it has been possible to measure mass and radius and to get insights on the atmosphere's chemistry. Conversely, although fundamental for the determination of inner structure, thermal behavior, and their evolution (Unterborn et al., 2014), the composition and mineralogy of exoplanets can be only indirectly constrained. It is commonly accepted that the bulk elemental composition of planets depends on the host star composition and the condensation sequence of the accretion disk (e.g., Duffy et al., 2015; Kuchner & Seager, 2005; Mena et al., 2010; Moriarty et al., 2014). Along with sun-like stars, surveys have proved the existence of host stars with diverse chemical compositions (Bond et al., 2010, and references therein) and, in particular, with unusual high value of carbon. The carbon to oxygen ratio (C/O) deeply affects the mineralogy of a planet, defining the distributions of major elements (e.g., Fe, Si, and Mg) among carbides and oxides (Bond et al., 2010). A value of the C/O ratio higher than 0.8 is expected to lead to planets that, while still involving Si, Fe, and Mg, as main available elements, are prevalently made by carbon-bearing compound (C-rich planets) instead of oxides (Bond et al., 2010; Kuchner & Seager, 2005). The discovery of 55 Cancri-e, a planet orbiting around a star with C/O = 1.12 ± 0.19 (Mena et al., 2010), boosted the interest for C-rich planets, promoting studies on iron and silicon carbides under high pressures. Madhusudhan et al.

(2012) provided the first models, suggesting that a wide range of composition in the Fe–Si–C system can satisfy the mass and radius observed for 55 Cancri-e, especially when errors on measurements are properly taken into account. A recent revision of the estimates, due to the problematic assignment of an oxygen spectral line in previous works (see details in Nissen, 2013; Nissen et al., 2014; Teske et al., 2013), supports a value of C/O of 0.78 (±0.08) instead of 1.12 and, more generally, revised downward the estimates of the C/O abundances for many hosts. Thus, the actual existence of C-rich exoplanets, at least around the so far discovered host stars, seems unlikely. Nonetheless, in view of the increasingly large variability in stars composition and the ongoing space survey for new exoplanets, the study of C-rich mineralogical assemblages remains of direct interest. Noteworthy, the revised C/O value for 55 Cancri-e is still higher than the C/O of the sun (C/O = 0.58; Nissen, 2013) and may lead to differences in the mineralogical assemblages of the planets. Moreover, C-rich planetesimals have been suggested to form even around moderately carbon-enhanced stars ($0.65 < C/O < 0.8$; Moriarty et al., 2014). In support of this, it should be noticed that silicon carbide grains (SiCs) were discovered as presolar grains in several meteorites (e.g., Hoppe et al., 2010; Lodders & Fegley, 1995). Finally, the recent launch of the Tess mission (https://tess.gsfc.nasa.gov/) will significantly increase the number of discovered exoplanets and very likely find candidates with exotic compositions, such as C-rich exoplanets. Therefore, investigating chemical variations in planetary systems, from Earth-like to carbon-enriched planets, is expected to gain even further importance in the near future. Are carbides stable at planetary conditions? Can they even be the main constituents of a planet? To address these questions, we performed an experimental study under high pressure and temperature and determined the phase diagram of the Si–C binary system and the equations of state (EoSs) of stable compounds, information essential to the modeling of C-rich exoplanets interior.

1.2. Silicon Carbide

SiC has always been considered a compound of great interest for materials science, with numerous uses both at ambient and high pressure and/or temperature conditions. Among different SiC polytypes stable at ambient conditions, we focused on the 3C structure (β-Sn), a cubic structure with a stacking made by three bilayers periodicity. This is the most studied structure, together with the hexagonal polymorph (SiC 6H), because it shows the highest symmetry and, consequently, the highest electron mobility. Pioneering works on SiC were performed with computational method (e.g., Chang & Cohen, 1987) and experimental methods, employing both static (e.g., Yoshida et al., 1993) and dynamic (e.g., Sekine & Kobayashim, 1997) compression. The bulk of carried-out work pointed out a pressure-induced phase transition to a cubic rock-salt structure, whose exact location in the pressure-temperature space is still matter of debate. Shock experiments studies locate the transition at higher pressure with respect to static experiments. According to the pioneering experimental study of Yoshida et al. (1993), in the 3C polymorph, the phase transition takes place at 100 GPa under ambient temperature, while different computational studies instead indicate a pressure range between 60 and 80 GPa (Thakore et al., 2013). The latter value is also supported by the experimental work by Daviau and Lee (2017a), which located the phase transition between 60 and 70 GPa. We also note that the complete transition is not described in this study. The latest report by Kidokoro et al. (2017) is based on a rescaling of calculations made by Catti (2011) and advocates for a higher transition pressure.

Pressure-volume EoS for the 3C structure was derived by Bassett et al. (1993) and Zhuravlev et al. (2013) from Raman and Brillouin spectroscopy studies, while Nisr et al. (2017) recently employed in situ X-ray diffraction (XRD) to determine its thermal EoS. Due to its possible application as an advanced ceramic, other studies provided the thermo-physical properties of SiC (e.g., Clayton, 2010; Karch et al., 1996; Stockmeier et al., 2009) and thermal parameters of B3 SiC. However, no experimental data at high temperature is available on the high-pressure polymorph with B1 structure. Wilson and Militzer (2014) first addressed the behavior of silicon carbide at extreme conditions by a density functional theory study. They present numerical simulations on the binary Si–C system up to 40 Mbar and provide a first model of a SiC-based exoplanet. Aside from this computational study, very little is known on Si–C binary system at extreme conditions.

In this work we present the results obtained from high pressure-high temperature experiments on both the B1 and B3 polymorphs of SiC-combining laser-heated diamond-anvil cells (LH DAC) and in situ XRD. The results allow us (1) to give a precise pressure range for the phase transition; (2) to define the thermal EoS for the low and high pressure polymorphs of SiC; (3) to experimentally determine the phase diagram of the Si–C binary system up to 200 GPa; and (4) to propose mass-radius relations and dynamics for idealized C-rich putative exoplanets.

2. Method

2.1. Samples

Starting materials were synthetized via physical vapor deposition (PVD). The PVD process consists in sputtering atoms from a chemically uniform target onto a specific substrate (a glass slide in our case). Elements extraction process in the target is enhanced by the generation of a magnetic field in a chamber filled with ionized argon plasma. The result is a homogeneous thin film deposition of the chosen chemical composition on the substrate. Starting materials synthesized with the same recipes and equipment have been employed in previous LH-DAC experiments studies (Hirose et al., 2017; Morard et al., 2017) and bring several advantages to the experiments.

The amount of material produced with one deposition is enough to provide samples for several experimental runs, guaranteeing the reproducibility of the experiments. The surface flatness also yields a better optical coupling with the infrared laser and a very stable heating. PVD samples are typically made by nanocrystalline grains, which would ideally be identified with diffraction by the presence of diffuse rings on the image plate. The low atomic weight of Si and C, however, makes it difficult to clearly identify the signal coming from the starting material prior to any heating. The absence of signal on the image plate, observed for each new location on the sample, is thus a guarantee for its textural homogeneity and the pristine nature of each new heating spot.

Samples consisted in nonstoichiometric SiC deposition, with a variable thickness, from 3.5 to 6 μm. Three compositions were chosen, two on the C-rich side of the binary Si–C phase diagram and one on the Si-rich side of the diagram. Electron microprobe analyses were performed on the starting materials (Centre Camparis, UPMC, Paris) using a Cameca SX100 wavelength dispersive spectrometer to measure the two main elements (C and Si). The average of the analyses for each samples results in a composition of 72.67 at % (±1.4) carbon and 27.33 at % (±2.26) silicon for SiC75, 68.7 at % (±1.47) carbon and 31.3 at % (±1.42) silicon for SiC65, and finally, 22.19 at % (±2.71) carbon and 77.81 at % (±2.77) silicon for SiC25.

2.2. Cell Assembly

Samples were loaded in preindented rhenium gaskets (initially 200 μm thick), with a drilled hole of 120, 70, and 35 μm, for diamonds with flat culets of 250 μm and beveled culets of 150/300- and 70/300-μm diameter, respectively. Dried grains of KCl were cold pressed into foils, and disks of the right diameter were cut by a femto-second laser and stored at 120 °C in an oven before the loading. Samples were sandwiched between two KCl disks to provide thermal and chemical insulation from the diamonds culets. KCl is not only a suitable pressure transmitting media and thermal insulator but also a reliable pressure calibrant. Such assemblages were loaded in membrane-driven Le Toullec-type diamond anvil cells, equipped with tungsten carbide seats designed for diamonds with a conical support (Boehler & De Hantsetters, 2004), providing a maximum 2-theta angle of 70°.

2.3. XRD Measurements at High Pressure and High Temperature

Angle dispersive XRD experiments were performed on the high-pressure beamline ID27 at the European Synchrotron Radiation Facility in Grenoble (Mezouar et al., 2005). The beamline setup provides a monochromatic beam of 33 KeV ($\lambda = 0.3738$ Å, Iodine k-edge) focused on a sample area of less than 3×3 μm^2 (full width at half maximum). Exposure time was usually between 10 and 30 s, and the diffraction signal was collected on a MAR CCD detector. Heating is provided by two continuous Nd:YAG fiber laser (Transverse Electromagnetic Mode (TEM) 00) focused over a heating spot >20 μm in diameter. The power on the two sides was adjusted independently, in order to minimize axial temperature gradients. Temperature was measured on both sides of the sample before and after the X-ray exposure (only upstream during the exposure), at the center of the hot spot region. The analysis of the thermal emission is made on a 2×2 μm^2 area selected by a pinhole placed at the entrance of the spectrometer. Temperatures are obtained by the spectroradiometric method, using reflective collective optics (Schultz et al., 2005). Uncertainties on the temperature measurements come from the temperature gradient in the sample and the uncertainties on the fitting procedure. Following Schultz et al. (2005), the gradient in the radial direction is less than 50 K in the X-ray spot, in virtue of the >20-μm heating spot versus the less than 3-μm diameter spot probed by the X-ray beam. The double side laser heating and the controlled geometry of the assembly contribute to maintain the axial gradient below 100 K. Therefore, for our experiments, we assumed an error on the sample's temperature of ±150 K

(Morard et al., 2011). Pressure was determined by the thermal EoS of KCl by Dewaele et al. (2012), assuming the temperature of KCl to be the average between the temperature on the culet of the diamond (295 K) and the temperature measured at the surface of the sample (Campbell et al., 2009). Uncertainties on pressure determination are obtained, as described in supporting information Text S1, accounting for the uncertainties on the temperature calibration for KCl.

Different experimental protocols have been used for the initial determination of the phase diagram, to refine the transition pressure and to measure the EoS. In the first case, the cells were first pressurized to a target pressure. Infrared lasers were then aligned, and the power increased step by step. Diffractions were collected for each temperature step. Once the pressure range of the phase transition was bracketed, two additional experimental runs were performed to narrow the pressure interval. In these runs, compression was cycled, both increasing and decreasing pressure at constant temperature. The first appearance upon compression of the high-pressure polymorph peaks (or disappearance of the low pressure polymorph) was taken as a reference for the phase transition. Coexistence of the two phases was also observed in several diffraction patterns.

The software DIOPTAS (Prescher & Prakapenka, 2015) was used to integrate the 2-D diffraction images. Diffraction of a CeO_2 powder standard allowed us to calibrate the detector distance and orientation parameters. Parameters of the unit cell were then calculated by fitting the peak positions with a pseudo-Voigt Gaussian curve, with the program PD Indexer (http://pmsl.planet.sci.kobe-u.ac.jp/~seto/).

2.4. Equations of State

There are several formalisms linking the variation of volume to that of pressure (isothermal EoS), each with its own assumption and mathematical development (e.g., Angel, 2000; Angel et al., 2014, 2017; Duffy & Wang, 1998; Kroll et al., 2012). Here we employed a Birch-Murnaghan EoS, that is a *finite strain EoS*, in which the strain energy of a solid undergoing compression is expressed as a Taylor series in the finite Eulerian strain f_E, where $f_E = \frac{1}{2}\left[\left(\frac{V_0}{V}\right)^{\frac{2}{3}} - 1\right]$ (Angel, 2000). The expansion to the third order in the finite strain yields to the relation:

$$P = \frac{3}{2} K_0 \left[\left(\frac{V_0}{V}\right)^{\frac{7}{3}} - \left(\frac{V_0}{V}\right)^{\frac{5}{3}}\right]\left\{1 + \frac{3}{4}\left[K_0' - 4\right]\left[\left(\frac{V_0}{V}\right)^{\frac{2}{3}} - 1\right]\right\}. \quad (1)$$

V is the volume, V_0 and K_0 are, respectively, the volume and bulk modulus at ambient pressure and reference temperature (here 300 K), and K_0' is the first pressure derivative of the bulk modulus ($\partial K/\partial P$). A second formalism largely used for EoS of solids is the one by Vinet, derived from interatomic potentials and designed to better represent materials under very high compression (Vinet et al., 1986, 1987), which gives

$$P = 3K_0 \frac{(1 - f_V)}{f_V^2} \exp\left(\frac{3}{2}\left(K_0' - 1\right)(1 - f_V)\right), \quad (2)$$

where $f_V = \left(\frac{V}{V_0}\right)^{\frac{1}{3}}$.

As those EoSs are both considered to satisfactorily describe the compression of solid materials over the pressure range of our interest, we decided to fit our data with both and then choose the one giving less residuals.

The thermal pressure EoS model, in which the volumes explicitly and independently depends on both pressure and temperature, can describe the high temperature behavior of compressed materials. This approach requires the determination of the pressure at reference temperature condition, that is, 300 K isotherm in our case $P(V,300\ \mathrm{K})$, and then thermal pressure with increasing temperature along isochors $P_{\mathrm{th}}(V,T)$. Consequently, the pressure at a given temperature is defined as:

$$P(V,T) = P(V,300\mathrm{K}) + P_{\mathrm{th}}(V,T). \quad (3)$$

To calculate the second term, two main thermal pressure EoSs are used in literature, the Mie Grüneisen Debye and the Thermal Pressure (TP) model (Kroll et al., 2012). The Mie Grüneisen Debye (MGD) model relies on a Debye-like approach, where the thermal-induced lattice vibrations are modeled as a series of harmonic

oscillators. The vibrational energy of the lattice is expressed as a function of the temperature T normalized to the characteristic Debye temperature θ_D and written as

$$E(T,\theta_D) = 9nRT\left(\frac{T}{\theta_D}\right)^3 \int_0^{\frac{\theta_D}{T}} \frac{t^3 dt}{e^t - 1}, \tag{4}$$

where n is the number of atoms per formula unit and R the gas constant. The Debye temperature

$$\theta_D = \theta_0 \ \exp\left[\frac{(\gamma_0 - \gamma(V))}{q}\right], \tag{5}$$

is a function of the Grüneisen parameter (γ) given by

$$\gamma(V) = \gamma_0 \left(\frac{V}{V_0}\right)^q, \tag{6}$$

where q corresponds to the logarithmic volume dependence of γ (V). γ and θ_D only depend on the volume and are constant along isochors. The vibrational energy, together with the Grüneisen parameter and the volume, defines the thermal pressure, with the Ec and Tc being energy and temperature at reference conditions:

$$P_{\text{th}} = \frac{\gamma(V)}{V}\left[E(T,\theta_D) - \mathrm{E_c}(T_c,\theta_D)\right]. \tag{7}$$

In summary, in the MGD model, parameters that control the thermal pressure and hence allow the description of the thermal state of the system are only three: the Debye temperature, the Grüneisen parameter, and q (see Angel et al., 2017, and references therein).

The second approach is the TP model. In this model the slope of an isochor in the pressure-temperature space is written as

$$\left(\frac{\partial P}{\partial T}\right)_V = \alpha_V K_0, \tag{8}$$

(Anderson 1984; Angel et al., 2017; Poirier, 1991) with α_V being the thermal expansion. Consequently, during an isochoric heating, thermal pressure can be written as

$$P_{\text{th}} = \int_{T_0}^{T} \alpha_V K_0 \partial T. \tag{9}$$

The product $\alpha_V K_0$ is usually assumed to be constant along an isochor, as isochors are linear for T above the Debye temperature. Holland and Powell (2011) also defined an approximation for the integral of P_{th}, explicitly introducing the dependence upon the Einstein function to account for the decrease to 0 as temperature decreases to 0 K (Angel et al., 2017; Holland & Powell, 2011).

$$\xi = \frac{u^2 e^u}{(e^u - 1)^2}, \tag{10}$$

with $u = \theta_E/T$ and θ_E being the Einstein temperature. Following Holland and Powell (2011), P_{th} can then be written as

$$P_{\text{th}} = \alpha_{V0} K_0 \left(\frac{\theta_E}{\xi_0}\right)\left(\frac{1}{\exp\left(\frac{\theta_E}{T}\right) - 1} - \frac{1}{\exp\left(\frac{\theta_E}{T_0}\right) - 1}\right), \tag{11}$$

with ξ (T_0) as in the thermal expansion equation from Kroll et al. (2012).

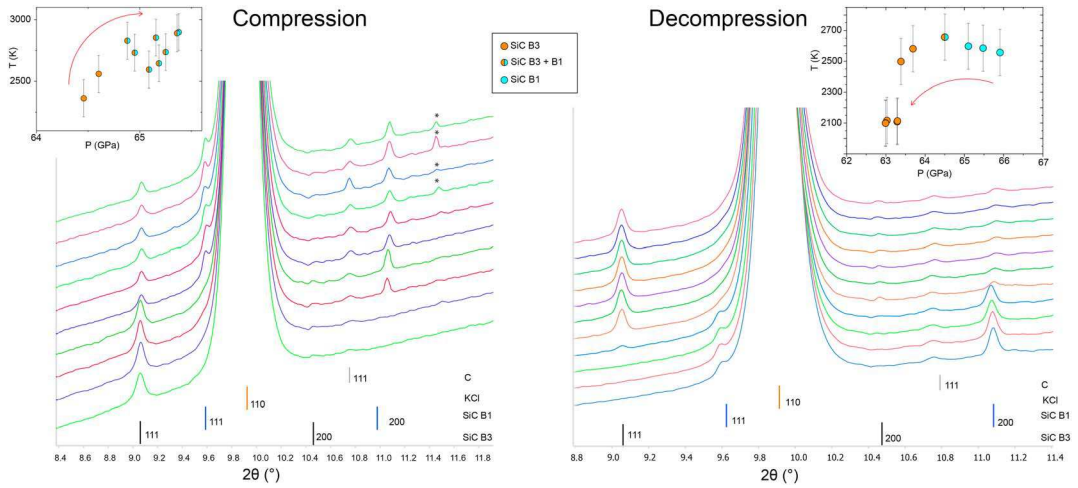

Figure 1. Diffraction patterns collected on SiC75 along selected pressure-temperature paths (displayed in the insets) showing the phase transition from the zinc-blende structure to the rock-salt structure upon compression (left) and decompression (right). Reflections for SiC B3, B1, C, and KCl are labeled. The star signs identify peaks coming from a spurious spot on the image plate.

$$\zeta(T_0) = \frac{\left(\frac{\theta_E}{T_0}\right)^2 \exp\left(\frac{\theta_E}{T_0}\right)}{\left[\exp\left(\frac{\theta_E}{T_0}\right) - 1\right]^2}. \tag{12}$$

The Einstein temperature (θ_E) can be assessed from the measured entropy. In particular, for end-members, the value of θ_E = 10,363/(S/n + 6.44), with S being the molar entropy and n the numbers of atoms (Holland & Powell, 2011). Alternatively, the Einstein temperature can be calculated from the Debye temperature, employing the relation ($\theta_E = \theta_D$ * 0.806). In the TP model, thermal pressure only depends on two parameters: the coefficient of thermal expansion (α_v) and the Einstein temperature (θ_E; which is usually fixed).

Both the MGD and the TP thermal models were used to fit our data. Indeed, MGD is one of the most common parameterization to represent the pressure-volume-temperature relations of a solid material under extreme conditions and has already been used for the B3 structure by Nisr et al. (2017). On the other hand, TP is typically used for rigid structures, and recent studies (e.g., Angel et al., 2017; Milani et al., 2017) demonstrate that TP provides a reliable and trustworthy thermal model especially for compounds that, as SiC, have properties similar to diamond. However, it should be noted that assuming the product $\alpha_V K_0$ constant along an isochor is an approximation, and as such, it might not be always adequate (Jackson & Rigden, 1996). A discussion about the results and which model better matches our experimental data set will be presented in section 3.2.

3. Results and Discussion

3.1. Phase Transition

High-pressure and high-temperature experiments were performed up to 205 GPa and 3,500 K, respectively. As the starting materials were nonstoichiometric compounds, heated samples systematically disproportionated into SiC + Si or SiC + C, thus allowing us to study stoichiometric SiC simultaneously with the Si–C phase relations. KCl peaks only were visible on the diffraction patterns collected before laser heating. As previously said, with nanocrystalline grains produced by the PVD process, the low weight of both Si and C makes extremely difficult a clear identification of the diffuse signal on the image plate before any heating. SiC diffraction peaks indeed start being detectable after initial heating and recrystallization during lasers alignment. The B3 SiC diffraction pattern is then characterized by four reflections, 111, 200, 220, and, at higher angle, 311, sometimes merged with the 211 reflection from KCl. At low pressure, the most intense reflection is the 111 (Figure 1 and supporting information S1). After the phase transition to the B1 structure, occurring between 65 and 70 GPa, the 111 reflection shifts closer to the 110 reflection of KCl, almost merging with it, and the 200 becomes the most intense reflection. As highlighted in Figure 2a, the phase

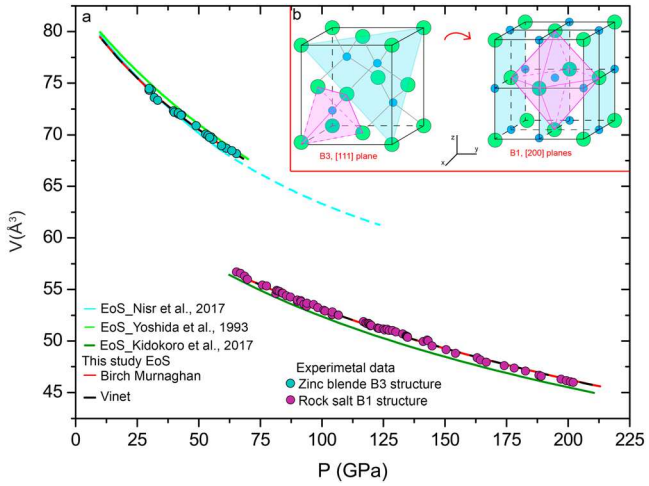

Figure 2. (a) Plot of the volume as a function of pressure at T = 300 K. Symbols represent the experimental data from this study, and the lines represent different fitted EoS. Two models from this study and three available from literature; (b) structure of the two SiC polymorphs. In light pink, the coordination of the atoms, and in light blue, the planes responsible for the most intense reflection, respectively, the 111 for SiC B3 and the 200 for SiC B1.

transition involves a significant volume reduction, with the value of the cell parameters changing, depending from actual temperature, from a = 4.09–4.10 Å (±0.002) (V = 68.80–69.06 (±0.1) Å^3) to a = 3.85–3.88 (±0.004) Å (V = 57.4–58.6 (±0.2) Å^3). Our measurements are in agreement with previous reports in literature (e.g., Daviau & Lee, 2017a; Thakore et al., 2013; Yoshida et al., 1993) and advocate for a structural transition from a cubic zinc-blende structure (B3) to a cubic rock-salt structure (B1), driven by a coordination change from tetrahedral to octahedral (Figure 2b).

The large pressure-temperature range explored during our experiments and the large number of data points allowed us to narrow down the range for the B3-B1 transition of SiC compound (Figure 3), solving the controversy between previous studies (e.g., Daviau & Lee, 2017a; Yoshida et al., 1993). Noteworthy, the fine texture of our samples, highlighted by the continuous diffraction rings on our collected patterns, helps to unambiguously define the structural transition. Our findings clearly place the transition at 66 ± 2 GPa at room temperature and between 65 and 70 GPa at high temperature, in agreement with suggestion from previous LH DAC experiments (Daviau & Lee, 2017a) and the computational work (Thakore et al., 2013). This transition pressure is significantly lower than earlier determination at ambient temperature by Yoshida et al. (1993) and the recent proposition at high temperature by Kidokoro et al. (2017). As in Daviau and Lee (2017a), we find no evidence of intermediate structures on the transition pathway, such as the orthorhombic or tetragonal structures reported in several computational works (e.g., Catti, 2001; Durandurdu, 2004).

Diffraction patterns showing the coexistence of both phases define a steep, almost vertical (0.001 GPa/K) Clapeyron slope in the pressure-temperature space for the B3-B1 phase transition (Figure 3). This behavior differs from what proposed by Daviau and Lee (2017a). Indeed, if their first point at higher pressure showing coexistence falls within our coexistence range, their second point is located in a region where we only observe the stable B3 structure. Comparison with Kidokoro et al. (2017) further supports a negative Clapeyron slope, although, as already mentioned, there is a shift in the reported pressure range of the phase transition (which is 10 GPa lower in our case).

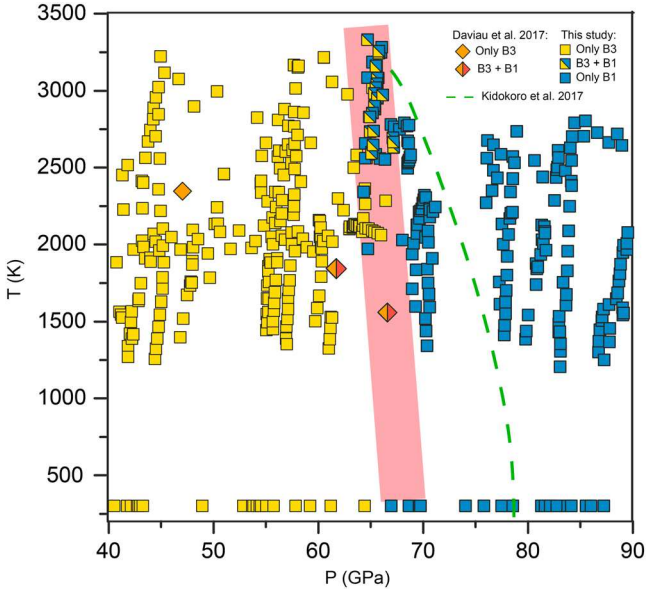

Figure 3. (Squares) Data from this study at P = 40–90 GPa and T = 300–3,500 K. SiC B3, B1, and B3-B1 coexistence are reported in different colors; the phase transition region is highlighted by the light red band. Diamonds illustrate the data from Daviau and Lee (2017a). The green dashed line is the slope showed in Kidokoro et al. (2017) obtained after a rescaling of results by Catti (2001).

3.2. Equation of State

3.2.1. Room Temperature EoS

The room temperature EoS and the thermal EoS were defined for both the low-pressure B3 and the high-pressure B1 structures. The data taken at ambient temperature were fitted with both the third-order Birch Murnaghan (BM3) and the Vinet EoS. As laser heating was required to crystallize the sample, it was not possible to collect data points below 25 GPa where melting of the KCl pressure medium occurs at too low temperature. Thus, the lack of those points does not allow a reliable determination of V_0. As a consequence, a V_0 value fixed to that determined by Nisr et al. (2017) was employed to fit the B3 structure EoS. The fitting was performed using the EosFit suite (Angel et al., 2014; Gonzalez-Platas et al., 2016). Obtained fit parameters, along with the data from previous work, are summarized in Table 1. Parameters obtained using BM3 and Vinet are within the error bars, but we observe a better fit using BM3 (for the rock-salt structure χ^2 are 5.1 and 5.43, respectively, for BM3 and Vinet). Accordingly, we decided to employ the values obtained with the BM3 EoS as a reference for the thermal EoS.

Table 1
Pressure-Volume Equations of State Fit Results for Both the Low Pressure (B3) and High Pressure (B1) Structure

	Zinc-blende structure					Rock-salt structure		
	This study		Yoshida et al., 1993	Zhuravlev et al., 2013	Nisr et al., 2017	This study		Kidokoro et al., 2017
EoS	BM	Vinet	BM	BM	Vinet	BM	Vinet	BM
V_0 (Å^3)	82.80[a]	82.80[a]	82.92	82.96	82.80	66.3 (0.1)	66.3 (1.4)	67.5
K_0 (GPa)	224 (5)	222 (5)	260	218	243	323 (3)	324 (2)	235
K_0'	4.1 (0.3)	4.3 (0.4)	2.9	3.75	2.68	3.1 (0.43)	3.3 (0.52)	4

Note. Data from previous experimental works are also shown. EoS = equation of state; BM = Birch Murnaghan.
[a]Value from Nisr et al. (2017).

Our compressibility value for the B3 structure is lower than the values found in previous XRD work on powders (e.g., Nisr et al., 2017; Yoshida et al., 1993) but is comparable with the values reported for SiC single crystal using combined XRD and Brillouin spectroscopy (Zhuravlev et al., 2013). Regarding the B1 structure, the obtained values for K_0 and K_0' are respectively higher and lower than those proposed by Kidokoro et al. (2017). The differences can be partially explained by the different orders used for the Birch Murnaghan EoS (second order for Kidokoro et al., 2017, i.e., K_0' fixed to 4, and third order in this study). However, we consistently obtain a higher bulk modulus of 323–324 GPa, even when the reference volume is fixed. It is thus unlikely this difference only originates in the pressure scale. We think the larger data set and pressure range used in our study may help to set harder constraints on the EoS as it shows the need for a third-order EoS.

3.2.2. Thermal EoS

The thermal EoSs were also determined for both the low pressure and high pressure structures. For the zinc-blende B3 structure, as far as Debye temperature, γ_0, and V_0, we used the values determined from previous literature works (i.e., Clayton, 2010; Karch et al., 1996; Stockmeier et al., 2009). For the high pressure B1 structure, instead, we fixed the Debye temperature as in Varshney et al. (2015) and refined all the other parameters.

For both structures, the fitting of the EoS was performed using the EoSFit suite (Angel et al., 2014; Gonzalez-Platas et al., 2016). For the zinc-blende structure, we collected 105 data points with pressure ranging between 25 and 65 GPa and temperature between 300 and 2,500 K. The fit of the MGD model results in a compressibility of 228 ± 7 GPa, and a K_0' of 3.9 ± 0.3. The only parameter refined for the thermal model (q) has a value of −1.3. A negative value of q implies that the Grüneisen parameter increases with compression. Although quite an unusual behavior, this was already reported by Nisr et al. (2017) for one of the pressure scales they used. Most likely, the negative value of q does not have a physical meaning and simply is a numerical consequence of a fit performed over relatively limited pressure range with points showing some scatter, in particular at high temperature.

Fit to the data with the TP model yields better residuals in pressure (i.e., smaller difference between actual measurements and pressure given by the EoS; Figure 4b). The value of the Einstein temperature was fixed to that calculated from the Debye temperature of the MGD model ($\theta_E = \theta_D * 0.806$). The obtained parameters for the zinc-blende B3 structure are K_0 = 224 ± 2 GPa and K_0' = 4.08 ± 0.2 with $\alpha_V = 0.62\ 10^{-5} \pm 0.1\ K^{-1}$. The latter is lower than previous experimental determination by Nisr et al. (2017) but is close the values derived from calculations by Varshney et al. (2015). The compressibility and pressure derivative have the same values as in the Birch-Murnaghan 300 K EoS with smaller errors on the parameters, while the values found with the thermal MGD model are slightly different. The isotherms shown in Figure 4a nicely account for the entire data set with a χ^2 of 0.70.

In the stability field of the high-pressure rock-salt (B1) structure, 348 points were used to refine the thermal EoS, over a pressure range between 65 and 205 GPa and temperatures between 300 and 3,000 K. In the MGD thermal model refinement, the Debye temperature was kept fixed to the value reported by Varshney et al. (2015), and the reference pressure is considered equal to zero. As a standard procedure for the fit, we first refined only γ_0 and q using the V_0, K_0, and K_0' obtained with the EoS at 300 K. Then, for the final processing cycle, also the value of V_0, K_0, and K_0' were refined together with the other parameters of the thermal model. The best-fit solution yields V_0 = 65.90 ± 0.04 Å^3, K_0 = 340 ± 10 GPa, and K_0' = 3.06 ± 0.06, with a Debye

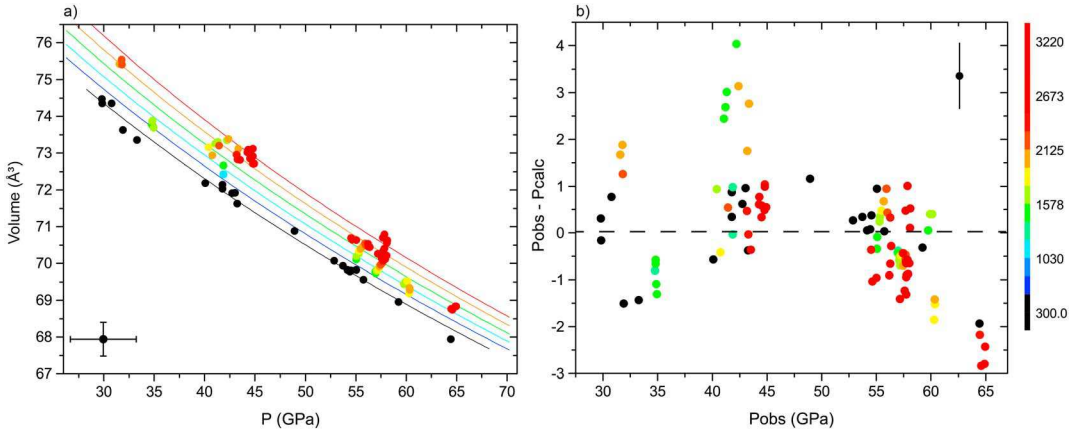

Figure 4. Results obtained fitting the zinc-blende structure with the Thermal Pressure model: (a) experimental data points and isotherms; (b) pressure residuals of the fit. On the right the temperature scale.

temperature of 1,200 K, $\gamma_0 = 0.50 \pm 0.05$ and $q = 1.6 \pm 0.5$, with $\chi^2 = 2.46$. The here-obtained value of γ_0 is lower (0.5 vs. 1.06) than that from previous computational work (i.e., Varshney et al., 2015). Effect of the dependence on γ_0 of the fits was also investigated (details in Text S2). The plot of the pressure residuals shown in Figure 5b highlights the high quality of the fit, which stays within ±5 GPa over the whole pressure-temperature range investigated.

The same procedure, fixing the value of the Einstein temperature, was followed for the TP model. The obtained results are $V_0 = 65.9 \pm 0.04$ Å^3, $K_0 = 339 \pm 2$ GPa, $K_0' = 3.03 \pm 0.02$, and $\alpha = 0.58 \times 10^{-5} \pm 0.01$ K^{-1} with the Einstein temperature calculated from of the Debye temperature of B1 structure. The refined values for V_0, K_0, and K_0' are the same as for the MGD model within error bars, and $\chi^2 = 2.67$ (see Figure S6). The coefficient of thermal expansion falls within the range of values derived from theoretical models (Varshney et al., 2015) which also predicted a significant decrease across the transition from the B3 to the B1 structure. The obtained results are presented in Table 2. Refined V_0, K_0, and K_0' show a reasonable agreement, that is, almost within error bars, with parameters determined at ambient temperature. Accordingly, we consider the V_0, K_0, and K_0' obtained with the two thermal models as our preferred set of parameters to describe the high pressure-high temperature behavior of SiC high-pressure (B1) structure.

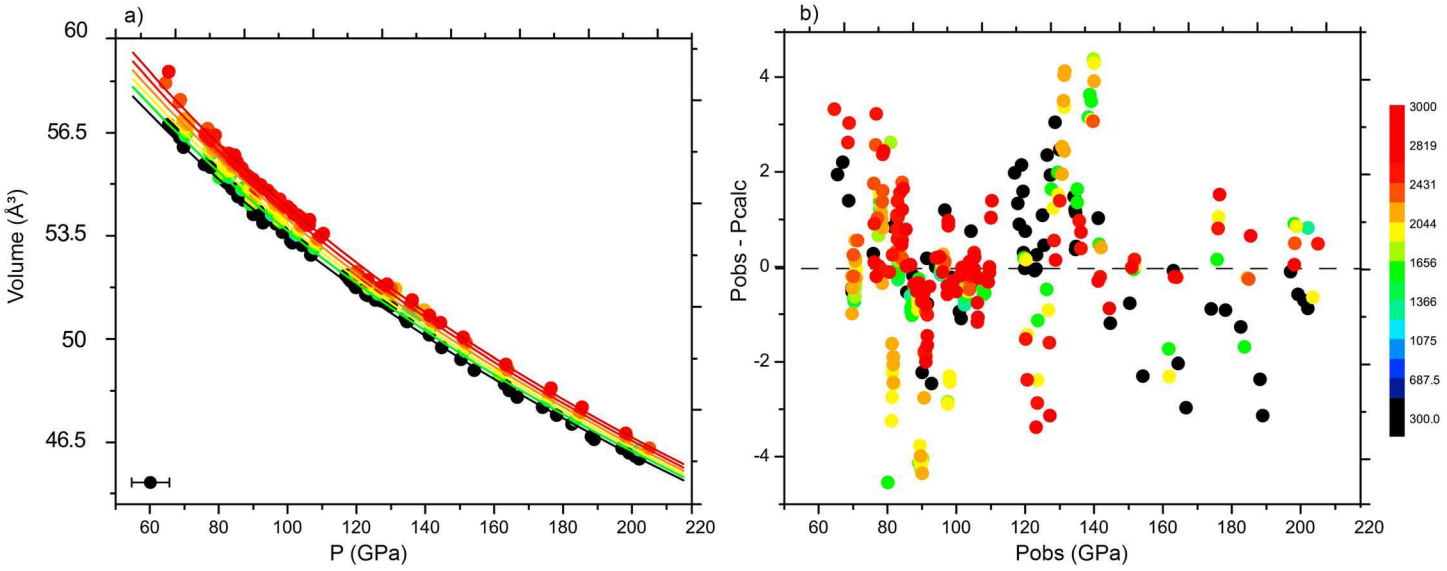

Figure 5. Results obtained fitting our data for the B1 structure with the Mie Grüneisen Debye thermal model: (a) experimental points and isotherms from 300 to 3,000 K; (b) pressure residuals for the fit. On the right the temperature scale.

Table 2
Values of the Thermal Equation of State for the Two Structures, Fitted With Both the Mie Grüneisen Debye and the Thermal Pressure Models

	Zinc-blende structure		Rock-salt structure	
	MGD	TP	MGD	TP
Number of data points	105	105	348	
V_0 (Å^3)	82.80[a]	82.80[a]	65.8 (0.04)	65.9 (0.04)
K_0 (GPa)	228 (7)	224 (2)	339 (10)	339 (2)
K_0'	3.9 (0.3)	4.1 (0.14)	3.06 (0.06)	3.03 (0.02)
T Debye (K)	1,200[a]		1,200[a]	
γ_0	1.06[a]		0.50 (0.05)	
q	−1.3 (0.5)		1.67 (0.5)	
T Einstein (K)		976.2[a]		976.2[a]
Alpha(10^{-5} K^{-1})		0.62 (0.11)		0.56 (0.01)

Note. MGD = Mie Grüneisen Debye; TP = Thermal Pressure.
[a]Parameters are kept fixed.

3.3. Phase Diagram

Having performed measurements with starting materials of different composition allowed us to probe not only SiC compound EoS but also to explore the binary Si–C system. Notably, the three different Si–C compositions employed for the experiments enabled us to study both the silicon-rich side and the carbon-rich side of the phase diagram. Our main conclusion regarding the binary mixing is that, over the entire pressure and temperature range of this study, no intermediate compound has been observed. A SiC + Si assemblage is stable on the Si-rich side of the diagram, whereas a SiC + C assemblage is observed on the C-rich side of the diagram (Figure 6). This is in disagreement with the stability of silicon dicarbide (SiC_2) predicted by theory at pressure of 25 GPa by Andrew et al. (2012) and suggested to appear only above 10 Mbar by Wilson and Militzer (2014). In addition, we do not observe any decomposition of SiC compound or change in diffraction peaks intensity over 2,000 K, in the pressure range 30–60 GPa as described in Daviau and Lee (2017b).

On the Si-rich side of the diagram, we have been able to determine the melting temperature at 2,100 K and 60 GPa for the sample SiC25, based on the disappearance of the solid diffraction peaks and a simultaneous plateau in the laser power versus temperature curve. Due to the low Z of the material, we could not detect the appearance of diffuse scattering. Our melting criterion thus possibly leads to overestimating the melting temperature (Figure 6). As no other signatures of melting were observed, we hypothesize the composition with 77.81 at % Si and 22.19 at % C to be close to the eutectic. On the C-rich side, no melting was detected in the whole examined pressure range for temperature up to 3,500 K. This could be related to the difference of melting temperature of the two end-members, Si and C. Diamond has indeed a very high melting temperature, much larger than that of Si. Such a large difference in the melting temperature can have strong implications for planetary dynamics through melt production for any small Si enrichment, whereas the two-phase assemblage (i.e., SiC + C) can stay solid in C-rich systems. Overall, the resulting phase diagram is in agreement with the phase diagrams from Wilson and Militzer (2014).

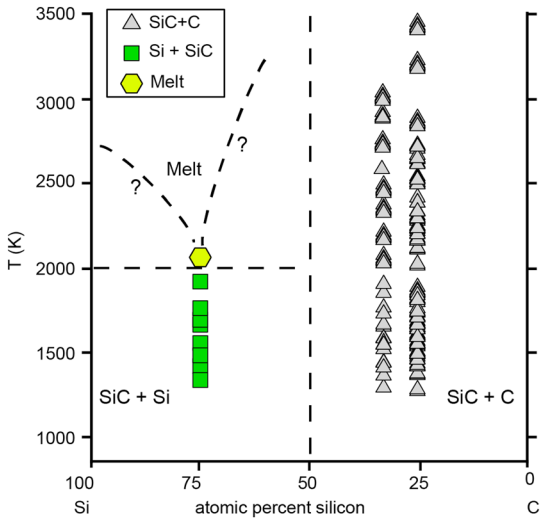

Figure 6. Phase diagram of the Si–C binary system at P = 60 GPa.

4. Implications for Exoplanets Studies

4.1. Mass-Radius Relation for SiC-Based Planets

The parameters obtained on the Si–C binary system for the EoSs and phase diagram were used to model mass-radius curves for different C-rich planets composition (Figure 7). Extrapolations have been limited by the validity of the used equations. Accordingly, we only modeled planets up to 5 times the mass of the Earth. Similar models have already been proposed in the past, usually plotting mass-radius relations for archetypal planets made entirely by one element (i.e., carbon or iron) or one compound (i.e., $MgSiO_3$, SiC, and H_2O), as in Duffy et al. (2015).

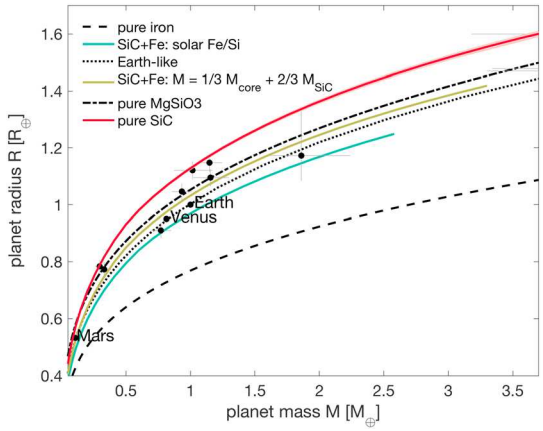

Figure 7. Mass-radius relations for different idealized exoplanet interiors together with the standard comparison curves (pure Fe, $MgSiO_3$, and earth like). We propose several C-rich end-members: a pure SiC planet, an iron core + SiC mantle planet with mass proportions similar to the Earth's core and mantle, and finally, an iron core + SiC mantle planet with a bulk ratio of Fe/Si that matches solar abundances. The black dots show the measured masses and radii for solar system planets and some observed exoplanets. Details on the calculation of the M/R plot are provided in supporting informations, Text S3.

In this study, along with the mass-radius plots for commonly considered end-members (i.e., pure SiC and $MgSiO_3$), we present the mass-radius curves for several idealized carbon-rich differentiated planets in which a pure iron core is assumed (EoS from Bouchet et al., 2013). The proposed inner compositions represent end-members that are unlikely to occur in nature, due to the absence of both Mg and O, as equally unlikely end-members (due to the lack of major rock-forming elements) are planets entirely made of pure $MgSiO_3$ or pure Fe. Nonetheless, such Mg- and O-free end-members were already studied by different authors (e.g., Madhusudhan et al., 2012; Nisr et al., 2017; Wilson & Militzer, 2014). Studying end-member compositions, we provide reference limit values of the bulk density that can be used to interpret the possible interiors of such exoplanets. Planets less dense than pure $MgSiO_3$, for example, are classically believed to incorporate a high amount of volatiles. Very interestingly, our data show that planets with carbon-rich interiors can also be less dense than a pure $MgSiO_3$ (see Figure 7).

Along with a hypothetical planet made by pure SiC, as already done in previous literature, we also considered two models that include Fe, in different proportions, as Fe is consider one of the most common elements in C-rich exoplanets. In the first model of an Earth-like planet, the iron core makes up a third of the planets mass. In the second model, the proportions of Fe and SiC are chosen so as the bulk composition of the planet matches solar Fe/Si abundances (solar Fe/Si; Lodders et al., 2009). In the pressure range examined in this experimental study, our density estimates agree very well with theoretical density functional theory calculations from Wilson and Militzer (2014; i.e., less than 1% variation on R at 2 Me for pure SiC planets). As expected, the addition of iron to a pure SiC interior increases the planet density. The Fe + SiC model with core mass proportions similar to Earth's core yields to a mass-radius relationship very similar to the Earth-like case. Thus, in this case, it is almost impossible to discriminate between an Earth-like interior and a carbon-rich interior on the sole basis of mass and radius. This highlights the importance of having independent constrains on the composition of planetary interiors.

4.2. Estimations on the Geodynamics of SiC Planets

The thermal evolution of a planet is governed by its geodynamical regime, affecting both deep and shallow processes. The growing knowledge about properties of Earth's minerals contributes to improve the models representing the dynamical behavior of silicate-rich planets. Nevertheless, little is known about the potential effects of carbides, in particular SiC, on convection.

Studies focused on deep Earth's minerals highlighted how phase transitions might have a first-order effect on the dynamics of a planet (Green & Borch, 1987; Karato & Wu, 1993; Karato & Jung, 2003 in Text S4). The upper to lower mantle transition at 660-km depth is known to have an effect on the dynamic topography (Flament et al., 2013) and the geoid (Hager, 1984; Ricard et al., 1993), due to an increase in viscosity (~30). On the other hand, phase transitions such as the perovskite to bridgmandite generate a small viscosity jump ($\ll$1; e.g., Nakagawa & Tackley, 2011; Yamazaki et al., 2006). As SiC undergoes a phase transition that involves a large volume change, it is of primary interest to evaluate the effect of a potential viscosity jump on the rheological behavior and, consequently, on planet's dynamics. Unfortunately, parameters such as viscosity, deformation mechanism, and activation energies have only been evaluated at ambient pressure on SiC compounds often doped with other chemical elements, to enhance the quality for industrial application. The absence of those parameters for the pure compound, coupled with the uncertainties regarding the characteristic of C-rich exoplanets, thus limits the possibilities of running complex numerical models. We thus decided to investigate how different values of viscosity jump and activation volume affect the dynamic of a planet, by mapping the onset of mantle convection, for different initial temperatures.

We performed numerical simulations on a pure SiC mantle for a planet with one Earth mass (B3–B1 phase transition occurring around 1,830-km depth), employing the thermodynamic parameters obtained in this study and the rheological data from Carter et al. (1984). All details about the employed equations,

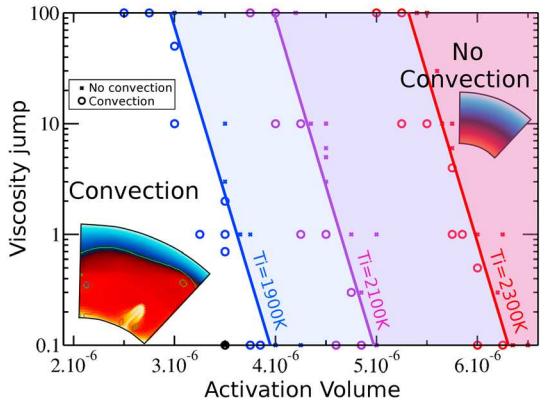

Figure 8. Map of the onset of convection in all numerical simulations. Open circles show simulation in which convection started, and crosses show when convection never started. Blue, purple, and red data represent cases with initial mantle potential temperature of 1,900, 2,100, and 2,300 K, respectively. Thick lines represent the regime boundary between convection and diffusion (see equation (13)). The 2-D images show two examples of temperature field with convection (bottom left) or not (top right) in our computational domain. The isocontours show viscosities of $\eta = 10^{19}$ pa.S (red), $\eta = 10^{21}$ pa.S (green), and $\eta = 10^{23}$ pa.S (blue).

numerical setup (Balay et al., 1997; Davis, 2004; Harlow & Welch, 1965; Hernlund & Tackley, 2008; Tackley, 2008), and boundary conditions (Rozel et al., 2014; Solomatov, 2012) are provided in Text S4. A surface thermal conductivity of 270 $W{\cdot}m^{-1}{\cdot}K^{-1}$ (Goldberg et al., 2001) was employed in this study. To account for high pressure effects, the conductivity across the mantle was multiplied by the ratio between density under pressure and at the surface.

The obtained results are summarized in Figure 8. The viscosity jump from 0.1 to 100 was imposed at the phase transition, and we explored values of the activation volume from 2×10^{-6} to 6×10^{-6} m^3/mol together with three different initial potential mantle temperatures: 1,900, 2,100, and 2,300 K (for details: Golabek et al., 2011; Hartmann & Davis, 1975; Herzberg et al., 2010; Keller & Schoene, 2018). For each initial temperature, our results show that convection only starts in simulations considering low activation volumes (3 10^{-6} to 6 10^{-6} m^3/mol). The viscosity jump employed seems to have little impact on convection as the boundary curves are quite vertical. The boundary between simulations undergoing convection and the stable ones can be approximated by the following equation

$$V_c = 3.62 \times 10^{-6} + \frac{(T_i - 1900)^{1.205}}{400} 6.9 \times 10^{-7} - \ 3.3 \times 10^{-7} \log(\Delta\eta), \quad (13)$$

where V_c is the critical activation volume below which convection starts. This boundary coincides with the blue, purple, and red thick lines in Figure 8 (i.e., for initial temperature equal to 1,900, 2,100, and 2,300 K).

In conclusion, we observed that the onset of convection (after the magma ocean crystallization) strongly depends on the activation volume and the initial temperature. Activation volumes required for convection (~ 3–6 · 10^{-6} m^3/mol) have been found to be lower by a factor of 2 to 10 than typical values for Earth materials. Our estimations demonstrate that dynamics in C-rich exoplanets might be far from what is commonly accepted for Earth. Moreover, we provide a first exploration of the possible geodynamic scenario for planets made by pure SiC.

5. Conclusions

Following the renewed interest for carbon-bearing species and driven by the potential discovery of C-rich exoplanets, our experimental work provides useful information on the behavior of SiC, often considered as one of the main component of carbon-rich exoplanets. In this study we narrow the pressure range for the phase transition. We report a steep Clapeyron slope (0.001 GPa/K) with a precise determination of the volume and density changes across the B3-B1 transition of this compound. We also provide new thermal EoSs, extended up to 200 GPa and 3,000 K. Furthermore, our data can be used to model M/R plots and infer dynamics for different types of C-rich exoplanets. Our results shows that it is difficult to distinguish a carbon-rich planet from an Earth-like planet solely based on bulk density and observed M/R relations. Though the improved and enhanced information we gathered on the high pressure and high temperature behavior of the possible main constituent (SiC) is crucial to narrow the range of mineralogical composition likely to be present in such C-rich exoplanets.

Acknowledgments
The authors wish to thank Stany Bauchau and Jeroen Jacobs (ESRF) for their help with the X-ray experiments and diamond anvil cell preparation. We would like also to thank the two anonymous reviewers for their detailed comments and suggestions for improving the manuscript. Femtosecond laser micromachining at the Institut de Minéralogie de Physique des Matériaux et de Cosmochimie (IMPMC), Paris, has been developed and realized by the "Cellule Project" with the financial support of ANR 2010-JCJC-604-01. This project and F. M., G. M., and G. F. have received funding from the European Research Council (ERC) under the European Union's Horizon 2020 research and innovation Programme (grant agreement 670787). C. D. is funded by the Swiss National Science Foundation under the Ambizione grant PZ00P2_174028. A. B. R received founding from the European Research Council under the European Union Seventh Framework Programme (FP/20072013)/ERC grant agreement 320639 project iGEO and from ETH Zürich. Data are available as supporting information.

References

Anderson, O. L. (1984). A universal thermal equation-of-state. *Journal of Geodynamics*, *1*(2), 185–214.
Andrew, R. C., Braun, M., & Chetty, N. (2012). A theoretical investigation of the stability of crystalline silicon dicarbide. *Computational Materials Science*, *55*, 186–191. https://doi.org/10.1016/j.commatsci.2011.10.040
Angel, R. J. (2000). Equations of state. *Reviews in Mineralogy and Geochemistry*, *41*(1), 35–59. https://doi.org/10.2138/rmg.2000.41.2
Angel, R. J., Alvaro, M., & Nestola, F. (2017). 40 years of mineral elasticity: A critical review and a new parameterisation of equations of state for mantle olivines and diamond inclusions. *Physics and Chemistry of Minerals*, 1–19.
Angel, R. J., Gonzalez-Platas, J., & Alvaro, M. (2014). EosFit7c and a Fortran module (library) for equation of state calculations. *Zeitschrift für Kristallographie*, *229*, 405–419.

Balay, S., Gropp, W. D., McInnes, L. C., & Smith, B. F. (1997). Efficient management of parallelism in object oriented numerical software libraries. In E. Arge, A. M. Bruaset, & H. P. Langtangen (Eds.), *Modern software tools in scientific computing* (pp. 163–202). Boston, MA: Birkhäuser.

Bassett, W. A., Weathers, M. S., Wu, T. C., & Holmquist, T. (1993). Compressibility of SiC up to 68.4 GPa. *Journal of Applied Physics*, *74*(6), 3824–3826. https://doi.org/10.1063/1.354476

Boehler, R., & De Hantsetters, K. (2004). New anvil designs in diamond-cells. *High Pressure Research*, *24*(3), 391–396. https://doi.org/10.1080/08957950412331323924

Bond, J. C., O'Brien, D. P., & Lauretta, D. S. (2010). The compositional diversity of extrasolar terrestrial planets. I. in Situ Simulations. *The Astrophysical Journal*, *715*(2), 1050–1070. https://doi.org/10.1088/0004-637X/715/2/1050

Borucki, W. J., Koch, D. G., Basri, G., Batalha, N., Boss, A., Brown, T. M., et al. (2011). Characteristics of Kepler planetary candidates based on the first data set. *The Astrophysical Journal*, *728*(2), 117. https://doi.org/10.1088/0004-637X/728/2/117

Bouchet, J., Mazevet, S., Morard, G., Guyot, F., & Musella, R. (2013). Ab initio equation of state of iron up to 1500 GPa. *Physical Review B*, *87*(9), 094102. https://doi.org/10.1103/PhysRevB.87.094102

Campbell, A. J., Danielson, L., Righter, K., Seagle, C. T., Wang, Y., & Prakapenka, V. B. (2009). High pressure effects on the iron–iron oxide and nickel–nickel oxide oxygen fugacity buffers. *Earth and Planetary Science Letters*, *286*(3–4), 556–564. https://doi.org/10.1016/j.epsl.2009.07.022

Carter, C. H., Davis, R. F., & Bentley, J. (1984). Kinetics and mechanisms of high-temperature creep in silicon carbide: I, reaction-bonded. *Journal of the American Ceramic Society*, *67*(6), 409–417. https://doi.org/10.1111/j.1151-2916.1984.tb19726.x

Catti, M. (2001). Orthorhombic intermediate state in the zinc blende to rocksalt transformation path of SiC at high pressure. *Physical Review Letters*, *87*(3), 035504. https://doi.org/10.1103/PhysRevLett.87.035504

Chang, K. J., & Cohen, M. L. (1987). Ab initio pseudopotential study of structural and high-pressure properties of SiC. *Physical Review B*, *35*(15), 8196–8201. https://doi.org/10.1103/PhysRevB.35.8196

Clayton, J. A. (2010). Geometrically non-linear model of ceramic crystals with defects applied to silicon carbide (SiC). ARL-TR-5096, Army Res. Lab. Aberdeen Proving Ground, Maryland

Daviau, K., & Lee, K. K. M. (2017a). Zinc-blende to rocksalt transition in SiC in a laser-heated diamond-anvil cell. *Physical Review B*, *95*, 1–6.

Daviau, K., & Lee, K. K. M. (2017b). Decomposition of silicon carbide at high pressures and temperatures. *Physical Review B*, *96*(17), 174,102. https://doi.org/10.1103/PhysRevB.96.174102

Davis, T. (2004). Algorithm 832: Umfpack, an unsymmetric-pattern multifrontal method. *ACM Transactions on Mathematical Software*, *30*(2), 196–199. https://doi.org/10.1145/992200.992206

Dewaele, A., Belonoshko, A. B., Garbarino, G., Ocelli, F., Bouvier, P., Hanfland, M., & Mezouar, M. (2012). High-pressure high-temperature equation of state of KCl and KBr. *Physical Review B*, *85*(21), 214,105. https://doi.org/10.1103/PhysRevB.85.214105

Duffy, T., Madhusudhan, N., & Lee, K. K. M. (2015). Mineralogy of Super-Earth Planets. In *Treatise on Geophysics* (Vol. 2, pp. 149–178). Elsevier B.V. https://doi.org/10.1016/B978-0-444-53802-4.00053-1

Duffy, T. S., & Wang, Y. (1998). Pressure-volume-temperature equations of state. *Reviews in Mineralogy and Geochemistry*, *37*(1), 425–457.

Durandurdu, M. (2004). Pressure-induced phase transition of SiC. *Journal of Physics: Condensed Matter*, *16*, 4411–4417.

Flament, N., Gurnis, M., & Müller, R. D. (2013). A review of observations and models of dynamic topography. *Lithosphere*, *5*(2), 189–210. https://doi.org/10.1130/L245.1

Golabek, G. J., Keller, T., Gerya, T. V., Zhu, G., Tackley, P. J., & Connolly, J. A. (2011). Origin of the Martian dichotomy and Tharsis from a giant impact causing massive magmatism. *Icarus*, *215*(1), 346–357. https://doi.org/10.1016/j.icarus.2011.06.012

Goldberg, Y., Levinshtein, M. E., & Rumyantsev, S. L. (Eds.) (2001). *Properties of advanced semiconductor materials GaN, AlN, SiC, BN, SiC, SiGe* (p. 93). New York: Wiley.

Gonzalez-Platas, J., Alvaro, M., Nestola, F., & Angel, R. J. (2016). EosFit7-GUI: A new GUI tool for equation of state calculations, analyses and teaching. *Journal of Applied Crystallography*, *49*, 1377–1382.

Green, H., & Borch, R. (1987). The pressure dependence of creep. *Acta Metallurgica*, *35*(6), 1301–1305. https://doi.org/10.1016/0001-6160(87)90011-3

Hager, B. H. (1984). Subducted slabs and the geoid: Constraints on mantle rheology and flow. *Journal of Geophysical Research*, *89*(B7), 6003–6015. https://doi.org/10.1029/JB089iB07p06003

Harlow, F., & Welch, J. (1965). Numerical calculation of time-dependent viscous incompressible flow of fluid with a free surface. *Physics of Fluids*, *8*(12), 2182–2189.

Hartmann, W. K., & Davis, D. R. (1975). Satellite-sized planetesimal and lunar origin. *Icarus*, *24*(4), 504–515. https://doi.org/10.1016/0019-1035(75)90070-6

Hernlund, J. W., & Tackley, P. J. (2008). Modeling mantle convection in the spherical annulus. *Physics of the Earth and Planetary Interiors*, *171*(1-4), 48–54. https://doi.org/10.1016/j.pepi.2008.07.037, recent advances in computational geodynamics: Theory, Numerics and Applications.

Herzberg, C., Condie, K., & Korenaga, J. (2010). Thermal history of the Earth and its petrological expression. *Earth and Planetary Science Letters*, *292*, 79–88.

Hirose, K., Morard, G., Sinmyo, R., Umemoto, K., Hernlund, J., Helffrich, G., & Labrosse, S. (2017). Crystallization of silicon dioxide and compositional evolution of the Earth's core. *Nature*, *543*(7643), 99–102. https://doi.org/10.1038/nature21367

Holland, T. J. B., & Powell, R. (2011). An improved and extended internally consistent thermodynamic dataset for phases of petrological interest, involving a new equation of state for solids. *Journal of Metamorphic Geology*, *29*(3), 333–383. https://doi.org/10.1111/j.1525-1314.2010.00923.x

Hoppe, P., Leitner, J., Groner, E., Marhas, K., Meyer, B. S., & Amari, S. (2010). NanoSIMS studies of small presolar SiC grains: New insights into supernova nucleosynthesis, chemistry, and dust formation. *The Astrophysical Journal*, *719*(2), 1370–1384. https://doi.org/10.1088/0004-637X/719/2/1370

Jackson, I., & Rigden, S. M. (1996). Analysis of PVT data: Constraints on the thermoelastic properties of high-pressure minerals. *Physics of the Earth and Planetary Interiors*, *96*(2–3), 85–112. https://doi.org/10.1016/0031-9201(96)03143-3

Karato, S.-I., & Jung, H. (2003). Effects of pressure on high-temperature dislocation creep in olivine. *Philosophical Magazine*, *83*(3), 401–414. https://doi.org/10.1080/0141861021000025829

Karato, S. I., & Wu, P. (1993). Rheology of the upper mantle: A synthesis. *Science*, *260*(5109), 771–778. https://doi.org/10.1126/science.260.5109.771

Karch, K., Pavone, P., Mayer, A. P., Bechstedt, F., & Strauch, D. (1996). First-principles study of thermal properties of 3C SiC. *Physica B*, *220*, 448–450.

Keller, B., & Schoene, B. (2018). Plate tectonics and continental basaltic geochemistry throughout Earth history. *Earth and Planetary Science Letters*, *481*, 290–304. https://doi.org/10.1016/j.epsl.2017.10.031

Kidokoro, Y., Umemoto, K., Hirose, K., & Ohishi, Y. (2017). Phase transition in SiC from zinc-blende to rock-salt structure and implications for carbon-rich extrasolar planets. *American Mineralogist*, *102*(11), 2230–2234. https://doi.org/10.2138/am-2017-6033

Kroll, H., Kirfel, A., Heinemann, R., & Barbier, B. (2012). Axial thermal expansion and related thermophysical parameters in the Mg, Fe olivine solid-solution series. *European Journal of Mineralogy*, *26*(5), 607–621.

Kuchner, M. J., & Seager, S. (2005). Extrasolar carbon planets. *arXiv preprint astro-ph/0504214*.

Lodders, K., & Fegley, B. (1995). The origin of circumstellar silicon carbide grains found in meteorites. *Meteoritics*, *30*(6), 661–678. https://doi.org/10.1111/j.1945-5100.1995.tb01164.x

Lodders, K., Palme, H., & Gail, H. P. (2009). 4.4 Abundances of the elements in the Solar System. In J. Trümper (Ed.), *Solar System. Landolt-Börnstein—Group VI astronomy and astrophysics (numerical data and functional relationships in science and technology)* (Vol. 4B, pp. 712–770). Berlin: Springer.

Madhusudhan, N., Lee, K. K. M., & Mousis, O. (2012). A possible carbon-rich interior in super-Earth 55 Cancri e. *The Astrophysical Journal Letters*, *759*(2), L40. https://doi.org/10.1088/2041-8205/759/2/L40

Mayor, M., & Queloz, D. A. (1995). Jupiter-mass companion to a solar-type star. *Nature*, *378*(6555), 355–359. https://doi.org/10.1038/378355a0

Mena, E. D., Israelian, G., Hernández, J. G., Bond, J. C., Santos, N. C., Udry, S., & Mayor, M. (2010). Chemical clues on the formation of planetary systems: C/O versus Mg/Si for HARPS GTO sample. *The Astrophysical Journal*, *725*(2), 2349–2358. https://doi.org/10.1088/0004-637X/725/2/2349

Mezouar, M., Crichton, W. A., Bauchau, S., Thurel, F., Witsch, H., Torrecillas, F., et al. (2005). Development of a new state-of-the-art beamline optimized for monochromatic single-crystal and powder X-ray diffraction under extreme conditions at the ESRF. *Journal of Synchrotron Radiation*, *12*(5), 659–664. https://doi.org/10.1107/S0909049505023216

Milani, S., Angel, R. J., Scandolo, L., Mazzucchelli, M. L., Ballaran, T. B., Klemme, S., et al. (2017). Thermo-elastic behavior of grossular garnet at high pressures and temperatures. *American Mineralogist*, *102*(4), 851–859. https://doi.org/10.2138/am-2017-5855

Morard, G., Andrault, D., Antonangeli, D., Nakajima, Y., Azuende, A. L., Boulard, E., et al. (2017). Fe-FeO and Fe-Fe_3C melting relations at Earth's core-mantle boundary conditions: Implications for a volatile-rich or oxygen-rich core. *Earth and Planetary Science Letters*, *473*, 94–103. https://doi.org/10.1016/j.epsl.2017.05.024

Morard, G., Andrault, D., Guignot, N., Siebert, J., Garbarino, G., & Antonangeli, D. (2011). Melting of Fe-Ni-Si and Fe-Ni-S alloys at megabar pressures: Implications for the core-mantle boundary temperature. *Physics and Chemistry of Minerals*, *38*(10), 767–776. https://doi.org/10.1007/s00269-011-0449-9

Moriarty, J., Madhusudhan, N., & Fischer, D. (2014). Chemistry in an evolving protoplanetary disk: Effects on terrestrial planet composition. *The Astrophysical Journal*, *787*(1), 81. https://doi.org/10.1088/0004-637X/787/1/81

Nakagawa, T., & Tackley, P. J. (2011). Effects of low-viscosity post-perovskite on thermo-chemical mantle convection in a 3-D spherical shell. *Geophysical Research Letters*, *38*, L04309. https://doi.org/10.1029/2010GL046494

Nisr, C., Meng, Y., MacDowell, A. A., Yan, J., Prakapenka, V., & Shim, S.-H. (2017). Thermal expansion of SiC at high pressure-temperature and implications for thermal convection in the deep interiors of carbide exoplanets. *Journal of Geophysical Research: Planets*, *122*, 124–133. https://doi.org/10.1002/2016JE005158

Nissen, P. E. (2013). The carbon-to-oxygen ratio in stars with planets. *Astronomy & Astrophysics*, *552*, A73. https://doi.org/10.1051/0004-6361/201321234

Nissen, P. E., Chen, Y. Q., Carigi, L., Schuster, W. J., & Zhaom, G. (2014). Carbon and oxygen abundances in stellar populations. *A&A*, *568*(25), 1–19. https://doi.org/10.1051/0004-6361/201424184

Poirier, J. P. (1991). *Introduction to the physics of the Earth's interior*. Cambridge University Press.

Prescher, C., & Prakapenka, V. B. (2015). DIOPTAS: A program for reduction of two-dimensional X-ray diffraction data and data exploration. *High Pressure Research*, *35*(3), 223–230. https://doi.org/10.1080/08957959.2015.1059835

Ricard, Y., Richards, M., Lithgow-Bertelloni, C., & Le Stunff, Y. (1993). A geodynamic model of mantle density heterogeneity. *Journal of Geophysical Research*, *98*(B12), 21,895–21,909. https://doi.org/10.1029/93JB02216

Rozel, A., Besserer, J., Golabek, G. J., Kaplan, M., & Tackley, P. J. (2014). Self-consistent generation of single-plume state for Enceladus using non-Newtonian rheology. *Journal of Geophysical Research: Planets*, *119*, 416–439. https://doi.org/10.1002/2013JE004473

Schultz, E., Mezouar, M., Crichton, W., Bauchau, S., Blattman, G., Andrault, D., et al. (2005). High pressure–high temperature monochromatic X-ray diffraction at the Esrf. *High Pressure Research*, *25*(1), 71–83. https://doi.org/10.1080/08957950500076031

Sekine, T., & Kobayashim, T. (1997). Shock compression of 6H Polytype SiC to 160 GPa. *Physical Review B*, *55*(13), 8034–8037. https://doi.org/10.1103/PhysRevB.55.8034

Solomatov, V. (2012). Localized subcritical convective cells in temperature-dependent viscosity fluids. *Physics of the Earth and Planetary Interiors*, *200-201*, 63–71. https://doi.org/10.1016/j.pepi.2012.04.005

Stockmeier, M., Müller, R., Sakwe, S. A., Wellmann, P. J., & Magerl, A. (2009). On the lattice parameters of silicon carbide. *Journal of Applied Physics*, *105*, 3–7.

Tackley, P. J. (2008). Modelling compressible mantle convection with large viscosity contrasts in a three-dimensional spherical shell using the yin-yang grid. *Physics of the Earth and Planetary Interiors*, *171*(1-4), 7–18. https://doi.org/10.1016/j.pepi.2008.08.005, recent advances in computational geodynamics: Theory, Numerics and Applications

Teske, J. K., Katia, C., Simon, C. S., Caitlin, A. G., & Verne, V. S. (2013). Carbon and oxygen abundances in cool metal-rich exoplanet hosts: A case study of the C/O ratio of 55 Cancri. *The Astrophysical Journal*, *778*(2), 132. https://doi.org/10.1088/0004-637X/778/2/132

Thakore, B. Y., Khambholja, S. G., Vahora, A. Y., Bhatt, N. K., & Jani, A. R. (2013). Thermodynamic properties of 3C—SiC. *Chinese Physics B*, *22*(10), 106401. https://doi.org/10.1088/1674-1056/22/10/106401

Unterborn, C. T., Kabbes, J. E., Pigott, J. S., Reaman, D. M., & Panero, W. R. (2014). The role of carbon in extrasolar planetary geodynamics and habitability. *The Astrophysical Journal*, *793*(2), 124.

Varshney, D., Shriya, S., Varshney, M., Singh, N., & Khenata, R. (2015). Elastic and thermodynamical properties of cubic (3C) silicon carbide under high pressure and high temperature. *Journal of Theoretical and Applied Physics*, *9*(3), 221–249. https://doi.org/10.1007/s40094-015-0183-7

Vinet, P., Ferrante, J., Rose, J. H., & Smith, J. R. (1987). Compressibility of solids. *Journal of Geophysical Research*, *92*(B9), 9319–9325. https://doi.org/10.1029/JB092iB09p09319

Vinet, P., Ferrante, J., Smith, J. R., & Rose, J. H. (1986). A universal equation of state for solids. *Journal of Physics C: Solid State*, *19*(20), L467–L473. https://doi.org/10.1088/0022-3719/19/20/001

Wilson, H. F., & Militzer, B. (2014). Interior phase transformations and mass-radius relationships of silicon-carbon planets. *The Astrophysical Journal*, *793*(1), 34. https://doi.org/10.1088/0004-637X/793/1/34

Yamazaki, D., Yoshino, T., Ohfuji, H., Ando, J. I., & Yoneda, A. (2006). Origin of seismic anisotropy in the D″ layer inferred from shear deformation experiments on post-perovskite phase. *Earth and Planetary Science Letters*, *252*(3–4), 372–378. https://doi.org/10.1016/j.epsl.2006.10.004

Yoshida, M., Onodera, A., Ueno, M., Takemura, K., & Shimomura, O. (1993). Pressure-induced phase transition in SiC. *Physical Review B*, *48*(14), 10,587–10,590. https://doi.org/10.1103/PhysRevB.48.10587

Zhuravlev, K. K., Goncharov, A. F., Tkachev, S. N., Dera, P., & Prakapenka, V. B. (2013). Vibrational, elastic, and structural properties of cubic silicon carbide under pressure up to 75 GPa: Implication for a primary pressure scale. *Journal of Applied Physics*, *113*(11), 113503. https://doi.org/10.1063/1.4795348

Earth and Planetary Science Letters 515 (2019) 135–144

Contents lists available at ScienceDirect

Earth and Planetary Science Letters

www.elsevier.com/locate/epsl

Melting experiments on the Fe–C binary system up to 255 GPa: Constraints on the carbon content in the Earth's core

Izumi Mashino [a,*,1], Francesca Miozzi [b], Kei Hirose [a,c], Guillaume Morard [b], Ryosuke Sinmyo [a]

[a] Department of Earth and Planetary Science, The University of Tokyo, Hongo, Tokyo, 113-0033, Japan
[b] Sorbonne Université, Muséum National d'Histoire Naturelle, UMR CNRS 7590, Institut de Minéralogie, de Physique des Matériaux et de Cosmochimie, IMPMC, 75005 Paris, France
[c] Earth-Life Science Institute, Tokyo Institute of Technology, Meguro, Tokyo 152-8550, Japan

ARTICLE INFO

Article history:
Received 27 December 2018
Received in revised form 4 March 2019
Accepted 8 March 2019
Available online xxxx
Editor: J. Brodholt

Keywords:
core
iron alloy
carbon
eutectic liquid
high pressure

ABSTRACT

Phase relations, including the eutectic liquid composition in the Fe–C binary system, remain unclear under the core pressure range, which makes estimating the carbon budget in the Earth's core difficult. To explore this issue, we have conducted melting and subsolidus experiments on Fe–C alloys in a diamond-anvil cell up to 255 GPa. Textural and compositional characterizations of quenched samples show that carbon concentration in the eutectic liquid slightly decreases with increasing pressure and is about 3 wt.% at the inner core boundary (ICB) pressure. The solubility of carbon in solid Fe is found to be almost constant at ~1.0 wt.%. *In situ* X-ray diffraction data indicate that Fe forms eutectic melting with Fe_3C to 203 GPa and with Fe_7C_3 at 255 GPa.

Previous studies on liquid Fe–C alloys suggested that the density of the outer core is explained by liquid Fe containing 1.8 to 4.2 wt.% C. If the liquid core includes <3 wt.% C as a single light element, hexagonal close-packed (hcp) Fe crystallizes at the ICB. However, the carbon content in such solid Fe is ≤1 wt.%, less than that required to account for the inner core density deficit from pure iron. When the outer core includes ≥3 wt.% C, it forms Fe_7C_3 at the ICB, whose density is too small for the inner core. Carbon is therefore not a primary light element in the core. Nevertheless, the outer core liquid can be Fe–C–Si, Fe–C–S, or Fe–C–H. Such core liquid crystallizes solid Fe with light elements including less than 1 wt.% C, which may explain the density and the sound velocities observed in the inner core.

1. Introduction

Carbon has been believed to be one of feasible light elements contained in planetary cores because of its high abundance in the solar system and strong affinity to molten iron (Benz and Elliott, 1961; Anders and Grevesse, 1989; Wood, 1993). Recent first-principles calculations predicted that the incorporation of a small amount of carbon in hcp Fe is compatible with the density and sound velocities observed in the Earth's inner core (Li et al., 2018).

In order to reveal the abundance of carbon in the core, it is important to understand the Fe–C phase diagram at high pressure, in particular at 330 GPa, which corresponds to the conditions at the ICB. Wood (1993) first thermodynamically calculated the phase relations in the Fe–C system up to 136 GPa and predicted that the Earth's core could contain ~4 wt.% C. Nakajima et al. (2009) experimentally determined the melting phase relationships in the Fe-rich portion of the Fe–C system up to 29 GPa and demonstrated that Fe_7C_3 appears as a liquidus phase. Using an *in situ* X-radiographic imaging technique, Lord et al. (2009) found that carbon concentration in the eutectic liquid in the Fe–C binary system decreases substantially with increasing pressure to 70 GPa. The thermodynamic modeling by Fei and Brosh (2014) based on multi-anvil experiments up to 25 GPa predicted that the Fe–C eutectic liquid composition includes 2.2 wt.% C at 330 GPa. More recently Morard et al. (2017a) reported the change in carbon concentration in the eutectic liquid in the Fe–Fe_3C binary up to 107 GPa and estimated it to be 2.6 wt.% C at the core–mantle boundary (CMB). However, they obtained liquid compositions from X-ray diffraction (XRD) patterns with the Rietveld method, which includes great uncertainty. So far, melting experiments on the Fe–C system have not been carried out under the core pressure range (>136 GPa). Moreover, the solubility of carbon in solid iron also remains un-

* Corresponding author.
E-mail address: izumi.mashino@erdw.ethz.ch (I. Mashino).
[1] Now at ETH.

https://doi.org/10.1016/j.epsl.2019.03.020
0012-821X/

known above 25 GPa (Chabot et al., 2008; Walker et al., 2013; Fei and Brosh, 2014).

It is also important to verify the change in liquidus phase in the Fe–C system. It has been suggested that the liquidus field of Fe_7C_3 expands with respect to that of Fe_3C and eutectic melting occurs between Fe and Fe_7C_3 above 120 GPa (Lord et al., 2009; Fei and Brosh, 2014). Furthermore, the recent experiments by Liu et al. (2016) showed the decomposition of Fe_3C into Fe + Fe_7C_3 above 145 GPa, but it contradicts the formation of Fe_3C at >300 GPa and >5000 K reported by Tateno et al. (2010). Fe_7C_3 has been regarded as a possible constituent in the inner core because it provides a good match for both compressional (V_P) and shear velocities (V_S) (or Poisson's ratio) of the inner core under relevant conditions (Nakajima et al., 2009; Mookherjee et al., 2011; Chen et al., 2014; Prescher et al., 2015). The calculations by Li et al. (2016), however, demonstrated that the density of Fe_7C_3 is too small for the inner core.

Recent progress in melting experiments in a diamond-anvil cell (DAC) combined with a focused ion beam (FIB) technique has enabled us to determine the eutectic liquid composition to the core pressure range (Ozawa et al., 2016; Mori et al., 2017; Hirose et al., 2017). In this study, we have conducted both subsolidus and melting experiments on Fe–C alloys up to 255 GPa in order to determine the change in melting phase relations with increasing pressure, in particular 1) the stability of Fe_7C_3 at liquidus, 2) carbon concentration in eutectic liquid, and 3) the solubility of carbon in solid iron. Based on these results, we discuss the possible carbon content in the Earth's core and the mineralogy of the inner core.

2. Experimental methods

High-pressure and -temperature (*P-T*) conditions were generated in a laser-heated DAC using double-, single-beveled, and flat diamond anvils with 60, 90, 150, and 300 μm culet size. Starting materials were foils of Fe containing 1.9 wt.% C and 4.0 wt.% C, which are homogeneous mixtures of fine-grained Fe and Fe_3C synthesized by an ultra-rapid quenching method (Morard et al., 2011, 2017a). Rhenium gaskets were pre-indented to about 40 μm thickness before laser drilling or spark erosion of sample holes with 30–100 μm diameters. Sample pellets were loaded between two pieces of about 10 μm thick dry Al_2O_3, which served as a pressure-transmitting medium and a thermal insulator from the diamond anvils. After loading, the whole DAC was dried in a vacuum oven at 423 K for more than 12 hrs, and subsequently a sample chamber was flushed with dry argon and squeezed in an argon atmosphere.

After compression to a desired pressure, the sample was heated from both sides with a couple of 100-W single-mode Yb fiber lasers. We used beam-shaping optics, which converts a Gaussian beam to one with a flat energy distribution and thus reduces radial temperature gradient in the sample. A laser-heated spot was up to ~20 μm across. One-dimensional temperature distributions on the surface of the sample were obtained using a spectro-radiometric method (Ohishi et al., 2008). Heating duration was limited to about 5 s in order to avoid fluctuations in temperature, which would otherwise cause complex melting textures. The experimental temperature reported in this study is that at the solid/liquid boundary, which is obtained by combining the measured radial temperature distribution with the melting texture observed in a sample's cross section (Fig. 1) (see Ozawa et al., 2016 for details). We polished the sample using an FIB from both sides little by little (~1 μm for each step) in order to have a cross section at the center of a liquid pool. The sample was thinned to about 3 μm thickness at the end. The uncertainty in temperature is ±5% according to Mori et al. (2017), which includes uncertainties in the width of the liquid pool as well as those derived from the facts that we calculated temperature from integrated light not only from the sample surface but also from the pressure medium and that spatial resolution of the temperature profile was 2 to 3 μm.

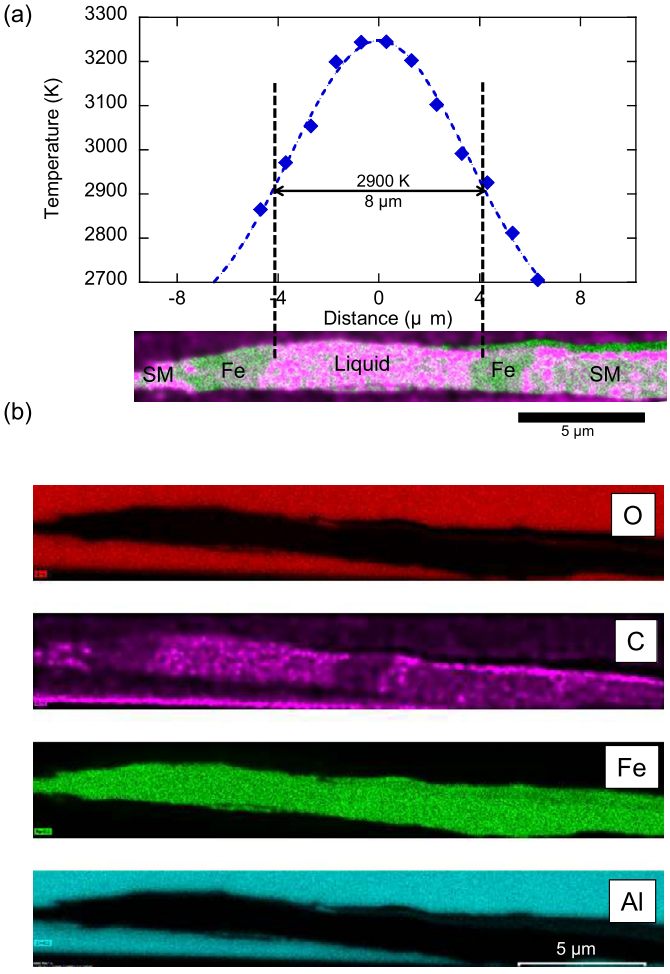

Fig. 1. (a) Temperature profile and (b) composite X-ray maps for oxygen (red), carbon (purple), iron (green), and aluminum (light blue) for run #3 performed at 138 GPa (see Fig. S1 for raw radiation spectra). Homogeneous quenched liquid is found at the center (hot part) surrounded by solid layers of iron. A measured temperature profile is combined in (a), which provides temperature at the liquid/solid boundary. (For interpretation of the colors in the figure(s), the reader is referred to the web version of this article.)

Pressure at room temperature was obtained based on the Raman shift of a diamond anvil (Akahama and Kawamura, 2007). It was then corrected for a contribution of thermal pressure. According to Andrault et al. (1998), when purely isochoric heating is made, the thermal pressure is written as $\Delta P = \alpha K_T T$, in which α is thermal expansivity and K_T is isothermal bulk modulus. Assuming the thermal parameters for liquid Fe–C same as those for pure iron, we employ $\alpha K_T = 9$ MPa/K (Ichikawa et al., 2014) for runs performed above 83 GPa. Andrault et al. (1998) demonstrated that 90% of such isochoric thermal pressure contributes to an experimental pressure increase at the core pressure range. For runs #1, #2, and #5 conducted at relatively low pressures, the lower αK_T value of 4 MPa/K and 60% of the theoretical value were applied (Morard et al., 2011; Andrault et al., 1998). The overall errors in pressure should be less than ±10% in the present experiments including the uncertainty in thermal pressure estimate, as argued in Mori et al. (2017). Indeed, we found 191 GPa at 2300 K in run #7 based on the volume and equation of state (EoS) of Fe_3C (Sata et al., 2010), which is consistent with 194 GPa calculated with the thermal pressure correction.

Table 1
Experimental results in the Fe–C binary system.

Run#	Starting material	*P* (GPa)	Eutectic *T* (K)	Phases present	Liquid			Solid iron		
					C (wt.%)	Fe (wt.%)	O (wt.%)	C (wt.%)	Fe (wt.%)	O (wt.%)
1	Fe-1.9 wt.% C	23(2)	1950(100)	Liq + Fe	4.04(30)	96.30(30)	0.16(5)	0.85(24)	99.08(16)	0.07(11)
2	Fe-1.9 wt.% C	54(5)	2550(130)	Liq + Fe + Fe_3C	4.45(32)	95.70(30)	0.34(30)	1.00(45)	98.89(51)	0.11(7)
3	Fe-1.9 wt.% C	138(14)	2900(150)	Liq + Fe	3.95(22)	94.84(21)	1.70(17)	0.68(48)	99.38(29)	0.05(11)
4	Fe-1.9 wt.% C	211(21)	3230(160)	Liq + Fe + Fe_3C	4.19(20)	95.23(30)	0.95(30)	1.04(22)	98.96(24)	not detected
5	Fe-4.0 wt.% C	40(4)	2300(120)	Liq + Fe + Fe_3C	3.83(24)	96.50(23)	0.17(22)	0.64(4)	99.49(20)	not detected
6	Fe-4.0 wt.% C	83(8)	2640(130)	Liq + Fe_3C	3.90(23)	95.72(12)	0.88(8)	-	-	-
7	Fe-4.0 wt.% C	203(20)	3350(170)	Liq + Fe_3C	3.92(9)	95.39(22)	1.19(21)	-	-	-
8	Fe-4.0 wt.% C	255(25)	3570(180)	Liq + Fe + Fe_7C_3	3.60(21)	96.84(49)	0.07(50)	0.61(34)	99.43(31)	not detected

Numbers in parentheses are standard deviation uncertainties in the last digit(s).

Synchrotron XRD measurements were carried out *in situ* at high *P-T* in runs #7 and #8 at BL10XU, SPring-8 (Ohishi et al., 2008) using an X-ray beam with an energy of ~30 keV. Angle-dispersive XRD spectra were collected on a flat panel detector (Perkin Elmer) with typical exposure time of 200 ms. A monochromatic incident X-ray beam was collimated to 2 μm (FWHM). Visible fluorescent light induced by X-rays in a diamond was used to precisely align the laser-heated spot with the X-ray beam. Two-dimensional XRD images were integrated to produce a conventional one-dimensional diffraction profile using the IPAnalyzer software (Seto et al., 2010).

Recovered samples from our DAC experiments were cross-sectioned using a Ga^+ focused ion beam (FIB) instrument (FEI VersaTM3D DualBeamTM). During FIB sectioning, sample was monitored by scanning electron microscopy using back-scattered electrons to precisely section the center of a heated spot. The sample cross sections were then examined by a field-emission-type scanning electron microscope (FE-SEM) and energy dispersive X-ray spectrometry (EDS) with a silicon drift detector. The section was then mounted on a Cu grid and further thinned to approximately 3 μm thickness for further analysis with a field-emission-type electron probe microanalyzer (FE-EPMA, JXA-8530F, JEOL) in order to determine chemical compositions. Since Fe–C samples are good electric conductors, no coating material was necessary for EPMA analysis with an accelerating voltage of 10 kV and a beam current of 15 nA. A focused electron beam for spot analyses was less than 50 nm in size. We used both Fe_3C and Fe_7C_3 as standards that were synthesized at 5 GPa/1473 K and applied the ZAF correction (Nakajima et al., 2009). Corundum (for Al and O) and pure iron (for Fe) were also used for standards. The X-ray counting time for peak/background was 20 s/10 s. LDE2 (C), TAP (Al), LIFH (Fe), and LDE1H (O) were analyzing crystals.

Very minor amounts of aluminum and oxygen were found when analyzing the sample, most likely due to a signal from a neighboring/underlying Al_2O_3 insulation layer. We estimated the carbon concentrations in quenched liquid and solid metals after subtracting Al_2O_3 from raw analyses. In addition, we analyzed two samples (runs #2 & #6) by EPMA with a liquid nitrogen cold finger (JXA-8530FPlus HyperProbe Electron Probe Microanalyzer) at both 10 kV and 15 kV accelerating voltage (Table S1). The results demonstrate that the carbon contents obtained with and without the cold finger are similar to each other. We repeated the analyses of the Fe_3C standard twenty times and found that the carbon concentration changed only by ±0.1766 atm%. While chemical compositions were calculated by using both the 'standard' ZAF correction and the phi-rho-z type procedure, the results are consistent with each other (see Table S1).

3. Results

3.1. Carbon contents in eutectic liquid and coexisting solid iron

We have conducted eight separate DAC runs for melting experiments in a pressure range from 23 GPa to 255 GPa (Table 1). Figs. 1 and 2 show typical melting textures on recovered samples. There is a chemically homogeneous part at the center of a laser-heating spot, which is non-stoichiometric in composition and should represent a quenched liquid. The liquidus phase (solid phase in contact with liquid) is found at both sides of the liquid. The outermost low-temperature area remained subsolidus. We observed iron carbide (Fe_3C or Fe_7C_3) or metallic iron (or both) as liquidus phase(s). In runs #2, #4, #5, and #8, both iron carbide and iron were present, suggesting that the quenched liquid in these runs may represent a eutectic liquid in the Fe–C binary system. Carbon diffusivity in liquid iron was estimated to be about 10^{-8} m^2/s under the present *P-T* conditions (Helffrich, 2014), indicating that 1 s is long enough for carbon to diffuse in the present liquid pool that was less than 20 μm across (Figs. 1 and 2). Since melting/crystallization at the liquid/solid boundary occurs almost instantaneously, chemical homogeneity in the liquid assures that chemical equilibrium was attained in the present heating duration of about 5 s. The Fe–C liquids obtained in the core pressure range included about 1 wt.% oxygen in addition to carbon (Table 1), which might have affected phase relations in the Fe–C binary system.

We determined the carbon concentration in quenched liquid up to 255 GPa, the conditions corresponding to the middle of the outer core, more than twice the pressure compared to previous experimental studies (e.g., Lord et al., 2009; Fei and Brosh, 2014; Morard et al., 2017a). Fig. 3 demonstrates the carbon concentrations in liquids as a function of pressure, which constrains the change in eutectic liquid composition, considering that they indicate the lower and upper bounds for the carbon content in eutectic liquid at each pressure when coexisting with iron and iron carbides, respectively. These data show a small reduction in carbon content in the eutectic liquid with increasing pressure above 23 GPa. Our results are not consistent with the continuous reduction that was thermodynamically predicted by Fei and Brosh (2014) and experimentally reported by Lord et al. (2009) (Fig. 3). The difference from Lord et al. (2009) may be attributed to the difference in analytical method: Lord and others employed an X-radiographic imaging technique for chemical analysis, while we based our measurements on electron microprobe analyses.

We also obtained the carbon concentrations in solid iron coexisting with Fe–C liquid as a function of pressure (Fig. 4). Liquid Fe–C coexists with face-centered cubic (fcc) iron at relatively low pressure range, in which carbon atoms occupy the octahedral interstitial sites (Fei and Brosh, 2014). Previous studies reported that the maximum solubility of carbon in fcc-Fe is <2.1 wt.% at 1 bar and predicted that it decreases at higher pressures (Walker et al.,

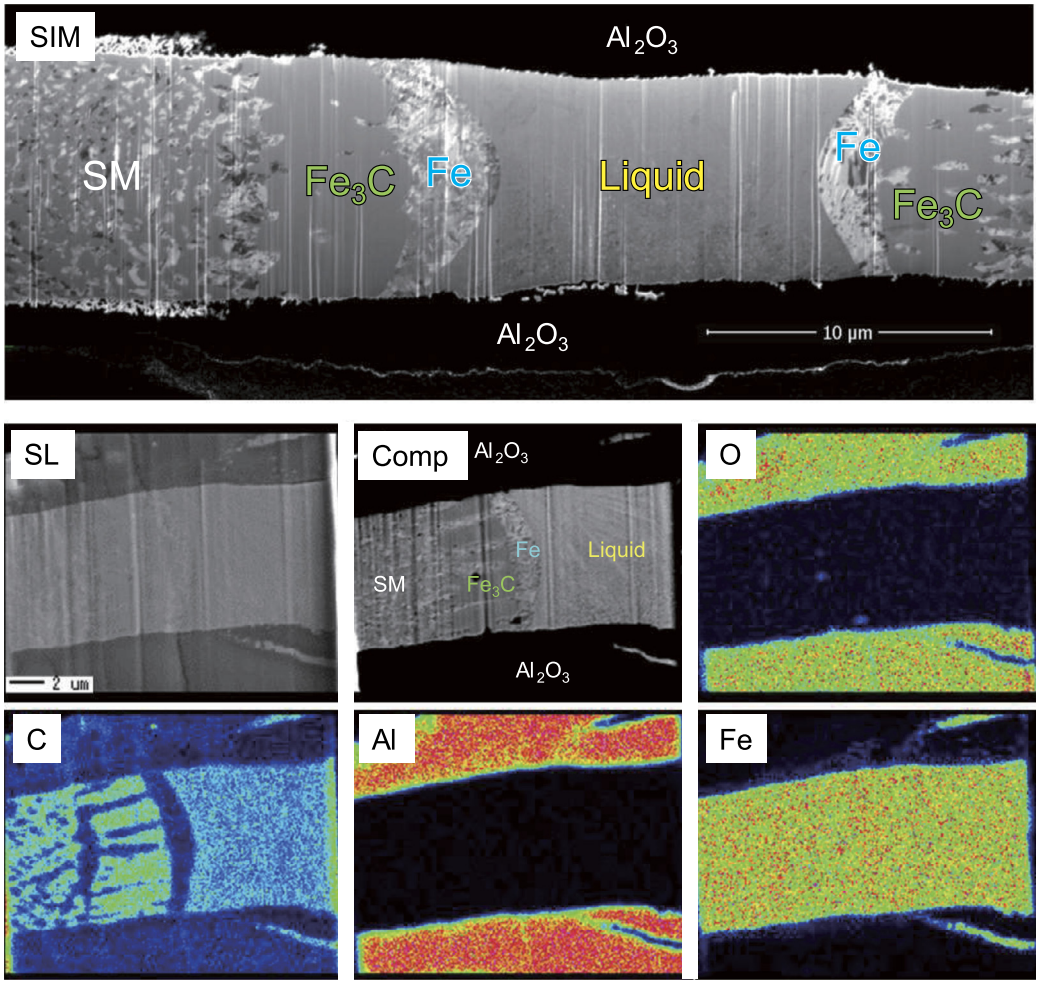

Fig. 2. Typical melting texture of a quenched sample and composite X-ray maps for oxygen, carbon, aluminum, and iron for run #5 at 40 GPa. SIM, scanning ion microscope image; SL, secondary electron image; Comp, backscattered image. Homogeneous quenched liquid is found at the center surrounded by solid layers of Fe and Fe_3C.

2013; Fei and Brosh, 2014). Our results show about 1.0 wt.% in fcc-Fe from 23 to 54 GPa, in good agreement with such predictions. Above 138 GPa in the present experiments, hcp Fe should have crystallized from Fe–C liquid and again included 1.0 wt.% or less C. The effect of pressure on the solubility of carbon in hcp Fe was not observed.

3.2. Eutectic temperature in the Fe–C system

The temperature at the solid/liquid boundary gives the upper bound for eutectic temperature. These temperatures are plotted as a function of pressure in Fig. 5a, which constrains the eutectic melting curve to mid-outer core pressures. We fit the Simon-Glatzel equation to the data (Simon and Glatzel, 1929):

$$T_m = T_{mref}\left(\frac{P - P_{ref}}{a} + 1\right)^{1/c} \quad (1)$$

where T_m is eutectic temperature, and both a and c are fitting parameters. $T_{mref} = 1513$ K at $P_{ref} = 5$ GPa is employed as a reference eutectic temperature from previous data obtained using a large-volume press (Fei and Brosh, 2014). The best fitted parameters are $a = 8.4 \pm 3.3$ GPa and $c = 4.1 \pm 0.5$. The obtained eutectic melting curve shown in Fig. 5a is consistent with those of previous studies by Liu et al. (2016) and Morard et al. (2017a) within experimental uncertainties. Fig. 5b compares the eutectic melting curves of iron alloys. Under the core pressure range, the Fe–C system exhibits a eutectic temperature lower than those of Fe (Anzellini et al., 2013), Fe–FeSi (Fischer et al., 2013), and Fe–FeO (Morard et al., 2017a). And, the Fe–C eutectic melting temperature is higher than that in Fe–Fe_3S below ~250 GPa, but is lower at higher pressures including the ICB pressure (Mori et al., 2017).

3.3. Liquidus field of Fe_7C_3

In runs #7 and #8 using the Fe-4.0 wt.% C starting material, the sample was initially compressed at room temperature to 176 GPa and 226 GPa, respectively (Fig. 6). Broad XRD peaks from hcp Fe and Fe_3C were observed before heating in both runs. The peaks from both phases became sharper and spotty upon heating to 2300 K in run #7, in which more than 10 peaks were indexed to Fe_3C cementite (Sata et al., 2010), and only Fe_3C phase was observed from the sample in the XRD pattern during melting at 203 GPa and 3350 K. In addition, we confirmed with an FE-EPMA that the quenched liquid was surrounded by Fe_3C in the recovered sample (Fig. 7a). These indicate that Fe forms eutectic melting with Fe_3C at 203 GPa.

In the case of run #8, the diffraction peaks from hcp Fe and Fe_3C became sharper and spotty upon heating. We then observed the appearance of the peaks that are assigned to Fe_7C_3 (orthorhombic, *Pbca*) (Prescher et al., 2015) after we melted the sample by increasing temperature to 3570 K at 255 GPa. After quenching this sample, we confirmed with the FE-EPMA that the liquid was in contact with both Fe and Fe_7C_3, whereas the subsolidus part was composed of Fe and Fe_3C (Fig. 7b). These show

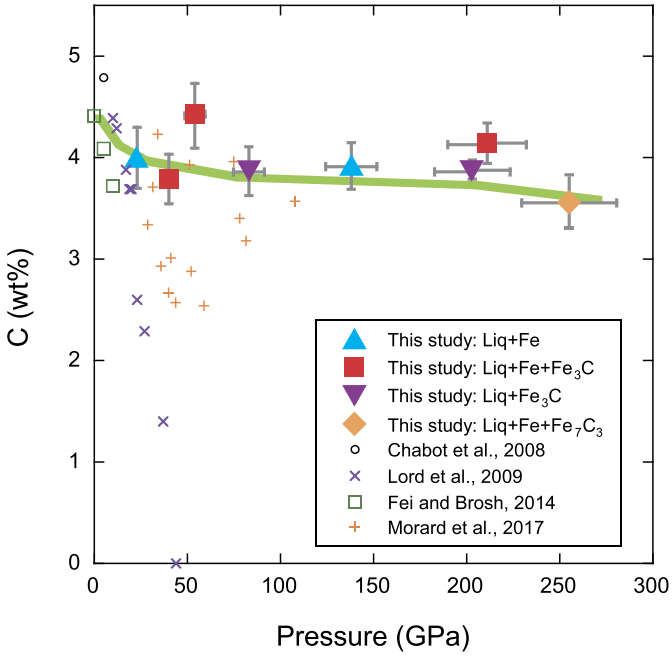

Fig. 3. Carbon concentrations in liquids obtained in this study. Liquid compositions are shown by triangles (blue) when coexisting with solid Fe, inverse triangles (purple) when in contact with Fe_3C, squares (red) when both solid Fe and Fe_3C were found, and a diamond (orange) when solid Fe and Fe_7C_3 were formed. The triangles and inverse triangles give lower and upper bounds for carbon concentration in eutectic liquid, respectively. Open and cross symbols represent eutectic compositions reported by previous studies (Chabot et al., 2008; Lord et al., 2009; Fei and Brosh, 2014; Morard et al., 2017a). Green curve shows the change in eutectic liquid composition with increasing pressure.

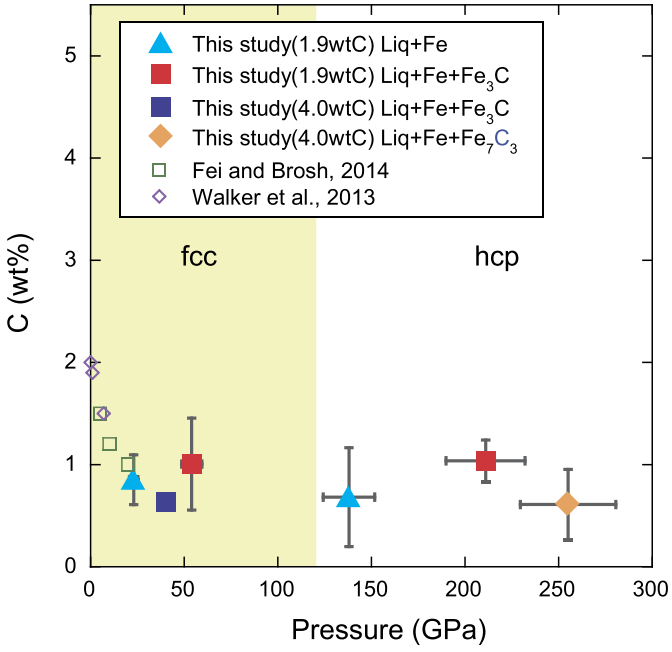

Fig. 4. Carbon contents in solid iron found in this study. Closed symbols are the same as in Fig. 3. Previous reports on the maximum solubility of carbon in solid iron are shown by open symbols (Walker et al., 2013; Fei and Brosh, 2014).

that eutectic melting occurs between Fe and Fe_7C_3 at 255 GPa. This observation is not consistent with Liu et al. (2016), who argued that Fe_3C dissociates into Fe + Fe_7C_3 at subsolidus above 145 GPa when using Fe_3C as a sample. Liu and others based their

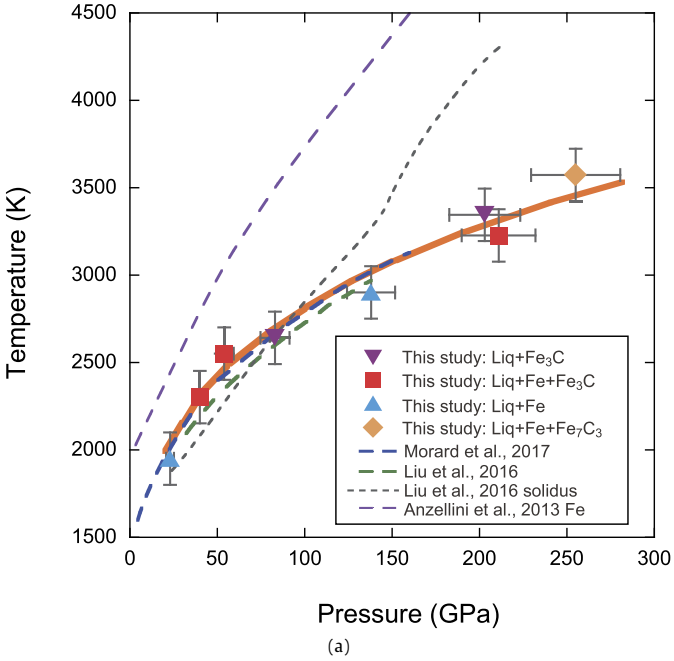

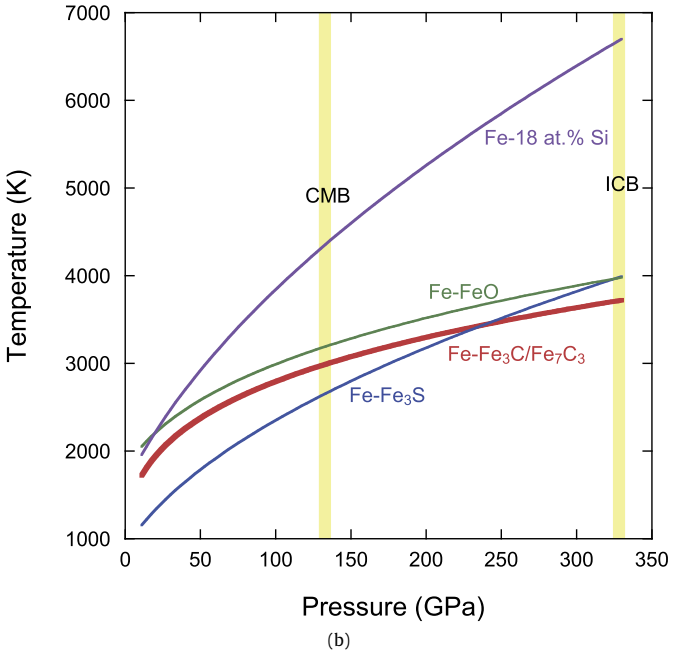

Fig. 5. (a) Fe–Fe_3C (or Fe–Fe_7C_3 above 255 GPa) eutectic melting curve (orange) obtained in this study (closed symbols). It agrees well with the previously determined Fe–C melting curves by Morard et al. (2017a) (blue) and Liu et al. (2016) (green). Black dotted curve represents the solidus of Fe_3C composition reported by Liu et al. (2016). Purple dashed curve shows the melting temperature of pure Fe (Anzellini et al., 2013). (b) Eutectic melting curve of the Fe–C system obtained in this study compared with those of the Fe–Fe_3S (Mori et al., 2017), Fe–FeO (Morard et al., 2017a), and Fe–FeSi (Fischer et al., 2013) binary systems.

conclusions purely on the change in XRD patterns, and they may have collected them above eutectic temperature.

4. Discussion

4.1. Phase diagram of Fe–C system at ICB

The eutectic liquid composition (Fig. 3) and eutectic melting curve obtained in this study (Fig. 5) indicate that eutectic melting occurs in Fe–Fe_3C at Fe + 3.5 wt.% C at 135 GPa and 3000 K.

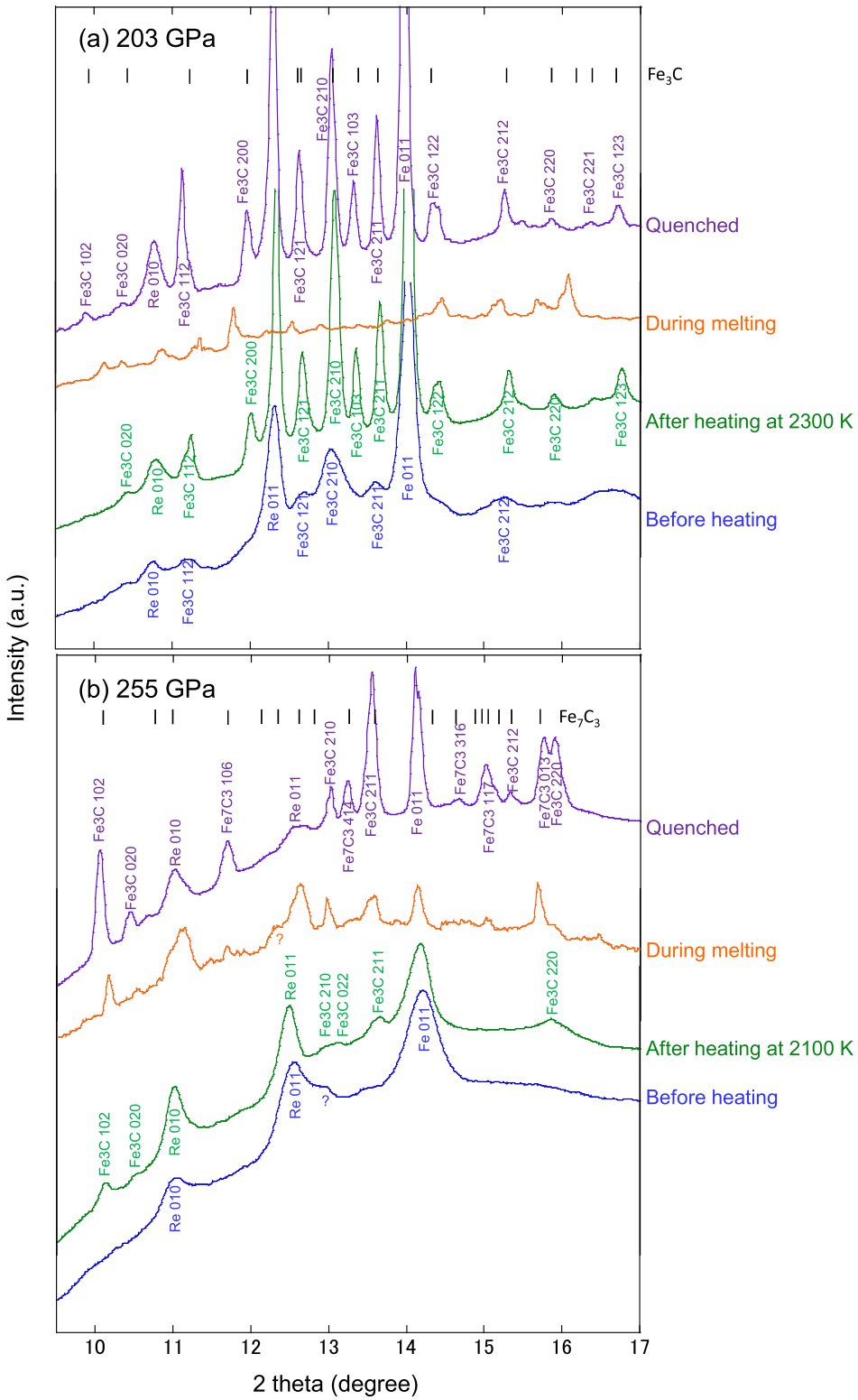

Fig. 6. XRD patterns of Fe + 4.0 wt.% C obtained before and after heating (no melting), and during and after melting (a) at 203 GPa in run #7 and (b) 255 GPa in run #8. The unit-cell parameters and volumes of Fe_3C and Fe_7C_3 are $a = 3.95(1)$ Å, $b = 4.54(1)$ Å, $c = 5.95(1)$ Å, and $V = 106.9(4)$ Å^3 for Fe_3C, and $a = 10.40(1)$ Å, $b = 3.96(1)$ Å, $c = 12.06(1)$ Å, and $V = 496.4(3)$ Å^3 for Fe_7C_3.

And, these data determined up to 255 GPa suggest that the eutectic liquid includes about 3 wt.% C at 330 GPa and 3750 K.

We model the liquidus curve for the Fe-rich side of the eutectic to 330 GPa (Fig. 8). Considering an ideal solution, a molar ratio of Fe in liquid at T is given by:

$$\chi_{\mathrm{Fe\ liq}} = \exp\left\{\frac{\overline{G}^0_{\mathrm{Fe\ sol}} - \overline{G}^0_{\mathrm{Fe\ liq}}}{RT}\right\} = \exp\left\{-\int_{T_{m\ \mathrm{Fe}}}^{T} \frac{\overline{H}^0_{\mathrm{Fe\ sol}} - \overline{H}^0_{\mathrm{Fe\ liq}}}{RT^2} dT\right\} \quad (2)$$

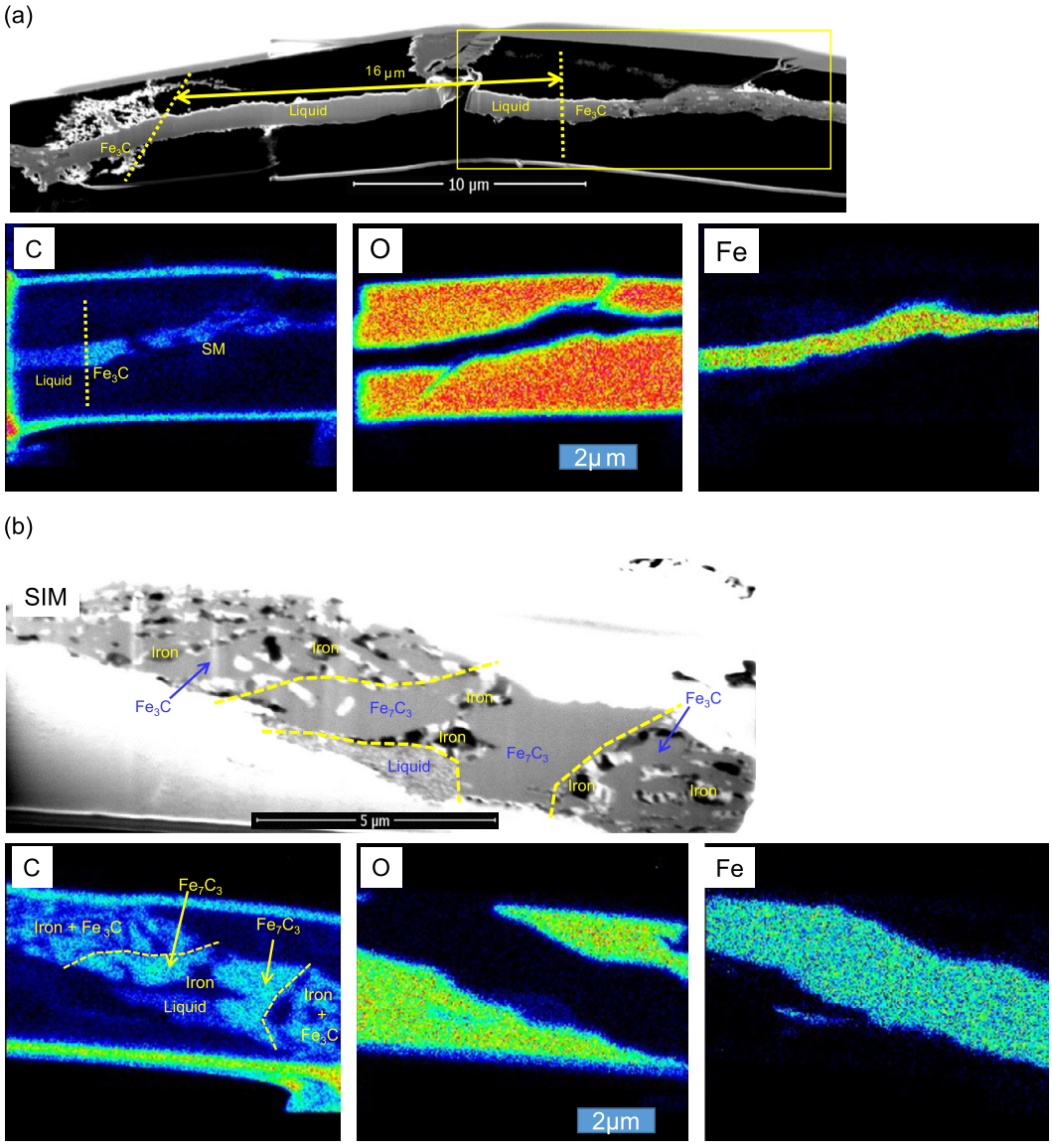

Fig. 7. Quenched textures and composite X-ray maps for carbon, oxygen, and iron at (a) 203 GPa (run #7) and (b) 255 GPa (run #8). While liquid was surrounded by Fe_3C in the sample quenched at 203 GPa, it was in contact with Fe_7C_3 and Fe at 255 GPa (the subsolidus part was composed of Fe_3C and Fe).

where $\overline{G}^0_{\mathrm{Fe}\ i}$ and $\overline{H}^0_{\mathrm{Fe}\ i}$ are standard Gibbs free energy and the enthalpy of phase i, respectively, $T_{m\ \mathrm{Fe}}$ is the melting temperature of pure Fe, and R is gas constant. When we assume that an enthalpy change upon fusion, $\overline{H}^0_{\mathrm{Fe\ liq}} - \overline{H}^0_{\mathrm{Fe\ sol}}$, is independent from temperature, Eq. (2) is written as:

$$\chi_{\mathrm{Fe\ liq}} = \exp\left\{\left(\frac{\overline{H}^0_{\mathrm{Fe\ liq}} - \overline{H}^0_{\mathrm{Fe\ sol}}}{RT_{m\ \mathrm{Fe}}}\right) \times \left(1 - \frac{T_{m\ \mathrm{Fe}}}{T}\right)\right\}$$
$$= \exp\left\{A \times \left(1 - \frac{T_{m\ \mathrm{Fe}}}{T}\right)\right\} \quad (3)$$

Here A is constant and calculated from $T_{m\ \mathrm{Fe}}$ (Anzellini et al., 2013), eutectic temperature, and eutectic composition (Figs. 3 and 5) at a given pressure (see also Mori et al., 2017).

4.2. Fe–C core liquid?

Melting phase relations in the Fe–C system constrain the carbon budget in the Earth's core and the mineralogy of the solid inner core. The maximum carbon content in the outer core has been estimated from the core density deficit. Recent experimental and computational studies on the density of liquid Fe–C alloys indicate 1.8 to 4.2 wt.% C in the liquid core at the ICB (Badro et al., 2014: Nakajima et al., 2015; Morard et al., 2017b), although earlier estimates based on the EoS of solid Fe_3C suggested higher carbon concentration (7.7–9.2 wt.% C) (Sata et al., 2010). Since the eutectic point is located at about 3 wt.% C at 330 GPa (Fig. 8), if the Fe–C outer core includes less than 3 wt.% C, it crystallizes hcp Fe with $\leq$1 wt.% C at the ICB (Fig. 4). In this case, however, the difference in carbon concentration between the liquid and solid core is too small to explain the density jump (4.5 to 6.5%) across the ICB (Shearer and Masters, 1990; Masters and Gubbins, 2003). Moreover, assuming a linear density change between pure Fe (Sakamaki et al., 2016), Fe_3C (Sata et al., 2010), and Fe_7C_3 (Prescher et al., 2015), hcp Fe with 1.0 wt.% C is found to be only 1.3% lighter than pure iron, which is not enough to account for the inner core density deficit of 4–6% (Brown and McQueen, 1986; Shearer and Masters, 1990; Masters and Gubbins, 2003; Dewaele et al., 2006; Komabayashi and Fei, 2010). This is supported by the recent calculations by Li et al. (2018). Less than 3 wt.% C as a single light element in the core is therefore unlikely.

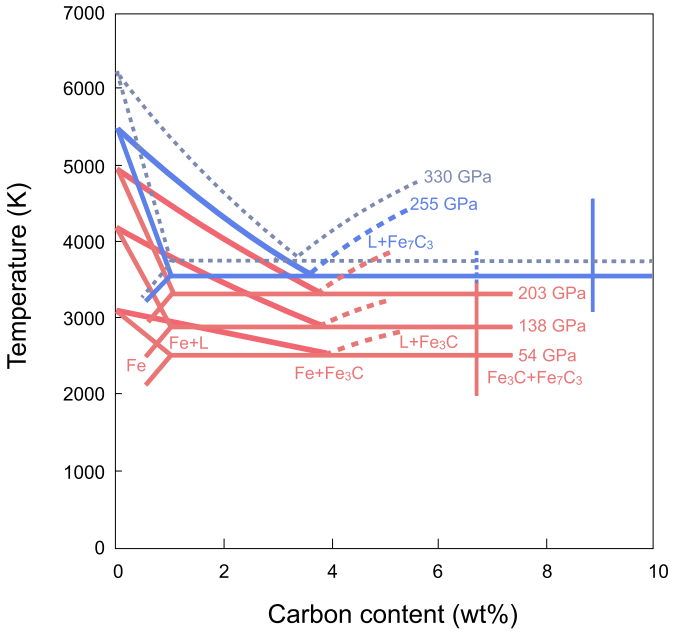

Fig. 8. Phase diagrams for the iron-rich portion of the Fe–C binary system at 54, 138, 203, and 255 GPa from the present experiments and at ICB conditions (330 GPa) by extrapolation. Red and blue (and gray) curves represent Fe–Fe_3C and Fe–Fe_7C_3 eutectic, respectively.

Next we consider the case that the liquid core contains more than 3 wt.% C as the sole light component, from which Fe_7C_3 crystallizes at the ICB (Fig. 8). It has been suggested that both V_P and V_S—in particular the slow V_S (high Poisson's ratio)—of the inner core could be reconciled with non-magnetic Fe_7C_3 (Mookherjee et al., 2011; Chen et al., 2014; Prescher et al., 2015). If the inner core is composed of solid Fe_7C_3, the liquid outer core should include 5.4–6.7 wt.% C according to Badro et al. (2014) or 5.2–6.0 wt.% C based on Nakajima et al. (2015), considering that the outer core should be 4.5–6.5% less dense than solid Fe_7C_3 (Chen et al., 2014). More than 5 wt.% C in liquid iron, however, leads to a bulk sound velocity and a density much higher and lower than those observed for the outer core, respectively (Badro et al., 2014; Nakajima et al., 2015; Morard et al., 2017b) and is thus unlikely. The computational study by Li et al. (2016) also showed that the density of Fe_7C_3 is too low to be a major constituent of the inner core.

These suggest that carbon cannot be a predominant light element in the outer core. It is indeed consistent with Wood et al. (2013), who proposed that the maximum carbon content in the core is 1.0 wt.%, which was deduced from the carbon isotopic signature in silicate Earth and the silicate-metal fractionation factors. It has also been argued that the outer core velocity is explained by the incorporation of a small amount of carbon that is not enough to account for its density deficit from pure iron (Badro et al., 2014; Nakajima et al., 2015).

4.3. Fe–C–X core liquid?

Furthermore, we consider the Fe–C–X (X = Si, S, O, or H) ternary systems to seek possible ranges of outer core composition, from which hcp Fe crystallizes (Figs. 9a–d). The eutectic liquid composition in each Fe–X binary system has been estimated to be Fe with 3 wt.% C (this study), 1.5 wt.% Si (Ozawa et al., 2016), 5 wt.% S (Mori et al., 2017), and >10 wt.% O (Morard et al., 2017a) at 330 GPa. The hydrogen concentration in the Fe–H eutectic liquid is unclear, but it would be around 1 wt.% H according to Fukai (1992) and Shibazaki et al. (2014). The ternary eutectic points in

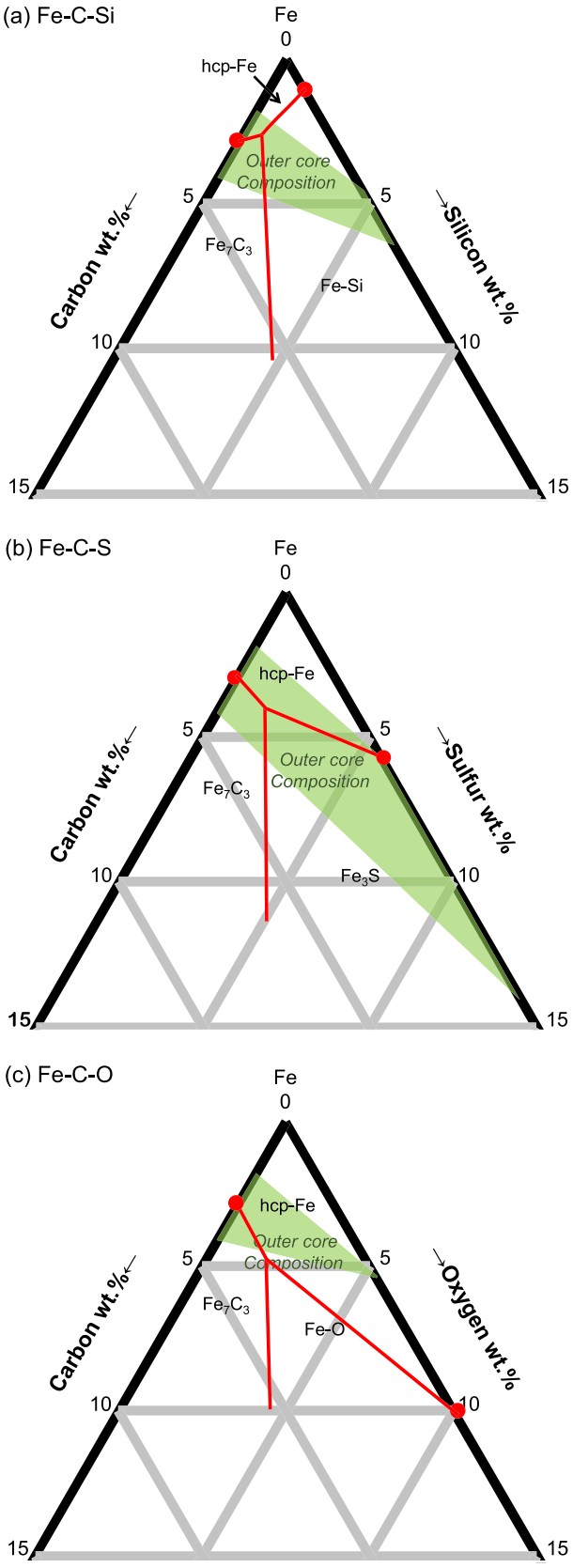

Fig. 9. Likely liquidus phase relations in the Fe–C–X ternary systems at 330 GPa. Red circles represent the eutectic compositions in the Fe–C (this study), Fe–Si (Ozawa et al., 2016), Fe–S (Mori et al., 2017), Fe–O (Morard et al., 2017a), and Fe–H binary systems (Fukai, 1992). Green regions show the range of possible composition of the outer core that explains its density based on studies on liquid iron alloys (Morard et al., 2013; Badro et al., 2014; Umemoto et al., 2014; Umemoto and Hirose, 2015; Nakajima et al., 2015; Kawaguchi et al., 2017).

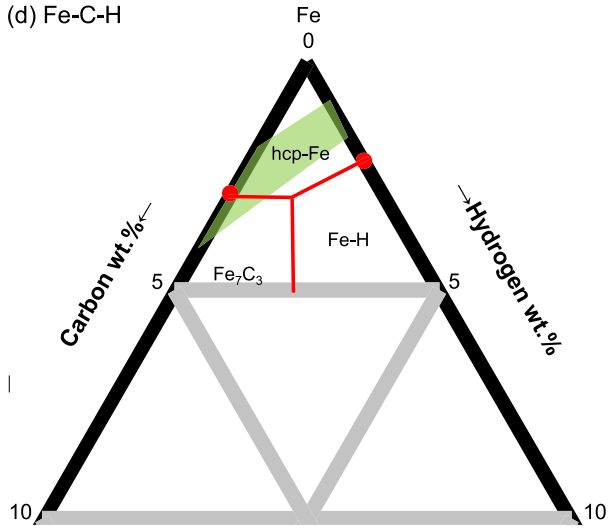

Fig. 9. (*continued*)

these systems are not exactly known, but the recent melting experiments performed by Tateno et al. (2018) have demonstrated that the Fe–Si–S ternary eutectic point is located 1) near the tie line between the Fe–FeSi and Fe–Fe_3S binary eutectic points and 2) close to the Fe–Fe_3S binary join because the eutectic temperature in Fe–Fe_3S is much lower than that in Fe–FeSi. The present data show that the eutectic temperature in the Fe–C binary system is low compared to those in other systems (Fe–Si, Fe–S, and Fe–O) at 330 GPa (Fig. 5). On the basis of these observations, Figs. 9a–d illustrate the liquidus phase relations (showing a compositional range from which a specific solid phase first crystallizes) in the Fe–C–X ternary systems at the ICB, with each ternary eutectic point located relatively close to the Fe–C binary eutectic point except for the Fe–C–H system.

Previous experiments and calculations have estimated the maximum amount of each light element in the liquid core to explain the outer core density deficit. Estimates based on liquid iron alloys show 4.6–6.4 wt.% Si (Morard et al., 2013; Badro et al., 2014), 5.8–14.0 wt.% S (Morard et al., 2013; Badro et al., 2014; Umemoto et al., 2014; Kawaguchi et al., 2017), 5.5 wt.% O (Badro et al., 2014), and 1.0 wt.% H (Umemoto and Hirose, 2015) at the ICB, which are again less than those obtained by the earlier study on the EoSs of solid FeSi, FeS, and $Fe_{0.95}O$ (Sata et al., 2010). These give the possible compositional range of Fe–C–X ternary outer core liquid in Figs. 9a–d (green area).

We find that hcp Fe crystallizes from possible liquid core compositions in all of the Fe–C–Si, Fe–C–S, Fe–C–O, and Fe–C–H systems. The recent calculations by Li et al. (2018) proposed that all of the density, V_P, and V_S of the solid inner core are explained by hcp $Fe_{30}C_1Si_1$ (Fe + 0.7 wt.% C + 1.6 wt.% Si). Such inner core composition is feasible, considering that the maximum solubilities of silicon and sulfur in hcp Fe when coexisting with liquid alloys are $\leq$1.5 wt.% Si and 4 wt.% S at the ICB, respectively (Ozawa et al., 2016; Mori et al., 2017). Hcp Fe + 1 wt.% C + 4.0 wt.% S also could account for the inner core density (Sakai et al., 2012). Hydrogen is known to be soluble in solid Fe (Fukai, 1992; Shibazaki et al., 2012; Terasaki et al., 2012), suggesting that the hcp Fe–C–H inner core is also feasible. On the other hand, solid Fe crystallizing from liquid Fe–C–O contains $\leq$1 wt.% carbon and a negligible amount of oxygen (Ozawa et al., 2010), which does not account for the inner core density deficit (Li et al., 2018). Therefore, while carbon is not a predominant light element in the core, the outer core liquid can be Fe–C–Si, Fe–C–S, or Fe–C–H.

5. Conclusion

We have conducted melting experiments on the Fe–C binary system up to 255 GPa by using a laser-heated DAC. The carbon concentration in eutectic liquid and the solubility of carbon in solid iron were determined based on textual and chemical characterizations for samples recovered from the DAC. Results show that 1) the carbon content in eutectic liquid slightly decreases with increasing pressure from 4.3 wt.% C at ambient pressure to 3.6 wt.% C at 255 GPa, 2) eutectic melting occurs between Fe and Fe_3C to 203 GPa and between Fe and Fe_7C_3 at 255 GPa, and 3) the maximum solubility of carbon in solid iron is almost constant ($\leq$1 wt.%) up to 255 GPa. The eutectic liquid in the Fe–C binary system includes about 3 wt.% C at 330 GPa.

If carbon is the sole light element in the core and the outer core includes <3 wt.% C, hcp Fe crystallizes at the ICB but includes only less than 1 wt.% C, which does not explain the inner core density deficit. If the liquid core contains more than 3 wt.% C, it forms Fe_7C_3 at the ICB, whose density is too low for the inner core. These indicate that carbon is not a primary light element in the core. On the other hand, the outer core can be liquid Fe–C–Si, Fe–C–S, or Fe–C–H. It crystallizes hcp Fe including light elements with less than 1 wt.% C, which may explain the density and the sound velocities observed in the inner core.

Acknowledgements

We appreciate Y. Nakajima for his help in quantitative determination of carbon content with an EPMA. We also thank K. Yonemitsu, H. Yoshida, S. Tagawa, S. Tateno, and Y. Kuwayama for their support during experiments. Comments provided anonymous reviewers were helpful, in particular on the EPMA analysis of carbon. This work was supported by the JSPS research grant 16H06285 to K.H. XRD measurements were performed at BL10XU, SPring-8 (proposals no. 2017A0072 and 2017B0072). F.M. and G.M. received funding from the European Research Council (ERC) under the European Union's Horizon 2020 research and innovation Programme (grant agreement no. 670787).

Appendix A. Supplementary material

Supplementary material related to this article can be found online at https://doi.org/10.1016/j.epsl.2019.03.020.

References

Akahama, Y., Kawamura, H., 2007. Diamond anvil Raman gauge in multimegabar pressure range. High Press. Res. 27, 473–482. https://doi.org/10.1080/08957950701659544.

Anders, E., Grevesse, N., 1989. Abundances of the elements: meteoritic and solar. Geochim. Cosmochim. Acta 53, 197–214. https://doi.org/10.1016/0016-7037(89)90286-X.

Andrault, D., Fiquet, G., Itie, J.P., Richet, P., Gillet, P., Hausermann, D., Hanfland, M., 1998. Thermal pressure in the laser-heated diamond-anvil cell: an X-ray diffraction study. Eur. J. Mineral. 10, 931–940.

Anzellini, S., Dewaele, A., Mezouar, M., Loubeyre, P., Morard, G., 2013. Melting of iron at Earth's inner core boundary based on fast X-ray diffraction. Science 340, 464–466. https://doi.org/10.1126/science.1233514.

Badro, J., Cote, A.S., Brodholt, J.P., 2014. A seismologically consistent compositional model of Earth's core. Proc. Natl. Acad. Sci. USA 111, 7542–7545. https://doi.org/10.1073/pnas.1316708111.

Benz, M., Elliott, J., 1961. The austenite solidus and revised iron-carbon diagram. Trans. Metall. Soc. AIME 221, 323–331.

Brown, J.M., McQueen, G., 1986. Phase transitions, Grüneisen parameter, and elasticity for shocked iron between 77 GPa and 400 GPa. J. Geophys. Res. 91, 7485–7494. https://doi.org/10.1029/JB091iB07p07485.

Chabot, N.L., Campbell, A.J., McDonough, W.F., Draper, D.S., Agee, C.B., Humayun, M., Watson, H.C., Cottrell, E., Saslow, S.A., 2008. The Fe–C system at 5 GPa and implications for Earth's core. Geochim. Cosmochim. Acta 72, 4146–4158. https://doi.org/10.1016/j.gca.2008.06.006.

Chen, B., Li, Z., Zhang, D., Liu, J., Hu, M.Y., Zhao, J., Bi, W., Alp, E.E., 2014. Hidden carbon in Earth's inner core revealed by shear softening in dense Fe_7C_3. Proc. Natl. Acad. Sci. USA 111, 17755–17758. https://doi.org/10.1073/pnas.1411154111.

Dewaele, A., Loubeyre, P., Occelli, F., Mezouar, M., Dorogokupets, P.I., Torrent, M., 2006. Quasihydrostatic equation of state of iron above 2 Mbar. Phys. Rev. Lett. 97, 215504. https://doi.org/10.1103/PhysRevLett.97.215504.

Fei, Y., Brosh, E., 2014. Experimental study and thermodynamic calculations of phase relations in the Fe–C system at high pressure. Earth Planet. Sci. Lett. 408, 155–162. https://doi.org/10.1016/j.epsl.2014.09.044.

Fischer, R.A., Campbell, A.J., Reaman, D.M., Miller, N.A., Heinz, D.L., Dera, P., Prakapenka, V.B., 2013. Phase relations in the Fe–FeSi system at high pressures and temperatures. Earth Planet. Sci. Lett. 373, 54–64. https://doi.org/10.1016/j.epsl.2013.04.035.

Fukai, Y., 1992. Some properties of the Fe–H system at high pressures and temperatures, and their implications for the Earth's core. In: Syono, Y., Manghnani, M.H. (Eds.), High-Pressure Research: Application to Earth and Planetary Sciences. In: AGU Monogr. Ser., vol. 67, pp. 373–385.

Helffrich, G., 2014. Outer core compositional layering and constraints on core liquid transport properties. Earth Planet. Sci. Lett. 391, 256–262. https://doi.org/10.1016/j.epsl.2014.01.039.

Hirose, K., Morard, G., Sinmyo, R., Umemoto, K., Hernlund, J.W., Labrosse, S., 2017. Crystallization of silicon dioxide and compositional evolution of the Earth's core. Nature 543, 99–102. https://doi.org/10.1038/nature21367.

Ichikawa, H., Tsuchiya, T., Tange, Y., 2014. The P-V-T equation of state and thermodynamic properties of liquid iron. J. Geophys. Res., Solid Earth 119, 240–252. https://doi.org/10.1002/2013JB010732.

Kawaguchi, S.I., Nakajima, Y., Hirose, K., Komabayashi, T., Ozawa, H., Tateno, S., Kuwayama, Y., Tsutsui, S., Baron, A.Q., 2017. Sound velocity of liquid Fe–Ni–S at high pressure. J. Geophys. Res., Solid Earth 122, 3624–3634. https://doi.org/10.1002/2016JB013609.

Komabayashi, T., Fei, Y., 2010. Internally consistent thermodynamic database for iron to the Earth's core conditions. J. Geophys. Res., Solid Earth 115, 1–12. https://doi.org/10.1029/2009JB006442.

Li, Y., Vočadlo, L., Brodholt, J., Wood, I.G., 2016. Thermoelasticity of Fe_7C_3 under inner core conditions. J. Geophys. Res., Solid Earth 121, 5828–5837. https://doi.org/10.1002/2016JB013155.

Li, Y., Vočadlo, L., Brodholt, J.P., 2018. The elastic properties of hcp-Fe alloys under the conditions of the Earth's inner core. Earth Planet. Sci. Lett. 493, 118–127. https://doi.org/10.1016/j.epsl.2018.04.013.

Liu, J., Lin, J., Prakapenka, V.B., Prescher, C., Yoshino, T., 2016. Phase relations of Fe_3C and Fe_7C_3 up to 185 GPa and 5200 K: implication for the stability of iron carbide in the Earth's core. Geophys. Res. Lett. 43, 12415–12422. https://doi.org/10.1002/2016GL071353.

Lord, O.T., Walter, M.J., Dasgupta, R., Walker, D., Clark, S.M., 2009. Melting in the Fe–C system to 70 GPa. Earth Planet. Sci. Lett. 284, 157–167. https://doi.org/10.1016/j.epsl.2009.04.017.

Masters, G., Gubbins, D., 2003. On the resolution of density within the Earth. Phys. Earth Planet. Inter. 140, 159–167. https://doi.org/10.1016/j.pepi.2003.07.008.

Mookherjee, M., Nakajima, Y., Neumann, G.S., Glazyrin, K., Wu, X., Dubrovinsky, L., Mccammon, C., Chumakov, A., 2011. High-pressure behavior of iron carbide (Fe_7C_3) at inner core conditions. J. Geophys. Res., Solid Earth 116, 1–13. https://doi.org/10.1029/2010JB007819.

Morard, G., Andrault, D., Guignot, N., Siebert, J., Garbarino, G., Antonangeli, D., 2011. Melting of Fe–Ni–Si and Fe–Ni–S alloys at megabar pressures: implications for the core-mantle boundary temperature. Phys. Chem. Miner. 38, 767–776. https://doi.org/10.1007/s00269-011-0449-9.

Morard, G., Siebert, J., Andrault, D., Guignot, N., Garbarino, G., Guyot, F., Antonangeli, D., 2013. The Earth's core composition from high pressure density measurements of liquid iron alloys. Earth Planet. Sci. Lett. 373, 169–178. https://doi.org/10.1016/j.epsl.2013.04.040.

Morard, G., Andrault, D., Antonangeli, D., Nakajima, Y., Auzende, A.L., Boulard, E., Cervera, S., Clark, A., Lord, O.T., Siebert, J., Svitlyk, V., Garbarino, G., Mezouar, M., 2017a. Fe–FeO and Fe–Fe_3C melting relations at Earth's core-mantle boundary conditions: implications for a volatile-rich or oxygen-rich core. Earth Planet. Sci. Lett. 473, 94–103. https://doi.org/10.1016/j.epsl.2017.05.024.

Morard, G., Nakajima, Y., Andrault, D., Antonangeli, D., Auzende, A.L., Boulard, E., Cervera, S., Clark, A.N., Lord, O.T., Siebert, J., Svitlyk, V., Garbarino, G., Mezouar, M., 2017b. Structure and density of Fe–C liquid alloys under high pressure. J. Geophys. Res., Solid Earth 122, 7813–7823. https://doi.org/10.1002/2017JB014779.

Mori, Y., Ozawa, H., Hirose, K., Sinmyo, R., Tateno, S., Morard, G., Ohishi, Y., 2017. Melting experiments on Fe–Fe_3S system to 254 GPa. Earth Planet. Sci. Lett. 464, 135–141. https://doi.org/10.1016/j.epsl.2017.02.021.

Nakajima, Y., Takahashi, E., Suzuki, T., Funakoshi, K., 2009. "Carbon in the core" revisited. Phys. Earth Planet. Inter. 174, 202–211. https://doi.org/10.1016/j.pepi.2008.05.014.

Nakajima, Y., Imada, S., Hirose, K., Komabayashi, T., Ozawa, H., Tateno, S., Tsutsui, S., Kuwayama, Y., Baron, A.Q.R., 2015. Carbon-depleted outer core revealed by sound velocity measurements of liquid iron-carbon alloy. Nat. Commun. 6, 1–7. https://doi.org/10.1038/ncomms9942.

Ohishi, Y., Hirao, N., Sata, N., Hirose, K., Takata, M., 2008. Highly intense monochromatic X-ray diffraction facility for high-pressure research at SPring-8. High Press. Res. 28, 163–173. https://doi.org/10.1080/08957950802208910.

Ozawa, H., Hirose, K., Tateno, S., Sata, N., Ohishi, Y., 2010. Phase transition boundary between B1 and B8 structures of FeO up to 210 GPa. Phys. Earth Planet. Inter. 179, 157–163. https://doi.org/10.1016/j.pepi.2009.11.005.

Ozawa, H., Hirose, K., Yonemitsu, K., Ohishi, Y., 2016. High-pressure melting experiments on Fe–Si alloys and implications for silicon as a light element in the core. Earth Planet. Sci. Lett. 456, 47–54. https://doi.org/10.1016/j.epsl.2016.08.042.

Prescher, C., Dubrovinsky, L., Bykova, E., Kupenko, I., Glazyrin, K., Kantor, A., McCammon, C., Mookherjee, M., Nakajima, Y., Miyajima, N., Sinmyo, R., Cerantola, V., Dubrovinskaia, N., Prakapenka, V., Rüffer, R., Chumakov, A., Hanfland, M., 2015. High Poisson's ratio of Earth's inner core explained by carbon alloying. Nat. Geosci. 8, 220–223. https://doi.org/10.1038/ngeo2370.

Sakai, T., Ohtani, E., Kamada, S., Terasaki, H., Hirao, N., 2012. Compression of $Fe_{88.1}Ni_{9.1}S_{2.8}$ alloy up to the pressure of Earth's inner core. J. Geophys. Res., Solid Earth 117, B02210. https://doi.org/10.1029/2011JB008745.

Sakamaki, T., Ohtani, E., Fukui, H., Kamada, S., Takahashi, S., Sakairi, T., Takahata, A., Sakai, T., Tsutsui, S., Ishikawa, D., Shiraishi, R., Seto, Y., Tsuchiya, T., Baron, A.Q.R., 2016. Constraints on Earth's inner core composition inferred from measurements of the sound velocity of hcp-iron in extreme conditions. Sci. Adv. 2, e1500802. https://doi.org/10.1126/sciadv.1500802.

Sata, N., Hirose, K., Shen, G., Nakajima, Y., Ohishi, Y., Hirao, N., 2010. Compression of FeSi, Fe_3C, $Fe_{0.95}O$, and FeS under the core pressures and implication for light element in the Earth's core. J. Geophys. Res., Solid Earth 115, 1–13. https://doi.org/10.1029/2009JB006975.

Seto, Y., Nishio-Hamane, D., Nagai, T., Sata, N., 2010. Development of a software suite on X-ray diffraction experiments. Rev. High Press. Sci. Technol. 20, 269–276. https://doi.org/10.4131/jshpreview.20.269.

Shearer, P., Masters, G., 1990. The density and shear velocity contrasts at the inner core boundary. Geophys. J. Int. 102, 408–491. https://doi.org/10.1111/j.1365-246X.1990.tb04481.x.

Shibazaki, Y., Ohtani, E., Fukui, H., Sakai, T., Kamada, S., Ishikawa, D., Tsutsui, S., Baron, A.Q.R., Nishitani, N., Hirao, N., Takemura, K., 2012. Sound velocity measurements in dhcp-FeH up to 70 GPa with inelastic X-ray scattering: implications for the composition of the Earth's core. Earth Planet. Sci. Lett. 313–314, 79–85. https://doi.org/10.1016/j.epsl.2011.11.002.

Shibazaki, Y., Terasaki, H., Ohtani, E., Tateyama, R., Nishida, K., Funakoshi, K., Higo, Y., 2014. High-pressure and high-temperature phase diagram for $Fe_{0.9}Ni_{0.1}$–H alloy. Phys. Earth Planet. Inter. 228, 192–201. https://doi.org/10.1016/j.pepi.2013.12.013.

Simon, F., Glatzel, G., 1929. Remarks on fusion pressure curve. Z. Anorg. Allg. Chem. 178, 309–316. https://doi.org/10.1002/zaac.19291780123.

Tateno, S., Hirose, K., Ohishi, Y., Tatsumi, Y., 2010. The structure of iron in Earth's inner core. Science 330, 359–361. https://doi.org/10.1126/science.1194662.

Tateno, S., Hirose, K., Sinmyo, R., Morard, G., Hirao, N., Ohishi, Y., 2018. Melting experiments on Fe–Si–S alloys to core pressures: silicon in the core? Am. Mineral. 103, 742–748. http://doi.org/10.2138/am-2018-6299.

Terasaki, H., Ohtani, E., Sakai, T., Kamada, S., Asanuma, H., Shibazaki, Y., Hirao, N., Sata, N., Ohishi, Y., Sakamaki, T., Suzuki, A., Funakoshi, K., 2012. Stability of Fe–Ni hydride after the reaction between Fe–Ni alloy and hydrous phase (δ-AlOOH) up to 1.2 Mbar: possibility of H contribution to the core density deficit. Phys. Earth Planet. Inter. 194–195, 18–24. https://doi.org/10.1016/j.pepi.2012.01.002.

Umemoto, K., Hirose, K., 2015. Liquid iron–hydrogen alloys at outer core conditions by first-principles calculations. Geophys. Res. Lett. 42, 7513–7520. https://doi.org/10.1002/2015GL065899.

Umemoto, K., Hirose, K., Imada, S., Nakajima, Y., Komabayashi, T., Tsutsui, S., Baron, A.Q.R., 2014. Liquid iron–sulfur alloys at outer core conditions by first-principles calculations. Geophys. Res. Lett. 41, 6712–6717. https://doi.org/10.1002/2014GL061233.

Walker, D., Dasgupta, R., Li, J., Buono, A., 2013. Nonstoichiometry and growth of some Fe carbides. Contrib. Mineral. Petrol. 166, 935–957. https://doi.org/10.1007/s00410-013-0900-7.

Wood, B.J., 1993. Carbon in the core. Earth Planet. Sci. Lett. 117, 593–607.

Wood, B.J., Li, J., Shahar, A., 2013. Carbon in the core: its influence on the properties of core and mantle. In: Hazen, R.M., Jones, A.P., Baross, J.A. (Eds.), Carbon in Earth. Rev. Mineral. Geochem. 75, 231–250. https://doi.org/10.2138/rmg.2013.75.8.

Geophysical Research Letters

RESEARCH LETTER
10.1029/2018GL079950

Key Points:
- Melting curve and phase diagram of pure Fe has been measured by in situ X-ray absorption up to 130 GPa
- Overall agreement between different in situ studies leads to a melting temperature of 4250 ± 250 K at core-mantle boundary pressure
- Discrepancies with previous measurements is unambiguously attributed to carbon contamination from the diamonds or thermal pressure overestimation

Supporting Information:
- Supporting Information S1

Correspondence to:
G. Morard,
guillaume.morard@upmc.fr

Citation:
Morard, G., Boccato, S., Rosa, A. D., Anzellini, S., Miozzi, F., Henry, L., et al. (2018). Solving controversies on the iron phase diagram under high pressure. *Geophysical Research Letters*, *45*, 11,074–11,082. https://doi.org/10.1029/2018GL079950

Received 7 AUG 2018
Accepted 8 OCT 2018
Accepted article online 12 OCT 2018
Published online 25 OCT 2018

Solving Controversies on the Iron Phase Diagram Under High Pressure

Guillaume Morard[1], Silvia Boccato[2], Angelika D. Rosa[2], Simone Anzellini[3], Francesca Miozzi[1], Laura Henry[2], Gaston Garbarino[2], Mohamed Mezouar[2], Marion Harmand[1], François Guyot[1], Eglantine Boulard[1], Innokenty Kantor[2,4], Tetsuo Irifune[5], and Raffaella Torchio[2]

[1]Sorbonne Université, Institut de Minéralogie, de Physique des Matériaux et de Cosmochimie, IMPMC, Museum National d'Histoire Naturelle, UMR CNRS 7590, IRD, Paris, France, [2]European Synchrotron Radiation Facility, Grenoble, France, [3]Diamond Light Source Ltd., Didcot, UK, [4]Institut for Fysik, Danmarks Tekniske Universitet, Kongens Lyngby, Denmark, [5]Geodynamics Research Center, Ehime University, Matsuyama, Japan

Abstract As the main constituent of planetary cores, pure iron phase diagram under high pressure and temperature is of fundamental importance in geophysics and planetary science. However, previously reported iron-melting curves show large discrepancies (up to 1000 K at the Earth's core–mantle boundary, 136 GPa), resulting in persisting high uncertainties on the solid-liquid phase boundary. Here we unambiguously show that the observed differences commonly attributed to the nature of the used melting diagnostic are due to a carbon contamination of the sample as well as pressure overestimation at high temperature. The high melting temperature of pure iron under core-mantle boundary (4250 ± 250 K), here determined by X-ray absorption experiments at the Fe K-edge, indicates that volatile light elements such as sulfur, carbon, or hydrogen are required to lower the crystallization temperature of the Earth's liquid outer core in order to prevent extended melting of the surrounding silicate mantle.

Plain Language Summary Iron is the main constituent of planetary cores; however, there are still large controversies regarding its melting temperature and phase diagram under planetary interior conditions. The present study reconciles different experimental approaches using laser-heated diamond anvil cell with different in situ X-ray diagnostics (absorption, diffraction, and Mossbauer spectroscopy). The main reason of discrepancies (over 1000 K at core-mantle boundary conditions) is attributed to carbon contamination from the diamond anvils and metrology issues related to thermal pressure overestimation. A high-melting temperature for iron at core-mantle boundary pressure would imply the presence of volatile elements in the liquid outer core, such as sulfur, carbon, or hydrogen, in order to lower its crystallization temperature and avoid extended melting of the surrounding silicate mantle.

1. Introduction

Iron represents the main constituent of planetary cores in our solar system. Its physical properties under high pressure and temperature conditions are therefore extremely important to determine the internal structure and dynamics of telluric planets. One of the key parameters of its phase diagram is the melting curve. Its extrapolation up to the inner-outer core boundary conditions can, in fact, provide information about the temperature profile in planetary cores. This information places important constraints on parameters like heat flux to the mantle, convectional mode, and cooling rate, all of which are fundamental to the planets heat budget and dynamics. However, despite intensive experimental and theoretical efforts, a consensus on the melting line of pure iron has not been found during the last decades.

Pioneering work performed in laser-heated diamond anvil cells (LH-DAC) was using laser speckle technique to detect movement on the sample surface as melting diagnostic (Boehler, 1993). This study has been later confirmed by an in situ LH-DAC X-ray Diffraction (XRD) study using the appearance of diffuse scattering as melting criterion (Boehler et al., 2008) and recently confirmed again by in situ X-ray absorption technique in LH-DAC (Aquilanti et al., 2015). Another recent in situ LH-DAC XRD experiment, also using the appearance of diffuse scattering as melting criterion (Anzellini et al., 2013) has obtained a melting line higher by more than 1000 K above 100 GPa with respect to the X-ray absorption spectroscopy (XAS) measurement (Aquilanti et al., 2015), but in a good agreement with shock experiments (Brown & Mcqueen, 1986;

Nguyen & Holmes, 2004) and ab initio calculations (Alfè, 2009; Alfè et al., 2002). Finally, recent LH-DAC Synchrotron Mossbauer Spectroscopy (SMS) experiments (Jackson et al., 2013; Zhang et al., 2015) have determined a melting temperature falling in between the two previous curves.

The persisting discrepancies in the reported results have caused a long-standing debate among the scientists in the last years, in particular, while comparing the adopted in situ techniques. In fact, even if probing the sample under different scales of resolution of the atomic arrangement (XAS, SMS, and XRD), these techniques should provide the same results within the experimental errors. However, while performing a LH-DAC experiment, several aspects must be considered together with the melting diagnostic to obtain reliable data, which include the sample configuration, possible chemical reactions, and the adopted metrology (see Mezouar et al., 2017). Furthermore, an accurate pressure and temperature evaluation at simultaneous high P/T conditions together with a critical assessment of their errors is essential to provide a reliable measure of the melting line.

In the present study, with the purpose of performing a critical comparison between different melting diagnostics, the melting line of pure Fe has been investigated in situ in LH-DAC by energy dispersed XAS. This is a probe similar to the one employed in Aquilanti et al. (2015). The sample geometry of this study is identical to the one adopted in Jackson et al. (2013) and in Anzellini et al. (2013) but strongly different than the one used in Aquilanti et al. (2015); where the iron sample is contained in a cavity drilled by focused ion beam (FIB) technique in Al_2O_3 single crystals). In addition, a critical analysis of the metrology has been performed during the experiment in order to establish realistic error bars. Finally, an ex situ analysis of the recovered samples has been performed by XRD and SEM techniques to evaluate the presence of chemical reactions and to validate the adopted melting criterion.

The obtained results reveal the different origins of discrepancies between previous studies therefore placing higher constrains on the iron melting line. We show that low melting line is related to carbon contamination and difference in the pressure determination at high temperature. Moreover, the present study provides a refined iron phase diagram up to core-mantle boundary (CMB) pressure, allowing a better evaluation of the amount of light elements present in the core.

2. Materials and Methods

2.1. Experimental Procedure

Laser-heating diamond anvil cell experiments were performed on the energy dispersive X-ray absorption beamline ID24 at the European Synchrotron Radiation Facility, Grenoble (Pascarelli et al., 2016). A highly focused X-ray beam was employed (down to 3*3 μm^2 full width at half maximum) covering an energy range of more than 800 eV (i.e., from 7,000 to 7,800 eV). Two Nd:YAG lasers are focused on the sample using two separate planoconvex lenses with a focal distance of 50 mm, to obtain a laser hotspot on the sample of 15–20 μm of diameter. Detailed description of the laser-heating experimental setup available on ID24 beamline is detailed in Kantor et al. (2018).

Membrane-driven LeToullec-type diamond anvil cells were used to pressurize the sample equipped with either single-crystal or sintered nanopolycrystalline diamonds (Ishimatsu et al., 2012), having culet sizes ranging from flat 300 to beveled 300/150 μm. The latter allowed acquiring glitch-free XAS data over the entire energy range accessible at ID24. The sample consists of a 5-μm thick Fe foil (99.99% purity, GoodFellow), providing an optimized absorption jump. The employment of such thin samples further minimizes axial temperature gradients during laser heating. For all experiments, the Fe foil was sandwiched between two disks of KCl. These disks were prepared by compressing KCl powder to the target thickness (Sigma Aldrich, 99.99% purity). Single disks were then laser-cut using the femto-laser micromachining facility available at Institut de Minéralogie, de Physique des Matériaux et de Cosmochimie laboratory. The employment of pre-compressed KCl disks ensures a controlled and homogeneous insulation thickness, which is a prerequisite for generating a homogenous laser-heating spot reducing the temperature gradients seen by the X-rays. The disks further allowed performing reproducible and fast loadings. In order to limit and remove any contamination of moisture from air, the loading of the pressure medium and the sample were performed within 1 hr, and the loaded DAC was kept open in a vacuum oven at 120 °C for more than 12 hr before pressurizing.

The temperature on the sample was gradually increased by adjusting the laser output power carefully stepwise every 0.1%. The temperature was measured with 1 to 0.01 s exposure time. The typical laser heating

duration is 1.2 s, with a delay of 100 ms before starting the temperature measurement. XAS data were simultaneously acquired by accumulating 10 spectra with 100 ms exposure time. After each temperature step, a spectrum of the quenched sample was acquired to verify that the sample did not react. Details about the data acquisition procedure can be found in Boccato et al. (2017).

The absence of reaction products such as Fe_3C was verified in all recovered samples by acquiring finely meshed (5-μm step size) 2-D XRD maps at the diffraction beamline ID27 using a highly focused X-ray beam of $3 \times 3\ \mu m^2$ ($\lambda = 0.3738$ Å; Mezouar et al., 2005). Diffraction images were integrated with Dioptas (Prescher & Prakapenka, 2015). The Fe_3C phase could be identified in few samples through the presence of single-diffraction spots of the most intense peaks of Fe_3C, that is, (102) at 2.068 Å.

Recovered samples were cut through the hotspot area to analyze the texture using the analysis platform available at Institut de Minéralogie, de Physique des Matériaux et de Cosmochimie. The developed technique combines femtosecond-pulsed laser machining, ion polishing, and FIB cutting, to remove the sample from the gasket and expose the laser-heated area, in order to perform accurate SEM imaging. Extended description of sample preparation can be found in Morard et al. (2017).

2.2. Thermal Pressure Calculation

The pressure was determined at room temperature before and after each heating cycle using either the Raman peak position of the single-crystalline diamond measured at the center of the culet (Akahama & Kawamura, 2004) or using the position of the fluorescence line of a ruby sphere placed in the sample chamber (Dewaele et al., 2008). The sample pressure during laser heating was then calculated following the procedure established in Lord, Wood, et al. (2014) and the equation

$$P = P_{\text{before}} + \frac{P_{\text{after}} + \Delta P - P_{\text{before}}}{T_{\text{max}} - 300} \times (T - 300),$$

where P_{before} and P_{after} are the different pressures measured before and after the heating cycle, T_{max} is the maximal temperature of the heating cycle, and ΔP is the pressure difference between the pressure at high temperature and the pressure measured after the heating cycle. This pressure difference is kept constant for the pressure–temperature range investigated in the present study and fixed at 2 GPa, as highlighted in a recent XRD experiment (Miozzi et al., 2018; see supporting information, and references therein for more details; Campbell et al., 2009; Lord, Wann, et al., 2014). It should be noticed that this equation is only valid for T_{max} superior to 2000 K, as the observed scattering of ΔP (2 ± 1.5 GPa, Figure S4) does not allow us assigning a dependence of ΔP over pressure or temperature.

3. Results

Solid-solid and solid-liquid phase transitions in iron can be unambiguously identified from changes in the X-ray Absorption Near Edge Structure (XANES) region of the absorption spectra at the Fe K-edge (Harmand et al., 2015; Marini et al., 2014; Torchio et al., 2016). In particular, the transition from the high-pressure hcp (hexagonal close-packed) structure to the high-temperature fcc (face centered cubic) structure results in a strong modification of the first XANES oscillation and the appearance of a double feature at 7,130 and 7,140 eV (Figure 1). Similarly, the solid to liquid transition results in marked changes of several XANES features (1) in the preedge regions the shoulder at 7,120 eV disappears and (2) the first XANES oscillation flattens. On this last point, it should be noticed that damping of these features related to melting is different from temperature damping of EXAFS oscillations due to Debye-Waller effect. The K-edge XANES of iron mirrors the electronic transition from the 1s to the empty 4p states. The observed smoothening of the XANES features in the liquid phase can be related to a broader distribution of empty 4p states due to the breaking of crystalline long-range order (Mazevet et al., 2014).

In order to confirm the validity of these in situ X-ray diagnostics, analysis of recovered samples were performed using a FIB (Figure 2). The protocol for studying the recovered samples has been detailed in our previous work on iron alloys (Morard et al., 2017). Borders of the solid and the molten portions of the recovered samples exhibit a regular and an irregular shape, respectively, allowing to discriminate between them. In addition, the texture related with solid grains twinning is visible in the solid portion of the sample,

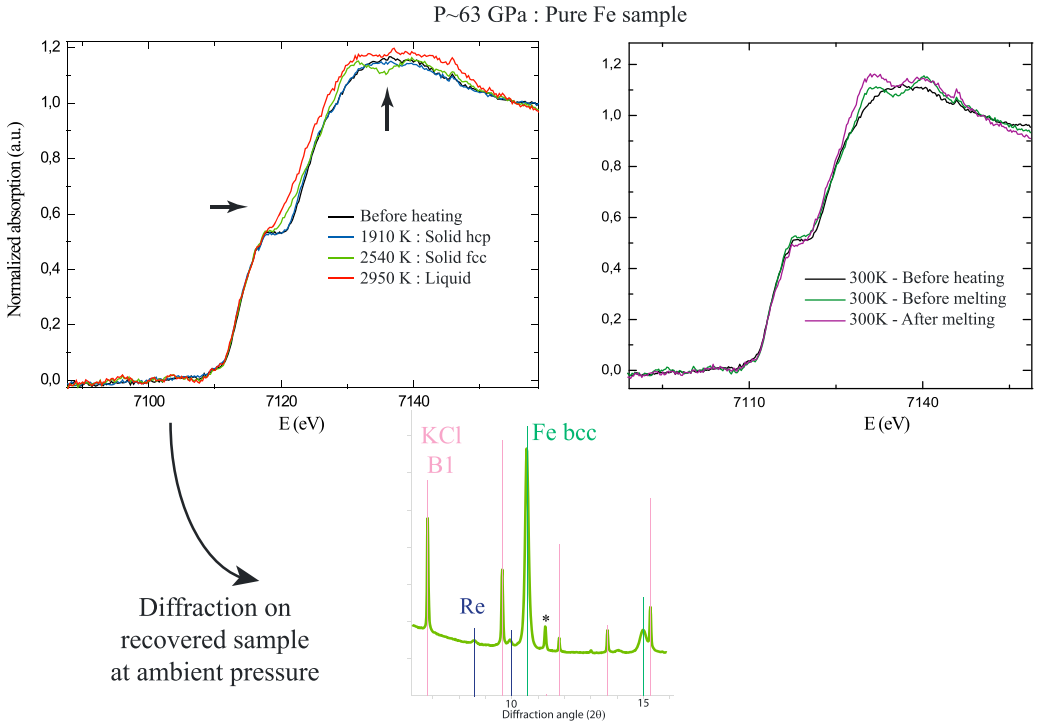

Figure 1. Evolution of X-ray Absorption Near Edge Structure (XANES) spectra at Fe absorption edge upon melting**.** Evolution of XANES spectra from hcp structure (in blue), to fcc structure (in green), and above the melting point (in red). Changes related to the hcp-fcc transition are visible in the edge, with a change from one to two features. Changes related to melting is visible with the disappearance of the feature in the preedge and the flattening in the edge. Arrows indicate these modifications on the XANES signal. Corresponding spectra of quenched sample after each temperature do not show any change in the flank, in agreement with the absence of sample contamination. Diffraction pattern of recovered sample indicates no additional phases, except one peak potentially belonging to the gasket holder (signaled by a star). hcp = hexagonal close-packed; fcc = face centered cubic.

whereas the liquid portion is found to be homogeneous (central portion of the sample on Figures 2 and S5). Thanks to these ex situ analyses we were able to validate the use of the disappearance of the features in the first oscillation and the flattening of the preedge in the XAS spectra, as melting criteria for Fe, similar to our conclusions for the melting of Ni under high pressure (Boccato et al., 2017).

Along with the validation of the in situ melting criterion, a critical examination of the adopted metrology has been performed during the experiment. In particular, each temperature measurement has been analyzed via two-color pyrometry (Benedetti & Loubeyre, 2004), and individual error bars have been assigned (Figure S2). Concerning the pressure measurement, its value under high temperature is estimated considering the thermal contribution. In particular, the value of this thermal pressure strongly depends on the pressure medium compressibility (Lord, Wood, et al., 2014), leading to small value when KCl is used: here a constant value of 2 GPa has been assigned as based on XRD measurements of KCl embedded samples (see section 2 and supporting information). Individual error bars for pressure of ±5 GPa is estimated to summarize the addition of different pressure uncertainties, such as pressure gradient in the sample chamber or uncertainty on the thermal pressure estimation, for example.

Following the previous considerations, the melting points resulting from the SMS study (Jackson et al., 2013; Zhang et al., 2015), who used a sample geometry similar to the present one (Fe foil embedded in KCl), have been revised. In particular, the thermal pressure calculation presented here in the supporting information can be applied to the SMS studies (Jackson et al., 2013; Zhang et al., 2015), resulting in an excellent agreement between their recalculated melting temperatures, our XANES study, and the previous XRD study of Anzellini et al. (2013; Figure 3). The obtained results highlight the fact that these different in situ techniques are all valid, and the previously observed differences arise from uncertainties in the metrology rather than on the adopted melting criteria. Therefore, a revised fit for the different phase boundary is presented to take into

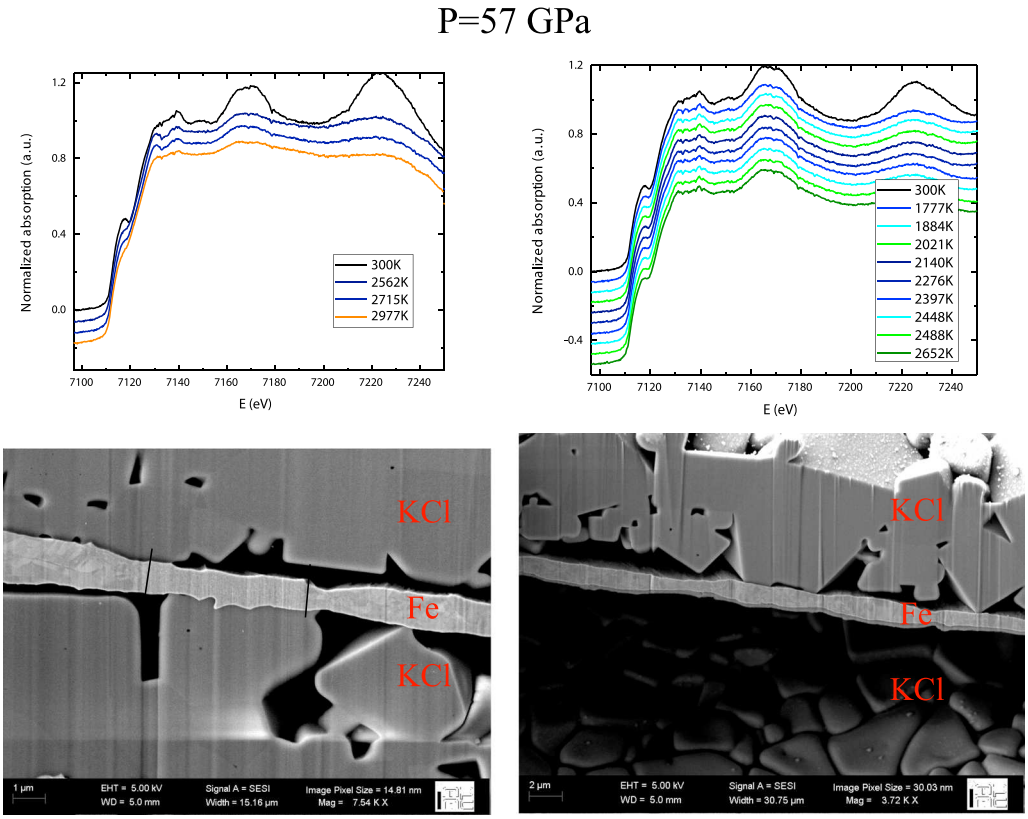

Figure 2. Validation of the melting criteria related to Fe XANES changes. Series of XANES spectra as a function of increasing temperature above (left) and below (right) the melting temperature of Fe. This melting criterion has been validated by focused ion beam cutting and SEM imaging of the hotspot cross section. Changes in the texture and irregular borders due to melting are identified on SEM figure on the left (the black lines delimitate the liquid portion of the sample). Full SEM images with a better resolution are available in the supporting information (Figures S5 and S6). XANES = X-ray Absorption Near Edge Structure; SEM = Scanning Electron Microscope.

account small divergence (below 200 K) between XANES, SMS, and XRD results, especially around the liquid-hcp-fcc triple point (Figure 3 and supporting information; Simon & Glatzel, 1929; Swartzendruber, 1982).

The collected data allowed to bracket the melting curve of iron, between the last solid and the first appearance of the melt (Figure 3 and Table S1). The measurements show an excellent agreement with the melting data from Anzellini et al. (2013) from ambient pressure up to 80 GPa. A small discrepancy can be noticed around 80–100 GPa, where the present study supports a slight bending of the pure Fe melting curve around the hcp-fcc-liquid triple point. A flattening of the melting curve around the triple point can be expected, in relation to change in entropy of melting between the two solid polymorphs. A similar behavior is in fact observed in the case of tin (Barnett et al., 1963). According to our measurements, the triple point of pure Fe is located at 100 ± 10 GPa and 3,500 ± 200 K.

Under higher pressures, our data set follows a similar trend as Anzellini et al. (2013), however, potentially showing higher melting temperature. But significant error bars on these two extreme pressure-melting points (over 500 K) do not allow us to highlight a real divergence between the two studies at the CMB pressure. A melting temperature of 4250 ± 250 K is well representative of the present melting measurements.

In few laser-heating runs of the present study, significantly lower melting temperatures were obtained. Interestingly, these points agree with those reported in previous studies employing the XAS and/or speckle-melting criterion (Aquilanti et al., 2015; Boehler, 1993; Figure 4). For these samples, the melting signature on the Fe XANES is relatively similar to the highest-temperature melting points (Figure 5). However, the signal of the quenched sample between each laser heating clearly highlights an evolution toward the

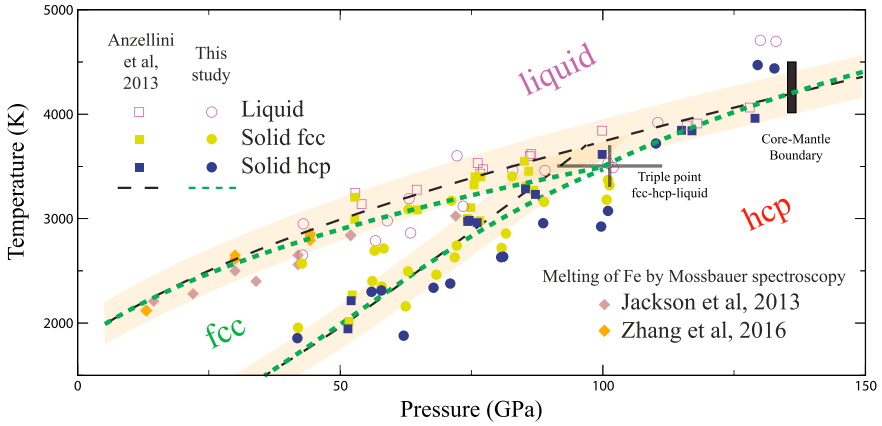

Figure 3. Iron phase diagram combining our X-ray Absorption Near Edge Structure (XANES) data set and previously published Synchrotron Mossbauer Spectroscopy (SMS) and X-ray Diffraction (XRD) data set. Full squares and circles indicate the sample in the solid state for XRD (Anzellini et al., 2013) and XANES experiments respectively. Green color indicates the presence of fcc iron, and blue color indicates the presence of hcp iron. Empty symbols indicate the presence of the first melt. Diamond symbols represent the melting of pure Fe measured by SMS (Jackson et al., 2013; Zhang et al., 2015), with thermal pressure rescaled following the present method (see supporting information for more information). The black dashed line represents the phase diagram boundaries from Anzellini et al. (2013), whereas the green dashed line is adjusted to take into account the three different studies presented here (SMS, XRD, and XANES studies; fitting parameters are available in the supporting information).

disappearance of the preedge signal (Figure 5). We relate the lower melting temperatures to chemical reactions between the sample and the diamond anvils. Indeed, all low melting points are positioned relatively close to the Fe-Fe_3C eutectic melting line (Lord et al., 2009; Morard et al., 2017). In fact, the ex situ XRD analyses of recovered samples with low melting points show clearly the presence of Fe_3C diffraction peaks (Figure 5).

4. Discussion

The present experimental results highlight a convergence between the different experimental techniques used to probe melting in LH-DAC experiments. The melting criterion associated with changes in the

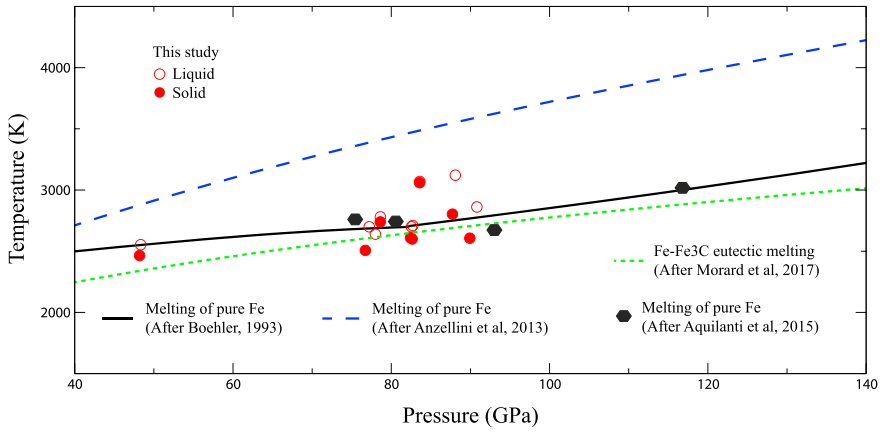

Figure 4. Melting curve of Fe-Fe_3C compared with previous melting of pure Fe measurements and C-contaminated samples from this study. Red circles represent last solid (full symbols) and first liquid (empty symbols) for melting measured by XANES in this study for carbon-contaminated samples (see Figure 5). These measurements are in good agreement with previous melting of Fe determination by speckle (Boehler, 1993) and by XANES (Aquilanti et al., 2015), highlighting that these studies may have determined melting of carbon-contaminated Fe samples. For comparison, the eutectic melting in Fe-Fe_3C system (Morard et al., 2017) is shown as green dashed line and pure Fe melting curve (Anzellini et al., 2013) is shown as blue dashed line. XANES = X-ray Absorption Near Edge Structure.

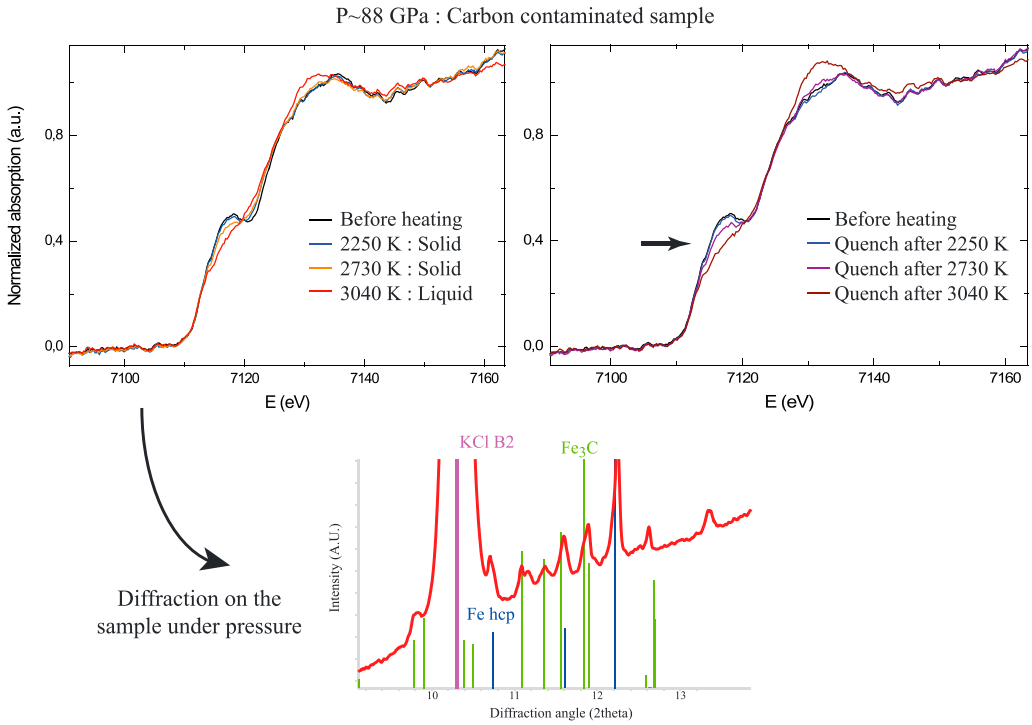

Figure 5. X-ray Absorption Near Edge Structure spectra for carbon-contaminated samples. Melting signature is relatively similar to the one for a pure Fe sample, whereas quench spectra clearly show an evolution related to the carbon enrichment (indicated by an arrow). In addition, diffraction on the sample kept under high pressure clearly shows diffraction peaks of Fe + Fe_3C mixture.

XANES features has been validated through a textural study of the recovered samples from high-pressure laser-heating experiments. Probing the local environment of Fe atoms (XANES and SMS) gives the same melting temperature as probing longer-range structural change evidenced in XRD diffuse scattering appearance. The present critical record of sample reaction after each temperature step and analysis of recovered samples allowed us to evidence that lower-melting temperatures are due to a carbon contamination of Fe sample. This contamination is related to C migration through the pressure medium, reacting with iron in the solid state to form carbides, for example, Fe_3C. This phenomenon has already been discussed in a previous study about carbon transport in LH-DAC (Prakapenka et al., 2003).

We also demonstrate that the thermal pressure determination is an important origin of the observed discrepancies. Estimation of pressure at high temperatures is not straightforward for experiments where XRD signals are not available in situ. In the present study, the thermal pressure is estimated following XRD experiments with similar sample configurations, and it allowed us to reconcile SMS, XRD, and XANES results. We would like to mention the recent attention on the careful comparison between reflective and refractive optics for temperature measurements (Giampaoli et al., 2018; Mezouar et al., 2017). In the present data set an individual error bar is associated to each temperature measurement, using the sliding two-color analysis performed on a large range of wavelengths (from 650 to 900 nm^{-1}; Figure S2). This allows to evaluate the robustness of the temperature for each individual X-ray acquisition.

Combining previous XRD and SMS data set with the present XANES measurements allows to set the position of the triple point hcp-fcc-liquid in the iron phase diagram at 100 ± 10 GPa and 3500 ± 200 K. The location of this specific point is of first importance for the thermodynamic modeling of iron under high pressure (Komabayashi & Fei, 2010). For example, the entropy change upon melting influencing the heat flow at the CMB could be derived from the position of the triple point (Anderson, 1990).

In addition, the melting temperature of pure Fe under CMB pressure is constrained at 4250 ± 250 K. This temperature is close to the solidus temperature of mantle materials (4180 K for peridotitic mantle, Fiquet et al., 2010, and 4150 K for chondritic mantle, Andrault et al., 2011). However, the absence of extended silicate

melting in contact with the metallic liquid outer core at the CMB implies that iron should be alloyed with light elements efficiently lowering its melting temperature. Therefore, volatile elements, such as sulfur, carbon, or hydrogen (Morard et al., 2017; Mori et al., 2016), instead of silicon or oxygen, are required to significantly decrease the temperature of iron crystallization under Earth's core pressure.

5. Conclusions

Combined in situ XANES at Fe edge in LH-DAC and ex situ study of recovered samples by X-ray diffraction and microscopy analysis allowed an unambiguous determination of pure iron-melting curve and phase diagram up to CMB pressure conditions. This data set presents an excellent agreement with previous in situ XRD (Anzellini et al., 2013) and SMS (Jackson et al., 2013), after recalculation of the thermal pressure estimation for the latest one. The triple-point hcp-fcc-liquid in the iron phase diagram is estimated at 100 ± 10 GPa and 3500 ± 200 K and the melting temperature at CMB pressure (136 GPa) at 4250 ± 250 K. This melting temperature, relatively close to the melting temperature of mantle silicates at CMB pressure (Andrault et al., 2011; Fiquet et al., 2010), indicates that volatile light elements such as sulfur, carbon, or hydrogen are required to lower the crystallization temperature of the Earth's liquid outer core and prevent extended melting of the mantle at the contact with the core.

Acknowledgments

Femtosecond laser micromachining at the Institute de Minéralogie de Physique des Matériaux et de Cosmochimie (IMPMC), Paris, has been developed and realized by the "Cellule Project" with the financial support of ANR 2010-JCJC-604-01. Analysis of the recovered samples was performed with the help of I. Estève at the Focused Ion Beam (FIB) and Scanning Electron Microscope (SEM) facility of the Institute de Minéralogie de Physique des Matériaux et de Cosmochimie, supported by Région Ile de France grant SESAME 2006 N°I-07-593/R, INSU-CNRS, INP-CNRS, University Pierre et Marie Curie-Paris 6, and by the French National Research Agency (ANR) grant ANR-07-BLAN-0124-01. This project has received funding from the European Research Council (ERC) under the European Union's Horizon 2020 research and innovation program (grant agreement 670787). Data are available as supporting information.

References

Akahama, Y., & Kawamura, H. (2004). High-pressure Raman spectroscopy of diamond anvils to 250 GPa: Method for pressure determination in the multimegabar pressure range. *Journal of Applied Physics*, *96*(7), 3748–3751. https://doi.org/10.1063/1.1778482

Alfè, D. (2009). Temperature of the inner-core boundary of the Earth: Melting of iron at high pressure from first-principles coexistence simulations. *Physical Review B: Condensed Matter and Materials Physics*, *79*(6), 1–4. https://doi.org/10.1103/PhysRevB.79.060101

Alfè, D., Price, G. D., & Gillan, M. J. (2002). Iron under Earth's core conditions: Liquid-state thermodynamics and high-pressure melting curve from ab initio calculations. *Physical Review B*, *65*(16), 165118. https://doi.org/10.1103/PhysRevB.65.165118

Anderson, O. L. (1990). The high-pressure triple points of iron and their effects on the heat flow from the Earth's core. *Journal of Geophysical Research*, *95*(B13), 21,697–21,707. https://doi.org/10.1029/JB095iB13p21697

Andrault, D., Bolfan-Casanova, N., Lo Nigro, G., Bouhifd, M. A., Garbarino, G., & Mezouar, M. (2011). Solidus and liquidus profiles of chondritic mantle: Implication for melting of the Earth across its history. *Earth and Planetary Science Letters*, *304*(1–2), 251–259. https://doi.org/10.1016/j.epsl.2011.02.006

Anzellini, S., Dewaele, A., Mezouar, M., Loubeyre, P., & Morard, G. (2013). Melting of iron at Earth's inner core boundary based on fast X-ray diffraction. *Science*, *340*(6131). https://doi.org/10.1126/science.1233514

Aquilanti, G., Trapananti, A., Karandikar, A., Kantor, I., Marini, C., Mathon, O., et al. (2015). Melting of iron determined by X-ray absorption spectroscopy to 100 GPa. *Proceedings of the National Academy of Sciences*, *112*(39), 12,042–12,045. https://doi.org/10.1073/pnas.1502363112

Barnett, J. D., Bennion, R. B., & Hall, H. T. (1963). X-ray diffraction studies on tin at high pressure and high temperature. *Science*, *141*, 1041.

Benedetti, L., & Loubeyre, P. (2004). Temperature gradients, wavelength-dependent emissivity, and accuracy of high and very-high temperatures measured in the laser-heated diamond cell. *High Pressure Research*, *24*(4), 423–445. https://doi.org/10.1080/08957950412331331718

Boccato, S., Torchio, R., Kantor, I., Morard, G., Anzellini, S., Giampaoli, R., et al. (2017). The melting curve of nickel up to 100 GPa explored by XAS. *Journal of Geophysical Research: Solid Earth*, *122*, 9921–9930. https://doi.org/10.1002/2017JB014807

Boehler, R. (1993). Temperatures in the Earth's core from melting-point measurements of iron at high static pressures. *Nature*, *363*(6429), 534–536. https://doi.org/10.1038/363534a0

Boehler, R., Santamaría-Pérez, D., Errandonea, D., & Mezouar, M. (2008). Melting, density, and anisotropy of iron at core conditions: New X-ray measurements to 150 GPa. *Journal of Physics: Conference Series*, *121*(PART 2). https://doi.org/10.1088/1742-6596/121/2/022018

Brown, J. M., & Mcqueen, G. (1986). Phase transitions, Griineisen parameter, and elasticity. *Journal of Geophysical Research*, *91*(B7), 7485–7494. https://doi.org/10.1029/JB091iB07p07485

Campbell, A. J., Danielson, L., Righter, K., Seagle, C. T., Wang, Y., & Prakapenka, V. B. (2009). High pressure effects on the iron-iron oxide and nickel-nickel oxide oxygen fugacity buffers. *Earth and Planetary Science Letters*, *286*(3–4), 556–564. https://doi.org/10.1016/j.epsl.2009.07.022

Dewaele, A., Torrent, M., Loubeyre, P., & Mezouar, M. (2008). Compression curves of transition metals in the Mbar range: Experiments and projector augmented-wave calculations. *Physical Review B: Condensed Matter and Materials Physics*, *78*(10), 1–13. https://doi.org/10.1103/PhysRevB.78.104102

Fiquet, G., Auzende, A. L., Siebert, J., Corgne, A., Bureau, H., Ozawa, H., & Garbarino, G. (2010). Melting of peridotite at 140 gigapascals. *Science*, *329*, 1516–1518.

Giampaoli, R., Kantor, I., Mezouar, M., Boccato, S., Rosa, A. D., Torchio, R., et al. (2018). Measurement of temperature in the laser heated diamond anvil cell: Comparison between reflective and refractive Ooptics. *High Pressure Research*, *38*(3). https://doi.org/10.1080/08957959.2018.1480017

Harmand, M., Ravasio, A., Mazevet, S., Bouchet, J., Denoeud, A., Dorchies, F., et al. (2015). X-ray absorption spectroscopy of iron at multi-megabar pressures in laser shock experiments. *Physical Review B: Condensed Matter and Materials Physics*, *92*(2), 1–7. https://doi.org/10.1103/PhysRevB.92.024108

Ishimatsu, N., Matsumoto, K., Maruyama, H., Kawamura, N., Mizumaki, M., Sumiya, H., & Irifune, T. (2012). Glitch-free X-ray absorption spectrum under high pressure obtained using nano-polycrystalline diamond anvils. *Journal of Synchrotron Radiation*, *19*(5), 768–772. https://doi.org/10.1107/S0909049512026088

Jackson, J. M., Sturhahn, W., Lerche, M., Zhao, J., Toellner, T. S., Alp, E. E., et al. (2013). Melting of compressed iron by monitoring atomic dynamics. *Earth and Planetary Science Letters*, *362*, 143–150. https://doi.org/10.1016/j.epsl.2012.11.048

Kantor, I., Marini, C., Mathon, O., & Pascarelli, S. (2018). A laser heating facility for energy-dispersive X-ray absorption spectroscopy. *The Review of Scientific Instruments*, *89*(1), 013,111–013,113. https://doi.org/10.1063/1.5010345

Komabayashi, T., & Fei, Y. (2010). Internally consistent thermodynamic database for iron to the Earth's core conditions. *Journal of Geophysical Research*, *115*, B03202. https://doi.org/10.1029/2009JB006442

Lord, O. T., Walter, M. J., Dasgupta, R., Walker, D., & Clark, S. M. (2009). Melting in the Fe-C system to 70 GPa. *Earth and Planetary Science Letters*, *284*(1–2), 157–167. https://doi.org/10.1016/j.epsl.2009.04.017

Lord, O. T., Wann, E. T. H., Hunt, S. A., Walker, A. M., Santangeli, J., Walter, M. J., et al. (2014). The NiSi melting curve to 70GPa. *Physics of the Earth and Planetary Interiors*, *233*, 13–23. https://doi.org/10.1016/j.pepi.2014.05.005

Lord, O. T., Wood, I. G., Dobson, D. P., Vočadlo, L., Wang, W., Thomson, A. R., et al. (2015). The melting curve of Ni to 1 Mbar. *Earth and Planetary Science Letters*, *408*, 226–236. https://doi.org/10.1016/j.epsl.2014.09.046

Marini, C., Occelli, F., Mathon, O., Torchio, R., Recoules, V., Pascarelli, S., & Loubeyre, P. (2014). A microsecond time resolved X-ray absorption near edge structure synchrotron study of phase transitions in Fe undergoing ramp heating at high pressure. *Journal of Applied Physics*, *115*(9), 093,513–093,515. https://doi.org/10.1063/1.4867619

Mazevet, S., Recoules, V., Bouchet, J., Guyot, F., Harmand, M., Ravasio, A., & Benuzzi-Mounaix, A. (2014). Ab initio calculation of X-ray absorption of iron up to 3 Mbar and 8000 K. *Physical Review B: Condensed Matter and Materials Physics*, *89*(10), 1–5. https://doi.org/10.1103/PhysRevB.89.100103

Mezouar, M., Crichton, W. A., Bauchau, S., Thurel, F., Witsch, H., Torrecillas, F., et al. (2005). Development of a new state-of-the-art beamline optimized for monochromatic single-crystal and powder X-ray diffraction under extreme conditions at the ESRF. *Journal of Synchrotron Radiation*, *12*(5), 659–664. https://doi.org/10.1107/S0909049505023216

Mezouar, M., Giampaoli, R., Garbarino, G., Kantor, I., Dewaele, A., Weck, G., et al. (2017). Methodology for in situ synchrotron X-ray studies in the laser-heated diamond anvil cell. *High Pressure Research*, *37*(2), 170–180. https://doi.org/10.1080/08957959.2017.1306626

Miozzi, F., Morard, G., Antonangeli, D., Clark, A. N., Mezouar, M., Dorn, C., Rozel, A., & Fiquet, G. (2018). Equation of state of SiC at extreme conditions: New insight into the interior of carbon-rich exoplanets. *Journal of Geophysical Research: Planets*, *123*, 2295–2309. https://doi.org/10.1029/2018JE005582

Morard, G., Andrault, D., Antonangeli, D., Nakajima, Y., Auzende, A. L., Boulard, E., et al. (2017). Fe–FeO and Fe–Fe_3C melting relations at Earth's core–mantle boundary conditions: Implications for a volatile-rich or oxygen-rich core. *Earth and Planetary Science Letters*, *473*, 94–103. https://doi.org/10.1016/j.epsl.2017.05.024

Mori, Y., Ozawa, H., Hirose, K., Sinmyo, R., Tateno, S., Morard, G., & Ohishi, Y. (2016). Melting experiments on Fe–Fe_3S system to 254 GPa. *Earth and Planetary Science Letters*, *464*, 135–141. https://doi.org/10.1016/j.epsl.2017.02.021

Nguyen, J. H., & Holmes, N. C. (2004). Melting of iron at the physical conditions of the Earth's core. *Nature*, *427*(6972), 339–342. https://doi.org/10.1038/nature02248

Pascarelli, S., Mathon, O., Mairs, T., Kantor, I., Agostini, G., & Strohm, C. (2016). The time-resolved and extreme-conditions XAS (TEXAS) facility at the European Synchrotron Radiation Facility: The energy-dispersive X-ray absorption spectroscopy beamline ID24. *Journal of Synchrotron Radiation*, *23*(1), 353–368. https://doi.org/10.1107/S160057751501783X

Prakapenka, V., Shen, G., & Dubrovinsky, L. (2003). Carbon transport in diamond anvil cells. *High Pressure High Temperature*, *35/36*, 237–249. https://doi.org/10.1068/htjr098

Prescher, C., & Prakapenka, V. B. (2015). DIOPTAS: A program for reduction of two-dimensional X-ray diffraction data and data exploration. *High Pressure Research*, *35*(3), 223–230. https://doi.org/10.1080/08957959.2015.1059835

Simon, F., & Glatzel, G. (1929). Bernerkungen zur Schmelzdruckkurve. *Zeitschrift für Anorganische und Allgemeine Chemie*, *178*(1), 309–316. https://doi.org/10.1002/zaac.19291780123

Swartzendruber, L. J. (1982). The Fe (iron) system. *Bulletin of Alloy Phase Diagrams*, *3*(2), 161–165. https://doi.org/10.1007/BF02892374

Torchio, R., Occelli, F., Mathon, O., Sollier, A., Lescoute, E., Videau, L., et al. (2016). Probing local and electronic structure in warm dense matter: Single pulse synchrotron X-ray absorption spectroscopy on shocked Fe. *Scientific Reports*, *6*(1), 1–8. https://doi.org/10.1038/srep26402

Zhang, D., Jackson, J. M., Zhao, J., Sturhahn, W., Alp, E. E., Hu, M. Y., et al. (2015). Temperature of Earth's core constrained from melting of Fe and $Fe_{0.9}Ni_{0.1}$ at high pressures. *Earth and Planetary Science Letters*, *447*, 72–83. https://doi.org/10.1016/j.epsl.2016.04.026

JGR Solid Earth

RESEARCH ARTICLE
10.1029/2018JB016904

Velocity-Density Systematics of Fe-5wt%Si: Constraints on Si Content in the Earth's Inner Core

E. Edmund[1], D. Antonangeli[1], F. Decremps[1], F. Miozzi[1], G. Morard[1], E. Boulard[1], A. N. Clark[1], S. Ayrinhac[1], M. Gauthier[1], M. Morand[1], and M. Mezouar[2]

[1]Institut de Minéralogie, de Physique des Matériaux et de Cosmochimie (IMPMC), Sorbonne Université, UMR CNRS 7590, IRD, Muséum National d'Histoire Naturelle, Paris, France, [2]ESRF, Grenoble, France

Abstract The elasticity of hcp-Fe-5wt%Si has been investigated by synchrotron X-ray diffraction up to 110 GPa and 2,100 K and by picosecond acoustics measurements at ambient temperature up to 115 GPa. The established Pressure-Volume-Temperature equation of state shows that the density of the Earth's inner core can be matched by an Fe-Si alloy with 5wt% Si for all reasonable core temperatures, but that its compressional and shear velocities remain too high with respect to seismological observations. On the other hand, Fe-Si alloys whose velocities are expected to get close to seismological observations are too dense at relevant temperatures. Thus, based on these combined velocity-density measurements, silicon is not likely to be the sole light element in the inner core.

Plain Language Summary Combining measurements of sound velocity and density at high pressures and temperatures shows that while Fe-5wt% Si can match the density profile of the Earth's inner core, its sound velocity is too high with respect to seismological observations.

Key Points:
- Isothermal compression of Fe-5wt%Si at high temperatures up to 1.1 Mbar and 2100 K
- Measurement of Vp of Fe-5wt%Si under quasihydrostatic conditions to 1.1 Mbar
- Si cannot be the sole light element in the Earth's inner core

Supporting Information:
- Supporting Information S1
- Data Set S1
- Data Set S2
- Data Set S3

Correspondence to:
E. Edmund,
Eric.Edmund@upmc.fr

Citation:
Edmund, E., Antonangeli, D., Decremps, F., Miozzi, F., Morard, G., Boulard, E., et al. (2019). Velocity-density systematics of Fe-5wt%Si: Constraints on Si content in the Earth's inner core. *Journal of Geophysical Research: Solid Earth*, *124*. https://doi.org/10.1029/2018JB016904

Received 2 NOV 2018
Accepted 7 FEB 2019
Accepted article online 10 FEB 2019

1. Introduction

Iron and iron alloys at extreme conditions have garnered significant interest due to their relevance to the Earth's deep interior. While a first 1-D reference seismological model providing density (ρ), compressional (Vp) and shear (Vs) sound velocities as a function of depth into the Earth (PREM, Preliminary Reference Earth Model) was established in the 1980s (Dziewonski & Anderson, 1981), there is still considerable debate over the chemical composition of the Earth's core. On cosmochemical grounds, iron is considered to be the most abundant element in the Earth's core (e.g., Allégre et al., 1995; McDonough & Sun, 1995). However, early on in the study of Fe at extreme conditions, it was observed that Fe is too dense at the pressure (P) and temperature (T) conditions of the core to be the sole element present (Birch, 1952). Earth's solid inner core exists at pressures of 330–360 GPa, and at temperatures of 5,000–7,000 K based on the melting curve of Fe (Anzellini et al., 2013; Boehler, 1993; Nguyen & Holmes, 2004). As a consequence of the density difference between Fe and PREM, there needs to be some quantity of elements lighter than Fe alloyed to it in order to compensate for this density deficit. Among the potential light element candidates, Si has been favored by many recent studies but without reaching a firm consensus. Regardless of the nature of accretionary materials and redox path, all recent core differentiation models based on metal-silicate partitioning support the presence of Si in the core (Fischer et al., 2015; Siebert et al., 2013). The presence of Si is also advocated on the basis of isotopic arguments (Fitoussi et al., 2009). The possible presence and the quantity of Si in the Earth's core has important implications for geodynamic processes and the bulk redox state of the Earth's interior (Hirose et al., 2017; Wade & Wood, 2005; Wood et al., 1990). One possible way to constrain the Si content of the inner core is the comparison between seismological data and experimental measurements, or calculations, of ρ, Vp, and Vs of candidate materials at pertinent PT conditions (Sakairi et al., 2018; Sakamaki et al., 2016). Based off the measurement of Vp versus ρ at extreme conditions, estimates have varied from 1–2 wt% Si (Antonangeli et al., 2010; Badro et al., 2007) to ~8 wt% Si (Fischer et al., 2014; Z. Mao et al., 2012), with the most recent measurements putting an upper limit of 5 wt% Si (Antonangeli et al., 2018; Sakairi et al., 2018).

Thanks to the adaptation of Picosecond Acoustics (PA) to the Diamond Anvil Cell (DAC), it is possible to make direct measurements of the acoustic travel time of Fe-alloys, and metals in general, at very high pressures (Decremps et al., 2008, 2014). Additionally, PA has fewer limitations on sample dimensions

than conventional synchrotron-based techniques, allowing the measurement of Vp under quasihydrostatic conditions to Mbar pressures. We thus used PA to probe acoustic echoes and the compressional sound velocity of an Fe-Si alloy with 5 wt% Si up to 115 GPa. We complemented these measurements with synchrotron X-ray diffraction (XRD) measurements in laser-heated DACs up to 110 GPa and 2,100 K, deriving a Pressure-Volume-Temperature (P-V-T) equation of state. Our results provide tight constraints on the Si abundance in the Earth's inner core.

2. Methods

2.1. Sample Preparation

All experiments were performed on an Fe-Si alloy synthesized by melt spinning at ICMPE laboratory in Thiais, France (melt temperature T = 1,823 K, wheel velocity v = 20 m/s, Morard et al., 2011). Scanning electron microscopy measurements have shown the alloy to be chemically homogeneous and contain 5.2(2) wt% Si, and so the alloy will be referred to hereafter as Fe-5Si for brevity. Fe-5Si was also measured by grazing-incidence XRD at ambient conditions to check phase purity and density, showing minimal texture and excellent polycrystallinity. Experiments were performed using Le Toullec-type membrane-driven DACs with diamonds of culet size ranging from 250 μm down to 100 μm and equipped with Re gaskets. All experiments at ambient temperature were performed with Ne as the pressure-transmitting medium (PTM) to ensure quasihydrostatic conditions up to Mbar conditions. Samples were scraped from a large, thin ribbon, and sample dimensions were chosen such that there was no bridging between sample and diamonds, nor contact between gasket and sample. For PA experiments, the thickness of the sample was determined by the measured initial travel time and derived Vp from literature elastic constants (see section 2.3). In PA Run 1 the sample was determined to be 3.73(6) μm thick, and for Run 2 the sample was determined to be 1.84(3) μm thick. For high-T XRD the sample was 1–3 μm thick, and for ambient-T XRD the sample was 5–7 μm thick, estimated by optical microscopy (during sample loading) and observations of diffraction intensity relative to PTM.

2.2. X-ray Diffraction

For room temperature measurements, Fe-5Si was loaded alongside Mo (Pressure calibration: K_0 = 260(1) GPa, K′ = 4.19(5), using the reference volume of Mo − V_0 = 31.17 Å^3, Litasov et al., 2013; Ross & Hume-Rothery, 1963) or Pt (K_0 = 277.3 GPa, K′ = 5.12, V_0 = 60.38 Å^3, Dorogokupets & Oganov, 2007) as a pressure calibrant, with Ne as the PTM. For experiments at high temperatures, the samples were sandwiched between KCl disks which served as the PTM, and to thermally insulate the sample from the diamonds. KCl also served as the pressure calibrant. The samples' pressure at high temperatures was determined by diffraction of KCl, with the method for estimating temperature following Campbell et al. (2009) and the KCl pressure calibration of Dewaele et al. (2012). By virtue of its very low thermal pressure, uncertainties on pressure due to thermal gradients across KCl are below reported error bars. After loading the DAC, the assembly was left open to dry in a vacuum oven at 130 °C for at least 1 hr after which the DAC was closed. This practice ensures that moisture content is minimal within the sample chamber. Angle-dispersive XRD measurements were performed at beamline ID27 at the ESRF (Mezouar et al., 2005). The radiation was monochromatic (λ = 0.3738 nm) focused to approximately 3 × 3 μm^2 (horizontal × vertical full width at half maximum). Diffraction patterns were collected on a MarCCD camera, with collection times of 30–60 s. Samples were heated on both sides by two continuous Nd:YAG fiber lasers (TEM00), each one delivering up to 200 W. Hot spots were approximately 20 μm in diameter, much larger than the full width at half maximum of the focused X-ray beam. All temperatures were measured by the spectroradiometric method, using a Planck fit of the observed blackbody radiation from the center of the heating spot, as described by Mezouar et al. (2017). While absolute errors in temperature are on the order of 150 K, the measured temperature was seen to vary by less than 30 K during pattern integration (averaged over three to five measurements per diffraction pattern). Diffraction images were calibrated against a CeO_2 standard and then radially integrated using Dioptas image processing software (Prescher & Prakapenka, 2015). The integrated diffraction pattern was then analyzed by the use of Le Bail fits in the software Jana2006 (Václav et al., 2014).

2.3. Picosecond Acoustics

These experiments are performed in pump-probe configuration, where laser pulses generated by a Maitai Ti:Sapphire laser (λ = 800 nm, pulse duration = 100 fs) are separated into two beams which are focused at

the two opposing faces of the metallic sample. The majority of the intensity (~80%) of the laser is directed toward the pump side (30–100 mW depending on experimental conditions), where the beam generates a small thermal stress at the surface of the sample. The relaxation of this thermal stress generates an elastic wave which propagates through the sample. The probe beam, comprising the remainder of the lasing intensity, is analyzed by means of an interferometer, in order to detect the change of phase of reflectivity at the sample surface. This quantity changes abruptly upon arrival of the acoustic wave, and therefore provides an accurate determination of the acoustic travel time across the material. Further details of the setup are provided elsewhere (Decremps et al., 2015). At ambient conditions, the value of Vp was derived from single crystal elastic constants (Machová & Kadečková, 1977) using the Hashin-Strikman average (Hashin & Shtrikman, 1962) and combined with the measured acoustic travel time to determine initial thickness. The acoustic travel time used to determine the thickness of the sample was an average of several measurements across the sample surface, with the travel time of each location being derived from the time difference between the first and second acoustic echo. This procedure was performed before and after each experiment for each sample. The thickness at pressure was assumed to scale as $(V/V_0)^{1/3}$ where V_0 is the V_0 of bcc Fe-5Si, measured to be 23.34(4) [3] and V is determined from the fitted EoS for hcp-Fe-5Si. Thickness and travel times as a function of pressure were then combined to determine Vp up to Mbar pressures. Ruby fluorescence (H. K. Mao et al., 1986; Sokolova et al., 2013) and the Raman shift of the center of the diamond culet (Akahama & Kawamura, 2006) were used to assess pressure. Determination by ruby spectra and diamond edge Raman were within 2 GPa of each other at all pressures where both were measured. Ruby fluorescence was measured before and after every travel time measurement, and the reported pressure is an average of the two values. For Run 1, the difference in pressures determined from ruby fluorescence before and after measurement was less than 0.5 GPa, while for Run 2 it was less than 2 GPa. All reported pressures are derived from ruby fluorescence measurements with the calibration of Sokolova et al. (2013).

3. Results

3.1. X-ray Diffraction

Two runs were performed in Ne at 300 K, one of which used Pt as pressure calibrant to 41 GPa, and another run measured to 1.1 Mbar with Mo as the pressure calibrant. Diffraction of the pressure calibrant was collected independently from that of the sample by translating the cell a few microns from the sample position. As sample reflections were also observable at the calibrant position, the presented volumes are unweighted averages of all measured volumes at a given pressure step, and the reported pressure are averages of Mo/Pt measurements taken at the same pressure step, drift between pressure measurements was typically less than 0.2 GPa. While measurement error of Mo volume and the statistical errors in the calibrant EoS are small (<0.5%), the absolute error at 300 K due to the intrinsic uncertainty in pressure calibration and pressure gradients is ~2–3%. The bcc-hcp transition started at about 14 GPa and all bcc reflections were absent by 21 GPa.

In another set of experiments, Fe-5Si was compressed in a laser-heated membrane DAC along two high-temperature isotherms, at about 1,450 K and at about 2,100 K. Temperatures varied by less than 100 K along each isotherm ($1\sigma = 30$ K at 1,450 K and $1\sigma = 50$ K at 2,100 K). Temperatures were corrected downward by around 3% following standard methods (Campbell et al., 2009) to account for axial T gradients (however, this had a negligible effect on the fitted equation of state parameters). No phase other than hcp-Fe-5Si was observed at the HP-HT conditions of the present study, consistent with Tateno et al. (2015). Integrated diffraction patterns in Ne and at high temperatures are discussed in supporting information Text S1 and shown in Figures S1 and S2.

The ambient temperature component of the P-V-T thermal model employed in the present study consisted of either a Third Order Birch-Murnaghan (equation (1), Birch, 1947) or Vinet (equation (2), Vinet et al., 1989) EoS:

$$P_{300K}(V) = \frac{3}{2}K_0\left[\left(\frac{V_0}{V}\right)^{7/3} - \left(\frac{V_0}{V}\right)^{5/3}\right]\left\{1 + \frac{3}{4}\left(K' - 4\right)\left[\left(\frac{V_0}{V}\right)^{2/3} - 1\right]\right\}, \quad (1)$$

$$P_{300K}(V) = 3K_0\left(\frac{1-\eta}{\eta^2}\right)exp\left[\frac{3}{2}\left(K' - 1\right)(1-\eta)\right], \quad (2)$$

where V_0, K_0, and K' are the unit cell volume (Å^3), bulk modulus (GPa), and $\frac{dK}{dP}$ at ambient conditions. In equation (2) specifically, $\eta = \left(\frac{V}{V_0}\right)^{(1/3)}$.

The thermal parametrization is shown in equation (3).

$$P(V,T) = P_{300K}(V) + P_{vib}(V,T)|_{300}^{T} + P_{el+anh}(V,T)|_{300}^{T}. \quad (3)$$

In equation (3), $P_{vib}(V,T)$ is given by

$$P_{vib}(V,T) = \frac{9NR\gamma_{vib}}{V}\left[\frac{\theta_D}{8} + T\left(\frac{T}{\theta_D}\right)^3 \int_{300}^{\theta_D/T} \frac{x^3}{exp(x)-1}dx\right], \quad (4)$$

where γ_{vib} is the vibrational Grüneisen parameter, θ_D is the Debye temperature, N is the number of atoms per formula unit ($N = 2$ for hcp-structured Fe-alloys). R is the ideal gas constant, V is unit cell volume (in units of cm^3/mol) and T is the temperature (in K). The volume dependence of the vibrational Grüneisen parameter and Debye temperature are given by equations (5) and (6), respectively.

$$\left(\frac{\gamma_{vib}}{\gamma_{vib,0}}\right) = \left(\frac{V}{V_0}\right)^q, \quad (5)$$

$$\theta_D = \theta_{D,0}\exp\left[\left(\gamma_{vib,0} - \gamma_{vib}\right)/q\right]. \quad (6)$$

In equations (5) and (6) q characterizes the volume dependence of the vibrational contributions to thermal pressure. In the fitting process, $\theta_{D,0}$ was fixed to 422 K.

Due to the similar T^2 dependence of P_{el} and P_{anh}, a single electronic pressure term was used for fitting in the present thermal model:

$$P_{el}(V,T) = \frac{\gamma_e}{V}\beta_0\left(\frac{V}{V_0}\right)^k T^2, \quad (7)$$

where γ_e is the electronic Grüneisen parameter (here fixed to 2 after ; Fei et al., 2016), β_0 is the electronic heat capacity, and k (fixed to 1.34) is an exponent which characterizes the volume dependence of the electronic contribution to thermal pressure.

All parameters of the presented P-V-T EoS except k, γ_e, and θ_D were refined simultaneously by an unweighted least-squares fit to the entire data set. When the Debye temperature is fixed in literature, it is generally fixed to anywhere between 417 and 422 K for Fe and Fe-Si alloys (e.g., Dewaele et al., 2006; Fischer et al., 2012, 2014), however such differences are negligible with regards to the resultant EoS. Additionally, most of the studies which have constrained k either experimentally or by means of ab initio calculations (Boness et al., 1986; Dewaele et al., 2006; Fei et al., 2016) generally report a k value of ~1.34. Varying k on the order of ~0.1 in the fitting process produces deviations in extrapolated densities at inner core conditions of less than 0.2%, far below the error bar of the extrapolation (~1.5%). It is stressed that while electronic contributions to thermal pressure are relatively small (up to ~5 GPa at 2,100 K), it was not possible to fit the present data set to a purely vibrational model of thermal pressure, as such a model could not simultaneously reproduce the compressional behavior of both the 1,450 and 2,100 K isotherms. The fitted EoS parameters of this data set are shown in Table 1. All datapoints were within 2 GPa of the fitted EoS, irrespective of whether a 3BM or Vinet EoS was used for the ambient temperature compression curve.

At ambient temperature, the present data set is similar to recent measurements of Fe10Ni5Si (Morrison et al., 2018) and those of hcp-Fe in He (Dewaele et al., 2006). Discrepancies between the presented ambient temperature EoS parameters are primarily due to small systematic differences observed at low pressures (below ~60 GPa), as Fe, Fe10Ni5Si, and Fe5Si all have nearly identical volumes by 1 Mbar. Shown in Figure 1 as raw datapoints, the presented alloy exhibits a slightly higher volume than hcp-Fe, consistent with literature on Fe-Si alloys (Fischer et al., 2014; Lin, Campbell, et al.,2003; Tateno et al., 2015). While the Earth's core is likely to be composed of an Fe-Ni alloy, the addition of Ni likely does not significantly change the presented results and conclusions, due to the weak effect that Ni has on Vp relative to Fe and Si (Antonangeli et al., 2010; Liu et al., 2016; Martorell et al., 2013; Wakamatsu et al., 2018) and its weak effect on density

Table 1
P-V-T Equations of State of the Presented Alloy and Selected Literature

	Fe5Si	Fe5Si	Fe F16	Fe Y12	Fe9Si F14
Formalism	3BM	Vinet	3BM	3BM	3BM
V_0	22.524(62)	22.587(67)	**22.428**	22.15(5)	23.92(18)
K_0	172.4(6.0)	163.3(6.9)	172.7(1.4)	202(7)	129.1(1.4)
K'	4.64(14)	5.13(16)	4.79(0.05)	4.5(2)	5.29(8)
θ_D	**422**	**422**	**422**	1173(62)	**420**
γ_0	1.72(13)	1.73(13)	**1.74**	3.2(2)	1.14(14)
q	0.65(23)	0.67(23)	**0.78**	0.8(3)	**1**
β_0	3.20(85)	3.22(85)	3.91	*ab initio*	-
k	**1.34**	**1.34**	1.34	*ab initio*	-

Note. V_0 has units of Å^3, K_0 has units of GPa, θ_D has units of K, β_0 has units of cm^3 mol^{-1} J K^{-2} 10^{-6}, the other parameters are dimensionless. F16 denotes Fei et al. (2016), Y12 denotes Yamazaki et al. (2012), and F14 denotes Fischer et al. (2014). Parameters in bold font are those which have been fixed during the fitting process. The two thermal models of Fe5Si are based on different choices of ambient temperature EoS formalism.

(Morrison et al., 2018). However, it is stressed that at present there are few constraints on the thermoelastic behavior of Fe-Ni or Fe-Ni-Si alloys at simultaneous high P-T conditions.

It is immediately noticeable in Figure 2 that the P-V-T EoS of Fe-5Si measured here is similar to that of reported thermal parametrizations of hcp-Fe (Dewaele et al., 2006; Fei et al., 2016), considering the small differences in 300 K EoS in each study. Unsurprisingly, the fitted P-V-T EoS parameters of Fe-5Si are in good agreement with those of Fei et al. (2016), which employs the same type of thermal model. It is remarkable that the present XRD data set composed purely of static compression data is capable of producing a P-V-T EoS which is directly comparable to those incorporating extensive parametrization using shock compression data, ab initio calculations and/or NRIXS (e.g., Dewaele et al., 2006; Fei et al., 2016).

As the direct measurement of thermal EoS are at the cutting edge of experimental capabilities, it has been common in recent past to use ab initio parametrizations to account for P_{el} (e.g., Dewaele et al., 2006). Inputs from calculations have been used to constrain P_{el} and fit a purely vibrational model (Yamazaki et al., 2012) or to construct thermal models using purely ambient temperature experimental data (e.g., Lin, Campbell, et al.,2003; Morrison et al., 2018). Choice of parametrization can change electronic thermal pressures at core conditions by nearly 50%, and P_{el} itself is comparable in magnitude to P_{vib} at such conditions. Rescaling $P_{el} + P_{anh}$ of Dewaele et al. (2006) to the formalism used in the present study, $\beta_0 \approx 1.7$. As the fitted β_0 of the present work is ~3.2(9) and that of Fei et al. (2016) is 3.91, it is likely for a dilute Fe-alloy (of realistic composition for the Earth's inner core) that P_{el} is larger than that reported by Dewaele et al. (2006).

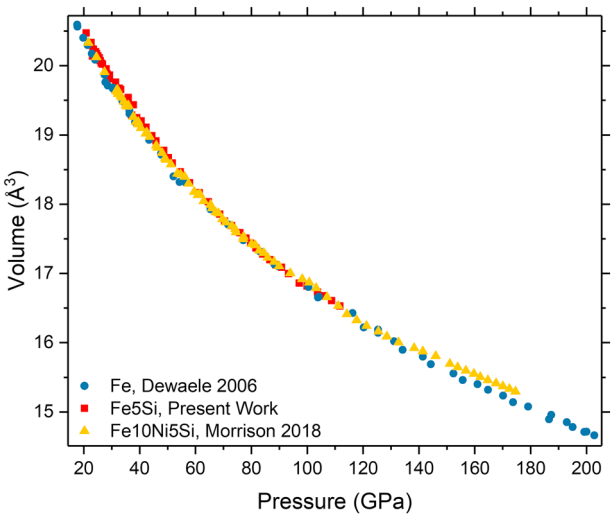

Figure 1. Ambient temperature Pressure-Volume relations of Fe-5Si (present work), pure Fe (Dewaele et al., 2006), and Fe10Ni5Si (Morrison et al., 2018). It is observed that Fe5Si and Fe10Ni5Si exhibit a small systematic difference up to 60 GPa, with their volumes becoming indistinguishable at higher pressures.

3.2. Picosecond Acoustics

Travel times were measured as a function of pressure (Figures 3 and 4) in two independent runs performed on samples of Fe-5Si alloy of different initial thickness. Errors in Vp were about 2% up to 60 GPa, and about 3% by 115 GPa. Shown in Figure 3 are background-subtracted time domain signals at 47 GPa before and after data treatment to extract Brillouin oscillations. Larger errors at high pressures are due to an increase in diffuse background caused by the progressive depolarization of the pump and probe beams resulting from increased defect scattering, stress gradients across the diamond anvil, and the cupping of the diamond culet- classical issues encountered by optical measurements at Mbar conditions (Merkel et al., 1999). Uncertainties of sample thickness, especially at high pressure, has only a small effect on the travel time compared to the change

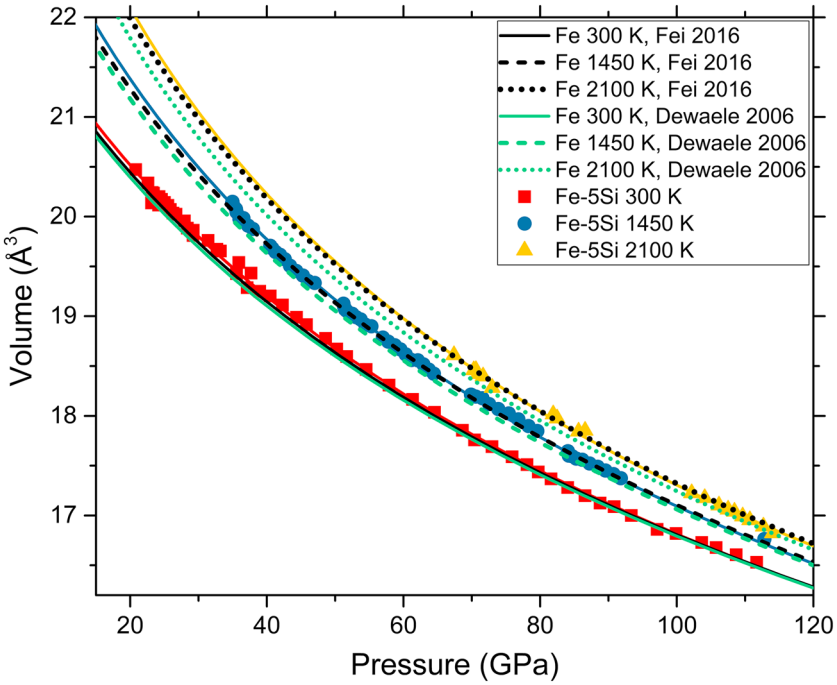

Figure 2. Pressure-Volume-Temperature data set measured in the present study. Shown as lines are the results of the 3BM EoS fit described here and the Pressure-Volume-Temperature relations reported by literature on hcp-Fe (Dewaele et al., 2006; Fei et al., 2016).

in velocity. As a matter of fact, by 1 Mbar, the thickness has changed by ~10% relative to ambient pressure, while the acoustic travel time is typically 50% its original value. Sample tilt within the sample chamber has a negligible effect on measured travel times due to the instrumental configuration and focusing strategy employed. In Run 1, it was seen that there were some residual stresses in the sample which induced local variation in measured travel times of about 2–3% in the bcc phase, and so for Run 2, the sample was

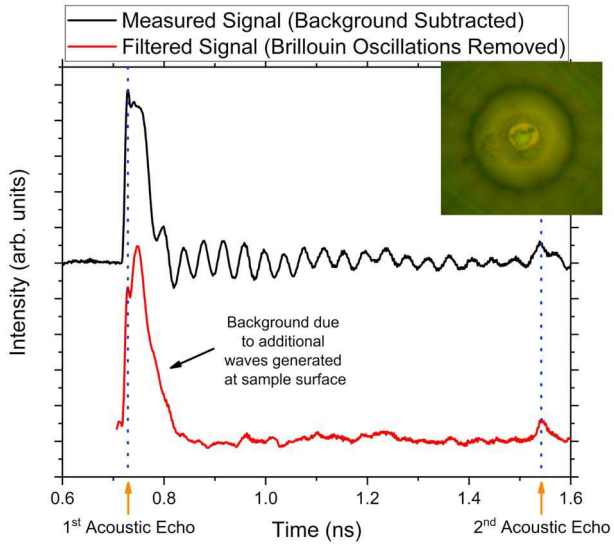

Figure 3. Travel Time measurement by Picosecond Acoustics at 47 GPa. The sharp peak associated with the first acoustic echo is clearly visible, followed by a background signal related to the generation of surface waves and Brillouin scattering in the Ne pressure-transmitting medium (filtered in the red curve). The difference between the travel time of filtered and unfiltered data changes by a maximum of 2 ps, or an error of 0.1–0.5% of Vp depending on sample thickness. Inset is the sample chamber of Run 2 at ~100 GPa.

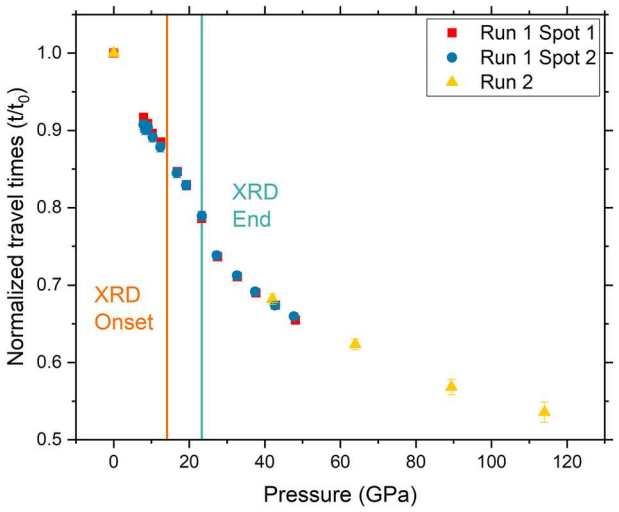

Figure 4. Normalized travel times of Fe-5Si from ~5 to 115 GPa. Observed scatter in the bcc-phase disappears above the bcc-hcp transition. The onset of the bcc-hcp transition measured by PA is in good agreement with that observed by XRD. XRD = X-ray diffraction.

additionally annealed under vacuum at ~ 400 K for 12 hr. This procedure effectively reduced scatter in measured travel times to less than 1% in the bcc phase. Normalized travel times for bcc and hcp Fe5Si are shown in Figure 4.

In Run 2, the initial travel time and travel time of the recovered samples are within error bar of each other, indicating negligible plastic deformation of the sample when compressed in Ne PTM up to 1.1 Mbar. Provided the volume decrease at the bcc-hcp transition is accounted for, the measured Vp varies by less than 0.5% depending on the choice of Fe or Fe-Si EoS, well within error at all pressures. The bcc-hcp transition is observed by PA to occur over a pressure range in close agreement with XRD measurements.

Following the transition region determined by both XRD and PA, a sharp rise in Vp is observed. While bcc peaks are absent from XRD by ~23 GPa, nonlinear variations in acoustic velocity have been observed up to ~30 GPa where the variation becomes regular. This is attributed to the slight development of preferred orientations in hcp-Fe-5Si at the end of the phase transition—XRD highlights a moderate change in the intensity ratio of the (002)/(100) peaks between 20 and 30 GPa, while at higher pressures this ratio does not vary any more. Due to the difference in measurement geometry between PA and XRD, the intensity reduction of the (002) peak observed by XRD reflects a larger contribution of the *c* axis to the measured travel time and hence a small increase in Vp (Antonangeli et al., 2006). As linearity in the Vp-ρ relation for hcp-Fe-5Si was observed by ~30 GPa, the following discussion will be limited to data measured at and above this pressure.

4. Discussion

4.1. Density of Fe-Si Alloys at the P-T Conditions of Earth's Inner Core

Extrapolated to Inner Core (IC) pressures and temperatures, the density of Fe-5Si is within error of PREM (~2%, Masters & Gubbins, 2003) for all reasonable core temperatures, with the best match for T = 5,500 K (Figure 5). As the compressional behavior of Fe-5Si and Fe are similar over the wide range of P-T conditions measured in this study, the dominant mechanism for density reduction even at core conditions is simply the difference in atomic mass between Fe and Si. Indeed, the density reduction between hcp-Fe and hcp-Fe-5Si is similar both at 300 K and at temperatures exceeding 5,000 K. While the recent measurements of Fe-10Ni-5Si exhibit less compressible behavior at ambient temperature, extrapolations of that EoS to core conditions results in densities very similar to those presented here. It is noted however that updating the Fe-10Ni-5Si thermal model with P_{el} determined here, there is a ~0.1 g/cm^3 (0.8%) decrease in density of the alloy at 5,500 K. This highlights the importance of accurate, high quality volume measurements at simultaneous high temperatures and high pressures, in order to constrain such effects at the conditions of the Earth's inner core.

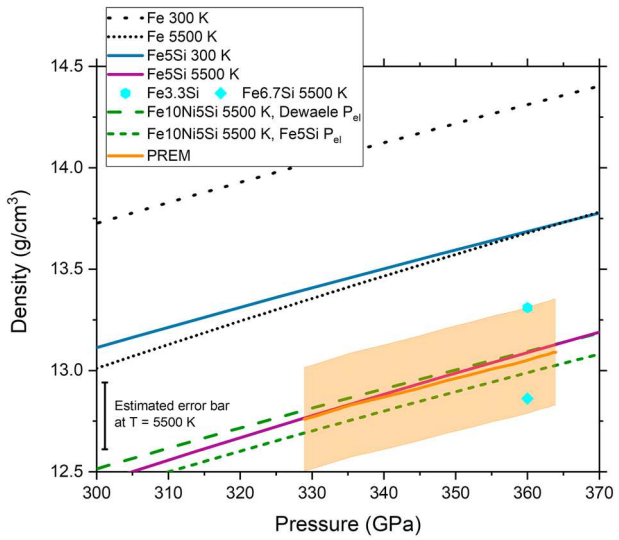

Figure 5. Density of Fe (Fei et al., 2016), Fe-5Si, Fe-10Ni-5Si (Morrison et al., 2018), Fe-3.3Si, and Fe-6.7Si (Martorell et al., 2016) at the pressures of the IC. Fe-5Si is within error bar of PREM for all reasonable core temperatures (5,000–7,000 K). Shaded region denotes expected error bar of PREM (~2%, Masters & Gubbins, 2003). Extrapolations of Fe-5Si to core temperatures and pressures have an error bar of ~1.5%.
PREM = Preliminary Reference Earth Model.

Our results are well compatible with the most recent ab initio calculations on Fe-Si alloys (Li et al., 2018; Martorell et al., 2016), the 5,500 K isotherm extrapolates to the midpoint between calculations of Fe-3.3Si and Fe-6.7Si at the same temperatures. The calculated thermodynamic grüneisen parameter of this alloy is between 1.5 and 1.6 at the ICB for temperatures of between 4,500 and 6,500 K, consistent with previous results on hcp-Fe (Dewaele et al., 2006; Fei et al., 2016; Vočadlo et al., 2003). This combined with the observation that Si alloying does not strongly affect the melting curve of iron (e.g., Fischer et al., 2013; Morard et al., 2017) indicates that Si-alloying would not likely have a strong effect on the thermal profile of the inner core.

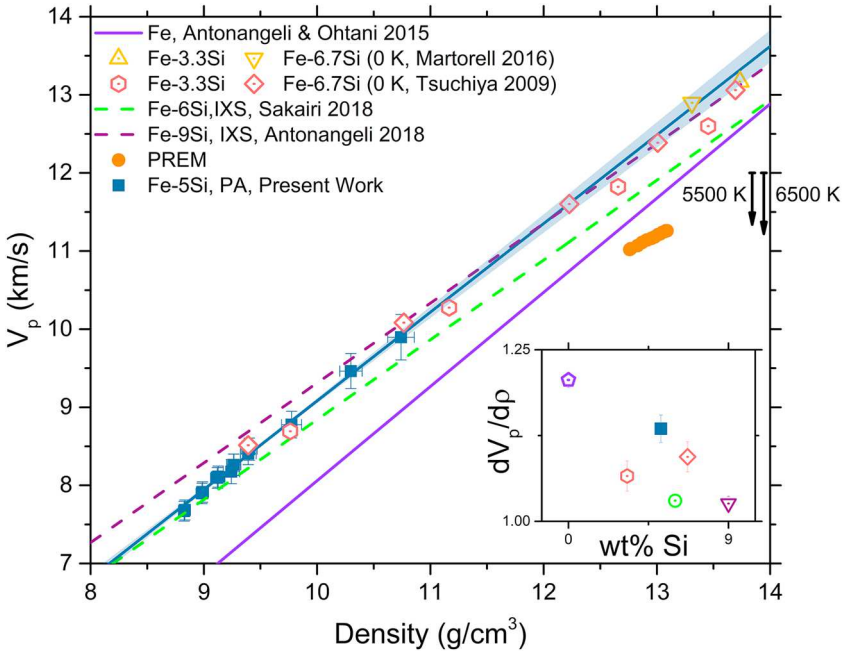

Figure 6. Compressional Sound Velocity versus Density for Fe and Fe-Si alloys in the hcp structure. Inset: the slope of linear fits to Velocity versus Density (dVp/dρ) versus Si content for the here-discussed Fe-xSi data sets (Antonangeli et al., 2018; Z. Mao et al., 2012; Martorell et al., 2016; Sakairi et al., 2018; Tsuchiya & Fujibuchi, 2009). Downward arrows indicate the maximum estimated magnitude of anharmonic effects at 5,500 and 6,500 K (after Martorell et al., 2016). PREM = Preliminary Reference Earth Model.

4.2. Sound Velocities of Fe-Si Alloys at Core Conditions

Vp measurements show a clear linear trend for the entire density range studied, with the fitted parameters $Vp(km/s) = 1.135(20) * \rho(g/cm^3) - 2.27(19)$ as shown in Figure 6. The dVp/dρ of Fe-5Si is reduced with respect to hcp-Fe Antonangeli and Ohtani (2015), although the effect is not as large as that reported by previous IXS measurements on samples with higher Si content (Antonangeli et al., 2018; Z. Mao et al., 2012; Sakairi et al., 2018), as shown in the inset of Figure 6.

Our measurements extrapolate at inner core densities somewhat higher than recent measurements by IXS on more Si-rich samples (Antonangeli et al., 2018; Z. Mao et al., 2012; Sakairi et al., 2018), but are in very good agreement with the result of athermal ab initio calculations on Fe-3.3Si and Fe-6.7Si (Martorell et al., 2016). We also observe agreement between Vp-ρ relations presented here and those reported in Tsuchiya and Fujibuchi (2009). We stress, however, that the agreement between our experiments and calculations worsen when looking at velocities versus pressure, in particular with respect to Tsuchiya and Fujibuchi (2009). In that study, at 40 GPa a linear interpolation of Fe3.3Si and Fe6.7Si exhibits a bulk modulus which is 28% higher than one derived from the present EoS, and the reported density is 4.5% higher.

Figure 6 shows that IXS results are generally parallel to each other (Antonangeli et al., 2018; Z. Mao et al., 2012; Sakairi et al., 2018), but in disagreement with the present work. It is evident based on the combined results of Antonangeli et al. (2018), Z. Mao et al. (2012), Sakairi et al. (2018), and (Tsuchiya & Fujibuchi, 2009) and the results of the present study that dVp/dρ decreases with increasing Si content (shown inset in Figure 6). While a linear decrease in dVp/dρ with Si content can rationalize a significant amount of the difference between PA and IXS, there are also systematic differences due to the different measurement geometries of the two techniques. PA measures acoustic travel times along the compression axis of the DAC, and as the sample is expected to develop texture,PA will preferentially sample the *c* axis of the alloy. By contrast, IXS measures phonon dispersions perpendicular to the DAC compression axis, and as such preferentially samples the basal plane of the Fe-alloy upon development of texture. In this way, textural effects bias PA and IXS measurements in opposite directions. Additionally, IXS measurements require larger sample volumes, and so are often measured in a solid PTM (Sakairi et al., 2018; Sakamaki et al., 2016) or no PTM at all (Antonangeli et al., 2018). We note, however, that the difference in extrapolations of PA and

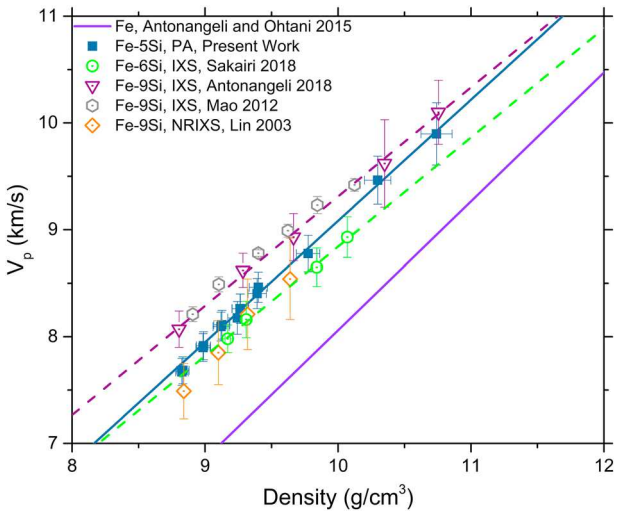

Figure 7. Vp versus Density measured for Fe-Si alloys in the hcp structure by different experimental techniques (Antonangeli et al., 2018; Lin, Struzhkin, et al.,2003; Z. Mao et al., 2012; Sakairi et al., 2018).

IXS measurements here observed for the Fe-Si system is much more significant than for the case of hcp-Fe (Antonangeli & Ohtani, 2015, references therein).

It is important to minimize texture by performing the experiments under quasihydrostatic conditions with noble gas media. While there is still some development of texture under compression in Ne, it is significantly weaker than the texture observed to occur in IXS experiments at comparable pressure conditions (Figures S1 and S3, Antonangeli et al., 2018; Sakairi et al., 2018). Figure 7 shows the individual datapoints of various studies in the hcp-Fe-Si system. Ultimately, the effect of preferred orientation is a relatively small effect, but is shown to systematically bias extrapolations (upward in the case of NRIXS) and downward (in the case of IXS) in Vp at core densities, which strongly hinders compositional modeling at core conditions. It can also be observed in Figure 7 that the present work has significantly improved data coverage to typical IXS or NRIXS experiments, and is measured over an extremely wide density range, under quasihydrostatic conditions, allowing for more robust extrapolations to core densities.

Having experimentally determined both the P-V-T EoS and Vp of Fe5Si, it is possible to combine these quantities to derive shear velocities. Figure 8 shows Vs plotted against density. Considering the model-dependence and large error bars of the present shear velocities (~8–10%), it is not unambiguously possible to determine whether these vary linearly or sublinearly with density (solid black lines). However, whether the data set is fit with a linear relation or power law relation as suggested by Z. Mao et al. (2012), Vs of Fe5Si is within error of ab initio calculations and seems higher than hcp-Fe (Antonangeli & Ohtani, 2015) at inner core densities. Recent IXS measurements on Fe9Si report a sublinear density dependence of Vs (Antonangeli et al., 2018), indicating that this may be a systematic effect of Si alloying. Shear moduli calculated by Tsuchiya and Fujibuchi (2009) are very similar to the present study at 40 and 120 GPa, and the discrepancies observed in Figure 8 arise primarily from the aforementioned differences in densities.

To meaningfully compare obtained Vp and Vs with PREM, high temperature effects have to be accounted for. At a constant density of 13 g/cm^3, the T corrections on Vp after experiments by Sakamaki et al. (2016; on hcp-Fe) and Sakairi et al. (2018; on Fe-6Si) yield Vp reductions of ~0.09 m·s^{-1}·K^{-1}, with almost no difference between Fe and Fe-6Si. Alternatively, by converting the constant pressure simulations of Martorell et al. (2016) to a constant density of 13 g/cm^3, it is possible to estimate the magnitude of anharmonic temperature effects to be ~0.11 m·s^{-1}·K^{-1} for Fe and Fe3.3Si, and ~0.05 m·s^{-1}·K^{-1} for Fe-6.7Si.

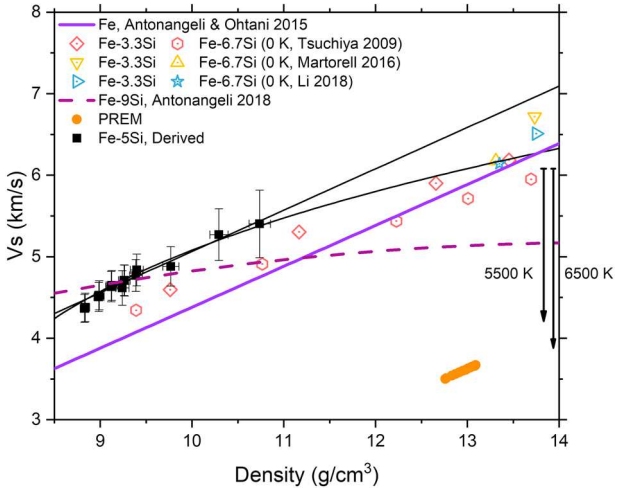

Figure 8. Derived Vs from the present study and selected literature (Antonangeli & Ohtani, 2015; Antonangeli et al., 2018; Li et al., 2018; Martorell et al., 2016; Tsuchiya & Fujibuchi, 2009). It is observed that the derived Vs of Fe5Si are higher than hcp-Fe at core densities irrespectively of the linear or sublinear extrapolation (solid black lines). Downward arrows indicate the maximum estimated magnitude of anharmonic effects at 5,500 and 6,500 K (after Martorell et al., 2016). PREM = Preliminary Reference Earth Model.

Regardless of the magnitude of anharmonic corrections for Vp at high temperature (Li et al., 2018; Martorell et al., 2016; Sakairi et al., 2018; Sakamaki et al., 2016), even when assuming the largest proposed effects (Martorell et al., 2016), PREM Vp is expected to be matched by an Fe-Si alloy only when containing <2wt% Si for T = 6,500 K and <1 wt% Si for T = 5,500 K. The largest anharmonic effects reported in recent literature come from ab initio calculations (Martorell et al., 2016), but a more recent ab initio study by the same group using larger simulation cells (Li et al., 2018) supports significantly reduced anharmonic effects compared to Martorell et al. (2016), such that the magnitude of anharmonic effects are more in line with those observed by IXS (Sakairi et al., 2018; Sakamaki et al., 2016). As such, constraints imposed by compressional sound velocity (at maximum <2wt% Si) are incompatible with constraints imposed by density (an Si alloy containing 5wt% Si has a density matching PREM at realistic core conditions). As a result, Si likely cannot be the sole light element in the Earth's core.

This mismatch between mineral-physics measurements and seismological observables is even worse when considering Vs. Assuming a power law extrapolation of Vs to core densities (representing a lower bound to the extrapolated Vs) and the largest possible magnitude of anharmonic effects (~0.34 $m \cdot s^{-1} \cdot K^{-1}$, ; Martorell et al., 2016), the Vs of an Fe-Si alloy of any composition cannot match PREM for temperatures below 6,500 K. Considering that such high core temperatures are likely to be unrealistic for a variety of geophysical and mineralogical reasons, this emphasizes the unsuitability of Si as the primary light element in the Earth's inner core. This study highlights the important point that density or velocity information alone can only be used to exclude possible core compositions and must be coupled together in order to develop accurate models of the Earth's interior.

5. Conclusions

The combination of P-V-T XRD measurements and 300 K PA Vp measurements under quasihydrostatic conditions of Fe-5wt% Si show that while an alloy with 5wt% Si can potentially match the PREM density of the Earth's inner core, this quantity of silicon is incompatible with seismological observations of Vp and Vs, even when accounting for anharmonic effects at high temperature. Thus, our paper supports the conclusion suggested by Martorell et al. (2016) that Si cannot be considered as the only light element in the Earth's inner core in the absence of other mechanisms, such as partial melting (Vočadlo, 2007) which significantly reduces density as well as sound velocities of Fe-Si alloys at core conditions.

Acknowledgments
This work was supported by the Investissements d'Avenir programme (reference ANR-11-IDEX-0004-02) and more specifically within the framework of the Cluster of Excellence MATriaux Interfaces Surfaces Environnement (MATISSE) led by Sorbonne Université (grant to DA and FD). Femtosecond laser micro-machining at the Institut de Minéralogie, de Physique des Matériaux et de Cosmochimie (IMPMC), Paris, has been developed and realized by the "Cellule Projet" with the financial support of ANR 2010-JCJC-604-01 (grant to DA). F. M. has received funding from the European Research Council (ERC) under the European Union's Horizon 2020 research and innovation Programme (grant agreement 670787). The authors wish to thank Jeroen Jacobs for technical assistance at the ESRF. All data used in the present work can be found in Data Sets S1–S3.

References

Akahama, Y., & Kawamura, H. (2006). Pressure calibration of diamond anvil Raman gauge to 310 GPa. *Journal of Applied Physics*, *100*(4), 43516. https://doi.org./10.1063/1.2335683

Allégre, C. J., Poirier, J.-P., Humler, E., & Hofmann, A. W. (1995). The chemical composition of the Earth. *Earth and Planetary Science Letters*, *134*(3), 515–526. https://doi.org./10.1016/0012-821X(95)00123-T

Antonangeli, D., Merkel, S., & Farber, D. L. (2006). Elastic anisotropy in hcp metals at high pressure and the sound wave anisotropy of the Earth's inner core. *Geophysical Research Letters*, *33*, L24303. https://doi.org./10.1029/2006GL028237

Antonangeli, D., Morard, G., Paolasini, L., Garbarino, G., Murphy, C. A., Edmund, E., et al. (2018). Sound velocities density measurements of solid hcp-Fe and hcp-Fe-Si (9 wt. inner core. *Earth and Planetary Science Letters*, *482*, 446–453. https://doi.org./10.1016/j.epsl.2017.11.043

Antonangeli, D., & Ohtani, E. (2015). Sound velocity of hcp-Fe at high pressure: Experimental constraints, extrapolations and comparison with seismic models. *Progress in Earth and Planetary Science*, *2*(1), 3. https://doi.org./10.1186/s40645-015-0034-9

Antonangeli, D., Siebert, J., Badro, J., Farber, D. L., Fiquet, G., Morard, G., & Ryerson, F. J. (2010). Composition of the Earth's inner core from high-pressure sound velocity measurements in Fe-Ni-Si alloys. *Earth and Planetary Science Letters*, *295*(1), 292–296. https://doi.org./10.1016/j.epsl.2010.04.018

Anzellini, S., Dewaele, A., Mezouar, M., Loubeyre, P., & Morard, G. (2013). Melting of Iron at Earth's inner core boundary based on fast X-ray diffraction. *Science*, *340*(6131), 464–466. https://doi.org./10.1126/science.1233514

Badro, J., Fiquet, G., Guyot, F., Gregoryanz, E., Occelli, F., Antonangeli, D., & d'Astuto, M. (2007). Effect of light elements on the sound velocities in solid iron: Implications for the composition of Earth's core. *Earth and Planetary Science Letters*, *254*(1), 233–238. https://doi.org./10.1016/j.epsl.2006.11.025

Birch, F. (1947). Finite elastic strain of cubic crystals. *Physical Review*, *71*, 809–824. https://doi.org./10.1103/PhysRev.71.809

Birch, F. (1952). Elasticity and constitution of the Earth's interior. *Journal of Geophysical Research*, *57*(2), 227–286. https://doi.org./10.1029/JZ057i002p00227

Boehler, R. (1993). Temperatures in the Earth's core from melting-point measurements of iron at high static pressures. *Nature*, *363*, 534.

Boness, D. A., Brown, J., & McMahan, A. (1986). The electronic thermodynamics of iron under Earth core conditions. *Physics of the Earth and Planetary Interiors*, *42*(4), 227–240. https://doi.org./10.1016/0031-9201(86)90025-7

Campbell, A. J., Danielson, L., Righter, K., Seagle, C. T., Wang, Y., & Prakapenka, V. B. (2009). High pressure effects on the iron-iron oxide and nickel-nickel oxide oxygen fugacity buffers. *Earth and Planetary Science Letters*, *286*(3), 556–564. https://doi.org./10.1016/j.epsl.2009.07.022

Decremps, F., Antonangeli, D., Gauthier, M., Ayrinhac, S., Morand, M., Marchand, G. L., et al. (2014). Sound velocity of iron up to 152 GPa by picosecond acoustics in diamond anvil cell. *Geophysical Research Letters*, *41*, 1459–1464. https://doi.org./10.1002/2013GL058859

Decremps, F., Belliard, L., Perrin, B., & Gauthier, M. (2008). Sound Velocity and Absorption Measurements under High Pressure Using Picosecond Ultrasonics in a Diamond Anvil Cell: Application to the Stability Study of AlPdMn. *Physical Review Letters*, *100*, 35502. https://doi.org./10.1103/PhysRevLett.100.035502

Decremps, F., Gauthier, M., Ayrinhac, S., Bove, L., Belliard, L., Perrin, B., et al. (2015). Picosecond acoustics method for measuring the thermodynamical properties of solids and liquids at high pressure and high temperature. *Ultrasonics*, *56*, 129–140. https://doi.org./10.1016/j.ultras.2014.04.011

Dewaele, A., Belonoshko, A. B., Garbarino, G., Occelli, F., Bouvier, P., Hanfland, M., & Mezouar, M. (2012). High-pressure–high-temperature equation of state of KCl and KBr. *Physical Review B*, *85*, 214105. https://doi.org./10.1103/PhysRevB.85.214105

Dewaele, A., Loubeyre, P., Occelli, F., Mezouar, M., Dorogokupets, P. I., & Torrent, M. (2006). Quasihydrostatic equation of state of iron above 2 Mbar. *Physical Review Letters*, *97*, 215504. https://doi.org./10.1103/PhysRevLett.97.215504

Dorogokupets, P. I., & Oganov, A. R. (2007). Ruby, metals, and MgO as alternative pressure scales: A semiempirical description of shock-wave, ultrasonic, x-ray, and thermochemical data at high temperatures and pressures. *Physical Review B*, *75*, 24115. https://doi.org./10.1103/PhysRevB.75.024115

Dziewonski, A. M., & Anderson, D. L. (1981). Preliminary reference Earth model. *Physics of the Earth and Planetary Interiors*, *25*(4), 297–356. https://doi.org./10.1016/0031-9201(81)90046-7

Fei, Y., Murphy, C., Shibazaki, Y., Shahar, A., & Huang, H. (2016). Thermal equation of state of hcp-iron: Constraint on the density deficit of Earth's solid inner core. *Geophysical Research Letters*, *43*, 6837–6843. https://doi.org./10.1002/2016GL069456

Fischer, R. A., Campbell, A. J., Caracas, R., Reaman, D. M., Dera, P., & Prakapenka, V. B. (2012). Equation of state and phase diagram of Fe-16Si alloy as a candidate component of Earth's core. *Earth and Planetary Science Letters*, *357-358*, 268–276. https://doi.org./10.1016/j.epsl.2012.09.022

Fischer, R. A., Campbell, A. J., Caracas, R., Reaman, D. M., Heinz, D. L., Dera, P., & Prakapenka, V. B. (2014). Equations of state in the Fe-FeSi system at high pressures and temperatures. *Journal of Geophysical Research: Solid Earth*, *119*, 2810–2827. https://doi.org./10.1002/2013JB010898

Fischer, R. A., Campbell, A. J., Reaman, D. M., Miller, N. A., Heinz, D. L., Dera, P., & Prakapenka, V. B. (2013). Phase relations in the Fe-FeSi system at high pressures and temperatures. *Earth and Planetary Science Letters*, *373*, 54–64. https://doi.org./10.1016/j.epsl.2013.04.035

Fischer, R. A., Nakajima, Y., Campbell, A. J., Frost, D. J., Harries, D., Langenhorst, F., et al. (2015). High pressure metal-silicate partitioning of Ni, Co, V, Cr, Si, and O. *Geochimica et Cosmochimica Acta*, *167*, 177–194. https://doi.org./10.1016/j.gca.2015.06.026

Fitoussi, C., Bourdon, B., Kleine, T., Oberli, F., & Reynolds, B. C. (2009). Si isotope systematics of meteorites and terrestrial peridotites: implications for Mg/Si fractionation in the solar nebula and for Si in the Earth's core. *Earth and Planetary Science Letters*, *287*(1), 77–85. https://doi.org./10.1016/j.epsl.2009.07.038

Hashin, Z., & Shtrikman, S. (1962). A variational approach to the theory of the elastic behaviour of polycrystals. *Journal of the Mechanics and Physics of Solids*, *10*(4), 343–352. https://doi.org./10.1016/0022-5096(62)90005-4

Hirose, K., Morard, G., Sinmyo, R., Umemoto, K., Hernlund, J., Helffrich, G., & Labrosse, S. (2017). Crystallization of silicon dioxide and compositional evolution of the Earth's core. *Nature*, *543*, 99.

Li, Y., Vočadlo, L., & Brodholt, J. P. (2018). The elastic properties of hcp-Fe alloys under the conditions of the Earth's inner core. *Earth and Planetary Science Letters*, *493*, 118–127. https://doi.org./10.1016/j.epsl.2018.04.013

Lin, J.-F., Campbell, A. J., Heinz, D. L., & Shen, G. (2003). Static compression of iron-silicon alloys: Implications for silicon in the Earth's core. *Journal of Geophysical Research*, *108*(B1), 2045. https://doi.org./10.1029/2002JB001978

Lin, J.-F., Struzhkin, V. V., Sturhahn, W., Huang, E., Zhao, J., Hu, M. Y., et al. (2003). Sound velocities of iron-nickel and iron-silicon alloys at high pressures. *Geophysical Research Letters*, *30*(21), 2112. https://doi.org./10.1029/2003GL018405

Litasov, K. D., Dorogokupets, P. I., Ohtani, E., Fei, Y., Shatskiy, A., Sharygin, I. S., et al. (2013). Thermal equation of state and thermodynamic properties of molybdenum at high pressures. *Journal of Applied Physics*, *113*(9), 93507. https://doi.org./10.1063/1.4794127

Liu, J., Lin, J.-F., Alatas, A., Hu, M. Y., Zhao, J., & Dubrovinsky, L. (2016). Seismic parameters of hcp-Fe alloyed with Ni and Si in the Earth's inner core. *Journal of Geophysical Research: Solid Earth*, *121*, 610–623. https://doi.org./10.1002/2015JB012625

Machová, A., & Kadečková, S. (1977). Elastic constants of iron-silicon alloy single crystals. *Czechoslovak Journal of Physics B*, *27*(5), 555–563. https://doi.org./10.1007/BF01587133

Mao, Z., Lin, J.-F., Liu, J., Alatas, A., Gao, L., Zhao, J., & Mao, H.-K. (2012). Sound velocities of Fe and Fe-Si alloy in the Earth's core. *Proceedings of the National Academy of Sciences*, *109*(26), 10,239–10,244. https://doi.org./10.1073/pnas.1207086109

Mao, H. K., Xu, J., & Bell, P. M. (1986). Calibration of the ruby pressure gauge to 800 kbar under quasi-hydrostatic conditions. *Journal of Geophysical Research*, *91*(B5), 4673–4676. https://doi.org./10.1029/JB091iB05p04673

Martorell, B., Brodholt, J., Wood, I. G., & Vočadlo, L. (2013). The effect of nickel on the properties of iron at the conditions of Earth's inner core: Ab initio calculations of seismic wave velocities of Fe-Ni alloys. *Earth and Planetary Science Letters*, *365*, 143–151.

Martorell, B., Wood, I. G., Brodholt, J., & Vočadlo, L. (2016). The elastic properties of hcp-Fe1-xSix at Earth's inner-core conditions. *Earth and Planetary Science Letters*, *451*, 89–96. https://doi.org./10.1016/j.epsl.2016.07.018

Masters, G., & Gubbins, D (2003). On the resolution of density within the Earth. *Physics of the Earth and Planetary Interiors*, *140*(1), 159–167. https://doi.org./10.1016/j.pepi.2003.07.008. Geophysical and Geochemical Evolution of the Deep Earth.

McDonough, W. F., & Sun, S.-s. (1995). The composition of the Earth. *Chemical Geology*, *120*(3), 223–253. https://doi.org./10.1016/0009-2541(94)00140-4. Chemical Evolution of the Mantle.

Merkel, S., Hemley, R. J., & Mao, H.-k. (1999). Finite-element modeling of diamond deformation at multimegabar pressures. *Applied Physics Letters*, *74*(5), 656–658. https://doi.org./10.1063/1.123031

Mezouar, M., Crichton, W. A., Bauchau, S., Thurel, F., Witsch, H., Torrecillas, F., et al. (2005). Development of a new state-of-the-art beamline optimized for monochromatic single-crystal and powder X-ray diffraction under extreme conditions at the ESRF. *Journal of Synchrotron Radiation*, *12*(5), 659–664. https://doi.org./10.1107/S0909049505023216

Mezouar, M., Giampaoli, R., Garbarino, G., Kantor, I., Dewaele, A., Weck, G., et al. (2017). Methodology for in situ synchrotron X-ray studies in the laser-heated diamond anvil cell. *High Pressure Research*, *37*(2), 170–180. https://doi.org./10.1080/08957959.2017.1306626

Morard, G., Andrault, D., Antonangeli, D., Nakajima, Y., Auzende, A., Boulard, E., et al. (2017). Fe-FeO and Fe-Fe3C melting relations at Earth's core-mantle boundary conditions: Implications for a volatile-rich or oxygen-rich core. *Earth and Planetary Science Letters*, *473*, 94–103. https://doi.org./10.1016/j.epsl.2017.05.024

Morard, G., Andrault, D., Guignot, N., Siebert, J., Garbarino, G., & Antonangeli, D. (2011). Melting of Fe–Ni–Si and Fe–Ni–S alloys at megabar pressures: implications for the core–mantle boundary temperature. *Physics and Chemistry of Minerals*, *38*(10), 767–776. https://doi.org./10.1007/s00269-011-0449-9

Morrison, R. A., Jackson, J. M., Sturhahn, W., Zhang, D., & Greenberg, E. (2018). Equations of state and anisotropy of Fe-Ni-Si alloys. *Journal of Geophysical Research: Solid Earth*, *123*, 4647–4675. https://doi.org./10.1029/2017JB015343

Nguyen, J. H., & Holmes, N. C. (2004). Melting of iron at the physical conditions of the Earth's core. *Nature*, *427*, 339.

Prescher, C., & Prakapenka, V. B. (2015). DIOPTAS: A program for reduction of two-dimensional X-ray diffraction data and data exploration. *High Pressure Research*, *35*(3), 223–230. https://doi.org./10.1080/08957959.2015.1059835

Ross, R., & Hume-Rothery, W. (1963). High temperature X-ray metallography: I. A new debye-scherrer camera for use at very high temperatures II. A new parafocusing camera III. Applications to the study of chromium, hafnium, molybdenum, rhodium, ruthenium and tungsten. *Journal of the Less Common Metals*, *5*(3), 258–270. https://doi.org./10.1016/0022-5088(63)90031-6

Sakairi, T., Sakamaki, T., Ohtani, E., Fukui, H., Kamada, S., Tsutsui, S., et al. (2018). Sound velocity measurements of hcp Fe-Si alloy at high pressure and high temperature by inelastic X-ray scattering. *American Mineralogist*, *103*(1), 85. https://doi.org./10.2138/am-2018-6072

Sakamaki, T., Ohtani, E., Fukui, H., Kamada, S., Takahashi, S., Sakairi, T., et al. (2016). Constraints on Earth's inner core composition inferred from measurements of the sound velocity of hcp-iron in extreme conditions. *Science Advances*, *2*(2), e1500802. https://doi.org./10.1126/sciadv.1500802

Siebert, J., Badro, J., Antonangeli, D., & Ryerson, F. J. (2013). Terrestrial accretion under oxidizing conditions. *Science*, *339*(6124), 1194–1197. https://doi.org./10.1126/science.1227923

Sokolova, T., Dorogokupets, P., & Litasov, K. (2013). Self-consistent pressure scales based on the equations of state for ruby, diamond, MgO, B2-NaCl, as well as Au, Pt, and other metals to 4 Mbar and 3000 K. *Russian Geology and Geophysics*, *54*(2), 181–199. https://doi.org./10.1016/j.rgg.2013.01.005

Tateno, S., Kuwayama, Y., Hirose, K., & Ohishi, Y. (2015). The structure of FeSi alloy in Earth's inner core. *Earth and Planetary Science Letters*, *418*, 11–19. https://doi.org./10.1016/j.epsl.2015.02.008

Tsuchiya, T., & Fujibuchi, M. (2009). Effects of Si on the elastic property of Fe at Earth's inner core pressures: First principles study. *Physics of the Earth and Planetary Interiors*, *174*, 212–219. https://doi.org./10.1016/j.pepi.2009.01.007

Václav, P., Michal, D., & Lukáš, P. (2014). Crystallographic computing system JANA2006. General features.

Vinet, P., Rose, J. H., Ferrante, J., & Smith, J. R. (1989). Universal features of the equation of state of solids. *Journal of Physics: Condensed Matter*, *1*(11), 1941.

Vočadlo, L. (2007). Ab initio calculations of the elasticity of iron and iron alloys at inner core conditions: Evidence for a partially molten inner core? *Earth and Planetary Science Letters*, *254*(1), 227–232. https://doi.org./10.1016/j.epsl.2006.09.046

Vočadlo, L., Alfè, D., Gillan, M., & Price, G. (2003). The properties of iron under core conditions from first principles calculations. *Physics of the Earth and Planetary Interiors*, *140*(1), 101–125. https://doi.org./10.1016/j.pepi.2003.08.001 Geophysical and Geochemical Evolution of the Deep Earth.

Wade, J., & Wood, B. (2005). Core formation and the oxidation state of the Earth. *Earth and Planetary Science Letters*, *236*(1), 78–95. https://doi.org./10.1016/j.epsl.2005.05.017

Wakamatsu, T., Ohta, K., Yagi, T., Hirose, K., & Ohishi, Y. (2018). Measurements of sound velocity in iron–nickel alloys by femtosecond laser pulses in a diamond anvil cell. *Physics and Chemistry of Minerals*, *45*, 589–595. https://doi.org./10.1007/s00269-018-0944-3

Wood, B. J., Bryndzia, L. T., & Johnson, K. E. (1990). Mantle oxidation state and its relationship to tectonic environment and fluid speciation. *Science*, *248*(4953), 337–345. https://doi.org./10.1126/science.248.4953.337

Yamazaki, D., Ito, E., Yoshino, T., Yoneda, A., Guo, X., Zhang, B., et al. (2012). P-V-T equation of state for epsilon-iron up to 80 GPa and 1900 K using the Kawai-type high pressure apparatus equipped with sintered diamond anvils. *Geophysical Research Letters*, *39*, L20308. https://doi.org./10.1029/2012GL053540

Fe7C3 from FeSi20C10, 300K + high temperature data
P GPa, T K, V A3
P sigP T sigT V sigV
189.4 0.010 300 3 131.2090.061
155.36 0.010 300 3 135.7680.106
195.6 0.010 300 3 129.0720.077
197.18 0.010 300 3 128.5940.143
196.16 0.010 300 3 129.23 0.135
192.68 0.010 300 3 129.7290.173
123.48 0.010 300 3 141.0270.083
126.41 0.010 300 3 140.2680.125
182.09 0.010 300 3 131.8490.048
189.32 0.010 300 3 131.11 0.09
146.42 0.010 300 3 137.5050.078
183 0.010 300 3 131.6820.047
164.33 0.010 300 3 134.4080.057
177.93 0.010 300 3 132.5470.09
128.39 0.010 300 3 140.7330.04
130.26 0.010 300 3 140.1310.061
169.1 0.010 300 3 133.5110.046
168.01 0.010 300 3 133.6950.056
159.49 1.380 1523 150 135.4590.051
173.19 1.380 1527 150 133.2140.048
184.76 1.380 1530.2 150 131.94 0.079
193.55 1.390 1535.5 150 130.4460.093
192.35 1.450 1588.3 150 129.6680.078
141.38 1.570 1695.7 150 139.0650.09
193.52 1.580 1701.3 150 130.4860.109
192.11 1.590 1716.8 150 129.7010.092
185.07 1.620 1739.5 150 131.9920.088
173.28 1.630 1746 150 133.2820.052
160.05 1.710 1825.4 150 135.5470.054
192.07 1.810 1907.3 150 129.8780.058
193.7 1.850 1944.3 150 130.5360.106
185.2 1.850 1946 150 132.0120.054
142.01 1.890 1979.5 150 138.74 0.059
122.9 1.910 2003.3 150 142.3090.087
173.84 1.930 2016.8 150 133.3610.034
127.57 1.940 2031.3 150 141.1320.086
123.8 1.950 2033.5 150 142.1050.053
123.9 1.970 2055.8 150 142.2110.067
160.59 1.980 2067.2 150 135.4850.043
143.26 2.060 2135 150 138.5310.062
192.29 2.070 2138.8 150 130.5570.067
193.94 2.070 2146.2 150 130.5380.08
144.44 2.240 2298.8 150 138.4260.072
128.11 2.260 2311 150 141.2750.154
194.04 2.260 2312.8 150 130.4610.071
174.42 2.260 2315 150 133.19 0.034
161.05 2.270 2322.2 150 135.3120.046
185.7 2.270 2323 150 131.9960.078
192.32 2.310 2354.8 150 131.2450.038
186.71 2.470 2501.6 150 131.8560.036
175.66 2.490 2520.5 150 133.2660.037
191.63 2.500 2525.4 150 131.8340.049

162.5	2.500	2526.2	150	135.1240.04
145.86	2.500	2526.8	150	138.5210.058
129.07	2.510	2532.5	150	141.5440.08
194.81	2.510	2537.6	150	130.3150.05
163.34	2.710	2717.8	150	135.1530.041
129.64	2.710	2719	150	141.7260.12
146.91	2.740	2744.8	150	139.2360.026
176.83	2.750	2746.4	150	133.5370.073
187.12	2.760	2759.2	150	132.1550.062
195.25	2.770	2764.7	150	130.2580.048
191.06	2.790	2789.2	150	132.4570.048
129.76	2.930	2915	150	142.1630.097
164.47	2.970	2950	150	135.5170.13
188.17	3.000	2975.4	150	132.4810.053
178.25	3.010	2981.4	150	133.98 0.027
190.42	3.040	3012.7	150	132.7910.044
165.28	3.070	3037.3	150	135.6040.072
147.9	3.100	3060	150	139.1990.054
189.36	3.130	3085.2	150	132.4120.051
178.82	3.130	3088.6	150	134.0560.03
190.34	3.260	3206.3	150	132.9350.026
131.35	3.870	3753.8	150	142.3190.077

FeSi from FeSi6C5, 300K+high temperature data

P GPa, T K, V A3

P	sigP	T	sigT	V	sigV
103.73	0.01	300	3	17.135	0.091
104.16	0.01	300	3	17.158	0.033
92.12	0.01	300	3	17.414	0.127
73.1	0.01	300	3	18.177	0.147
70.77	0.01	300	3	18.185	0.019
69.27	0.01	300	3	18.196	0.049
69.23	0.01	300	3	18.217	0.011
67.5	0.01	300	3	18.36	0.096
58.34	0.01	300	3	18.887	0.173
58.13	0.01	300	3	18.933	0.201
65.12	0.96	1148.5	150	18.406	0.042
69.76	1.18	1353	150	18.375	0.093
58.12	1.2	1369	150	18.966	0.117
72.63	1.29	1450.3	150	18.196	0.013
93.79	1.3	1460	150	17.428	0.14
88.48	1.31	1460.8	150	17.611	0.032
69.23	1.32	1469.5	150	18.395	0.107
69.31	1.33	1479	150	18.394	0.109
58.44	1.36	1506.8	150	18.987	0.09
69.29	1.38	1523	150	18.399	0.104
93.23	1.4	1542.3	150	17.492	0.048
69.34	1.4	1548.3	150	18.39	0.103
93.56	1.41	1554.5	150	17.539	0.129
58.56	1.46	1597	150	18.976	0.093
65.66	1.47	1603.3	150	18.431	0.049
93.86	1.48	1613.5	150	17.489	0.189
56.37	1.49	1624	150	18.993	0.003
69.44	1.49	1629.8	150	18.403	0.102
92.83	1.5	1635.5	150	17.487	0.032
106.33	1.53	1657.3	150	17.12	0.05
72.89	1.53	1660.8	150	18.318	0.004
89.37	1.54	1672	150	17.615	0.034
74.6	1.56	1684.8	150	18.133	0.196
75.88	1.58	1703.3	150	18.158	0.193
65.75	1.61	1732.3	150	18.447	0.051
56.24	1.64	1756	150	19.029	0.011
106.51	1.67	1783.3	150	17.184	0.097
75.72	1.69	1802.3	150	18.185	0.206
106.7	1.73	1842	150	17.172	0.09
91.92	1.77	1878.5	150	17.515	0.019
90.2	1.78	1883	150	17.609	0.026
75.99	1.8	1900.5	150	18.192	0.229
107.63	1.8	1904	150	17.113	0.047
56.37	1.83	1932	150	19.079	0.013
67.09	1.87	1962	150	18.514	0.092
90.45	1.88	1970.5	150	17.593	0.022
107.73	1.89	1983	150	17.121	0.048
75.08	1.93	2018.5	150	18.293	0.211
107.96	1.96	2041.8	150	17.116	0.058
91.42	1.98	2063.5	150	17.604	0.015

76.1	2	2084.8	150	18.134	0.137
74.37	2.03	2111.5	150	18.236	0.046
107.21	2.04	2114.3	150	17.145	0.071
67.5	2.08	2150	150	18.568	0.124
92.44	2.09	2159.5	150	17.588	0.006
107.39	2.09	2163.3	150	17.152	0.079
56.34	2.14	2209.8	150	19.21	0.12
91.88	2.22	2279.3	150	17.616	0.016
91.9	2.29	2342.3	150	17.63	0.016
92.1	2.33	2371.5	150	17.686	0.009
67.93	2.35	2393.8	150	18.595	0.155
107.75	2.37	2412.3	150	17.208	0.185
107.76	2.37	2415.3	150	17.18	0.127
93.21	2.38	2418.5	150	17.683	0.02
56.89	2.42	2453.8	150	19.237	0.15
68.09	2.47	2502.8	150	18.569	0.15
75.08	2.51	2538.8	150	18.35	0.056
92.55	2.55	2571.3	150	17.78	0.024
93.5	2.57	2586.8	150	17.664	0.054
68.79	2.57	2593.5	150	18.585	0.159
92.79	2.67	2676.5	150	17.884	0.115
108.58	2.69	2696.8	150	17.107	0.034
75.82	2.75	2750.5	150	18.456	0.095
109.45	2.83	2818.3	150	17.168	0.073
92.82	2.85	2837	150	17.812	0.051
92.96	2.89	2879.5	150	17.623	0.035
94.64	3.04	3006.8	150	17.617	0.043
109.9	3.07	3034.3	150	17.239	0.072
107.72	3.09	3054.3	150	17.175	0.154
93.21	3.1	3063.3	150	17.679	0.074
93.43	3.15	3108.5	150	17.842	0.113
75.79	3.16	3119.8	150	18.539	0.287
93.76	3.29	3231	150	17.614	0.075
76.15	3.34	3274.3	150	18.6	0.28
93.87	3.36	3297	150	17.61	0.369
110.62	3.38	3316.5	150	17.313	0.187
109.93	3.47	3397.5	150	17.265	0.247
75.27	3.63	3536	150	18.431	0.08

FeSi from FeSi10C20, 300K+high temperature data

#P GPa, T K, V A3#

1 Format P sigP T sigT V sigV

42.13	0.01	300	3	19.241	0.02
56.29	0.01	300	3	18.579	0.056
76.29	0.01	300	3	17.497	0.023
77.65	0.01	300	3	17.401	0.005
95.53	0.01	300	3	16.84	0.045
101.31	0.01	300	3	16.682	0.059
102.63	0.01	300	3	16.653	0.053
105.15	0.01	300	3	16.597	0.031
109.21	0.01	300	3	16.59	0.116
111.11	0.01	300	3	16.503	0.137
116.12	0.01	300	3	16.273	0.009
116.68	0.01	300	3	16.282	0.009
120.46	0.01	300	3	16.177	0.017
122.77	0.01	300	3	16.089	0.027
126.18	0.01	300	3	16.005	0.031
127.13	0.01	300	3	15.998	0.018
131.12	0.01	300	3	15.955	0.036
133.49	0.01	300	3	15.897	0.027
137.1	0.01	300	3	15.831	0.057
137.54	0.01	300	3	15.831	0.048
143.98	0.01	300	3	15.776	0.042
87.9	0.01	300	3	17.094	0.039
98.37	0.01	300	3	16.744	0.018
26.73	0.01	300	3	20.048	0.016
28.01	0.01	300	3	20.135	0.03
26.12	0.01	300	3	20.14	0.018
36.83	0.01	300	3	19.543	0.092
39.16	0.01	300	3	19.307	0.073
47.75	0.01	300	3	18.997	0.095
27.83	1.09	1270	150	20.133	0.036
28.58	1.09	1270	150	20.185	0.014
28.6	1.09	1270	150	20.177	0.011
53.1	1.12	1293.3	150	18.522	0.003
53.03	1.13	1304.3	150	18.55	0.007
53.19	1.16	1334	150	18.508	0.008
53.1	1.18	1350.5	150	18.529	0.004
39.83	1.2	1370	150	19.508	0.083
42.93	1.22	1381.7	150	19.165	0.024
87.82	1.22	1386.5	150	17.157	0.012
28.65	1.24	1400	150	20.257	0.009
102.21	1.24	1405.5	150	16.653	0.018
37.43	1.27	1425	150	19.514	0.011
43.22	1.27	1425.3	150	19.162	0.018
53.26	1.29	1445.8	150	18.521	0.004
28.8	1.29	1450	150	20.28	0.05
94.63	1.3	1451.5	150	16.877	0.019
42.75	1.31	1464	150	19.208	0.008
107.63	1.33	1479	150	16.613	0.071
75.82	1.33	1482	150	17.5	0.014

42.8	1.34	1488	150	19.214	0.002
129.95	1.34	1495.8	150	16.02	0.031
75.35	1.35	1496.3	150	17.529	0.008
94.88	1.35	1497	150	16.92	0.007
90.48	1.35	1500	150	17.154	0.054
94.34	1.35	1501	150	16.888	0.01
87.93	1.36	1507.5	150	17.159	0.012
94.6	1.36	1509	150	16.959	0.021
102.31	1.36	1511.5	150	16.662	0.013
42.84	1.37	1516	150	19.229	0.011
53.38	1.37	1522	150	18.526	0.005
48.64	1.4	1544.5	150	18.86	0.05
119.49	1.4	1549	150	16.304	0.018
37.51	1.41	1555	150	19.574	0.013
94.65	1.42	1559	150	16.898	0.013
28.36	1.42	1559.5	150	20.38	0.008
53.66	1.43	1570.7	150	18.527	0.002
88.2	1.44	1577.3	150	17.162	0.016
94.58	1.45	1587.3	150	16.891	0.018
40.14	1.46	1600	150	19.636	0.063
40.14	1.46	1602	150	19.645	0.115
37.54	1.47	1605	150	19.607	0.011
88.34	1.47	1610.5	150	17.17	0.015
42.7	1.48	1612	150	19.227	0.008
40.24	1.49	1621.8	150	19.625	0.038
28.6	1.49	1622.3	150	20.507	0.008
37.52	1.5	1630	150	19.659	0.008
97.87	1.51	1642.5	150	16.679	0.013
53.69	1.52	1650.8	150	18.545	0.004
37.43	1.55	1675	150	19.698	0.009
130.09	1.57	1695.3	150	16.019	0.029
93.85	1.57	1695.7	150	16.979	0.009
42.78	1.57	1697.3	150	19.26	0.009
94.8	1.58	1705.3	150	16.944	0.009
107.63	1.58	1708	150	16.628	0.04
88.85	1.58	1709.3	150	17.163	0.015
75.96	1.59	1712.8	150	17.538	0.007
37.6	1.59	1718	150	19.749	0.009
48.36	1.59	1719	150	18.956	0.014
53.84	1.6	1719.8	150	18.559	0.004
28.57	1.6	1726.8	150	20.646	0.007
119.81	1.61	1732.8	150	16.307	0.021
88.75	1.61	1735	150	17.173	0.013
39.65	1.62	1740	150	19.708	0.137
40.23	1.64	1760	150	19.77	0.079
78.32	1.67	1782.8	150	17.516	0.009
28.61	1.67	1787	150	20.701	0.005
88.52	1.67	1787.8	150	17.192	0.014
94.31	1.68	1790.8	150	16.928	0.014
42.73	1.68	1795	150	19.341	0.011
42.83	1.69	1803	150	19.391	0.014
94.72	1.69	1804.5	150	16.904	0.026
42.78	1.69	1808	150	19.389	0.009
78.6	1.71	1818.3	150	17.526	0.005
76.07	1.71	1824.3	150	17.564	0.01

88.52	1.72	1827.5	150	17.197	0.014
100.61	1.73	1842	150	16.7	0.014
42.78	1.75	1855.7	150	19.427	0.008
54.02	1.75	1858.8	150	18.596	0.002
37.66	1.76	1863.3	150	19.895	0.018
29.1	1.76	1867.5	150	20.65	0.05
42.82	1.76	1868.3	150	19.472	0.021
48.36	1.77	1879.3	150	19.096	0.026
76.05	1.78	1885	150	17.583	0.004
76.28	1.79	1889	150	17.574	0.005
130.43	1.79	1893.5	150	16.037	0.035
107.88	1.79	1894.3	150	16.59	0.066
54.02	1.8	1903.5	150	18.632	0.003
94.91	1.81	1909	150	16.97	0.008
42.73	1.81	1914.3	150	19.503	0.024
93.82	1.81	1915	150	17.002	0.004
47.96	1.81	1915	150	19.126	0.026
48.46	1.82	1917	150	19.253	0.009
120.32	1.83	1927.8	150	16.287	0.014
42.75	1.83	1928.8	150	19.532	0.012
88.64	1.83	1933.3	150	17.195	0.014
54.22	1.86	1955.3	150	18.643	0.003
29.09	1.87	1962.5	150	20.688	0.024
100.48	1.87	1966	150	16.731	0.015
76.41	1.88	1973.5	150	17.591	0.005
95.16	1.89	1978.3	150	16.898	0.039
78.41	1.89	1984	150	17.557	0.007
87.84	1.92	2007	150	17.297	0.016
42.7	1.92	2007.5	150	19.595	0.016
76.47	1.92	2010.3	150	17.599	0.003
49.61	1.93	2019.8	150	19.343	0.022
78.36	1.96	2042.5	150	17.577	0.007
55.8	1.97	2051.3	150	18.699	0.01
78.38	1.98	2063.3	150	17.584	0.006
95.07	1.99	2070.8	150	16.936	0.038
78.72	2.00	2079	150	17.581	0.004
76.52	2.01	2089.2	150	17.628	0.003
94.95	2.02	2096	150	17	0.003
130.74	2.03	2109	150	16.031	0.035
94.56	2.04	2117.3	150	17.017	0.004
120.47	2.04	2119.3	150	16.279	0.012
37.69	2.06	2133.5	150	20.112	0.096
50.76	2.09	2156.8	150	19.48	0.046
56.2	2.12	2187.8	150	18.776	0.008
78.79	2.12	2190.5	150	17.616	0.004
101.56	2.14	2208.5	150	16.691	0.017
95.05	2.17	2235.8	150	17.025	0.075
76.71	2.18	2241.5	150	17.67	0.004
87.83	2.19	2254.5	150	17.367	0.022
108.26	2.2	2262.4	150	16.59	0.051
38.67	2.2	2263.5	150	20.18	0.05
29.25	2.22	2280	150	20.784	0.098
107.81	2.23	2286.3	150	16.633	0.021
56.64	2.23	2290.3	150	18.844	0.023
120.54	2.25	2301.8	150	16.284	0.012

94.72	2.26	2312.5	150	17.052	0.004
78.87	2.26	2315.3	150	17.665	0.009
131.1	2.27	2324	150	16.026	0.025
39.2	2.28	2334.5	150	19.803	0.05
50.34	2.31	2357	150	19.63	0.227
76.9	2.31	2358	150	17.684	0.004
56.86	2.33	2377.5	150	18.898	0.021
95.21	2.33	2378	150	17.055	0.003
101.91	2.37	2414	150	16.702	0.02
93.01	2.37	2415	150	17.101	0.116
97.48	2.38	2417.8	150	17.2	0.05
29.56	2.39	2428.3	150	20.944	0.081
86.99	2.39	2428.5	150	17.523	0.02
77.08	2.39	2429.5	150	17.717	0.017
97.2	2.41	2444.5	150	17.263	0.04
57.02	2.43	2462.8	150	18.967	0.019
121.15	2.43	2465.8	150	16.28	0.016
131.91	2.44	2475	150	16.025	0.01
140.69	2.45	2479.3	150	15.877	0.059
141.36	2.46	2494	150	15.939	0.097
56.75	2.47	2503	150	18.971	0.022
56.83	2.47	2503	150	18.979	0.041
108.54	2.47	2504.6	150	16.642	0.018
77.16	2.51	2534.8	150	17.744	0.015
97.38	2.51	2535.8	150	17.152	0.05
96.16	2.53	2556.7	150	17.041	0.05
79.18	2.55	2570.4	150	17.817	0.008
89.34	2.57	2585.8	150	17.426	0.13
101.73	2.6	2615	150	16.76	0.03
57.03	2.61	2626.3	150	19.027	0.023
77.29	2.63	2645.3	150	17.776	0.067
49.42	2.65	2665.5	150	19.042	0.05
38.51	2.68	2688	150	19.798	0.05
29.9	2.7	2705.8	150	20.612	0.133
77.42	2.7	2706.3	150	17.776	0.048
121.34	2.7	2707	150	16.323	0.02
57.07	2.71	2711	150	19.063	0.033
90.04	2.71	2716	150	17.306	0.05
96.27	2.72	2720.8	150	17.076	0.069
108.92	2.72	2724.5	150	16.748	0.059
132.09	2.73	2731	150	16.038	0.024
102.04	2.77	2767.5	150	16.754	0.025
57.09	2.81	2801.3	150	19.071	0.036
79.42	2.84	2829.2	150	17.969	0.016
30.36	2.85	2840	150	20.684	0.212
90.6	2.9	2883.5	150	17.305	0.113
121.73	2.94	2920.3	150	16.372	0.017
96.77	3.01	2986	150	17.318	0.056
46.78	3.02	2992.3	150	19.46	0.05
104.72	3.03	3002	150	16.997	0.107
48.82	3.03	3002	150	19.429	0.05
132.6	3.04	3010.3	150	16.073	0.044
141.7	3.05	3014.3	150	15.895	0.087
91.1	3.05	3021.3	150	17.197	0.05
91.11	3.07	3034.3	150	17.371	0.049

49.52	3.07	3036	150	19.143	0.05
109.88	3.11	3068.5	150	16.829	0.095
122.15	3.16	3117.4	150	16.424	0.03
102.9	3.19	3143	150	16.79	0.038
105.49	3.24	3185.5	150	16.852	0.224
105.17	3.34	3280.5	150	16.835	0.217
144.11	3.37	3301	150	16.003	0.095
144.48	3.61	3518.7	150	16.003	0.095
144.69	3.75	3643	150	16.003	0.095
144.44	3.79	3676.7	150	16.045	0.029
144.89	3.81	3696.7	150	15.992	0.023
144.36	4.04	3900	150	16.034	0.012

FeSi from FeSi20C10, 300K+high temperature data

#P GPa, T K, V A3#

1 Format P sigP T sigT V sigV

101.74	0.01	300	3	16.548	0.008
94.77	0.01	300	3	16.759	0.042
189.4	0.01	300	3	14.868	0.006
52.58	0.01	300	3	18.394	0.077
19.78	0.01	300	3	20.231	0.041
87.64	0.01	300	3	17.091	0.04
90.39	0.01	300	3	16.988	0.011
87.49	0.01	300	3	17.07	0.063
86.44	0.01	300	3	17.131	0.035
54.15	0.01	300	3	18.269	0.072
86.59	0.01	300	3	17.076	0.054
87.32	0.01	300	3	17.078	0.051
87.2	0.01	300	3	17.105	0.027
197.18	0.01	300	3	14.576	0.05
88.49	0.01	300	3	17.088	0.022
89.06	0.01	300	3	17.075	0.035
196.16	0.01	300	3	14.644	0.025
164.33	0.01	300	3	15.259	0.015
155.36	0.01	300	3	15.411	0.009
90.51	0.01	300	3	16.982	0.012
91.04	0.01	300	3	16.953	0.014
130.26	0.01	300	3	15.944	0.017
126.41	0.01	300	3	15.99	0.007
94.27	0.01	300	3	16.809	0.013
123.48	0.01	300	3	16.084	0.006
97.97	0.01	300	3	16.723	0.028
98.1	0.01	300	3	16.65	0.071
101.12	0.01	300	3	16.583	0.032
95.5	0.01	300	3	16.755	0.058
177.93	0.01	300	3	15.033	0.007
102.36	0.01	300	3	16.552	0.019
182.09	0.01	300	3	14.943	0.007
91.54	0.01	300	3	16.93	0.015
92.13	0.01	300	3	16.902	0.015
90.28	0.01	300	3	16.991	0.01
90.57	0.01	300	3	16.965	0.008
189.32	0.01	300	3	14.84	0.011
107.68	0.01	300	3	16.524	0.027
102.31	0.01	300	3	16.528	0.035
192.68	0.01	300	3	14.7	0.037
183	0.01	300	3	14.92	0.009
128.39	0.01	300	3	16.02	0.019
94.26	0.01	300	3	16.827	0.014
90.7	0.01	300	3	16.968	0.014
89.74	0.01	300	3	16.964	0.05
85.77	0.01	300	3	17.137	0.024
168.01	0.01	300	3	15.173	0.02
90.22	0.01	300	3	17.058	0.013
169.1	0.01	300	3	15.15	0.014
146.42	0.01	300	3	15.631	0.015

101.97	0.01	300	3	16.593	0.024
92.78	0.01	300	3	16.872	0.015
90.42	0.01	300	3	16.985	0.012
195.6	0.01	300	3	14.645	0.006
91.42	0.01	300	3	17.022	0.032
90.67	0.01	300	3	16.974	0.013
87.73	0.01	300	3	17.024	0.021
88.36	0.01	300	3	17.086	0.024
87.59	0.01	300	3	17.093	0.036
95.74	0.01	300	3	16.788	0.011
89.51	0.01	300	3	17.025	0.008
103.27	0.01	300	3	16.567	0.019
95.01	0.01	300	3	16.731	0.061
93.34	0.01	300	3	16.843	0.015
54.35	1.08	1259.5	150	18.486	0.018
31.93	1.08	1259.8	150	19.79	0.032
20.26	1.1	1278	150	20.665	0.041
91.51	1.11	1288.5	150	17.051	0.053
49.82	1.15	1320.8	150	18.61	0.039
31.77	1.19	1354	150	19.816	0.021
90.7	1.23	1390	150	17.085	0.015
101.72	1.23	1390.5	150	16.58	0.018
84.44	1.23	1392.3	150	17.286	0.018
90.26	1.25	1411	150	17.208	0.034
97.6	1.26	1422.3	150	16.789	0.01
54.46	1.27	1428	150	18.473	0.007
31.65	1.27	1429.5	150	19.806	0.019
87.86	1.31	1463.5	150	17.148	0.021
89.93	1.32	1475	150	17.089	0.015
50.52	1.33	1483.3	150	18.629	0.023
84.87	1.33	1484.5	150	17.291	0.013
101.89	1.33	1486.5	150	16.575	0.019
20.15	1.34	1491	150	20.792	0.04
159.49	1.38	1523	150	15.369	0.016
97.73	1.38	1526.5	150	16.781	0.009
173.19	1.38	1527	150	15.097	0.009
184.76	1.38	1530.2	150	14.936	0.012
193.55	1.39	1535.5	150	14.762	0.012
54.67	1.39	1539.5	150	18.453	0.013
102.13	1.39	1540.3	150	16.567	0.021
31.71	1.4	1547.8	150	19.866	0.014
50.66	1.41	1555.5	150	18.637	0.026
90.81	1.42	1566	150	17.093	0.013
54.4	1.44	1582	150	18.485	0.016
192.35	1.45	1588.3	150	14.722	0.01
102.23	1.46	1595	150	16.559	0.023
121.55	1.47	1611.3	150	16.15	0.046
98.1	1.49	1622.3	150	16.777	0.009
31.66	1.49	1622.5	150	19.889	0.01
51.14	1.49	1622.5	150	18.677	0.025
55.61	1.51	1644.3	150	18.533	0.097
87.78	1.53	1660	150	17.16	0.013
31.82	1.55	1679.5	150	19.898	0.012
54.32	1.56	1687.5	150	18.546	0.05
102.49	1.56	1687.5	150	16.56	0.023

141.38	1.57	1695.7	150	15.817	0.017
193.52	1.58	1701.3	150	14.763	0.014
51.35	1.58	1705.8	150	18.695	0.019
192.11	1.59	1716.8	150	14.726	0.013
185.07	1.62	1739.5	150	14.94	0.01
98.31	1.62	1742.5	150	16.77	0.011
173.28	1.63	1746	150	15.102	0.009
54.38	1.63	1753.8	150	18.598	0.01
122.11	1.64	1756.3	150	16.186	0.023
51.4	1.64	1757.5	150	18.732	0.009
88.98	1.65	1772	150	17.118	0.017
31.9	1.66	1776.8	150	19.974	0.01
90.54	1.66	1780.5	150	17.058	0.004
103.09	1.7	1811.8	150	16.54	0.019
98.61	1.71	1820	150	16.753	0.01
160.05	1.71	1825.4	150	15.371	0.008
31.69	1.72	1833.3	150	19.799	0.022
54.84	1.75	1853.8	150	18.583	0.018
91.13	1.76	1865.3	150	17.069	0.002
90.62	1.77	1878	150	17.085	0.007
98.74	1.78	1880	150	16.745	0.007
103.47	1.79	1892.8	150	16.531	0.013
51.86	1.79	1896.3	150	18.741	0.009
192.07	1.81	1907.3	150	14.755	0.011
90.94	1.81	1907.8	150	17.124	0.011
122.45	1.82	1917.3	150	16.209	0.018
52.04	1.84	1938	150	18.736	0.007
98.94	1.85	1943.3	150	16.744	0.004
193.7	1.85	1944.3	150	14.767	0.014
55.5	1.85	1944.8	150	18.635	0.051
185.2	1.85	1946	150	14.944	0.009
142.01	1.89	1979.5	150	15.756	0.012
90.51	1.9	1994.5	150	17.103	0.003
103.78	1.91	2001	150	16.538	0.006
122.9	1.91	2003.3	150	16.206	0.007
86.32	1.91	2004.8	150	17.341	0.022
173.84	1.93	2016.8	150	15.112	0.013
127.57	1.94	2031.3	150	16.064	0.003
123.8	1.95	2033.5	150	16.193	0.006
56.16	1.95	2040.5	150	18.539	0.046
123.9	1.97	2055.8	150	16.207	0.004
99.31	1.98	2065.5	150	16.748	0.002
160.59	1.98	2067.2	150	15.377	0.015
90.32	1.99	2073.5	150	17.132	0.002
53.12	2	2081.8	150	18.7	0.074
103.78	2.01	2087.8	150	16.56	0.002
99.3	2.02	2095.5	150	16.753	0.002
143.26	2.06	2135	150	15.733	0.008
192.29	2.07	2138.8	150	14.825	0.016
91.56	2.07	2143.3	150	17.198	0.013
99.52	2.07	2145	150	16.758	0.006
193.94	2.07	2146.2	150	14.766	0.019
90.33	2.09	2160.5	150	17.143	0.005
56.43	2.11	2177.5	150	18.666	0.05
56.84	2.12	2184.3	150	18.598	0.028

103.81	2.13	2196.8	150	16.584	0.002
90.48	2.16	2224.5	150	17.148	0.003
99.78	2.18	2244.3	150	16.758	0.003
104.04	2.19	2250.7	150	16.575	0.003
99.88	2.21	2265.3	150	16.766	0.006
59.98	2.23	2285.5	150	18.539	0.05
56.14	2.24	2296.5	150	18.684	0.05
144.44	2.24	2298.8	150	15.715	0.014
128.11	2.26	2311	150	16.078	0.006
194.04	2.26	2312.8	150	14.762	0.02
99.8	2.26	2314.8	150	16.776	0.05
174.42	2.26	2315	150	15.108	0.027
161.05	2.27	2322.2	150	15.375	0.022
185.7	2.27	2323	150	14.938	0.01
104.14	2.28	2326.8	150	16.587	1E-3
192.32	2.31	2354.8	150	14.889	0.009
57.01	2.32	2364.3	150	18.568	0.05
99.97	2.35	2396	150	16.8	0.01
103.46	2.36	2402	150	16.654	0.008
53.98	2.37	2412	150	18.678	0.05
54.39	2.38	2421.8	150	18.671	0.05
91.58	2.45	2478.5	150	17.201	0.067
186.71	2.47	2501.6	150	14.929	0.008
100.04	2.48	2510	150	16.802	0.003
175.66	2.49	2520.5	150	15.108	0.008
110.22	2.49	2521.5	150	16.671	0.005
191.63	2.5	2525.4	150	14.94	0.009
162.5	2.5	2526.2	150	15.332	0.031
145.86	2.5	2526.8	150	15.72	0.008
56.23	2.5	2527.5	150	18.674	0.05
129.07	2.51	2532.5	150	16.108	0.004
194.81	2.51	2537.6	150	14.752	0.012
100.18	2.57	2590.3	150	16.666	0.019
110.08	2.6	2617	150	16.66	0.009
110.13	2.64	2648	150	16.633	0.013
110.23	2.66	2668.3	150	16.625	0.015
163.34	2.71	2717.8	150	15.345	0.019
129.64	2.71	2719	150	16.138	0.004
146.91	2.74	2744.8	150	15.834	0.008
176.83	2.75	2746.4	150	15.125	0.008
187.12	2.76	2759.2	150	14.968	0.012
195.25	2.77	2764.7	150	14.738	0.011
191.06	2.79	2789.2	150	15.003	0.014
110.15	2.8	2794	150	16.694	0.047
91.62	2.83	2822.3	150	17.116	0.05
110.09	2.83	2824	150	16.703	0.033
129.76	2.93	2915	150	16.177	0.008
164.47	2.97	2950	150	15.401	0.029
188.17	3	2975.4	150	15.002	0.01
178.25	3.01	2981.4	150	15.184	0.02
190.42	3.04	3012.7	150	15.029	0.009
165.28	3.07	3037.3	150	15.395	0.012
147.9	3.1	3060	150	15.874	0.032
91.59	3.11	3074.3	150	17.086	0.05
189.36	3.13	3085.2	150	15.011	0.018

178.82	3.13	3088.6	150	15.217	0.033
190.34	3.26	3206.3	150	15.064	0.014
131.35	3.87	3753.8	150	16.206	0.01

Fe(hcp) in FeSi3C3
Selected isotherms 1500, 1700, 2000, 2100, 2200, 2500, 2800, 2900.
P GPa T K V A^3

P	sigP	T	sigT	V	sigV
27.02	0.01	300.0	3	19.997	0.104
42.91	0.01	300.0	3	19.262	0.136
67.37	0.01	300.0	3	18.114	0.080
67.98	0.01	300.0	3	18.146	0.040
69.21	0.01	300.0	3	18.160	0.100
86.35	0.01	300.0	3	17.371	0.068
86.73	0.01	300.0	3	17.297	0.100
87.08	0.01	300.0	3	17.442	0.100
87.22	0.01	300.0	3	17.331	0.075
87.35	0.01	300.0	3	17.330	0.076
111.67	0.01	300.0	3	16.716	0.080
120.68	0.01	300.0	3	16.292	0.090
127.67	0.01	300.0	3	16.171	0.100
149.86	0.01	300.0	3	15.734	0.060
149.96	0.01	300.0	3	15.717	0.050
164.90	0.01	300.0	3	15.446	0.041
188.94	0.01	300.0	3	15.144	0.047
169.33	0.01	300.0	3	15.414	0.017
175.74	0.01	300.0	3	15.255	0.020
182.32	0.01	300.0	3	15.096	0.047
190.39	0.01	300.0	3	15.083	0.183
190.98	0.01	300.0	3	15.080	0.063
185.26	1.36	1505.0	150	15.101	0.083
86.37	1.36	1507.7	150	17.571	0.018
51.11	1.37	1515.3	150	18.988	0.038
100.82	1.37	1520.0	150	16.800	0.069
139.64	1.37	1520.0	150	15.944	0.100
43.52	1.39	1536.0	150	19.582	0.032
83.63	1.42	1559.5	150	17.677	0.012
169.26	1.42	1560.7	150	15.431	0.102
122.89	1.42	1562.0	150	16.418	0.100
169.10	1.42	1562.0	150	15.420	0.060
26.51	1.43	1570.0	150	20.470	0.680
43.24	1.45	1588.8	150	19.578	0.059
186.10	1.57	1700.7	150	15.097	0.043
86.99	1.58	1703.5	150	17.438	0.106
140.25	1.58	1703.7	150	15.912	0.100
169.45	1.58	1704.0	150	15.408	0.064
84.90	1.58	1707.5	150	17.702	0.048
101.30	1.59	1716.0	150	16.827	0.026
44.17	1.59	1717.0	150	19.460	0.054
86.66	1.60	1720.0	150	17.455	0.119
68.46	1.60	1723.0	150	18.363	0.015
86.66	1.60	1724.3	150	17.619	0.008
28.46	1.62	1744.0	150	20.299	0.053
44.73	1.64	1759.5	150	19.488	0.112
51.85	1.67	1782.8	150	19.112	0.034
45.22	1.68	1791.8	150	19.431	0.054
87.22	1.98	2059.0	150	17.497	0.125

52.52	1.98	2062.8	150	19.066	0.343
88.63	1.98	2065.0	150	17.366	0.091
85.78	1.98	2066.3	150	17.744	0.062
68.80	1.99	2067.3	150	18.591	0.198
141.89	1.99	2071.3	150	15.922	0.100
187.68	2.01	2088.0	150	15.139	0.272
111.89	2.02	2098.2	150	16.860	0.001
170.28	2.02	2101.0	150	15.422	0.057
118.88	2.03	2105.0	150	16.670	0.063
86.10	2.07	2140.5	150	17.746	0.164
69.40	2.12	2187.0	150	18.487	0.274
87.28	2.14	2210.0	150	17.507	0.126
52.68	2.18	2243.8	150	19.001	0.655
112.06	2.21	2269.0	150	16.887	0.034
86.42	2.23	2282.5	150	17.724	0.079
69.61	2.23	2288.8	150	18.540	0.311
142.88	2.24	2294.5	150	15.937	0.063
151.19	2.47	2502.3	150	15.776	0.068
170.70	2.49	2520.3	150	15.429	0.149
89.16	2.53	2550.0	150	17.538	0.150
69.96	2.57	2588.5	150	18.583	0.284
120.79	2.81	2801.5	150	16.691	0.254
151.94	2.89	2876.0	150	15.806	0.071
89.21	2.91	2890.0	150	17.573	0.153
70.57	2.92	2900.0	150	18.596	0.100
149.17	2.92	2901.7	150	15.941	0.285
189.41	2.93	2912.0	150	15.244	0.074
172.10	2.94	2922.2	150	15.492	0.100
121.00	3.01	2979.0	150	16.774	0.626
89.34	3.05	3019.5	150	17.465	0.136
190.45	3.15	3104.0	150	15.244	0.181
150.78	3.17	3125.0	150	15.990	0.316
89.62	3.20	3153.0	150	17.471	0.144
88.30	3.39	3322.0	150	17.528	0.100

Fe3C in FeSi3C3
Selected Isotherms: 1400,1500,1700,1800,1900, 2100, 2300, 2400, 2500, 2600, 2700, >3000

P GPa T K V A^3

P sigP T sigT V sigV

27.02	0.01	300.0	3	138.7530.010
67.37	0.01	300.0	3	125.7172.770
67.98	0.01	300.0	3	126.4390.725
86.35	0.01	300.0	3	122.2600.802
87.35	0.01	300.0	3	122.1620.954
87.22	0.01	300.0	3	122.1690.820
111.67	0.01	300.0	3	117.6440.371
149.86	0.01	300.0	3	111.0600.237
149.96	0.01	300.0	3	110.7780.514
164.90	0.01	300.0	3	108.8691.319
169.33	0.01	300.0	3	108.2291.977
175.74	0.01	300.0	3	107.6540.493
182.32	0.01	300.0	3	106.5790.597
188.94	0.01	300.0	3	106.9431.723
190.98	0.01	300.0	3	106.5741.585
190.39	0.01	300.0	3	106.3621.871
43.80	1.26	1418.3	150	135.4060.100
51.23	1.27	1431.5	150	132.0310.100
68.39	1.29	1448.0	150	127.5190.405
26.84	1.29	1449.0	150	141.1770.100
27.24	1.33	1486.0	150	141.1980.100
82.75	1.34	1494.8	150	124.4150.988
185.26	1.36	1505.0	150	106.3341.352
51.11	1.37	1515.3	150	132.1830.100
43.52	1.39	1536.0	150	136.0790.010
83.63	1.42	1559.5	150	124.1510.832
169.26	1.42	1560.7	150	109.0660.550
169.10	1.42	1562.0	150	108.7061.358
43.24	1.45	1588.8	150	136.1590.100
186.10	1.57	1700.7	150	106.6750.100
86.99	1.58	1703.5	150	123.1610.112
169.45	1.58	1704.0	150	108.9830.475
84.90	1.58	1707.5	150	124.2791.131
44.17	1.59	1717.0	150	135.1630.100
86.66	1.60	1720.0	150	123.2940.057
68.46	1.60	1723.0	150	128.3590.058
86.66	1.60	1724.3	150	123.3680.144
28.46	1.62	1744.0	150	140.3630.100
44.73	1.64	1759.5	150	134.9950.100
51.85	1.67	1782.8	150	133.3320.100
45.22	1.68	1791.8	150	135.4290.100
52.20	1.69	1801.3	150	133.2080.100
45.45	1.71	1825.0	150	135.3810.100
28.45	1.72	1830.0	150	140.5330.100
117.93	1.73	1841.5	150	116.8370.449
87.10	1.78	1881.0	150	123.4270.052
51.90	1.79	1889.0	150	133.5280.100
186.78	1.79	1893.5	150	106.1010.067

170.04	1.80	1899.5	150	108.9330.156
68.58	1.80	1905.5	150	128.6500.252
85.69	1.82	1919.5	150	124.3971.201
189.43	1.89	1980.0	150	106.8311.323
111.74	1.89	1980.7	150	118.4530.076
52.17	1.89	1981.0	150	132.9170.100
111.94	1.91	1996.3	150	118.5880.085
170.28	2.02	2101.0	150	109.1050.434
118.88	2.03	2105.0	150	116.8480.585
86.10	2.07	2140.5	150	124.8581.108
69.40	2.12	2187.0	150	128.2650.644
170.45	2.25	2303.3	150	109.1170.320
119.61	2.25	2305.0	150	117.2640.406
187.87	2.29	2338.8	150	107.2660.978
112.12	2.30	2348.0	150	118.9040.214
69.71	2.35	2389.0	150	128.2770.656
87.34	2.37	2412.5	150	123.9330.223
89.03	2.42	2451.5	150	123.2370.432
112.04	2.42	2459.4	150	118.9400.194
188.24	2.46	2487.5	150	107.2310.763
69.90	2.46	2491.3	150	128.3380.648
145.74	2.46	2495.3	150	112.1010.449
120.28	2.47	2496.0	150	117.5200.421
151.19	2.47	2502.3	150	111.7090.214
170.70	2.49	2520.3	150	109.1890.446
89.16	2.53	2550.0	150	123.6880.988
69.96	2.57	2588.5	150	128.6590.522
120.66	2.60	2615.0	150	117.6870.208
89.08	2.64	2650.0	150	123.5850.047
70.14	2.66	2669.2	150	127.9291.755
146.99	2.68	2691.3	150	112.1810.891
188.65	2.69	2699.5	150	107.2860.798
151.39	2.70	2709.0	150	111.7200.489
171.31	2.72	2719.5	150	109.1170.421
88.99	2.74	2745.0	150	124.2050.599
89.34	3.05	3019.5	150	124.2501.021
172.08	3.13	3085.2	150	109.5331.488
190.45	3.15	3104.0	150	107.2791.045
150.78	3.17	3125.0	150	112.5051.081
89.62	3.20	3153.0	150	124.1870.767

Fe7C3 from FeSi10C20, 300K+high temperature data

P GPa, T K, V A3

P	sigP	T	sigT	V	sigV
26.73	0.01	300.00	150.00	169.340	0.08
116.12	0.01	300.00	150.00	142.540	0.18
111.11	0.01	300.00	150.00	143.400	0.12
28.01	0.01	300.00	150.00	170.000	0.16
122.77	0.01	300.00	150.00	140.830	0.47
126.18	0.01	300.00	150.00	140.530	0.14
109.21	0.01	300.00	150.00	144.310	0.30
105.15	0.01	300.00	150.00	145.420	0.21
102.63	0.01	300.00	150.00	145.190	0.14
101.31	0.01	300.00	150.00	145.440	0.14
95.53	0.01	300.00	150.00	147.780	0.83
127.13	0.01	300.00	150.00	140.230	0.34
77.65	0.01	300.00	150.00	151.270	0.01
76.29	0.01	300.00	150.00	152.360	0.08
56.29	0.01	300.00	150.00	159.130	1.16
120.46	0.01	300.00	150.00	141.420	0.40
42.13	0.01	300.00	150.00	163.460	0.04
131.12	0.01	300.00	150.00	139.720	0.19
133.49	0.01	300.00	150.00	139.220	0.15
137.10	0.01	300.00	150.00	138.570	0.12
98.37	0.01	300.00	150.00	146.030	0.11
137.54	0.01	300.00	150.00	138.490	0.05
116.68	0.01	300.00	150.00	142.750	0.06
28.60	1.09	1270.00	150.00	170.980	0.26
28.58	1.09	1270.00	150.00	171.040	0.21
28.65	1.24	1400.00	150.00	171.520	0.10
53.26	1.29	1445.75	150.00	159.550	0.14
28.80	1.29	1450.00	150.00	171.680	0.05
107.63	1.33	1479.00	150.00	145.750	0.37
129.95	1.34	1495.75	150.00	140.750	0.19
94.88	1.35	1497.00	150.00	147.860	0.21
90.48	1.35	1500.00	150.00	148.070	1.15
87.93	1.36	1507.50	150.00	149.950	0.33
53.38	1.37	1522.00	150.00	159.770	0.15
48.64	1.40	1544.50	150.00	162.600	0.16
119.49	1.40	1549.00	150.00	143.270	0.08
37.51	1.41	1555.00	150.00	167.250	0.24
28.36	1.42	1559.50	150.00	171.910	0.18
53.66	1.43	1570.67	150.00	159.760	0.13
88.20	1.44	1577.25	150.00	149.650	0.32
94.58	1.45	1587.25	150.00	147.080	0.46
40.14	1.46	1600.00	150.00	166.730	0.05
40.14	1.46	1602.00	150.00	166.890	0.11
37.54	1.47	1605.00	150.00	167.250	0.31
88.34	1.47	1610.50	150.00	149.630	0.26
40.24	1.49	1621.75	150.00	166.460	0.06
28.60	1.49	1622.25	150.00	172.600	0.14
37.52	1.50	1630.00	150.00	167.440	0.28
97.87	1.51	1642.50	150.00	145.860	0.18
53.69	1.52	1650.75	150.00	159.890	0.08

37.43	1.55	1675.00150.00	167.5400.36
130.09	1.57	1695.25150.00	140.9600.12
94.80	1.58	1705.33150.00	148.0600.22
107.63	1.58	1708.00150.00	145.7500.32
88.85	1.58	1709.25150.00	149.8400.25
75.96	1.59	1712.75150.00	153.0700.29
37.60	1.59	1718.00150.00	167.6500.32
48.36	1.59	1719.00150.00	163.2600.07
53.84	1.60	1719.75150.00	160.0800.07
28.57	1.60	1726.75150.00	172.3900.55
119.81	1.61	1732.75150.00	143.2300.10
88.75	1.61	1735.00150.00	149.9700.28
40.23	1.64	1760.00150.00	167.6300.12
78.32	1.67	1782.75150.00	152.5400.05
88.52	1.67	1787.75150.00	150.0700.20
94.31	1.68	1790.75150.00	147.8100.10
42.83	1.69	1803.00150.00	165.6300.05
94.72	1.69	1804.50150.00	147.7700.51
42.78	1.69	1808.00150.00	165.6000.05
78.60	1.71	1818.25150.00	152.5300.08
76.07	1.71	1824.33150.00	153.0000.09
88.52	1.72	1827.50150.00	150.1600.23
100.61	1.73	1842.00150.00	146.3300.21
42.78	1.75	1855.67150.00	165.7700.04
54.02	1.75	1858.75150.00	160.3500.09
37.66	1.76	1863.25150.00	168.5300.14
42.82	1.76	1868.33150.00	165.7900.05
48.36	1.77	1879.25150.00	163.7400.24
76.05	1.78	1885.00150.00	153.1500.04
76.28	1.79	1889.00150.00	153.1500.11
130.43	1.79	1893.50150.00	140.7800.13
107.88	1.79	1894.25150.00	145.4800.28
54.02	1.80	1903.50150.00	160.5400.03
94.91	1.81	1909.00150.00	148.3000.22
42.73	1.81	1914.33150.00	165.9100.06
47.96	1.81	1915.00150.00	164.2600.13
93.82	1.81	1915.00150.00	148.4900.17
48.46	1.82	1917.00150.00	164.6900.14
120.32	1.83	1927.75150.00	143.0000.06
42.75	1.83	1928.75150.00	165.9300.03
88.64	1.83	1933.25150.00	150.2400.21
54.22	1.86	1955.25150.00	160.5800.06
100.48	1.87	1966.00150.00	146.5600.18
76.41	1.88	1973.50150.00	153.3000.06
95.16	1.89	1978.25150.00	147.8800.25
78.41	1.89	1984.00150.00	152.9500.03
87.84	1.92	2007.00150.00	150.8300.20
42.70	1.92	2007.50150.00	166.2200.02
76.47	1.92	2010.25150.00	153.3400.10
49.61	1.93	2019.75150.00	164.5800.76
78.36	1.96	2042.50150.00	153.0800.03
55.80	1.97	2051.25150.00	160.9400.13
78.38	1.98	2063.25150.00	153.1500.01
95.07	1.99	2070.75150.00	148.1200.40
78.72	2.00	2079.00150.00	153.0900.03

76.52	2.01	2089.20150.00	153.5500.03
94.95	2.02	2096.00150.00	148.7600.07
130.74	2.03	2109.00150.00	140.7000.11
94.56	2.04	2117.25150.00	148.8800.06
120.47	2.04	2119.25150.00	142.9000.06
50.76	2.09	2156.75150.00	164.5300.19
56.20	2.12	2187.75150.00	161.2000.09
78.79	2.12	2190.50150.00	153.3700.03
101.56	2.14	2208.50150.00	146.3100.17
95.05	2.17	2235.75150.00	148.8700.10
76.71	2.18	2241.50150.00	153.8500.05
87.83	2.19	2254.50150.00	150.9100.17
108.26	2.20	2262.40150.00	145.6400.04
107.81	2.23	2286.25150.00	145.6400.18
56.64	2.23	2290.25150.00	161.2500.07
120.54	2.25	2301.75150.00	142.9600.08
94.72	2.26	2312.50150.00	149.1300.07
78.87	2.26	2315.25150.00	153.6500.03
131.10	2.27	2324.00150.00	140.8300.06
50.34	2.31	2357.00150.00	164.7100.1
76.90	2.31	2358.00150.00	153.9900.03
56.86	2.33	2377.50150.00	161.3500.04
95.21	2.33	2378.00150.00	149.1700.07
101.91	2.37	2414.00150.00	146.5600.13
93.01	2.37	2415.00150.00	149.2400.18
97.48	2.38	2417.75150.00	149.0300.32
86.99	2.39	2428.50150.00	151.4700.18
77.08	2.39	2429.50150.00	154.1900.03
97.20	2.41	2444.50150.00	149.3400.29
57.02	2.43	2462.75150.00	161.5500.06
121.15	2.43	2465.75150.00	143.2300.14
131.91	2.44	2475.00150.00	140.6600.16
140.69	2.45	2479.25150.00	139.0200.19
141.36	2.46	2494.00150.00	139.5600.21
56.83	2.47	2503.00150.00	161.6400.12
56.75	2.47	2503.00150.00	161.5900.06
108.54	2.47	2504.60150.00	145.8900.17
77.16	2.51	2534.75150.00	154.3900.03
97.38	2.51	2535.75150.00	149.5300.10
96.16	2.53	2556.67150.00	149.1800.22
79.18	2.55	2570.40150.00	154.2600.03
89.34	2.57	2585.75150.00	151.3100.21
101.73	2.60	2615.00150.00	146.9700.13
57.03	2.61	2626.25150.00	161.6000.25
77.29	2.63	2645.25150.00	154.5800.07
77.42	2.70	2706.25150.00	154.6000.06
121.34	2.70	2707.00150.00	143.4700.09
57.07	2.71	2711.00150.00	161.6600.18
90.04	2.71	2716.00150.00	150.9300.27
96.27	2.72	2720.75150.00	149.3700.20
108.92	2.72	2724.50150.00	146.4800.10
132.09	2.73	2731.00150.00	140.8000.15
102.04	2.77	2767.50150.00	147.1300.16
57.09	2.81	2801.33150.00	161.4600.36
90.60	2.90	2883.50150.00	150.9800.42

121.73	2.94	2920.25	150.00	143.62 00.16
96.77	3.01	2986.00	150.00	149.66 00.18
104.72	3.03	3002.00	150.00	147.55 00.15
132.60	3.04	3010.25	150.00	141.55 00.17
141.70	3.05	3014.33	150.00	139.35 00.22
91.11	3.07	3034.25	150.00	150.43 00.24
109.88	3.11	3068.50	150.00	146.47 00.19
122.15	3.16	3117.40	150.00	143.18 00.59
102.90	3.19	3143.00	150.00	147.18 00.23
144.11	3.37	3301.00	150.00	139.44 00.17
144.48	3.61	3518.67	150.00	139.44 00.17
144.69	3.75	3643.00	150.00	139.44 00.17
144.44	3.79	3676.67	150.00	139.37 00.04
144.89	3.81	3696.67	150.00	139.44 00.18
144.36	4.04	3900.00	150.00	139.56 00.15